ICP/EXT-05-00979

Operable Unit 10-08 Summary Report on the Subregional-scale Two-dimensional Aquifer Model

September 2005

Idaho Cleanup Project

The Idaho Cleanup Project is operated for the
U.S. Department of Energy by CH2M◆WG Idaho, LLC

ICP/EXT-05-00979
Revision 0
Project No. 23368

Operable Unit 10-08 Summary Report on the Subregional-scale Two-dimensional Aquifer Model

Thomas R. Wood
Catherine M. Helm-Clark
Hai Huang
Swen Magnuson
Travis McCling
Bennon Orr
Michael Roddy
Michael J. Rohe
Mitchell A. Plummer
Robert Podgorney

September 2005

Idaho Cleanup Project

Idaho Falls, Idaho 83415

Prepared for the
U.S. Department of Energy
Assistant Secretary for Environmental Management
Under DOE Idaho Operations Office
Contract DE-AC07-05ID14516

ABSTRACT

This document presents a two-dimensional conceptual model and two-dimensional numerical model representing groundwater flow in the Snake River Plain Aquifer in the subregional area surrounding and beneath the Idaho National Laboratory Site. These modeling activities make up the initial step in a phased project that will ultimately result in a three-dimensional flow and transport model that will form the basis of the record of decision for Waste Area Group 10, Operable Unit 10-08. The Operable Unit 10-08 modeling study will address a need for a model scaled to an appropriate subregional domain, so that risk to groundwater receptors can be calculated anywhere within the Idaho National Laboratory Site. Operable Unit 10-08 groundwater studies address areas outside the boundaries of the other individual waste area groups and consider the potential for risk created by commingling of residual plumes left by those groups. The modeling studies will also serve to communicate the cumulative risks for the aquifer from site activities to concerned stakeholders. In this role, the model will serve to integrate knowledge gained during investigations of individual waste area groups into a comprehensive aquifer management tool that will allow incorporation of smaller individual aquifer models in a seamless, consistent manner. The activities conducted for Operable Unit 10-08 groundwater modeling studies are guided by the negotiated and agency-approved *Idaho National Engineering and Environmental Laboratory Operable Unit 10-08 Sitewide Groundwater Model Work Plan.*

The conceptual sitewide groundwater model presented in this document has been developed from supporting evidence and interpretations derived from the disciplines of geology, geochemistry, earth heat flow, and hydrology. Using the conceptual sitewide groundwater model as a foundation, the two-dimensional subregional-scale aquifer flow model was developed. The simulation domain was refined from the original study area outlined in the groundwater model work plan. Model development included using three inverse calibration methods: (1) the traditional zonation method, (2) the pilot-point method, and (3) a coupled zonation/pilot-point method. The latter method was employed in an attempt to honor the large-scale geologic features identified in the sitewide groundwater model. The different calibration approaches were evaluated based on the agreement between simulated and observed heads, the reasonableness of the estimated hydraulic conductivity fields, and the uncertainty in the estimated hydraulic conductivity fields. The two approaches using the pilot-point method were also evaluated using particle tracking with starting points at site facilities. The simulated heads were greatly improved with either of the two approaches using the pilot-point method, but the coupled zonation/pilot-point method yielded the best agreement. The coupled zonation/pilot-point method, however, had much greater uncertainty associated with the resulting hydraulic conductivity field. The sensitivity of simulation results to two conceptualizations of aquifer thickness were tested, as was the influence of hydrologic properties, perimeter water influxes, and spatially variable surface recharge.

The two-dimensional modeling approach is recognized in this document to have limitations that will require simulation of contaminant transport in three dimensions. These limitations range from the obvious where contaminants are required to be uniformly mixed over the entire vertical profile in two-dimensional models to more complex issues related to preferential flow pathways identified in geochemical and isotope studies. Groundwater modeling that will honor these inferred preferential flow pathways will require the capability to vary aquifer properties in three dimensions.

CONTENTS

FIGURES

TABLES

ACRONYMS

AVH	Axial Volcanic High
B&R	Basin and Range
BLT	Big Lost Trough
BSU	Boise State University
CERCLA	Comprehensive Environmental Response, Compensation, and Liability Act
CFA	Central Facilities Area
CFC	chlorofluorocarbon
cfs	cubic feet per second
DCE	dichloroethene
DEQ	Department of Environmental Quality
DOE-ID	U.S. Department of Energy Idaho Operations Office
EIS	environmental impact statement
EPA	U.S. Environmental Protection Agency
ESRP	eastern Snake River Plain
GMS	Groundwater Modeling System
INL	Idaho National Laboratory
INTEC	Idaho Nuclear Technology and Engineering Center
IWRRI	Idaho Water Resources Research Institute
MCL	maximum contaminant level
NWIS	National Water Information System
OU	operable unit
RI/FS	remedial investigation/feasibility study
ROD	record of decision
RTC	Reactor Technology Complex
RWMC	Radioactive Waste Management Complex

SRPA	Snake River Plain Aquifer
SWGM	sitewide groundwater model
TAN	Test Area North
TRA	Test Reactor Area
TSF	Technical Support Facility
USGS	United States Geological Survey
WAG	waste area group

Operable Unit 10-08 Summary Report on the Subregional-scale Two-dimensional Aquifer Model

1. INTRODUCTION

The purpose of Waste Area Group (WAG) 10, Operable Unit (OU) 10-08, groundwater modeling studies is to provide a comprehensive evaluation of environmental impacts from operations at the Idaho National Laboratory (INL) Site to the underlying Snake River Plain Aquifer (SRPA). In particular, OU 10-08 groundwater studies address areas outside the boundaries of the other individual INL WAGs and consider the potential for risk created by the commingling of residual plumes left by those WAGs. The cumulative impacts on the SRPA are being evaluated during the OU 10-08 remedial investigation/feasibility study (RI/FS).

The OU 10-08 groundwater modeling studies are guided by the *Idaho National Engineering and Environmental Laboratory Operable Unit 10-08 Sitewide Groundwater Model Work Plan* (DOE-ID 2004). That plan was developed in collaboration with and review by the U.S. Department of Energy Idaho Operations Office (DOE-ID), the Idaho Department of Environmental Quality (DEQ), and the U.S. Environmental Protection Agency (EPA) to ensure that the products of the modeling studies match those needed for the OU 10-08 RI/FS process. This approach is intended to significantly expand the regulatory agencies' involvement in the development of the model by engaging them early and frequently over the course of the project. The overall modeling objectives statement and issues resulting from the collaborative planning effort are documented in the groundwater model work plan (DOE-ID 2004).

To enhance integration with the numerous parties involved in modeling aquifer flow and transport in the region, the project is using a tiered approach to the model design. This report presents the first step in our numerical simulations, i.e., a steady-state two-dimensional flow model. Development and testing of the two-dimensional model has helped us identify problems—for example, issues related to the flow field, localized versus regional issues of scale, and usability of certain well data—that will be resolved in the final three-dimensional model. Once approved for release by the regulatory agencies, the two-dimensional model will also be a means for opening communications with interested stakeholders, such as personnel from other WAGs, the United States Geological Survey (USGS), and state and federal agencies, on the scope and breadth of the OU 10-08 sitewide groundwater model (SWGM). The tiered approach is cost-effective and will help to identify technical and administrative areas of conflict early enough in the process to solve issues in a timely manner during the RI/FS.

As indicated, this model is the first step in a process that will eventually lead to comprehensive transport simulations for the INL Site that have an adequate technical basis. The first step is a two-dimensional flow model. Therefore, transport is not discussed in this document, nor is risk. Implications for transport are discussed in terms of simulated flow paths and possible commingling of anthropogenic contaminant plumes.

1.1 Background

A key component of the RI/FS effort (DOE-ID 2002) and long-term stewardship of the groundwater resources at the INL Site is the development of an INL sitewide groundwater-flow and contaminant-transport numerical model. The model will support decisions and be a tool for managing, compiling, and synthesizing data regarding the SRPA beneath the INL Site. Currently, several different aquifer models are used at the INL Site to satisfy specific program needs. These models are not consistent

in some cases and are sometimes redundant in the regimes they represent. Preparation of the SWGM provides the opportunity to promote consistency and eliminate redundancies in INL aquifer models. In the short term, the SWGM will be used to satisfy requirements for preparation of the OU 10-08 record of decision (ROD) and will supplement and support existing aquifer models. However, the design of the SWGM will eventually allow incorporation of smaller individual aquifer models in a seamless, consistent manner. Although vadose zone transport modeling is the responsibility of individual WAGs, the assumptions and implementation used in the individual WAG vadose zone models will be reviewed as the contaminant fluxes are implemented into the SWGM.

The need for the SWGM is also driven by advancements in the understanding of the INL Site subsurface and greatly improved computational capabilities. During the past decade, INL Site contractors, the USGS, and numerous academic institutions have obtained information that significantly changes the conceptual model of the subsurface beneath the eastern Snake River Plain (ESRP). In order to use these new data in determining the risk posed by contaminants from the INL Site, the data must be compiled and used to update conceptual and numerical models of flow and transport.

To the extent possible, the SWGM will be structured to integrate with and complement existing groundwater-flow and contaminant-transport models developed by individual WAGs and the USGS. This approach will enhance consistency across the INL Site and help resolve differences raised by different interpretations of subsurface data. Communication, staff integration, and data sharing are the foremost components in the strategy for integrating the SWGM with existing models. Meetings are held at regular intervals for technical and management staff involved with the active development or application of numerical simulations of the subsurface at the INL Site. Additionally, senior technical staff have been recruited from the major facility-scale groundwater projects to act as technical consultants on the design and construction of the SWGM. Additionally, use of the Environmental Data Warehouse to share and store data will ensure that the SWGM is developed and based on a common and consistent set of data.

The underlying strategy for the SWGM is a departure from the strategies for other models that have sought a single, unique solution to groundwater flow and transport. The SWGM strategy assumes that different and sometimes competing interpretations of groundwater flow and transport will develop because of the relatively sparse subsurface data set for the complicated INL Site subsurface and the many programs utilizing these data for varied purposes. Consensus on a single conceptual model will be difficult to achieve and will evolve as more data become available. The SWGM strategy for integration includes the capability to test interpretations generated by various projects (solving specific problems). Cross comparison between interpretations will define the bounds of flow and transport in the SRPA at the scale of the INL Site. Thus, unique solutions derived by individual projects can be included in the SWGM as long as the solutions are consistent within a range that is reasonable for possible interpretations described by the subregional understanding of aquifer flow and transport.

1.1.1 Regulatory Background

The WAG 10 OU 10-08 RI/FS work plan (DOE-ID 2002) describes the enforceable milestone schedule for OU 10-08, and the reader is referred to that plan for a detailed summary of the events controlling the final deliverable date for the OU 10-08 ROD. The 10-08 ROD is expected to be the last major ROD completed at the INL Site, and the deliverable date depends on when the other WAG RODs are signed.

Currently, two other major RODs remain to be finished. The planned completion date for the OU 3-14 draft ROD is December 31, 2006, and the planned completion date for the draft OU 7-13/14 ROD is December 31, 2007. When the OU 7-13/14 ROD is signed (assumed to be 6 months later), the period for completing the OU 10-08 RI/FS begins. The draft OU 10-08 RI/FS report will be due to the

regulatory agencies for review within 15 months, and the draft OU 10-08 ROD will be due two years after the OU 7-13/14 ROD is signed. Assuming the OU 7-13/14 ROD is signed in June 2008, the draft OU 10-08 RI/FS report will be due September 2009 and the draft OU 10-08 ROD will be due June 2010. The current working schedule for the OU 10-08 RI/FS, which this groundwater modeling effort supports, will produce the RI/FS report in September 2009. Obviously, this schedule is subject to change. The phased approach for developing the OU 10-08 SWGM has the advantage of providing schedule flexibility to ramp up or down project activities to meet a moving deliverable date.

The schedule of the groundwater modeling project will also tie to and support the aquifer flow and transport models of the OU 3-13 and OU 7-13/14 RODs. It is critical that the OU 10-08 RI/FS activities overlap and are consistent with remedial decisions across the INL Site, because all WAGs will eventually be managed under WAG 10 as activities are completed at other WAGs. The schedule overlap with the other WAG groundwater models will ensure a smooth and cost-effective transfer to the long-term stewardship role of WAG 10. A final important need addressed under the current OU 10-08 RI/FS schedule is the ability for managers to consolidate all groundwater concerns into a single internally consistent representation of the aquifer beneath the INL Site for communication to concerned stakeholders. The importance of the OU 10-08 SWGM is demonstrated by two important facts: (1) the SRPA, a sole source aquifer, is the number one INL-related concern for the population of eastern Idaho, and (2) predicted contaminant levels in the SRPA drive the selection of most remedies for individual WAGs. For the aforementioned reasons, INL Site management team (including the agencies) has taken a proactive, technically robust approach for developing the SWGM.

1.1.2 Previous Modeling Studies

Numerical modeling of groundwater flow beneath the INL Site has been ongoing for many years, both at the INL sitewide scale and for much larger areas of interest. Numerical models for INL groundwater problems were utilized as early as the mid-1970s (Robertson 1974). The USGS Regional Aquifer-System Analysis Program produced several SRPA models at various scales for use as characterization tools dealing with regional water-resource issues. Recent numerical models have included the State of Idaho Regional Water Resource Model and the USGS Subregional Model. At the INL Site, remedial investigations mandated under the Comprehensive Environmental Response, Compensation, and Liability Act (CERCLA) have resulted in several flow and transport models; these include three numerical flow and transport models currently in preparation for WAGs 1, 3, and 7.

Historical modeling efforts are important, because they identify documented successes that can be incorporated into the SWGM and because they help to identify issues and problems that can be avoided. Several historical models provide input to the WAG 10 conceptual model and provide useful summaries of data to be used in the SWGM. The following subsections summarize basic features and applicable results for several regional ESRP and subregional INL Site models and three active individual WAG aquifer models.

1.1.2.1 Numerical Modeling Studies from 1974 to 1990. In one of the first comprehensive subregional numerical transport-modeling studies, Robertson (1974) calibrated a two-dimensional flow and transport model with data from the early 1940s through 1972 and used the calibrated model to predict solute transport to the year 2000. Solutions were obtained using the method of characteristics. The model assumed a constant aquifer thickness of 76 m (250 ft) and included both steady-state and transient-flow conditions. The minimum grid dimension was 1,275 m (4,183 ft) on a variable grid oriented to the interpreted principal direction of regional groundwater flow. The grid consisted of 39 rows of cells along the principal axis of flow (southwest) and 36 columns of cells along the axis perpendicular to flow (southeast). Robertson's model domain represented an area of 6,599 km^2 (2,548 mi^2) shown in Figure 1-1.

Robertson's transport model was used to predict concentrations in groundwater of tritium, chloride, and Sr-90 emanating from the Reactor Technology Complex (RTC) (formerly known as the Test Reactor Area [TRA]) and the Idaho Nuclear Technology and Engineering Center (INTEC). An important result of the work came from matching predicted chloride concentrations to observed chloride concentrations using an unexpectedly large ratio (1.5) of transverse (137 m [449 ft]) to longitudinal dispersivity (91 m [298 ft]). The model was first reworked by Lewis and Goldstein (1982) to evaluate this large ratio. Their analysis resulted in a list of problems with the original model, including a grid that was too coarse to produce an accurate simulation of contaminant plumes. Goode and Konikow (1990a) revisited the model a second time in an attempt to explain the transverse-to-longitudinal dispersivity ratio using transient recharge from the Big Lost River. Their results were inconclusive.

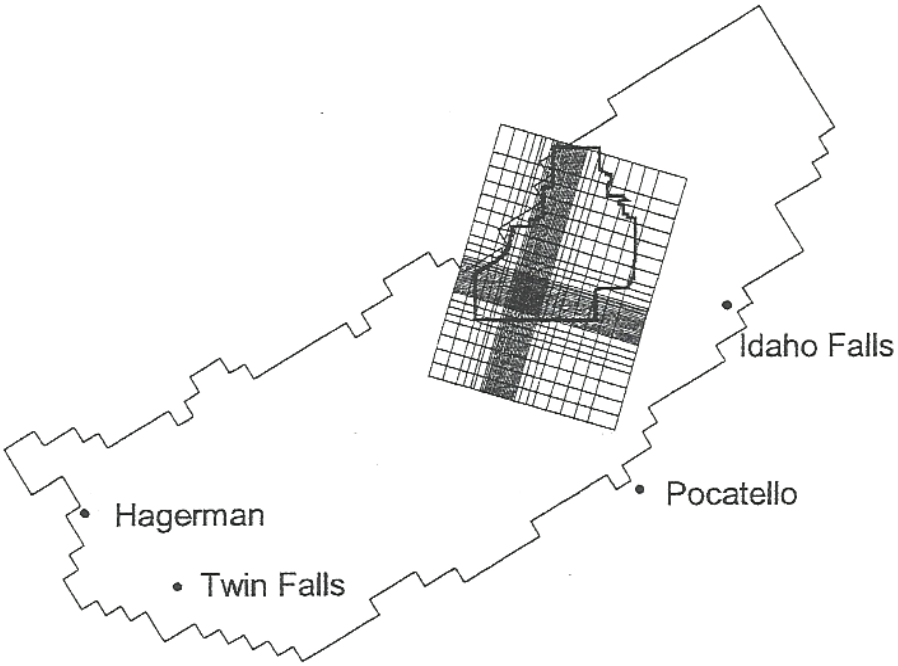

Figure 1-1. Domain and grid configuration of early flow and transport model (Robertson 1974).

1.1.2.2 Spent Nuclear Fuel Environmental Impact Statement Model (1990). A two-dimensional, steady-state flow and transport model was developed (Arnett and Springer 1993) for the INL Spent Nuclear Fuel Program's environmental impact statement (EIS). The flow model simulated an area larger than the INL Site in order to utilize natural boundary conditions. The 1990 EIS model domain was similar to Robertson's model, as shown in Figure 1-2. The northern and southern boundaries were chosen far from the contaminant transport area of interest to minimize their effects on the solutions. These boundaries were modeled with constant heads interpolated from regional head maps. Recharge and discharge from INL Site ponds and wells were neglected.

This EIS modeling effort assumed two-dimensional, horizontal-flow, and steady-state conditions in a heterogeneous, isotropic, confined aquifer. A structured, variable grid size was used with refinement in the transport areas of interest, which consisted of INTEC, the Naval Reactors Facility, the Radioactive Waste Management Complex (RWMC), Test Area North (TAN), and the RTC. The grid axes were rotated clockwise from true north to match the regional flow direction. The model was developed using MAGNUM-3D, a finite-element code designed to model two- or three-dimensional transient or steady-state groundwater flow.

The EIS transport model was constructed as a subarea of the flow model domain in the vicinity of INTEC, the RTC, and the RWMC and corresponding to the refined area of the flow model. The transport model simulated tritium, Sr-90, and I-129 plumes beneath the RTC and INTEC. Transport was simulated using CHAINT, which is a two-dimensional, finite-element solute transport code. Tritium data from 1985 were used to calibrate transmissivity and effective porosity; Sr-90 and I-129 plume data were used to calibrate the strontium and iodine retardation.

However, the EIS model was unable to satisfactorily simulate the observed plume configuration. The assumption of two-dimensional flow was considered reasonable for the regional-scale groundwater flow, but it was believed that a transient flow simulation would be required with this model to better simulate the highly dispersed observed contaminant plumes. As a result, this model significantly overpredicted I-129 concentrations in the SRPA downgradient of INTEC, as demonstrated by subsequent groundwater monitoring results for the period 1990 to 2005.

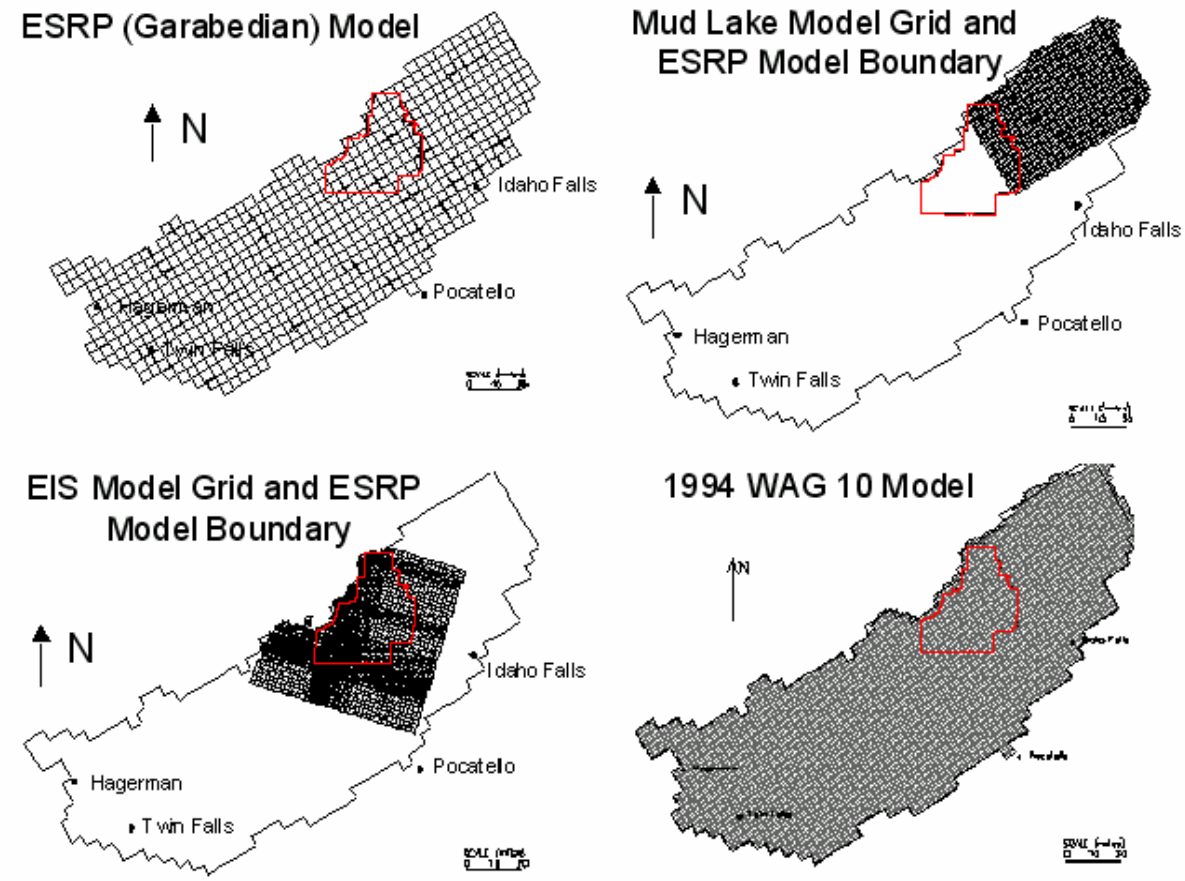

Figure 1-2. Domain and horizontal grids of four early regional and subregional models.

1.1.2.3 USGS ESRP Water Resource Model (Garabedian 1992). A numerical flow model of groundwater underlying the entire ESRP was prepared by Garabedian (1992) as part of the USGS regional aquifer systems analysis for management of the groundwater supply. This model did not include contaminant transport. The four-layer model was prepared using MODFLOW. Vertical variations in head within each model layer were assumed to be negligible, and head losses between layers were assumed to be controlled by confining beds near the base of each layer. This layered modeling approach is referred to a quasi-three-dimensional or multi-aquifer approach and is not fully three-dimensional. The ESRP Garabedian model grid consisted of uniformly dimensioned cells that were 6.4 km (4 mi) on a side

(Figure 1-2). The model layers varied in thickness. Grid axes were also rotated for better alignment with the principal direction of regional groundwater flow.

The Garabedian ESRP steady-state model was calibrated by the zonation approach using hydraulic conductivities and river conductances within reasonable ranges. Isotropic conditions were assumed for horizontal movement. The initial conditions for the transient model were derived from a pre-irrigation steady state, and the model simulated water-level changes from 1891 to 1980 by adding recharge from irrigation. The model is most useful for summarizing regional data and providing estimates of regional hydraulic properties. Although there are issues with this model regarding several features, including tributary valley average annual underflow rates near the INL Site and transmissivity values near the INL Site, the understanding of the overall regional flow system gained by development and application of the ESRP model provides helpful background information for the SWGM.

1.1.2.4 USGS Mud Lake Water Resource Model (Spinazola 1994). The USGS constructed a numerical groundwater flow model using MODFLOW to evaluate changing water-management practices in the Mud Lake area (Spinazola 1994). This model was a subregional five-layer model consisting of a uniformly sized grid of 40 rows and 64 columns, with each cell 1.6 km (1 mi) on a side, aligned similar to the ESRP model (rotated approximately 31° counterclockwise). The Mud Lake model domain, representing 5,698 km^2 (2,200 mi^2), is shown in Figure 1-2. Layers represented sub-unit thicknesses ranging from 30 m (100 ft) at the top of the aquifer to almost 305 m (1,000 ft) at its base.

Head-dependent flux boundary conditions were used for the southwest boundary and a portion of the southeastern boundary of the Mud Lake model. No-flow boundary conditions were used for parts of the northwestern boundary that abut mountain ranges and for parts of the southeastern boundary. Specified-flux conditions were used for portions of the northwestern boundary corresponding to tributary underflow and to simulate recharge from precipitation and withdrawals for pumping and irrigation.

The steady-state Mud Lake model was calibrated to 1980 conditions using the trial-and-error approach with multiple conductivity zones per layer. Some transient conditions were also calibrated. Evaluation criteria included configuration of measured and simulated water tables—in particular, the shape and position of specific contours. Significant discrepancies resulted between measured and simulated water levels. These discrepancies were from apparent cumulative effects of uncertainty in several components of recharge and discharge.

1.1.2.5 WAG 10 Regional Flow Model (1994). In 1994, a regional flow model was developed using MODFLOW to support WAG 10 objectives. These objectives included modeling future transport and defining regional flow at individual WAG scales. This model's domain covered the entire SRPA and was the same as the USGS ESRP model. Similar four-layer, quasi-three-dimensional approach and boundary conditions were used as well as similar recharge/discharge estimates. The USGS model discretization was subdivided from 6.4 km (4 mi) per grid side to 1.6 km (1 mi) per grid side (Figure 1-2) to provide better resolution for individual WAGs.

The 1994 WAG 10 model combined hydraulic conductivity zones from the USGS ESRP, Mud Lake, and EIS models. This combination allowed greater detail in the area immediately upgradient of the INL Site. The model successfully integrated INL Site and ESRP scales with regard to groundwater flow. Steady-state and transient conditions were used to calibrate hydraulic head, gradient, and overall water budget. The model was calibrated only to targets within the INL Site boundary and only within the top layer of the model. Hydraulic gradient targets were satisfied at intermediate scales but not local scales. The larger scale of the model limited the accuracy of the hydraulic gradient and flow directions for defining the regional setting of the local scale. The 1.6-km (1-mi) grid size proved too coarse to define boundary conditions at individual WAG scales.

1.1.3 Current Modeling Efforts

The following subsections describe several modeling efforts that are currently under way to define regional and subregional groundwater flow and transport in the SRPA and in the vicinity of the INL Site. The Idaho Water Resources Research Institute (IWRRI) at the University of Idaho is preparing a new water resources model. The USGS is developing new subregional flow and transport models. In addition, three WAG-specific groundwater models that are of interest to the WAG 10 groundwater modeling team have been developed.

1.1.3.1 State of Idaho Regional Water Resource Model. The State of Idaho has developed groundwater models to support water resource management and adjudication of groundwater and surface water rights on the ESRP. Recently, the IWRRI's Eastern Snake River Plain Aquifer Model Enhancement Program completed a refined regional SRPA flow model (Wylie 2003). The purpose of the effort is to better detail the extent and thickness of the aquifer domain by using grid refinement in areas of intensive groundwater use and groundwater/surface water interaction, particularly along the eastern and southeastern margins of the plain, and to improve the understanding of water table dynamics over the past 20 years.

The two-dimensional model consists of a single layer with variable thickness. The model grid consists of 104 rows and 209 columns of uniformly sized cells with dimensions of 1.6 km (1 mi) on a side. Grid axes are aligned with the principal direction of regional flow (rotated 31.4° counterclockwise). The model domain is shown in Figure 1-3 relative to INL Site boundaries. In the IWRRI model, the aquifer is treated as a confined system. The central focus of the model is on the interaction of the groundwater flow system with the Snake River and on seasonally varying inputs from tributary valley underflow.

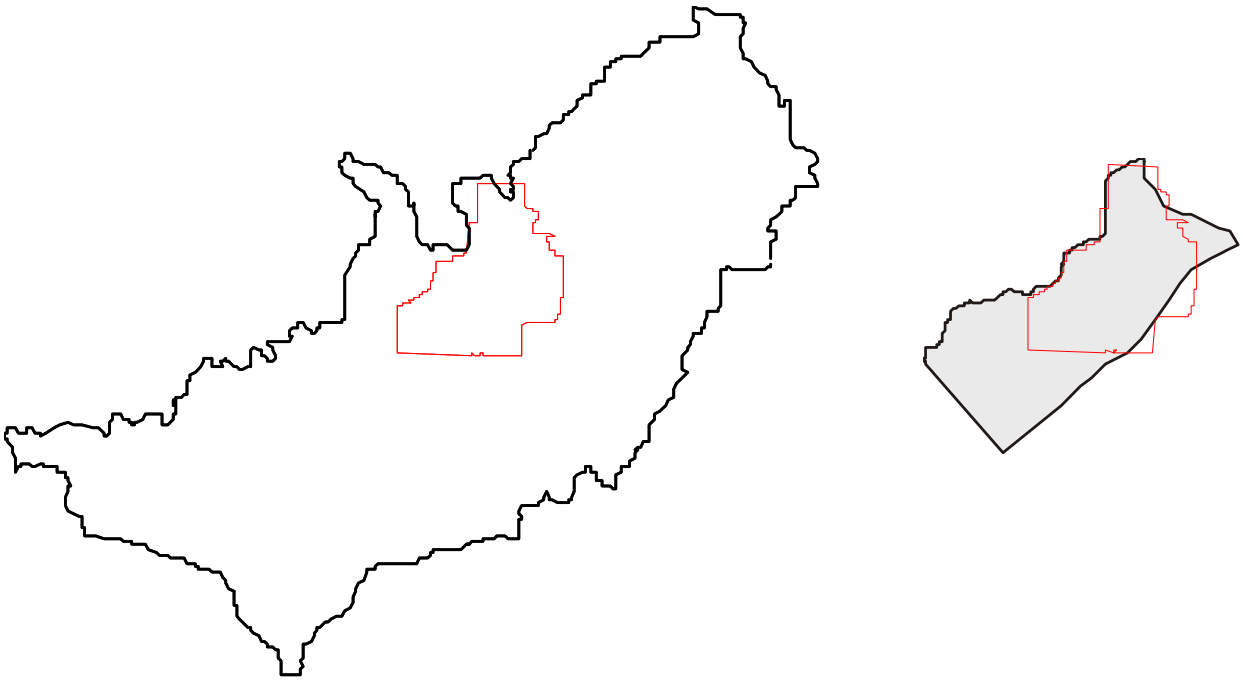

Figure 1-3. Model domain extent for two contemporary modeling efforts (State of Idaho Regional Water Resource model, left; USGS, right).

1.1.3.2 USGS Subregional Model. The USGS is currently developing a conceptual model that will support preparation of next-generation flow and transport models for a subregional domain surrounding the INL Site.[a] The features of the USGS conceptual model include multiple layers, variable aquifer thickness, and three major hydrogeologic units.

The current USGS conceptual model encompasses an area of 5,025 km^2 (1,940 mi^2), including most of the INL Site, and extends 121 km (75 mi) from northeast to southwest and 56 km (35 mi) from northwest to southeast (Figure 1-3). The aquifer is treated as an equivalent porous medium with nonuniform properties. Three major hydrogeologic units represent the hundreds of known individual basalt flows and sedimentary interbeds. These include younger, fractured basalts and permeable sediments; younger, dense-basalt, and less-permeable sediments; and older, much-less-permeable, altered basalts and interbedded sediments.

The conceptual model developed as part of the current USGS modeling study differs from conceptual model elements of the proposed SWGM. These differences include the estimates of maximum thickness of the effective aquifer, areal distribution of thickness, and downward flow and deep circulation of contaminants. The USGS model uses an assumed base of the aquifer delineated primarily from electrical resistivity soundings. These soundings indicate that the aquifer base ranges from 213 to 1,463 m (700 to 4,800 ft) below land surface. This results in an active aquifer thickness of over 1,067 m (3,500 ft) in some areas of the domain. This maximum thickness is significantly larger than that of the current OU 10-08 conceptual model. Additionally, the distribution of aquifer thickness differs from OU 10-08 thickness distributions, although the USGS thickness distribution generally trends from thinner in the north to thickest just south of the INL Site boundary.

Boundary conditions include a no-flow boundary to the southeast that corresponds to a groundwater flow path, as determined from the Garabedian (1992) model. Constant-flux boundaries are used to the northeast and southwest. Specified-flux boundaries are used along the northwest boundary to represent tributary underflow. Some downward groundwater flow is being included in areas of known vertical gradient, especially where the less-permeable, massive basalts apparently intersect the water table south of the INL Site. This implication of downward flow and deeper circulation of contaminants that migrate offsite is a third conceptual model difference from the OU 10-08 conceptual model.

1.1.3.3 INL Individual WAG Models. Numerical groundwater flow and contaminant transport models are in use for WAGs 1, 3, and 7. The models for WAGs 3 and 7 were developed to be coupled with vadose zone models. The WAG 1 model was developed for CERCLA risk assessment of the SRPA without vadose zone modeling. These three models are based on different numerical solution codes, grid dimensions, and contaminants of concern (Table 1-1).

WAG 1—The WAG 1 model consists of a saturated-only domain with a point source representing direct injection of waste to the aquifer via the TAN disposal well (Technical Support Facility [TSF]-05) and gradual release from a secondary source (sludges in the SRPA around the disposal well). The model contained a 1,600-m (5,249-ft) base grid dimension but was refined over six levels down to an 25 m (82 ft) grid dimension within the source area (disposal well). The model includes a far-field domain (the portion of the INL Site from TAN to the southern INL Site boundary). The model is a multi-layered, fully three-dimensional model bottomed by the QR interbed, which provided an effective base of the trichloroethene contamination zone. The model was initially developed using TETRAD but was later converted to MODFLOW using a smaller domain. An effective porosity of 0.03 was required to match tritium breakthrough observed in monitoring wells. The model domain is shown in plan view in Figure 1-4.

---

a. Ackerman, D. J., S. R. Anderson, L. C. Davis, B. R. Orr, G. W. Rattray, and J. P. Rousseau, 2001, *A Conceptual Model of Flow in the Snake River Plain Aquifer at and near the Idaho National Engineering and Environmental Laboratory with Implications for Contaminant Transport*, U.S. Geological Survey Draft Report.

Table 1-1. Summary of numerical modeling activities for WAGs 1, 3, and 7.

WAG	Model Code	Grid Dimensions	Contaminants of Concern
WAG 1 (TAN)	TETRAD, converted to MODFLOW, no vadose zone model	5,249 ft (82 ft refined)	Trichloroethene
WAG 3 (INTEC)	TETRAD, coupled with a TETRAD vadose zone model	1,312 ft (656 ft refined)	Sr-90, Tc-99
WAG 7 (RWMC)	TETRAD, coupled with a TETRAD vadose zone model	1,000 ft (500 ft refined)	Carbon tetrachloride

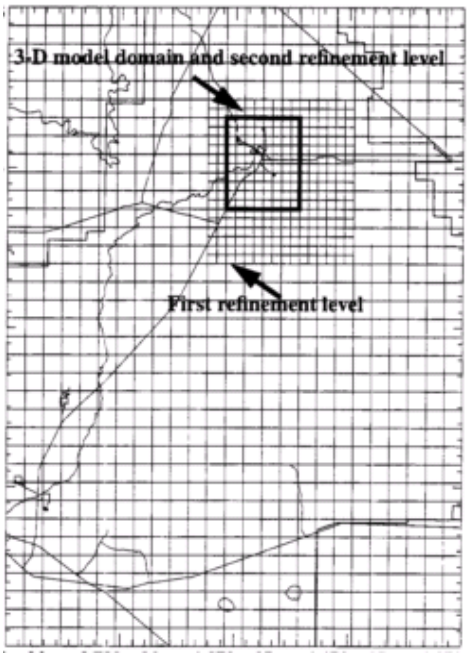

a) WAG 1 groundwater model

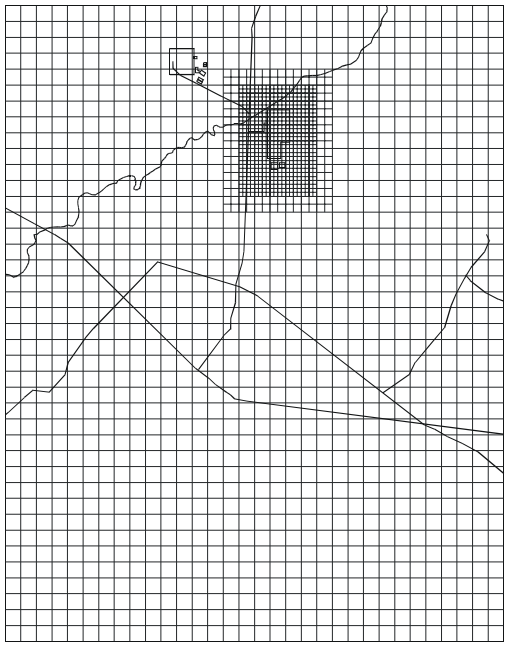

b) WAG 3 groundwater model

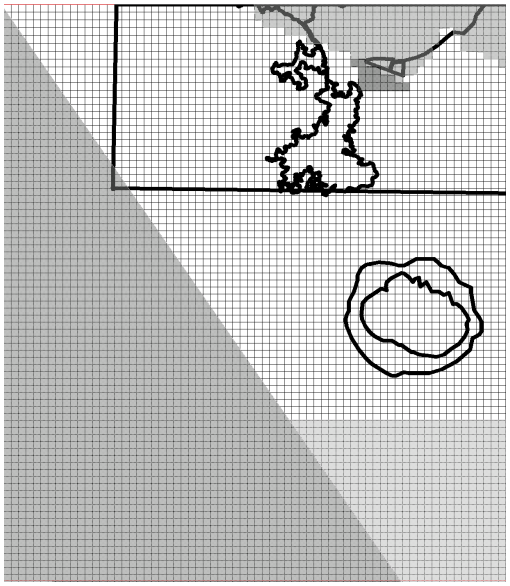

c) WAG 7 groundwater model

Figure 1-4. Model domain and grid layout for three individual WAG models.

WAG 7—The saturated groundwater model developed for WAG 7 is coupled to the WAG 7 vadose zone model. Both models use the TETRAD numerical code. The saturated model consists of a three-dimensional, seven-layer system employing five constant conductivity media types. The horizontal grid dimensions are 305 m (1,000 ft) per side, with grid refinement in the vicinity of the RWMC's Subsurface Disposal Area to 152 m (500 ft) per grid side (Figure 1-4). The model domain was recently extended to the southwest and now extends several kilometers south of the INL Site boundary. After this modification, the domain extends 21 km (12.9 mi) from east to west and 25 km (15.3 mi) from north to south. The flow model was calibrated to fall 2003 water-level data. Relative to the original domain, the fit between observed and simulated heads with the extended domain was poorer; this prompted discussion on the need for a new WAG 10 sitewide groundwater model to support individual WAG models.

1.2 Document Scope

This document addresses the conceptual SWGM and includes the supporting evidence and interpretations upon which the SWGM is based. The disciplines of geology, geochemistry, geothermal systems analysis, and hydrology are included in the development of the SWGM. Using the results of the SWGM, a two-dimensional sub-regional scale aquifer flow model is calibrated using three different inverse methods. The calibration results and uncertainty in estimated hydraulic conductivity are compared between the methods. Sensitivity to boundary conditions and estimated hydraulic properties are evaluated.

1.3 Document Overview

This document contains two primary parts. First, the conceptual model of the movement of water and the basis for the conceptual model are described. Second, the development of a two-dimensional flow model based on this conceptual model is described. The flow model includes different conceptualizations to test the effect of uncertainty in some aspects of the conceptual model.

2. OU 10-08 CONCEPTUAL MODEL OF GROUNDWATER FLOW

The OU 10-08 conceptual model of groundwater flow represents the current understanding of the geohydrologic features that control flow within the SRPA in the OU 10-08 study area. The two-dimensional numerical model is based on conceptual model elements. These elements, consisting of the geohydrologic framework and groundwater inflows and outflows, control the distribution of flow within the aquifer.

2.1 Geohydrologic Framework

Before describing the geology of the OU 10-08 groundwater model study area, it is necessary to briefly describe the geography and physiography of the study area, which is shown in Figure 2-1. The ESRP is a 298-km (185-mi) long, 59-km (37-mi) wide region of lowered elevation and suppressed topography surrounded by elongate Basin and Range (B&R) style mountains and valleys. The most prominent feature on the ESRP is a slightly elevated axial ridge that can be traced from Island Park in the northeast to Dietrich in the southwest. This feature, punctuated by several rhyolitic domes, including Big Southern Butte, is known as the Axial Volcanic High (AVH). Another prominent feature of the ESRP is the Great Rift of Idaho, which is an eruptive volcanic fissure complex at Craters of the Moon National Monument grading into multiple sets of Quaternary non-eruptive fissures north of Minidoka and then switching back to eruptive fissures and flows at southern edge of the rift at the Holocene Wapi Lava Field. A second volcanic rift is the Arco Rift, which extends from the town of Arco southeast past Big Southern and Cedar buttes.

The Big Lost River exits the B&R and flows onto the ESRP at Arco. Because of the elevated topography of the Arco Rift and the AVH, the Big Lost River is trapped in the Big Lost Trough (BLT), which is the prominent area of low elevation on the southern half of the INL Site. The sinks of both the Big Lost and Little Lost rivers are contained within the BLT. The sinks of Birch Creek are located at the northern edge of the BLT. Antelope and Circular buttes, just east of TAN, separate the sinks of Birch Creek from Mud Lake. The AVH forms a low ridge that separates Mud Creek from the now-almost-drained bed of Market Lake to the east. Market and Mud lakes are the remnants of a large pluvial lake, Lake Terreton, that once extended from Howe to Menan during the last glacial period.

The geohydrologic framework of the OU 10-08 study area consists of the geologic elements of the aquifer matrix. The following subsections describe the extent and boundaries of the study area, active aquifer thickness, major geologic units and hydrologic subdomains, and distribution of hydraulic properties.

2.1.1 Extent and Boundaries of the OU 10-08 Study Area

The OU 10-08 study area encompasses approximately 7,770 km^2 (3,000 mi^2) of the ESRP. This entire area is underlain by the SRPA (Figure 2-2) and extends beyond INL Site boundaries to "better accommodate regional effects and to ensure that groundwater movement beyond the [INL] boundaries can be included" (Arnett and Smith 2001). The OU 10-08 study area is bounded both by natural geohydrologic boundaries and by boundaries that have been set to most efficiently define the extent of active flow systems. These boundaries include natural boundaries to groundwater flow to the northwest, hydraulic boundaries to the southeast, and selected boundaries to the northeast and southwest.

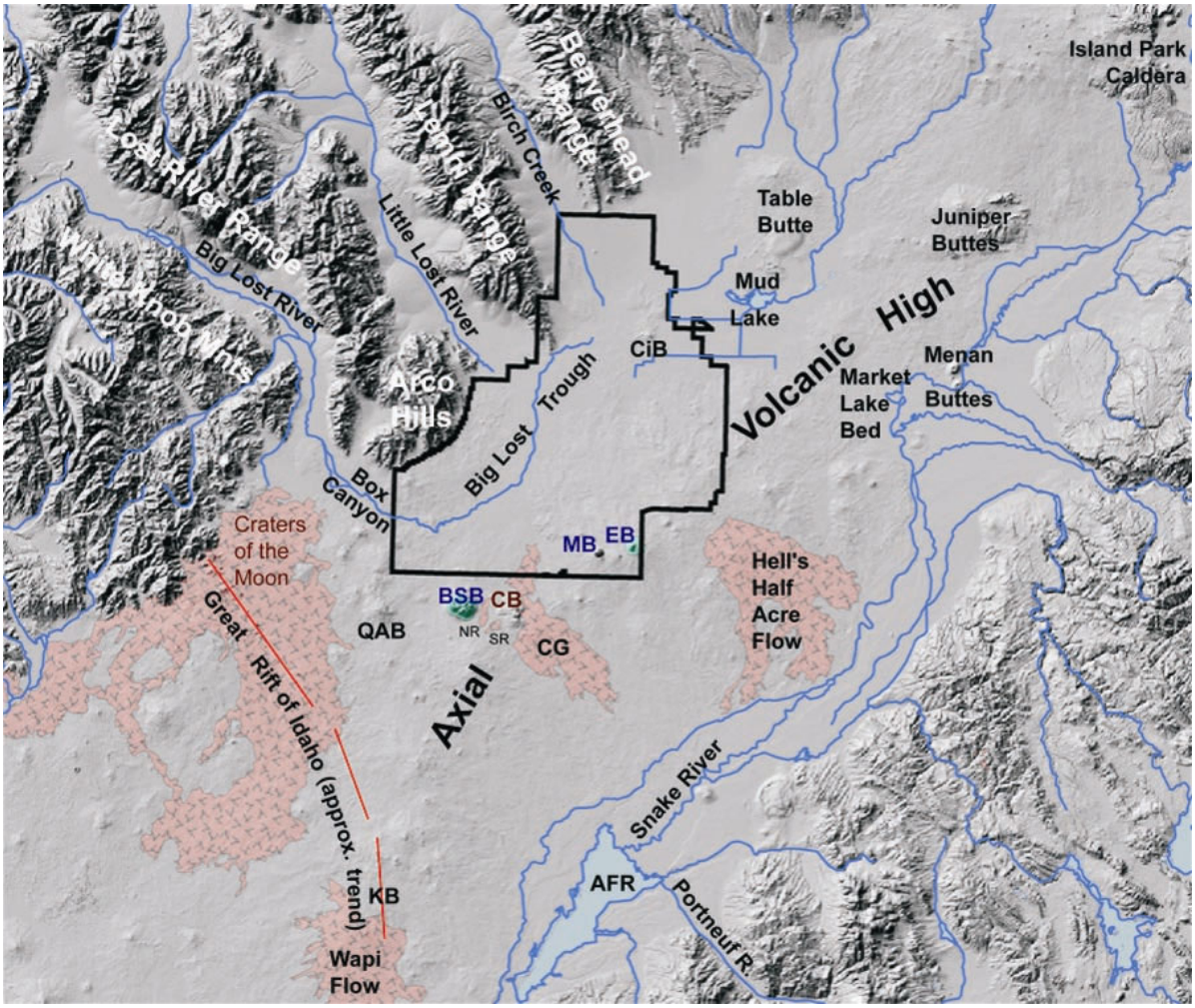

Figure 2-1. Geography and physiography of the region of the ESRP encompassing the OU 10-08 study area. (Flow and butte names in black indicate volcanic rocks that are basaltic in character, names in blue indicate volcanic rocks that are silicic in character, and names in brown indicate volcanic rocks that are intermediate in character between the pervious two types. Area abbreviations are as follows: AFR = American Falls Reservoir, BSB = Big Southern Butte, CB = Cedar Butte, CG = Cerro Grande Lava Flow, CiB = Circular Butte, EB = East Butte, KB = Kings Bowl Lava Flow and Crater, MB = Middle Butte, NR = North Robbers Lava Flow, QAB = Quaking Aspen Butte, SR = South Robbers Lava Flow.)

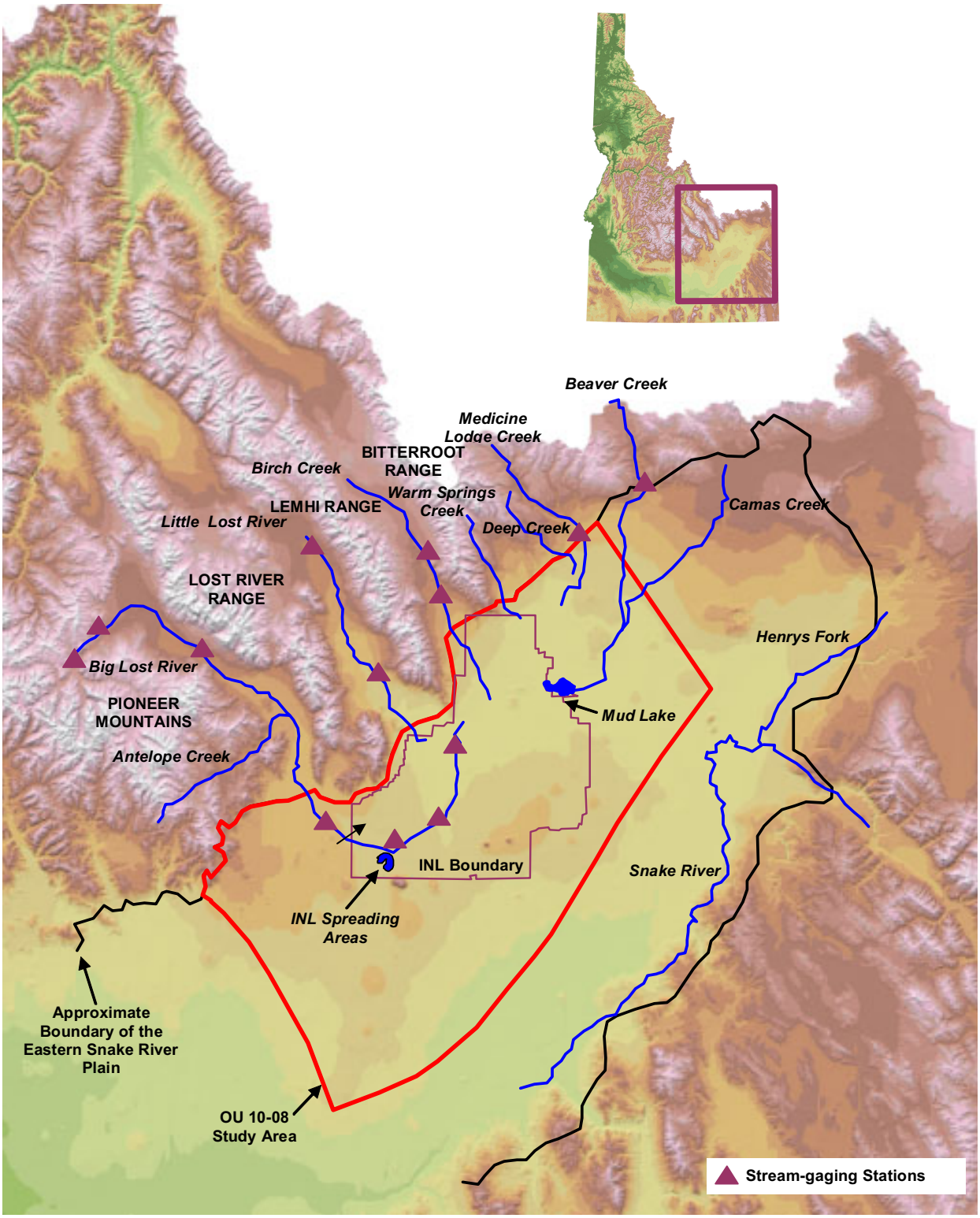

Figure 2-2. Location of the area of the ESRP represented by the OU 10-08 study area, surface-water features, and stream-gaging stations.

2.1.1.1 Northwestern Study Area Boundary.

The study area is bounded on the northwest by the mountains and tributary valleys of the Bitterroot, Lemhi, Lost River, and Pioneer ranges (Figure 2-2). These B&R mountains form the northwestern edge of the ESRP. The small-permeability sedimentary rocks composing these mountains are assumed to act as a no-flow boundary to the high-permeability basalts of the SRPA. Intervening tributary drainage basins provide a source of groundwater and surface-water inflow to the SRPA.

2.1.1.2 Southeastern Study Area Boundary.

The southeastern boundary of the study area (Figure 2-2) corresponds to a groundwater flow path defined by regional numerical modeling studies (Garabedian 1992; Ackerman 1995). This inferred flow path represents the general direction of flow from the northeast to the southwest and forms a hydraulic boundary across which no flow is considered to occur. This boundary was selected sufficiently distant from areas of interest to minimize the effects of this boundary on contaminant transport.

2.1.1.3 Northeastern Study Area Boundary.

The northeastern boundary of the study area (Figure 2-2) is located northeast of the INL Site in the Mud Lake area. This boundary does not represent a natural geohydrologic boundary, but it was selected to provide an upgradient cross section that is perpendicular to regional groundwater underflow and sufficiently distant from the INL Site to minimize the effects of fluxes from pumpage, irrigation, and seasonal changes on groundwater flow in the area of interest. This northeast study area boundary overlaps a part of the Mud Lake area that was numerically modeled by Spinazola (1994). The location of this boundary permits comparison of simulated underflow to groundwater fluxes estimated in Spinazola's study.

2.1.1.4 Southwestern Study Area Boundary.

The southwestern boundary of the study area (Figure 2-2) again does not represent a natural geohydrologic boundary. Rather, this study area boundary was selected to represent a cross section that is approximately perpendicular to groundwater flow and is sufficiently downgradient from the INL Site to accommodate known and predicted contaminant migration.

2.1.2 Active SRPA Thickness within the OU 10-08 Study Area

Representation of the geologic framework requires an understanding of the active SRPA thickness, defined as the thickness through which most groundwater flows. Most of the wells within the OU 10-08 study area are constructed only within the upper part of the aquifer and provide no direct information about the active aquifer thickness. Direct information about the active thickness is available from only eight wells that are located in the south-central part of the study area and fully penetrate the aquifer. These eight wells are INEL-1, Corehole 1, Corehole 2A, Site 14, C1A, WO-2, ANL-1, and Middle-1823.

Because most INL Site wells only penetrate the upper part of the SRPA, the thickness of basalts beneath the ESRP has been estimated primarily from electrical-resistivity geophysical data. Based on a study by Whitehead (1992, Plate 3), the estimated basalt thickness in the area represented by the OU 10-08 study area ranges from 30 m (100 ft) to more than 1,219 m (4,000 ft) thick. Lindholm (1996, p. A51) estimated that most regional groundwater flow in these basalts occurs within the upper 152 m (500 ft) of saturation.

Robertson (1974) estimated that the total aquifer system in the vicinity of the INL Site is probably more than 305 m (1,000 ft) thick, but he used a uniform thickness of 76 m (250 ft) in his numerical model to represent the upper active section of the aquifer, where most groundwater flow was believed to occur. In subsequent years, this 250-ft thickness has been widely accepted as an adequate estimate of the active thickness of the SRPA. Recent geophysical data are providing estimates of aquifer thickness that are more defensible technically.

Smith (2002) estimated the active thickness of the SRPA in the vicinity of the INL Site using a combination of direct and indirect information obtained from wells and surface geophysical surveys. The current estimates of the active aquifer thickness are derived from Smith's estimates and from recent deep corehole and temperature data. Direct evidence of the active aquifer thickness in these wells was obtained through analysis of temperature gradients, lithologic variations in drill cores, and aquifer tests (Smith 2002).

A series of temperature studies has been conducted since the 1960s to examine heat flow and structural features (Blackwell 1989 and 1990; Blackwell and Steele 1992; Blackwell et al. 1992; Olmsted 1962; Smith et al. 2001; Brott et al. 1981; and Wood and Bennecke 1994). Temperature logs from these studies provided direct information about the active thickness of the SRPA in the fully penetrating wells. The active thickness of the SRPA in the eight wells ranges from 102 m (334 ft) to 368 m (1,207 ft). The active thickness of the SRPA is characterized in these wells by nearly isothermal conditions, because the relatively fast-moving cold water in the aquifer dominates the regional geothermal gradient. Below the base of the active aquifer, the temperature profile represents the regional conductive temperature gradient.

Despite the sharp resolution of the aquifer profile obtained from any given well, the lack of deep wells across the OU 10-08 study area significantly limits the capability to establish an aquifer thickness profile across much of the INL Site. In those areas, aquifer thickness has been inferred from indirect measurements that include surface electrical-resistivity surveys and water-temperature data from shallow wells.

Two bounding estimates of thickness ("thick" and "thin") were developed for the OU 10-08 study area (Smith 2002). Both use the limited direct evidence of the aquifer base from the eight deep wells in the south-central part of the study area. The "thick" aquifer interpretation also utilizes electrical-resistivity data and water temperature at the top of the aquifer to extrapolate thickness estimates to the northeast and southwest. Colder water temperatures in those areas are correlated with assumed thicker aquifer sections, resulting in an upper bounding estimate for thickness distribution. The "thin" interpretation simply assumes a general tendency for the aquifer thickness to become gradually greater toward the center of the plain and does not utilize water-temperature information away from the area of direct evidence. Uncertainties in estimation methods and a lack of confirmatory data make it impossible to determine whether the thick or thin model best reflects actual subsurface conditions. Contour maps of the altitude of the effective base for the thick and thin interpretations are shown in Figures 2-3 and 2-4.

Cores collected from the deep wells provided additional information about the base of the active aquifer. In several wells, basalts characteristically were altered and mineralized below the depth of the temperature inflection that identifies the base. For example, Doherty et al. (1979, p. 3) observed propylitic alteration and secondary zeolite mineralization of the basalts below a depth of 488 m (1,600 ft) in well INEL-1. The capacity of underlying units to transmit water is typically considered to be orders of magnitude smaller than that of the active aquifer thickness. Aquifer tests conducted in several of the deep wells indicated that the hydraulic conductivity of rocks underlying the base of the aquifer is much smaller than that of the upper part of the aquifer. Mann (1986, p. 21) observed that the hydraulic conductivity of the upper section in the INEL-1 deep corehole (above a depth of 244 m [800 ft]) is from two to five orders of magnitude larger than that of the section below a depth of 457 m (1,500 ft). Hydraulic conductivity in the upper section ranges from 0.3 to 30 m/day (1 to 100 ft/day); hydraulic conductivity of basalts below a depth of 457 m (1,500 ft) ranges from 0.06 to 0.09 cm/day (0.002 to 0.03 ft/day). Mann (1986, p. 18) also noted a distinct change in solute chemistry between the same depth intervals.

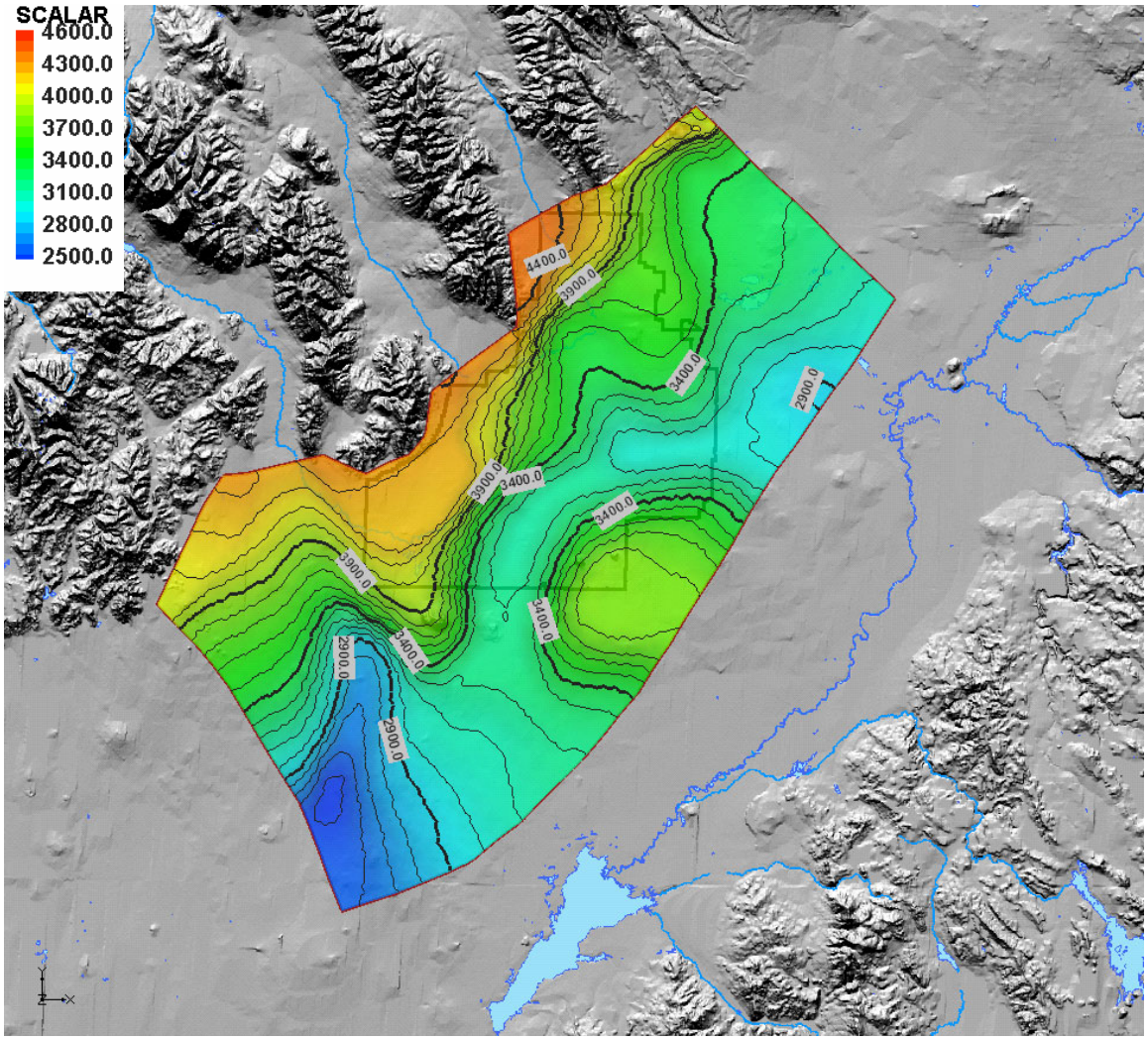

Figure 2-3. Estimated altitude of the active aquifer base in feet above sea level in the OU 10-08 study area (thick interpretation).

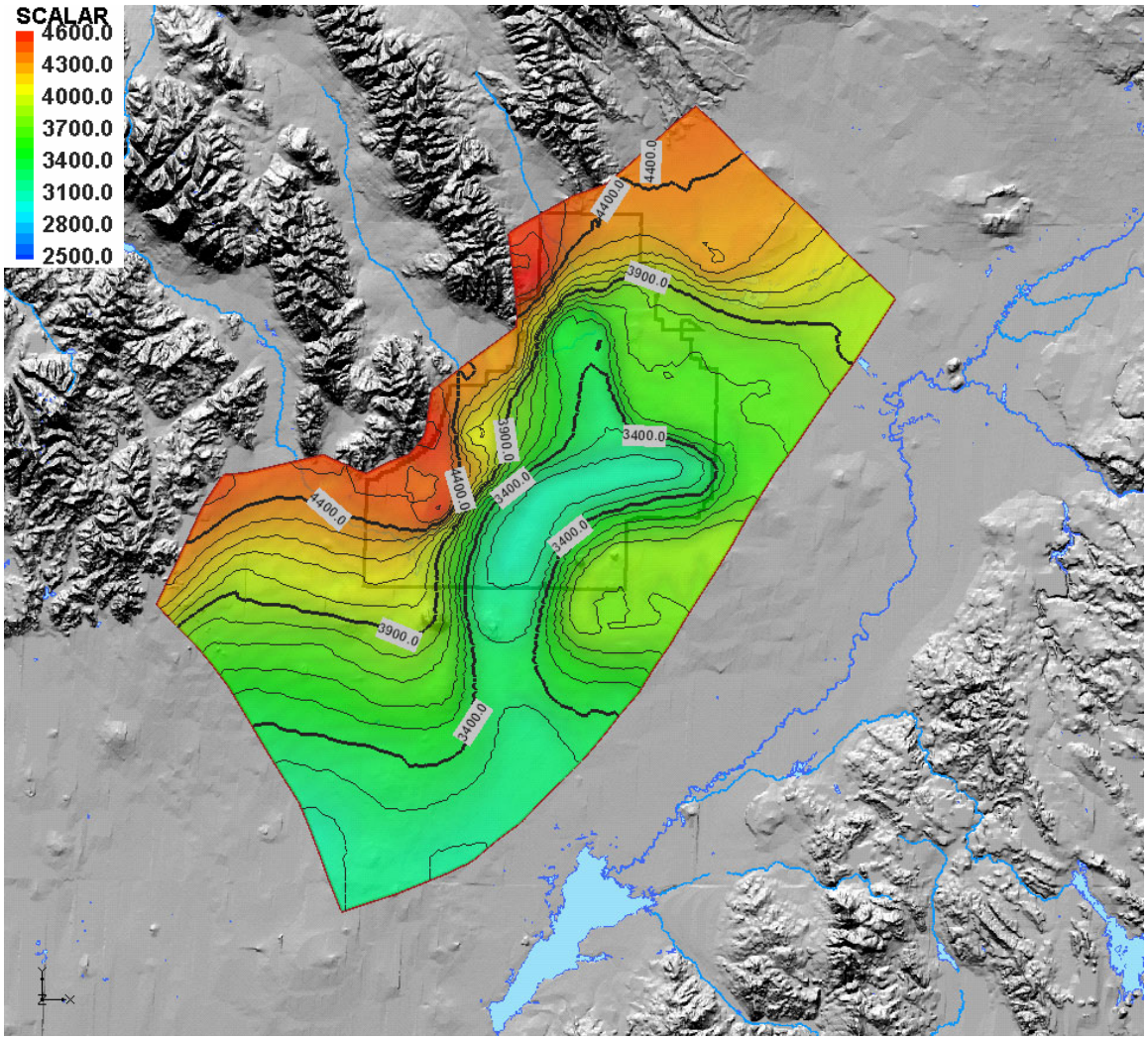

Figure 2-4. Estimated altitude of the active aquifer base in feet above sea level in the OU 10-08 study area (thin interpretation).

2.1.3 Major Geologic Units and Hydrologic Subdomains Composing the SRPA

The OU 10-08 study area can be divided into five general geologic types that consist of active volcanic rift zones, inactive volcanic rift zones, floodplains, sedimentation areas, and volcanic tablelands. These geologic types control groundwater flow by virtue of their intrinsic lithologic and stratigraphic properties.

Note that although this report describes the two-dimensional modeling effort, the division of the study area into geological units and subdomains is based on geologic features in three dimensions. While the two-dimensional model has used the surficial expression of the geologic subdomain boundaries in the construction of the model geometry, the stratigraphic nature of some of the subdomains will only be exploited to their fullest in the three-dimensional model. This caution about the three-dimensional nature of conceptual model subdomains also extends to what is shown on the location map of the subdomains. Some of the subdomains will appear to overlap when comparing their location maps; this is the simple consequence of displaying three-dimensional features in two-dimensional plan view.

2.1.3.1 Sedimentation Areas. The OU 10-08 groundwater model study area includes several areas that are mantled or interbedded with thick sequences of fine-grained sediments (Figure 2-5). There are large lakebed sequences in the north half of the study area: (a) a young pluvial sequence that is shallow and aerially exposed in places and (b) another lakebed sequence that occurs at depth and is interbedded with older basalt flows. The latter forms the top of the stratigraphic column of Subdomains 1a and 1b. The former is included in the subsurface of the volcanic tableland Subdomain 2b, as discussed in the subsections below. There is another major sediment type in Subdomain 1c of the study area, made up of a thick sequence of ponded river outwash deposits interfingered with basalt flows. These sediments are mostly fine-grained but do include some coarser sands and gravels. The three geologic subdomains where fine-grained sediments occur are described below.

Subdomains 1a and 1b - Pluvial Lakebeds—During glacial periods, pluvial lakes formed on the relatively flat ESRP, leading to widespread deposition of lacustrine sediments on top of basalt. In the northern half of the groundwater model study area, the playa deposits of Birch Creek, the Big Lost and Little Lost river sinks, and the modern Mud and Market lakes are remnants of the most recent pluvial lake known as Lake Terreton (Stearns et al. 1939). Within the study area, pluvial lakebeds are present at the surface and in the immediate subsurface stretching from Howe in the west, the Birch Creek Diversion Channel in the north, and Terreton in the east. These deposits form a thick mantle of lacustrine sediments on top of volcanic tableland basalts in much of the northern half of the study area. The base of the Lemhi Range and Lava Ridge immediately northeast of TAN divide the pluvial lakebeds and the modern river sinks at the surface into northern and southern sections. The northern section, designated as Subdomain 1a, includes Mud Lake and the sinks of Birch Creek. The southern section includes the pluvial lakebeds in the subsurface between TAN and the Naval Reactors Facility as well as the sinks of the Big Lost and Little Lost rivers. Subdomain 1b also includes a small amount of coarser-grained fluvial sediments from the Little Lost River that interfinger shallowly with both basalts and pluvial lake deposits. Under the pluvial lakebeds are thick sequences of volcanic tableland basalts with few sedimentary interbeds of mostly eolian character. The nature of volcanic tablelands is discussed in Subsection 2.1.3.2.

Subdomains 1c - Buried Inland Delta of the Big Lost River—A thick sediment mantle occurs where the Big Lost River exits the valley between the White Knob and Lost River ranges and flows onto the ESRP. The Big Lost River was captured within the BLT by the growth of the Arco Rift and the AVH. The trapping of the river caused sediment that would have originally traveled south or southwest to pond between the river's egress from the B&R and the AVH. This caused the growth of what is essentially a small inland delta that has interbedded with basalt flows erupted on the ESRP. The subsequent rise and growth of the Arco Rift, Great Rift, and other nearby eruptive centers have continued the pattern of trapping and ponding the fluvial sediment outwash at the mouth of the Arco Valley, creating an apron-shaped area where fluvial sediment and basalts interfinger and where shallow and perched B&R aquifers feed into the much deeper SRPA. This phenomenon is discussed in much greater detail in Subsection 2.2.2.4 (under the subheading Description and Location of Transition Zone Geohydrologic Features).

2.1.3.2 Volcanic Tablelands. The ESRP is an area of young volcanism. More than 99% of all volcanic rocks on the ESRP are pahoehoe-type basalt flows erupted from low-shield volcanoes, lava tubes, and fissures (see Figure 2-6). Once erupted, these basalts can travel anywhere from 0.1 km (0.6 mi) to more than 48 km (30 mi) from their eruptive vents as pahoehoe flows with an average thickness of 7 m (23 ft) (Knutson et al. 1992).

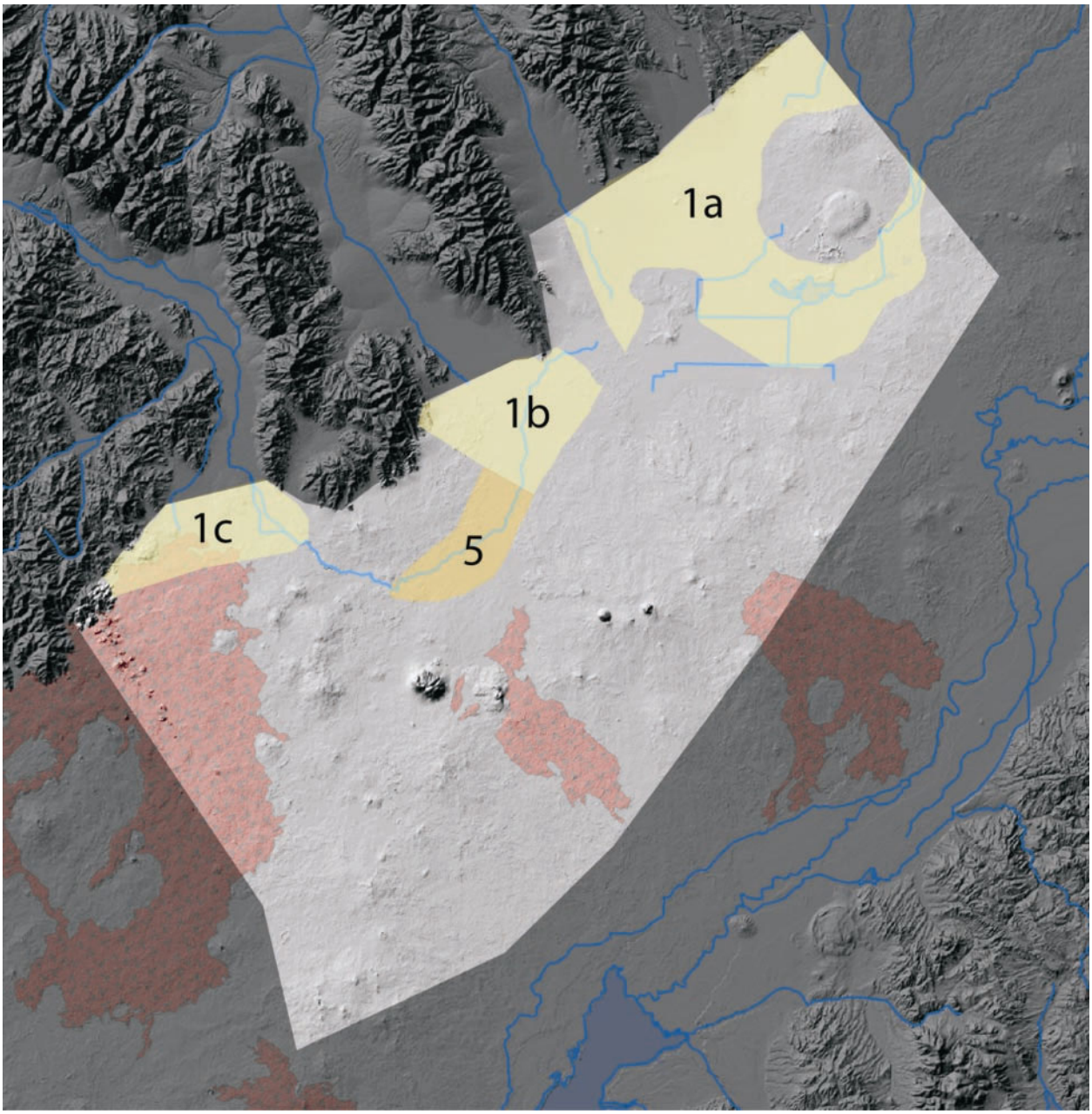

Figure 2-5. Locations of Subdomains 1a, 1b, 1c, and 5.

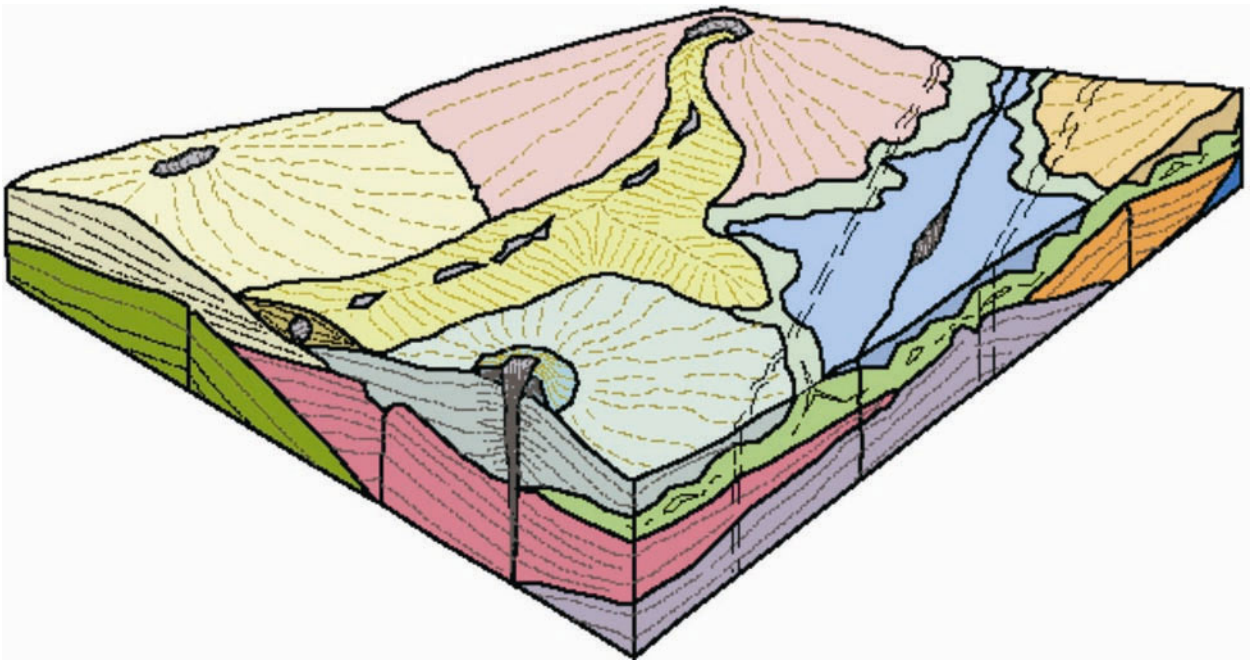

Figure 2-6. Typical ESRP pahoehoe flow eruptive styles. Basalt can erupt from fissures (shown in blue), the vents of low-angle shield volcanoes (shown in pale yellow and pale green), and vent-fed lava tubes (shown in darker yellow). The consequence of these eruptive styles coupled with the small volume of ESRP flows creates a subsurface stratigraphy that can be compared to a pile of randomly-stacked pancakes, all of different sizes (modified from Greeley [1982]).

The direction of lava flow is downhill away from vent areas. Flows stop traveling either because their vents stop feeding magma or flows become trapped within topographic lows like the BLT. Eruptive vents tend to be concentrated in areas known as volcanic rift zones such as the Great Rift of Idaho. The accumulation of these flows creates broad, mostly flat volcanic tablelands characterized by gradual topographic gradients between the elevated volcanic rift zones and the topographic lows of floodplains and sinks. The subsurface stratigraphy of the volcanic tablelands does not usually accumulate fluvial sediments, but they can include up to ~15% sedimentary materials, mostly as interbedded eolian loess. The locations of the volcanic tablelands of the conceptual model are shown in Figure 2-7.

Subdomain 2a - Table Butte Volcanic Tableland—Table Butte and the neighboring volcanoes rise above the pluvial lakebeds in the northernmost part of the study area. These basalts are all older than 700 ka. The vents of this tableland appear to be mostly in the middle of the elevated circular plateau formed by these buttes.

Subdomain 2b - West Axial Slope—This volcanic tableland was fed from vents along the AVH, with a small amount of basalt on its southern end originating from the Arco Rift. The subsurface of this tableland also includes a thick sequence of sediments named the Olduvai Lake beds (Bestland et al. 2002; Blair and Link 2000), because its age corresponds to the Olduvai normal polarity subchron of the paleomagnetic time scale, dated between 1.77 and 1.95 Ma (Cande and Kent 1995). In the extreme northern portion of the OU 10-08 study area, the Olduvai Lake sediments are shallow and above the SRPA stratigraphically. Like most other strata in the study area, however, these beds dip gradually to the south. Under TAN, the Olduvai beds intersect the SRPA. Under INTEC to the south, these beds have dipped beneath the SRPA, as shown in Figure 2-8.

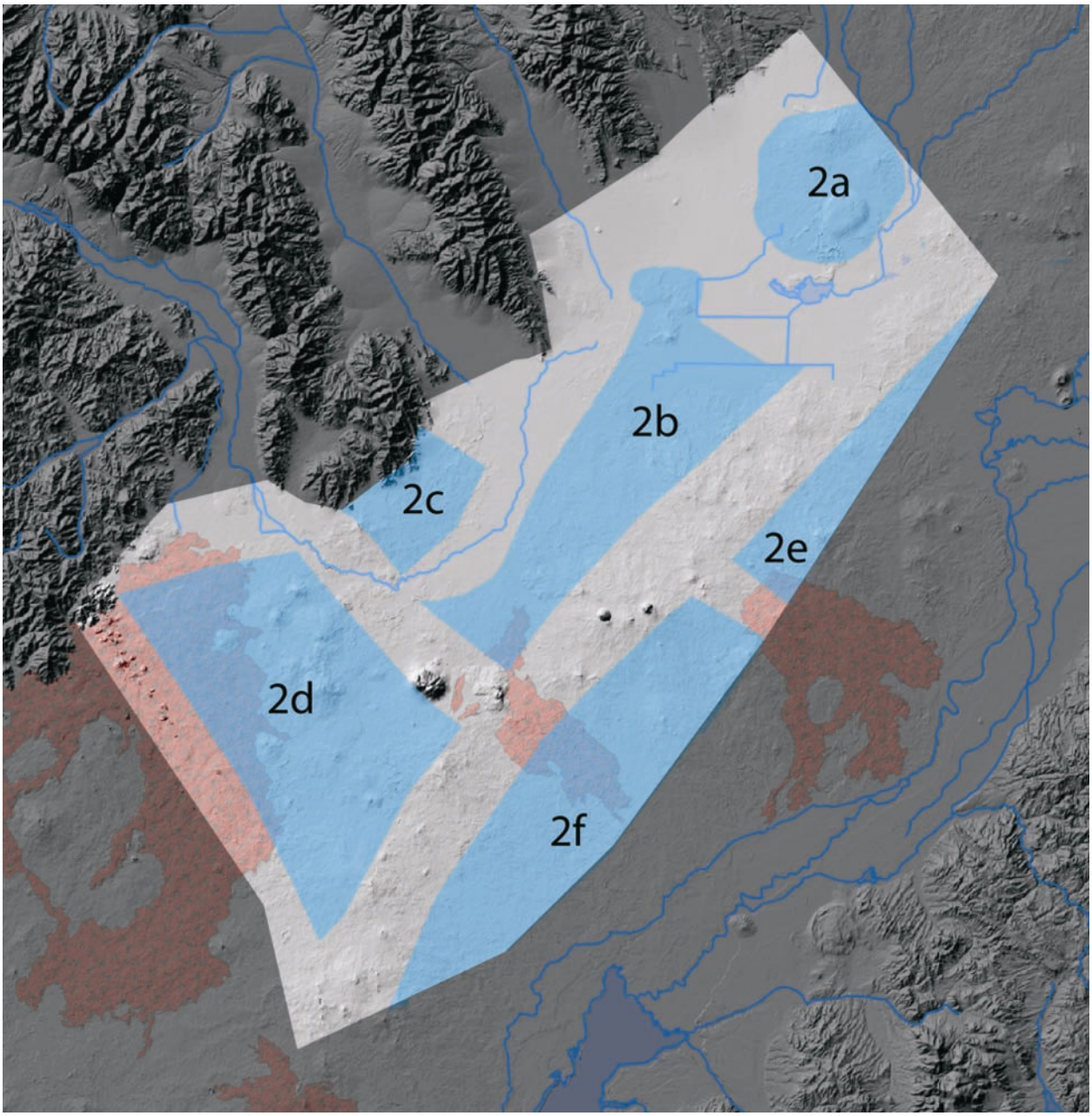

Figure 2-7. Locations of Subdomains 2a, 2b, 2c, 2d, 2e, and 2f.

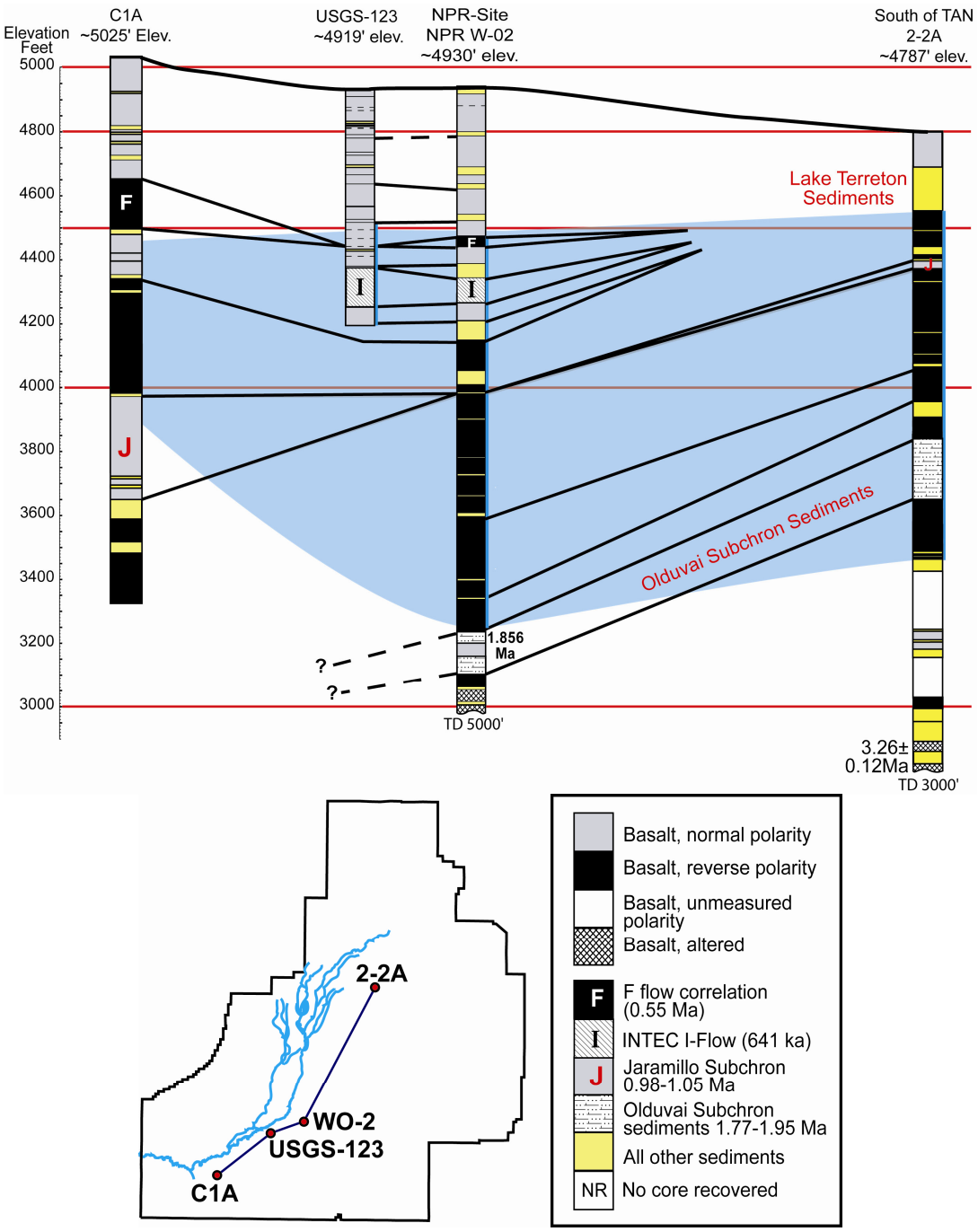

Figure 2-8. Illustration of how strata dip in a general southward direction at the INL Site in the middle of in the OU 10-08 study area. In the northern part of the study area, many flows with the oldest age dates are exposed at the surface, but in the southern part of the study area, flows of similar age are buried deep in the subsurface stratigraphy. In a similar manner, the approximately 2-million-year-old Olduvai Lake sediments are within the active SRPA flows on the north end of the INL Site and dip to the south so that they are underneath the SRPA in the south-central part of the INL Site. Flows and interbeds with radiometric age dates of approximately a half a million years old or less (the "F-flow" stratum) dip in an upward fashion from the center of the INL Site toward the southwest corner of the site; this is due to uplift of the Arco Rift, which has elevated an area that stretches from the town of Arco to the vents of the Cerro Grande Lava Field southeast of Big Southern Butte. The normal-polarity stratum shown in pink are hypothesized to be flows of Jaramillo Subchron age, based on a new radiometric age date for basalt core from well C1A just north of the RWMC (Helm-Clark and Rodgers 2004).

Subdomain 2c - Crater Butte Volcanic Tableland—The basalts of this tableland originated from Crater Butte and other Arco Rift vents or from the now inactive and mostly buried AEC Butte Rift. Along its western boundary, the basalts of this tableland interfinger with floodplain deposits of the Big Lost River. There is a thick sequence of sediments deep in the subsurface of this subdomain, but this sequence occurs below the base of the aquifer and, therefore, has no affect on groundwater flow.

Subdomain 2d - Quaking Aspen Butte Volcanic Tableland—This subdomain includes all of the tableland basalts between the Great Rift and the Arco Rift. The postulated Quaking Aspen Butte Rift runs through the center of this tableland. Because it lies within the loci of three active or recent rift features, this tableland is higher than all other volcanic tablelands on the ESRP. Its altitude leaves it more exposed to wind and wildfire, the two processes that act together to strip vegetation and prevent soil formation and sediment accumulation. As a result, the sediment-to-basalt ratio is lower here compared to other tablelands, less than 10% versus less than 15% elsewhere. Because of its proximity to three volcanic rifts, the amount of cinder and ash in the subsurface is higher than elsewhere.

Subdomains 2e and 2f - Southeast and Northeast Axial Slope—The volcanic tablelands east of the AVH receive more precipitation than the volcanic tablelands west of the AVH, which are in the rain shadow of the mountains to the northwest of the study area. Volcanic tablelands on the east side of the ESRP are also within the watershed of the Snake River, which provides more water and deposits more sediment than the rivers that feed the BLT. The volcanic tablelands on the east side of the ESRP may, therefore, have slightly more interbedded sediment in the subsurface as one approaches the Snake River. The tableland of the east slope of the AVH is divided in two, where the dividing line coincides with the non-eruptive fissures and elongated vent of the Hell's Half Acre Lava Field and Rift feature. Basalts north of this line originate from the AVH or from the nexus of volcanic vents centered on Butterfly and Kettle buttes west of Idaho Falls, just outside of the study area. Tableland basalts south of the Hell's Half Acre line originate from the AVH or from off-axis vents like Taber Butte.

2.1.3.3 Active Volcanic Rift Zones. The earth science community has not agreed on the number and exact character of volcanic rifts on the ESRP. Consequently, the geologic conceptual model for the SWGM restricts itself to rift features whose existence is beyond doubt or rift features that are known or suspected to have an influence of groundwater flow, most likely because rifts concentrate relatively low-permeability volcanic rocks like cinder and ash.

Within the study area, features are further divided into active rifts and older, inactive rifts. Active volcanic rifts on the ESRP share several distinguishing features: elevated topography, lines of vents and/or fissures (> 0.9 km [> 0.6 mi]) whose surface expression can be mapped, and surface evidence of Holocene and latest Pleistocene volcanism (< 20,000 years). The four features within the study area that satisfy these criteria are described below. The locations of active volcanic rifts are shown in Figure 2-9.

Subdomain 3a - Axial Volcanic High—The AVH is the largest, highest, and longest feature on the ESRP. Quaternary and latest Pleistocene volcanism occurs where the AVH intersects other active rift systems. Unlike other rift systems, however, the AVH is aligned roughly parallel to the general direction of groundwater flow in the SRPA. In terms of stratigraphy, the eruptive rocks of the AVH are derived from small basaltic vents and from large rhyolitic laccoliths like Big Southern Butte that are fed by small feeder dikes. The off-axis rocks of the AVH are mostly volcanic tableland basalts with one big difference: higher heat flow under the AVH. The AVH within the study area has a higher heat flux than its surroundings, resulting in a thicker transition between the aquifer and the subaquifer zone, which is an example of three-dimensional features that are not easily accommodated by two-dimensional modeling. The base of the SRPA is controlled by the horizon between fresh and altered basalts, where the altered basalt has lost all porosity due to the growth of authigenic and alteration minerals (Morse and McCurry 2002). The alteration of subsurface basalts is driven by temperature. Along the AVH where heat flux is higher, the transition from fresh basalt to porous-clogged altered basalt will be thicker compared to cooler areas such as the BLT.

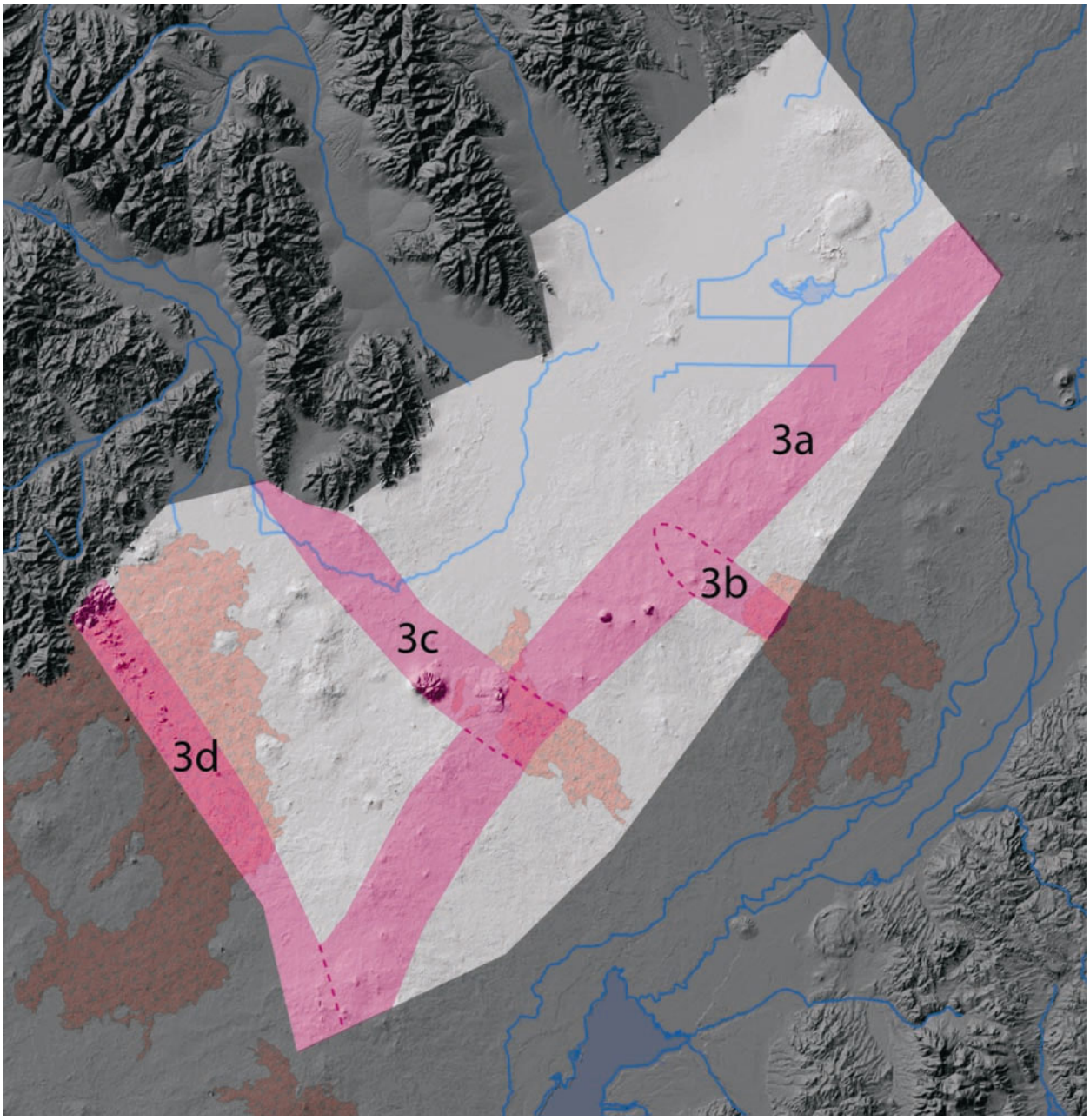

Figure 2-9. Locations of Subdomains 3a, 3b, 3c, and 3d.

Subdomain 3b – Hell's Half Acre Rift—The Hell's Half Acre Rift feature begins just off the axis of the AVH, where two sets of non-eruptive northwest-southeast trending fissures can be observed at the surface, disrupting a thin loess cover and ~350-ka basalts, from the edge of the lava field to almost as far as Route 20, 3 km (1.9 mi) away. Approximately 6 km (3.7 mi) to the southeast and in line with the fissure sets is the 0.9-km (0.6-mi) long linear crater that forms the vent of the 5.1-ka Hell's Half Acre lava flow.

Subdomain 3c - Arco Rift—The Arco Rift is a feature that is approximately 4 km (2.5 mi) wide. Its active portion is between the late Pleistocene Arco flow, west of the town of Arco, and the vents of the 13.4-ka Cerro Grand Lava Field south of Atomic City. The oldest dated feature along the Arco Rift is

Cedar Butte at ~400 ka. Between the 12-ka North and South Robbers flows and the Arco flow are several non-eruptive Quaternary fissures and vertical normal faults, two of which control the path of the Big Lost River through Box Canyon. The inactive extension of the rift along its southeasterly trend intersects Ferry Butte along the Snake River and Buckskin Butte south of Blackfoot.

Subdomain 3d - Great Rift of Idaho—The Great Rift of Idaho has already been described in the first paragraph of Subsection 2.1. Within the context of the groundwater model, the portion of the Great Rift within the Craters of the Moon National Monument forms part of the southwest boundary of the model domain.

2.1.3.4 Older Inactive Volcanic Rift Zones. Older inactive rifts included in the geologic conceptual model must meet two criteria. First, the rift feature must appear to affect local groundwater flow. Second, firm geologic evidence must exist in the subsurface to support the existence of the rift—for example, a line of volcanic vents surrounded by basalt flows or a sequence of scoria cones logged in core. Currently, the three features that meet these criteria are Lava Ridge, the AEC Butte Rift, and the Quaking Aspen Butte Rift (Figure 2-10).

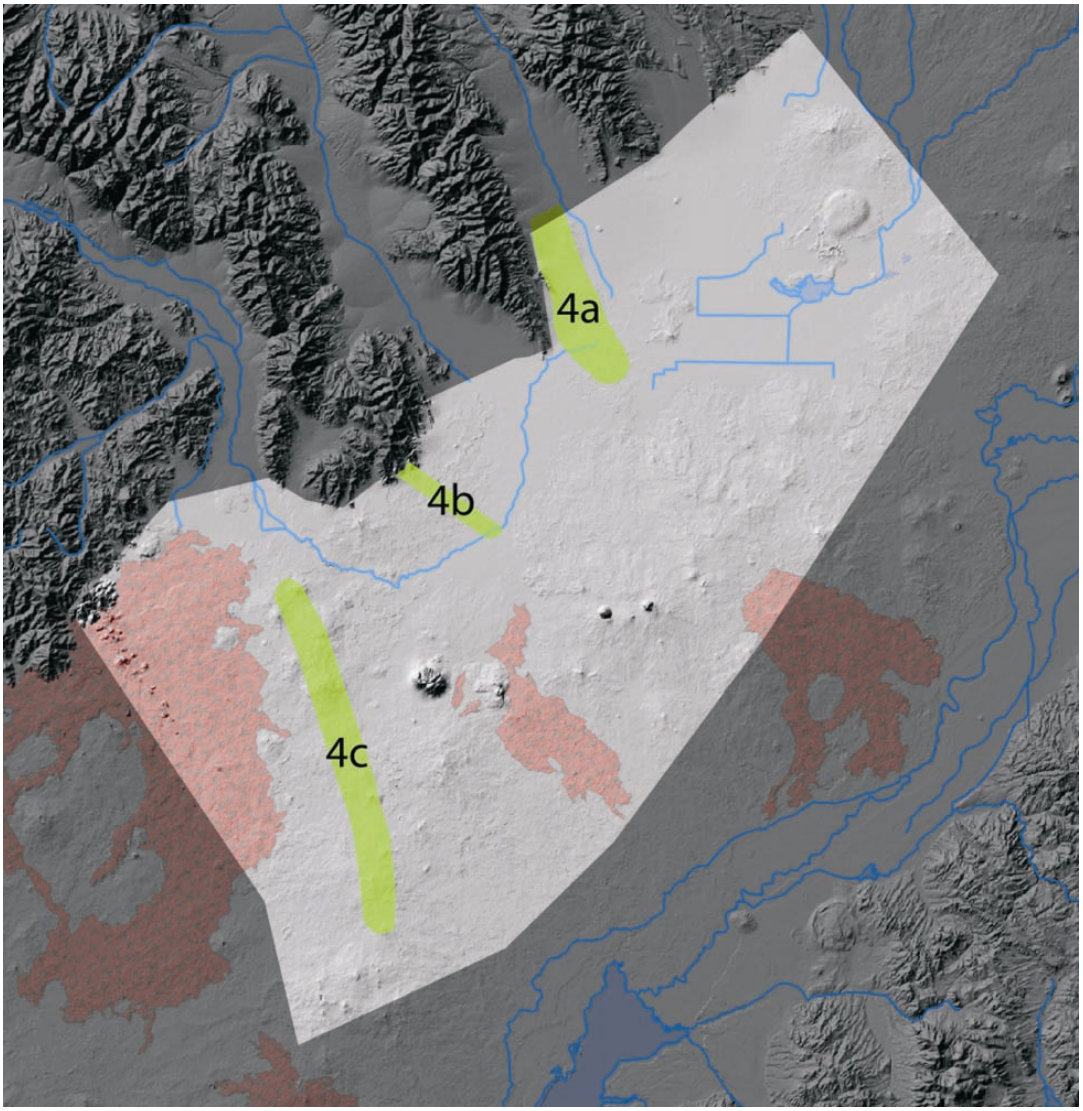

Figure 2-10. Locations of Subdomains 4a, 4b, and 4c.

Subdomain 4a - Lava Ridge—Lava Ridge is formed by a 8-km (5-mi) long line of shield volcanoes with ages between ~800 ka and ~1 Ma. The linear feature appears to influence the local flow of groundwater northeast of TAN.

Subdomains 4b - AEC Butte Rift—The surface expression of the AEC Butte Rift is a line of three volcanic vents, including the 626-ka AEC Butte itself immediately northwest of the RTC. The rift extends across the floodplain of the Big Lost River to INTEC, where scoria and other near vent facies occur at ~90 m (~300 ft) below land surface at the INTEC tank farm.[b] The thickness and dip of flows at the RTC also indicate that a vent or vents existed to the east of the floodplain between 640 and 350 ka (Helm-Clark et al. 2004). This rift feature might be the cause of a zone of lower transmissivity at INTEC and north of the RTC (Anderson et al. 1999).

Subdomain 4c - Quaking Aspen Butte Rift—The Quaking Aspen Butte Rift is a linear feature made up of shield volcanoes, many of which date between 40 and 64 ka. This line of vents extends from Wildhorse Butte on its north end to Mosby Butte in the south. This feature might account for the possible upflow, low-transmissivity feature responsible for the low water-level measurement at the Site-2 well in the tableland between the Arco Rift and the Great Rift.

2.1.3.5 Floodplain of the Big Lost River. Geologically, the floodplain of the Big Lost River, Subdomain 5 (see Figure 2-5), is the most complex portion of the study area, where meandering braided fluvium interfingers with pahoehoe basalts originating from several different volcanic rift zones surrounding the BLT. Sediments and basalt flows have deposited in the floodplain coming from three different directions, making a very complex stratigraphic column in the subsurface under the path of the river (Figure 2-11). An additional complication is the fact that basalt flows entering the floodplain area from the west and southwest are 61 to 122 m (200 to 400 ft) higher in elevation than flows of equivalent age that enter the floodplain area from the AVH to the east and southeast.

2.1.4 Distribution of Hydraulic Properties

A detailed literature search was performed to locate and identify aquifer test information on the ESRP in the vicinity of the study area. Ackerman (1991) summarized 183 aquifer tests conducted in 94 wells from the early 1950s to the early 1990s. Since that time, a large number of tests have been conducted in support of cleanup activities at INL Site facilities. Many of these tests are documented in INL Site reports, IWRRI reports, and engineering design files. In a number of cases, however, only a summary table (with no test data for review) could be located in correspondence control files in the INL Site archives.

A total of 306 tests were identified in 182 wells, inclusive of those reported by Ackerman (1991). Of these, 48 were multiple-well tests (with each observation well data set considered individually), 204 were single-well tests, 33 were packer tests, 13 were slug tests, seven were injection tests, and one was a recovery test. Most of these tests were conducted on the INL Site, with the tests being sparse near the boundaries of the study area and in the southwest portion of the study area. Specific capacity data from a number of wells in the Idaho Department of Water Resources well completion database were used to augment the data set to include measurements outside of the INL Site boundary. These data were generally from irrigation wells along the southeast boundary of the study area. The locations of wells with aquifer test data are shown on Figure 2-12. Table A-1 in Appendix A summarizes the test information, such as the discharge rate and duration, drawdown, calculated transmissivity, and analysis method. Most of the tests were analyzed using the regression method presented by Ackerman (1991), but type curve matching methods, such as the Theis (1935) or Neuman (1972) methods, were used whenever possible.

---

b. Catherine M. Helm-Clark, unpublished sampling log, Idaho National Laboratory, November 2004.

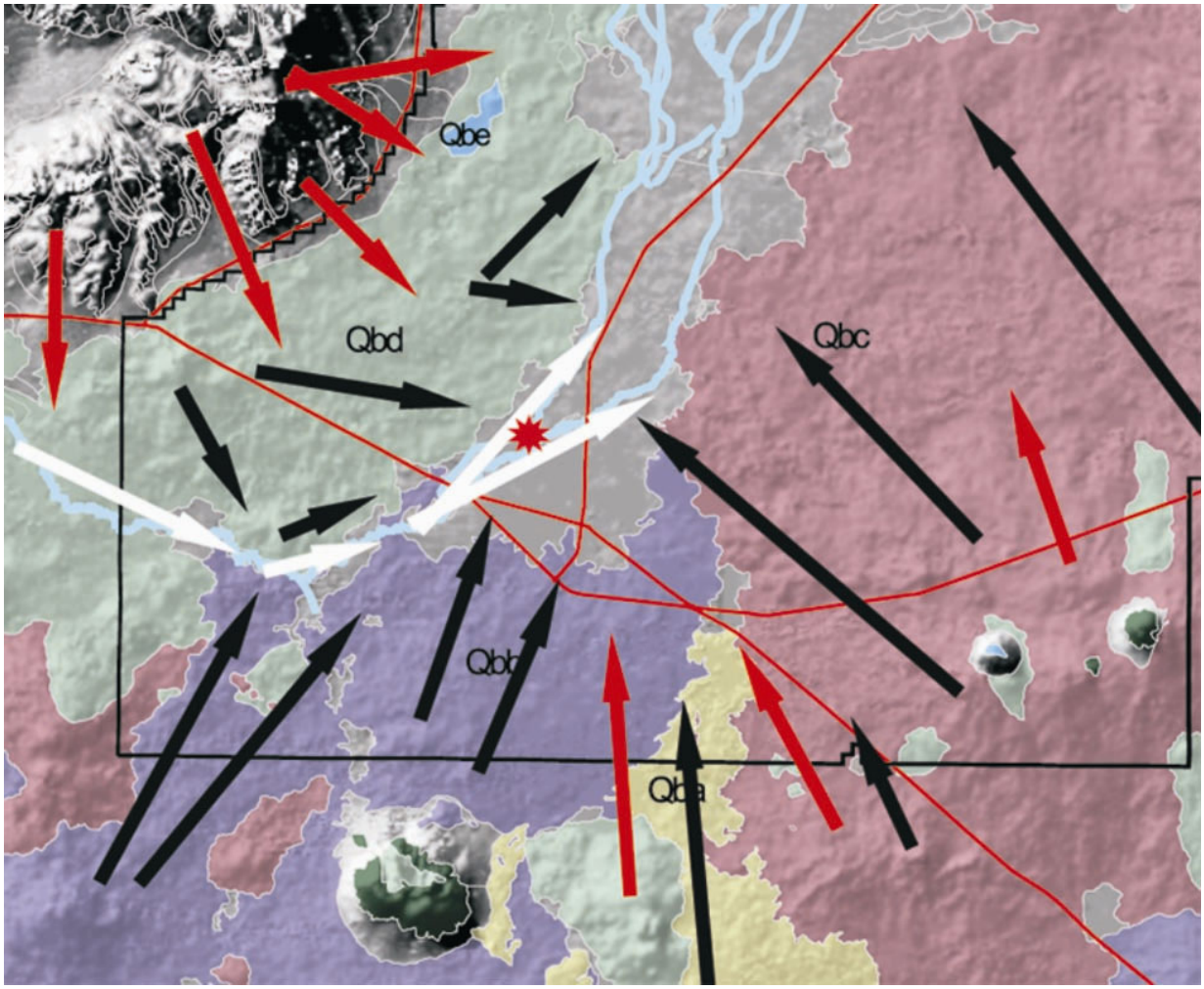

Figure 2-11. Travel directions of basalt flows and sediments into the floodplain of the Big Lost River. The red lines represent major roads, and the thin black line represents a portion of the INL Site boundary. White arrows show the path of fluvium. Red arrows show the path of alluvial materials. Black arrows show the travel paths of basalt flows simplified from Kuntz et al. (1994). The geologic unit symbols for basalts are the same as those from the most recent geologic map of the INL Site from Kuntz et al. (1994).

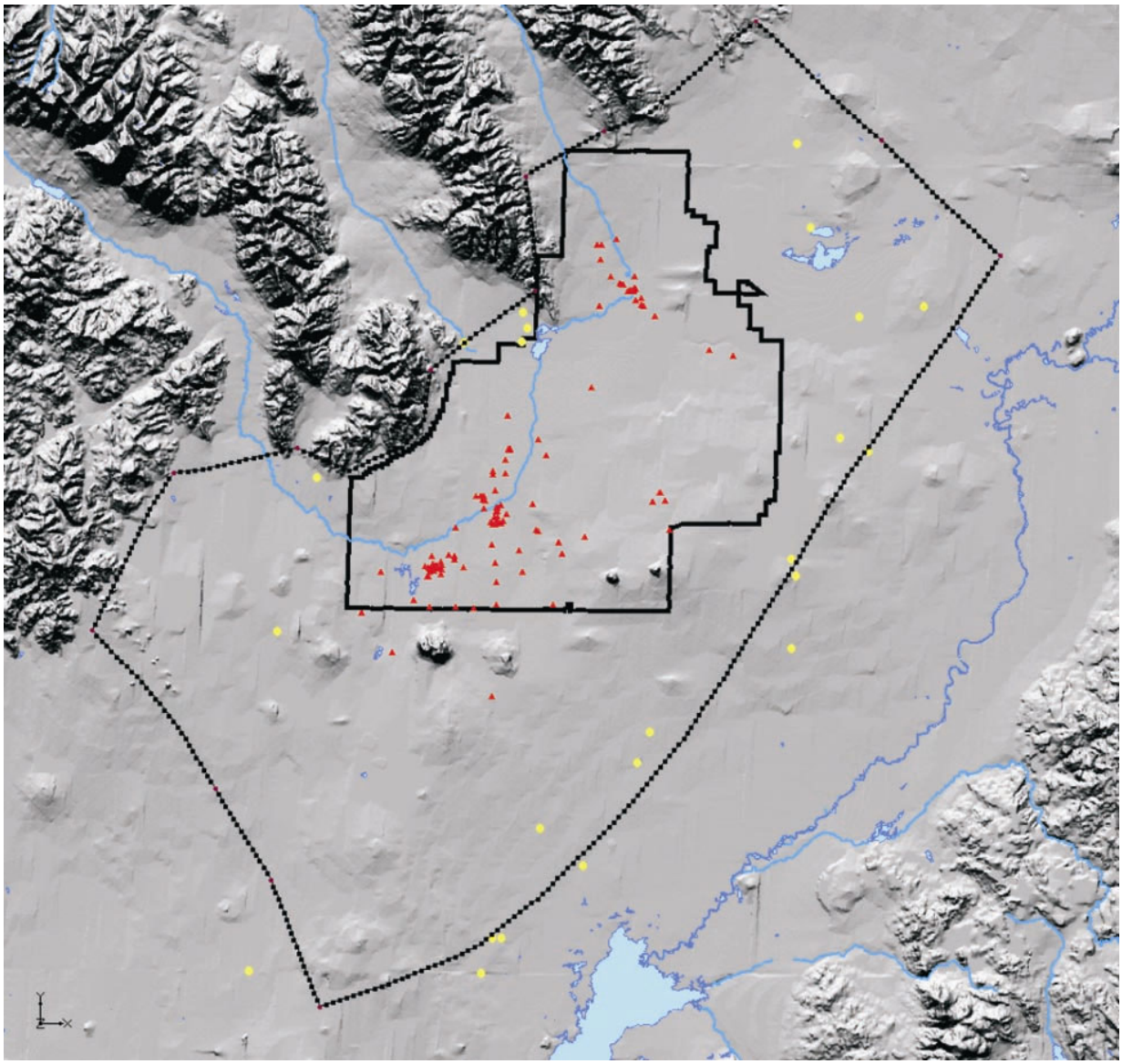

Figure 2-12. Well locations where aquifer test data are available. Red dots indicate INL Site or USGS well locations with aquifer test data. Yellow dots indicate irrigation wells with specific capacity data from the Idaho Department of Water Resources database that are used to augment the data set in areas of sparse aquifer test data.

Many of the wells on the INL Site have been tested numerous times. The oldest production wells (those drilled in the 1950s) have had as many as six aquifer tests. The test data from the wells with multiple tests were evaluated in order to assign a representative transmissivity value. Three basic variables were evaluated: the test time, the pumping rate, and the method used for the original aquifer test analysis. In general, tests with higher pumping rates and longer duration, and those analyzed with curve matching techniques, were found to be more representative in estimating aquifer parameters. This analysis is focused on preparing hydraulic property distributions for the two-dimensional model, so depth-specific packer tests, which evaluated only a small portion of the aquifer at low flow rates, were not used. These data will be used at a later date with the three-dimensional model.

Table A-2 in Appendix A summarizes the representative hydraulic conductivity and well completion information for the wells listed in Table A-1. Because the wells only partially penetrate the active portion of the aquifer, the hydraulic conductivity was calculated using laminar horizontal flow and assuming that the open interval of the well was the aquifer thickness. While this assumption will likely result in conservatively high estimates of the hydraulic conductivity, it allows for testing the various aquifer thickness scenarios using the numerical model. The hydraulic conductivity distribution over the study area is also shown graphically in Figure 2-13. In total, data from 146 wells were used to prepare the hydraulic conductivity distribution for the two-dimensional model. The calculated hydraulic conductivity ranged over seven orders of magnitude, with a mean value of 9.8×10^2 m/day (32×10^2 ft/day) and a range from 5.0×10^{-3} to 3.5×10^4 m/day (16.4×10^{-3} to 11.5×10^4 ft/day). This range equates to values representative of dense basalts and loess to highly fractured basalts, interbeds, and coarse gravels (Freeze and Cherry 1979). Figure 2-14 shows a histogram of the hydraulic conductivity values, where a nearly log-normal distribution can be seen.

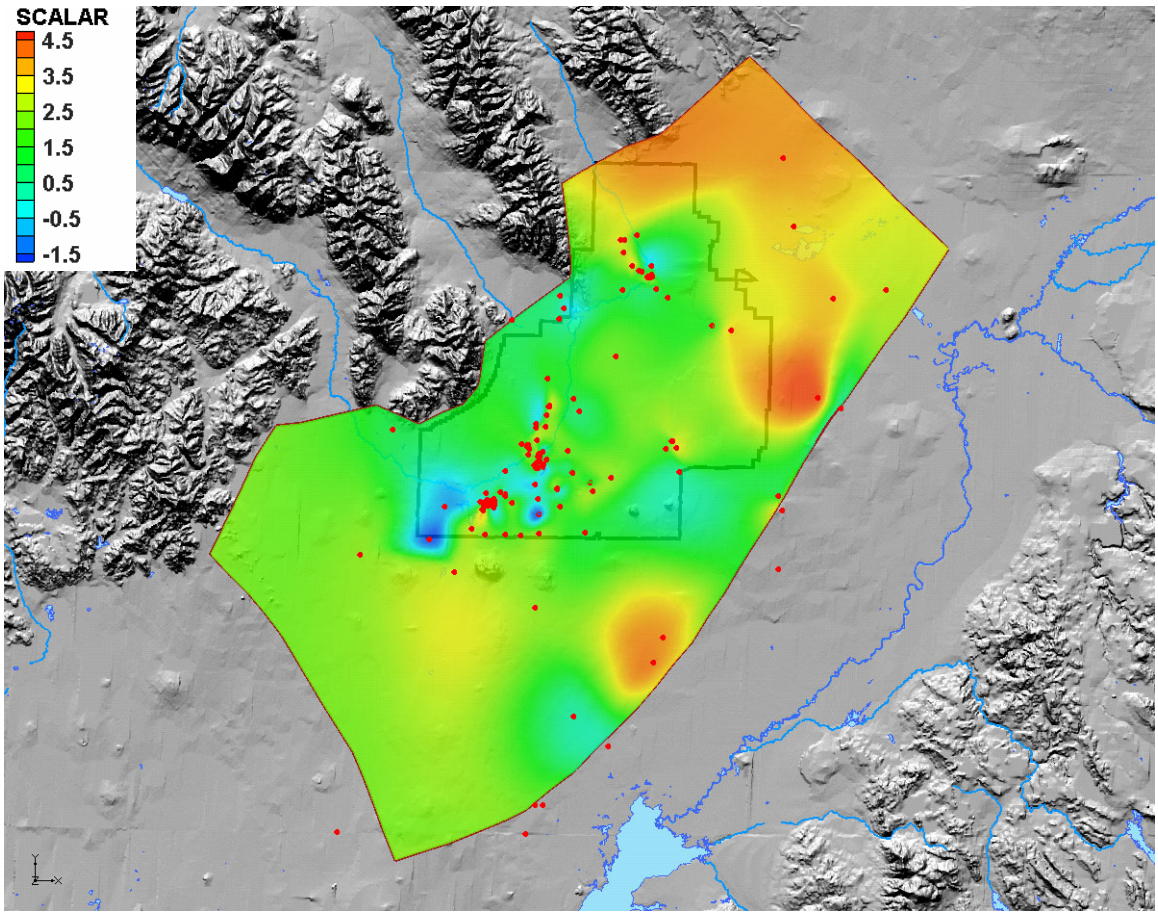

Figure 2-13. Hydraulic conductivity distribution of the study area. Red dots indicate well locations with aquifer test data. Shown is the log-transformed hydraulic conductivity in m/day.

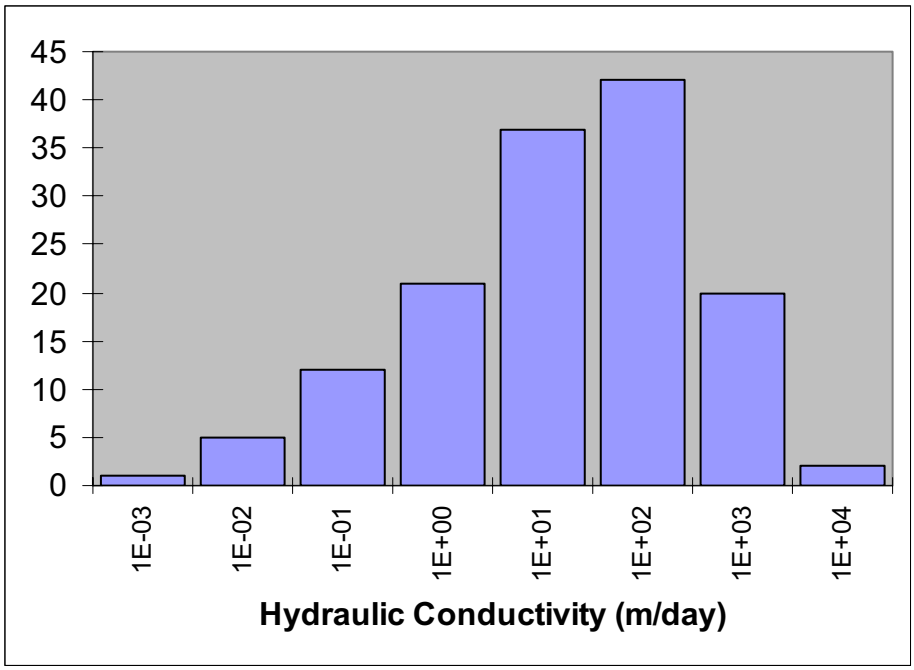

Figure 2-14. Distribution of the hydraulic conductivity binned on the logarithmic scale.

The aquifer test data were also evaluated based on the geologic subdomains presented in Subsection 2.1.3. Figure 2-15 shows the geologic subdomains overlain on the aquifer test location map. A number of subdomains, including all of the inactive rift zones and the subdomain at the mouth of the Big Lost River drainage, had no aquifer tests. Most of the aquifer tests were completed in the floodplain of the Big Lost River (Zone 5) and the volcanic tablelands in the central part of the INL Site (Zone 2b). These zones contain the major facilities on the INL Site and have been studied in the greatest detail. Table 2-1 summarizes the number of aquifer tests conducted in each subdomain and the range in hydraulic conductivity.

2.2 Inflows and Outflows

Major inflows to the SRPA within the OU 10-08 study area consist of regional underflow across the northeastern study area boundary, inflows derived from tributary basin underflow and streamflow, and recharge from infiltration of areal precipitation. Outflows occur as regional underflow across the southwestern study area boundary. Table 2-2 summarizes the water budget for the OU 10-08 study area. Values in this subsection represent annual averages for use in the two-dimensional steady-state flow model.

2.2.1 Regional Underflow into the OU 10-08 Study Area

Regional underflow enters the OU 10-08 study area from the Mud Lake area northeast of the INL Site. This regional underflow is derived from recharge of runoff from the Yellowstone Plateau to the northeast and from tributary basin inflows north of the INL Site. Groundwater flow in the Mud Lake area is characterized by extensive groundwater development for agricultural uses and by significant interaction between groundwater flow systems and surface-water features such as the Henry's Fork and its associated canal systems. This complex hydrologic system is marked by seasonally changing groundwater levels and distinct vertical hydraulic gradients within the SRPA.

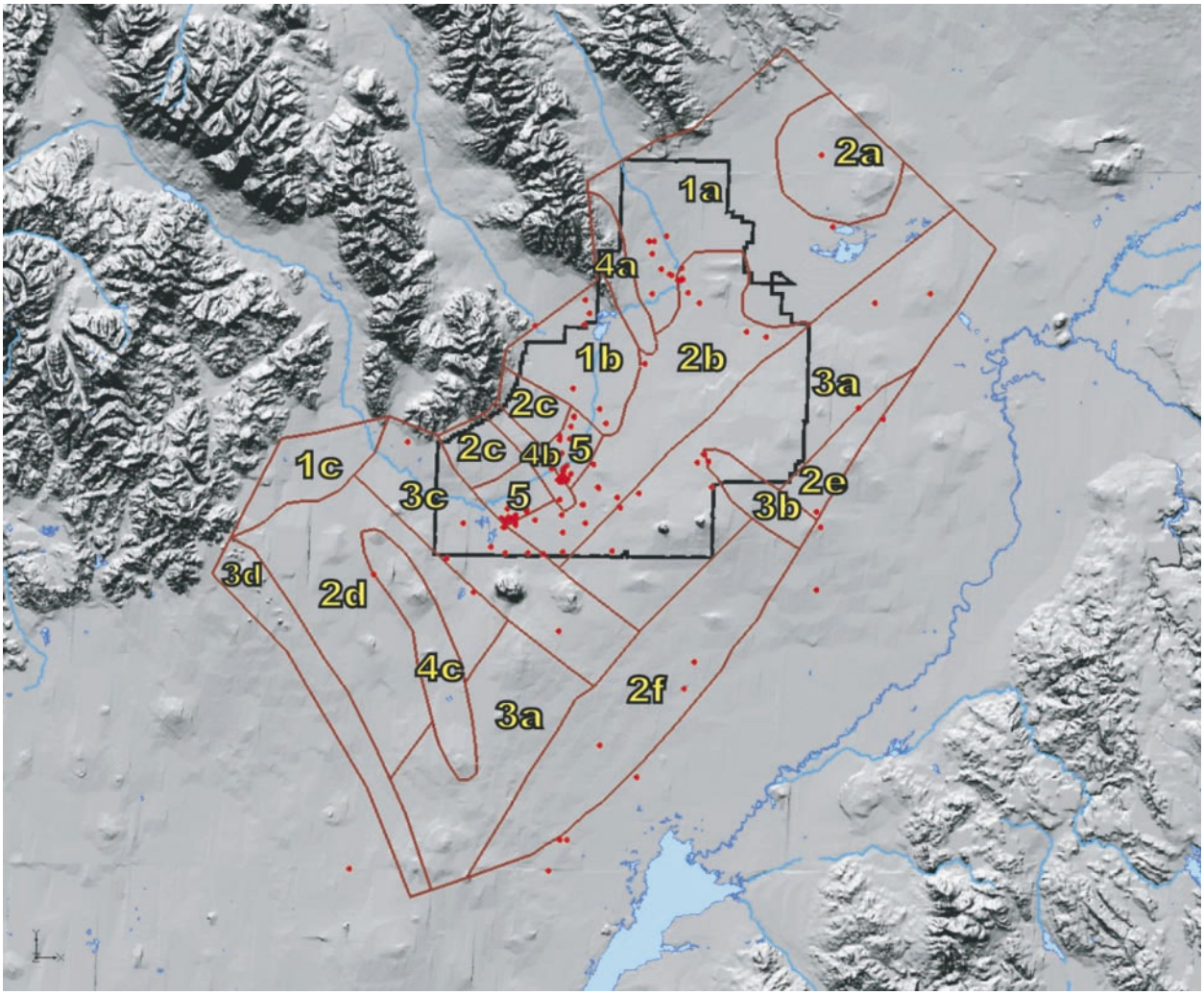

Figure 2-15. Map of the study area showing the distribution of aquifer tests within each subdomain.

Table 2-1. Subdomain hydraulic conductivity distribution.

Subdomain Number	Description	Number of Aquifer Tests	Hydraulic Conductivity Range (ft/day)	Hydraulic Conductivity Range (m/day)
Sedimentation Areas				
1a	Pluvial Lakebed	10	4.6E+01 to 8.8E+03	1.4E+01 to 2.7E+03
1b	Pluvial Lakebed	7	1.6E+00 to 1.6E+02	5.0E-01 to 4.9E+01
1c	Buried Inland Delta of the Big Lost River	0	Not applicable	Not applicable
Volcanic Tablelands				
2a	Table Butte Volcanic Tableland	1	2.9E+04 to 2.9E+04	8.8E+03 to 8.8E+03
2b	West Axial Slope	37	9.8E-01 to 9.6E+03	3.0E-01 to 2.9E+03
2c	Crater Butte Volcanic Tableland	1	3.6E+01 to 3.6E+01	1.1E+01 to 1.1E+01
2d	Quaking Aspen Butte Volcanic Tableland	2	8.1E+02 to 2.2E+03	2.5E+02 to 6.8E+02
2e	Northeast Axial Slope	4	8.5E-00 to 1.2E+05	2.6E+00 to 3.5E+04
2f	Southeast Axial Slope	8	5.6E+00 to 4.1E+01	1.7E+00 to 1.3E+01
Active Rift Zones				
3a	Axial Volcanic High	9	1.0E+01 to 1.2E+04	3.2E+00 to 3.6E+03
3b	Hell's Half Acre Rift	1	5.6E+03 to 5.6E+03	1.7E+03 to 1.7E+03
3c	Arco Rift	10	7.9E-02 to 1.9E+04	2.4E-02 to 5.9E+03
3d	Great Rift of Idaho	1	5.1E+02 to 5.1E+02	1.6E+02 to 1.6E+02
Inactive Rift Zones				
4a	Lava Ridge	0	Not applicable	Not applicable
4b	AEC Butte Rift	0	Not applicable	Not applicable
4c	Quaking Aspen Butte Rift	0	Not applicable	Not applicable
Big Lost River Floodplain				
5	Big Lost River Floodplain	55	1.6E-01 to 2.9E+04	5.0E-02 to 8.7E+03

Table 2-2. Sources of inflow and outflow for the OU 10-08 study area.

	cfs	acre-ft/yr	m^3/day
Inflows			
Regional underflow (Spinazola [1994] outflow minus Kjelstrom [1986] estimates of underflow from Medicine Lodge, Warm Springs, Deep, and Birch creeks[a])	1,105	799,993	2,703,799
Spinazola regional underflow minus Medicine Lodge, Warm Springs, Deep, and Birch creeks[a]	1,124	813,739	2,750,257
Medicine Lodge Creek	13	9,412	31,809
Warm Springs and Deep Creeks	42	30,407	102,768
Birch Creek underflow/streamflow[b]	108[b]	78,188	264,260
Little Lost River underflow/streamflow[b]	214[b]	154,929	523,625
Big Lost River underflow[b]	408[b]	295,379	998,314
Big Lost River streamflow	97	70,255	237,344
Areal precipitation (2%)	35	25,339	85,640
Areal precipitation (5%)	88	63,709	215,323
Outflows			
Underflow out of the OU 10-08 study area (2% precipitation)	2,022	1,463,871	4,947,559
Underflow out of the OU 10-08 study area (5% precipitation)	2,075	1,502,241	5,077,242

a. Spinazola's (1994) underflow of 1,268 cfs included inflow from Medicine Lodge, Warm Springs, Deep, and Birch creeks. His estimate also included areal precipitation recharge in the area of overlap, not subtracted here.
b. Kjelstrom's (1986) estimates of underflow from the tributary basins are presented here. Underflows added to the two-dimensional model from the Birch Creek, Little Lost River, and Big Lost River tributary basins were 102, 227, and 361 cfs, respectively, as derived from USGS preliminary models and within the uncertainties identified by Arnett and Smith (2001).
cfs = cubic feet per second

Spinazola (1994) constructed a numerical model to evaluate the consequences of increased development and reduced recharge on future water supplies in the Mud Lake area. The southwestern boundary of this numerical model overlaps the northeastern end of the OU 10-08 study area. Estimated underflow across Spinazola's southwest boundary is 1,268 cubic feet per second (cfs) (918,000 acre-ft) annually and includes water contributed to the system from the tributary basins to the northeast of the INL Site (Birch, Deep, Warm Springs, and Medicine Lodge creeks) and from direct precipitation in the study area overlap.

2.2.2 Inflows from Underflow and Streamflow in Major Drainage Basins Tributary to the Eastern Snake River Plain

The ESRP is bounded on the northwest by mountains and valleys of the B&R Province. This mountainous region forms a sequence of drainage basins that are tributary to the plain. Tributary basins contributing flow to the northwestern edge of the OU 10-08 study area include the Birch Creek, Little Lost River, and Big Lost River basins (Figure 2-2). Basins also include Medicine Lodge, Deep, and Warm Springs creeks to the northeast of the INL Site.

2.2.2.1 Tributary Basins to the Northeast of the INL Site. Medicine Lodge, Deep, and Warm Springs creeks drain tributary basins in the Centennial Mountains at the northern end of the ESRP. These drainages contribute streamflow and underflow to the regional flow system.

Kjelstrom (1986) used basin regression techniques to estimate underflow from these tributary basins (Table 2-1). Underflow from Medicine Lodge Creek was estimated to be 13 cfs (9,412 acre-ft/year). Combined underflow from Deep and Warm Springs creeks was estimated to be 42 cfs (30,407 acre-ft/year).

2.2.2.2 Birch Creek Tributary Basin. Birch Creek drains a tributary basin of more than 1,036 km^2 (400 $mi^{2)}$) that includes the mountains of the Lemhi and Bitterroot ranges and the intervening Birch Creek Valley. Streamflow in Birch Creek is sustained by discharge from springs and seeps where bedrock intersects the land surface.

A USGS gaging station was maintained seasonally on Birch Creek near the Reno Ranch from 1967 until 1987. Daily discharges for the period of record ranged from about 40 cfs to more than 80 cfs. The average annual discharge for 1967 and 1987 ranged from 56 to 62 cfs. Based on this intermittent record, streamflows in Birch Creek are relatively constant and probably represent groundwater discharge from tributary basin aquifers. All flows in Birch Creek are diverted to a ditch near the point of entry onto the ESRP. This ditch transports water east to the Reno Ranch and is used in power generation and irrigation upgradient from the INL Site.

Water derived from watershed runoff infiltrates the alluvial deposits filling the Birch Creek Valley and moves downgradient toward the intersection with the ESRP. Underflow within these deposits provides a source of inflow to the aquifer.

Kjelstrom (1986) used basin-yield equations to calculate an average annual rate of groundwater flow of 108 cfs (78,188 acre-ft/year) through these alluvial deposits. Garabedian (1992) used this underflow rate as a source of groundwater inflow to the SRPA. Spinazola (1994) estimated similar rates for underflow and streamflow from the Birch Creek tributary basin, varying rates annually based on water levels in an index well. He used a variable inflow based on a formula that calculated a single underflow and estimated monthly underflows using water levels in an index well.

2.2.2.3 Little Lost River Tributary Basin. The Little Lost River drains an area of about 2,494 km^2 (963 mi^2) of mountainous tributary basin (Swanson et al. 2002) that includes the northeastern slopes of the Lost River Range and the western slopes of the Lemhi Range (Figure 2-2). Most tributaries to the Little Lost River infiltrate before reaching the river and do not contribute significantly to streamflow.

Streamflows were monitored from 1941 through 1989 at a gaging station on the Little Lost River approximately 11 km (7 mi) upstream from Howe. Average annual discharge during this period was 77 cfs, ranging from 49 to 107 cfs. Downstream from this gaging station, most streamflows are diverted for irrigation or infiltrate. Streamflow contributions to inflow to the SRPA are considered to be inconsequential.

Kjelstrom (1986) used basin-yield equations to calculate an average annual rate of groundwater flow of 214 cfs (154,929 acre-ft/year) through the alluvial deposits of the Little Lost River tributary basin. Garabedian (1992) used this underflow rate as a source of groundwater inflow to the SRPA. Recharge likely takes place in a transitional area at the mouth of the Little Lost River Valley as downward leakage from perched systems derived from tributary basin underflow to the aquifer below.

2.2.2.4 Big Lost River Tributary Basin. The Big Lost River upstream from Arco drains a mountainous 3,652-km^2 (1,410-mi^2) tributary basin that includes the Lost River Range and Pioneer Mountains to the west of the ESRP (Figure 2-16). This basin ranges in altitude from about 1,615 m (5,300 ft) above sea level near Arco to more than 3,840 m (12,600 ft) above sea level in the Lost River Range. Mean elevation is approximately 2,347 m (7,700 ft).

Water derived from the Big Lost River watershed moves as streamflow down the Big Lost River and its tributaries or infiltrates alluvial deposits and moves downgradient as groundwater flow through alluvium-filled basins between the mountain ranges. Streamflows and tributary underflow provide sources of recharge to the SRPA.

Recharge to the SRPA from Infiltration of Streamflow in the Big Lost River—Recharge to the SRPA from infiltration of streamflow along the channel of the Big Lost River occurs in proximity to several major facilities and contaminant source terms at the INL Site. Because of this proximity, this source of recharge is critical to an evaluation of contaminant transport in the SRPA.

The Big Lost River flows to the southeast from its tributary drainage system onto the ESRP. Shortly after entering the ESRP, the stream channel is diverted to the east (Figure 2-16) by the topographically high vent areas associated with the Arco Rift. The Big Lost River channel continues to the east and then to the north, cutting a canyon through basalt flows in the southwestern part of the INL Site and flowing onto a broad floodplain that extends from near the RWMC north to a series of playa lakes. In the 1960s, a diversion channel was constructed to a series of low-lying areas south of the river to divert excess flows for downstream floodwater protection.

Streamflows in the Big Lost River are controlled by snowpack, storage in Mackay Reservoir, and downstream irrigation. Streamflows are monitored at a series of stream gaging stations operated by the USGS (USGS 2005). The average annual discharge for the Big Lost River near Arco for 48 years of streamflow data (1947 though 1960, 1967 through 1979, and 1983 through 2003) is shown in Figure 2-17. Based on this period of record, average annual discharge is variable, ranging from 488 cfs in 1984 to zero during several years. The average annual discharge for the period of record is 97.3 cfs (70,225 acre-ft/year).

Episodic recharge occurs in response to these variable streamflows as they rapidly infiltrate through the Big Lost River channel and in the INL Site spreading areas (Figure 2-2). Streamflow records measured from 1985 through 2003 at a series of stream gaging stations downstream from the Arco gage were used to estimate the percentage of water that infiltrated along specified reaches during that period. Streamflows and average infiltration estimates are shown in Table 2-3. These estimates were made assuming that recharge was rapid and evapotranspiration losses were minimal. Based on these data, as much as 14.5% (or approximately 14 cfs) of the Arco streamflows infiltrated in the reach extending from the Arco gage to a gaging station at the spreading area diversion channel, and 25.9% (or approximately 25 cfs) of the streamflows were diverted for recharge in the INL Site spreading areas. A total of 12.6% (or approximately 12 cfs) of the Arco streamflows infiltrated in the stream reach from the spreading-area diversion to Lincoln Boulevard. A total of 47% (or approximately 46 cfs) of the Arco streamflow was available for infiltration in the stream reach from Lincoln Boulevard to the Big Lost River sinks and playa to the north. These recharge estimates do not reflect the large range in discharge that occurs from year to year. They also do not take into account losses derived from evapotranspiration in the channel and streambank, diversions, and playas.

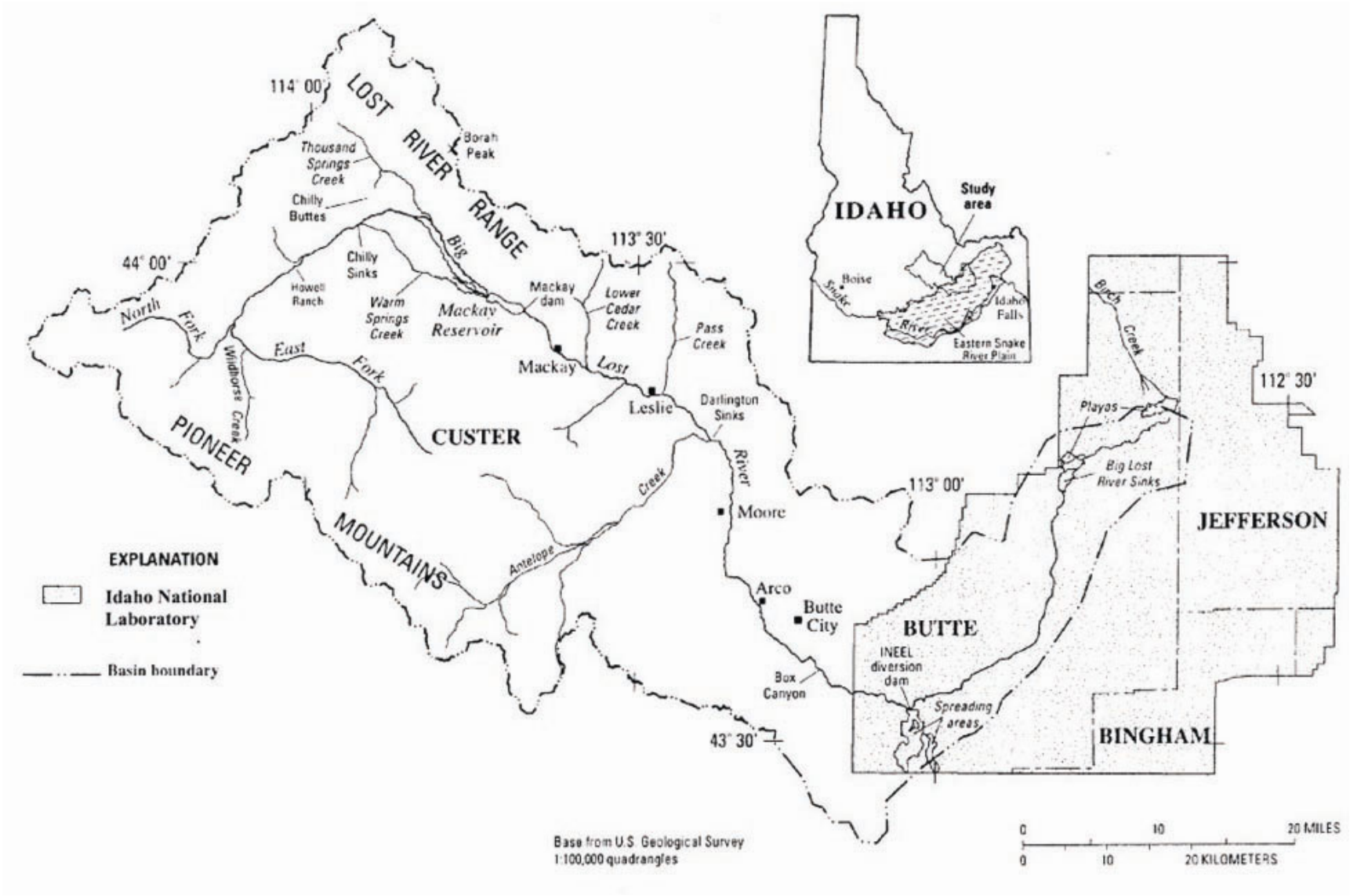

Figure 2-16. Big Lost River tributary drainage basin (modified from Hortness and Rousseau 2003.)

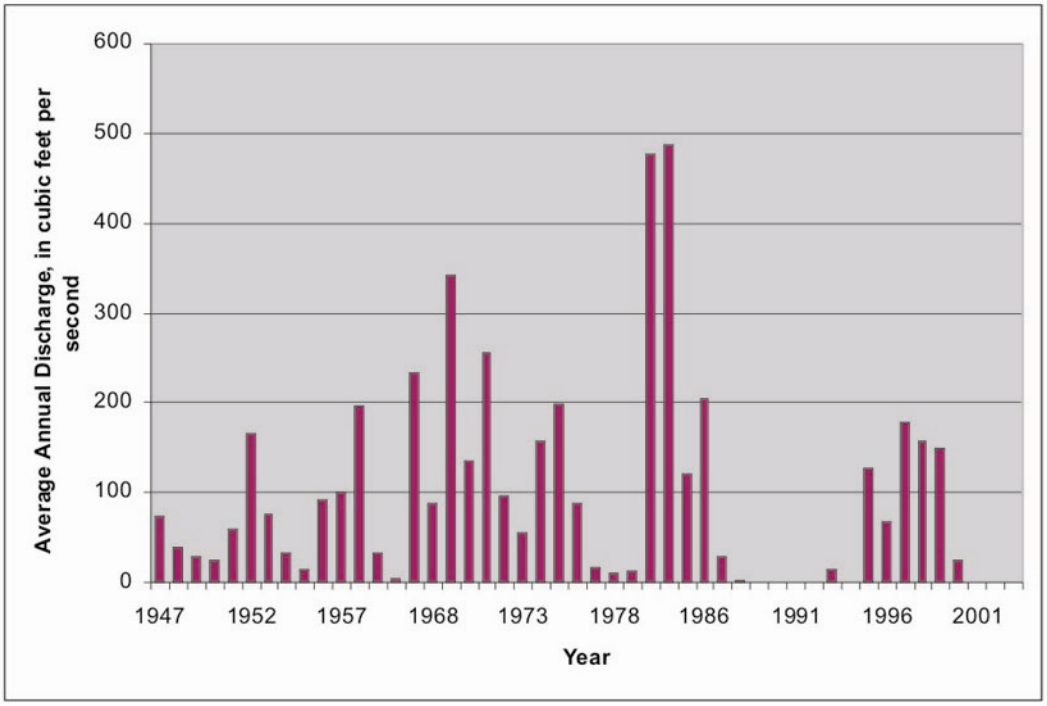

Figure 2-17. Average annual discharge for the Big Lost River near Arco from 1947 through 2003.

Table 2-3. Average annual discharge and estimated infiltration for the Big Lost River from Arco to the terminus (1985 through 2003).

Year	Average Discharge, Big Lost River near Arco (cfs)[a]	Flow Diverted to the INL Site Spreading Areas (cfs)[a]	Average Discharge in the Big Lost River near Arco minus flow to INL Site Spreading Areas	Average Discharge, Big Lost River below INL Site Spreading Areas (cfs)[a]	Estimated Infiltration Losses, Big Lost River near Arco to the INL Site Spreading Area Diversion (cfs)	Average Discharge, Big Lost River at Lincoln Boulevard (cfs)[a]	Estimated Infiltration Losses, INL Site Spreading Area Diversion to Big Lost River at Lincoln Boulevard (cfs)	Estimated Infiltration Losses, Big Lost River at Lincoln Boulevard to Playas (cfs)
1985	121	39.3	81.7	60.7	21	49.1	11..6	49.1
1986	205	59	146	122	24	99.8	22.2	99.8
1987	29.2	10.3	18.9	7.1	11.8	1.41	5.69	1.41
1988	2.91	0	2.91	0	2.91	0	0	0
1989	0	0	0	0	0	0	0	0
1990	0	0	0	0		0	0	0
1991	0	0	0	0	0	0	0	0
1992	0	0	0	0	0	0	0	0
1993	14.7	0.22	14.48	10.5	3.98	7.05	3.45	7.05
1994	0	0	0	0	0	0	0	0
1995	126	50.1	75.9	63.6	12.3	54.3	9.3	54.3
1996	67.3	4.52	62.78	42.4	20.38	36	6.4	36
1997	179	52.6	126.4	102	24.4	81.9	20.1	81.9
1998	157	32.1	124.9	108	16.9	88.2	19.8	88.2
1999	150	30.8	119.2	109	10.2	78.9	30.1	78.9
2000	24.3	0	24.3	16.2	8.1	8.69	7.51	8.69
2001	0	0	0	0	0	0	0	0
2002	0	0	0	0	0	0	0	0
2003	0	0	0	0	0	0	0	0
Sum of Average Annual Discharges	1,076	279			156	505	136	505
% of Arco Flows Available for Infiltration in a Specified Reach		25.9			14.5		12.6	47.0

a. From USGS (2005).

Water infiltrating the channel of the Big Lost River must move through a thick sequence of unsaturated basalts and interbedded sediments, with a vadose zone ranging from nearly 152 m (500 ft) near the RWMC to approximately 60 m (200 ft) near the playas. Water levels in shallow, vadose-zone wells located as much as 0.8 km (0.5 mi) away from the river channel have been observed to change rapidly in response to streamflows, indicating that infiltrating water spreads away from the channel in the shallow subsurface, and that the effective area of recharge might be much wider than the narrow river channel.

Recharge to the SRPA from Underflow within Big Lost River Tributary Basin Alluvial Deposits—Groundwater within the alluvial deposits of the Big Lost River and tributary valleys flows downgradient and eventually moves into the basalts and sediments of the ESRP in the vicinity of Arco. A series of USGS studies provided estimates of the magnitude of this groundwater influx. Kjelstrom (1986) used basin-yield equations to calculate an average annual rate of groundwater flow of 408 cfs (295,379 acre-ft/year) through these alluvial deposits. Garabedian (1992) used this underflow rate as a source of groundwater inflow to the SRPA. Although the annual flux might vary somewhat in response to climatologic changes and local groundwater usage, variability is probably minimal in comparison to episodic streamflow.

Groundwater levels in the Big Lost River alluvial aquifer typically are hundreds of feet higher than those in the SRPA to the east. A transition zone between groundwater flow in the Big Lost River basin and the SRPA occurs in the vicinity of Arco. This transition zone is characterized by decreasing head with depth, as observed in the drilling of several deep wells.

Within this transition zone, water moving out from the mouth of the Big Lost River Valley remains perched on sediments or, in some instances, on massive basalts, leaking slowly through those perching units and forming a sequence of perched water zones down to the water table. Recharge occurs to the top of the aquifer throughout the entire transition area.

Description and Location of Transition Zone Geohydrologic Features—Three mountain streams flow roughly southward onto the ESRP from the northernmost portion of the B&R Province: the Big Lost River, the Little Lost River, and Birch Creek (Figure 2-1). Though some studies have referred to these transition zones (e.g., Crosthwaite et al. 1970; Koslow 1984; Mundorff et al. 1964), the stratigraphic transitions from the B&R to the ESRP have not been studied before together or in detail. The OU 10-08 groundwater modeling work plan (DOE-ID 2004) identified this as a data gap. Subsequent subsections briefly outline the results of this effort. The Big Lost River is used as an example of how the stratigraphy and hydrostratigraphy of the transitions work, because it is the most complex of the three transition zones, whereas the other two transitions are essentially simplifications of the former.

The Big Lost River exits the B&R and flows onto the ESRP at Arco (see Figure 2-18). Between 1 and 2 Ma, the Big Lost River was trapped by the rise of the AVH, which prevented flow southward toward the ancestral Snake River. There is evidence that the Big Lost River once flowed to the southwest but was cut off from this route by the rise of the Great Rift and its predecessors that were active between 480 ka and 57 ka (dates from Kuntz et al. 2002). The river's buried paleo-channels to the east were shifted and occasionally blocked by the rise of Arco Rift and Quaking Aspen Butte Rift volcanoes. During the latest Pleistocene, the eruption of the Arco flow, a typical ESRP low-angle shield volcano, pushed the Big Lost River to the east, shifting it from a more southerly previous channel. Thick sequences of buried fluvial sediments both north and south of Box Canyon as well as east and west of the Arco flow suggest that the Big Lost River migrated extensively before Box Canyon was formed. Because of the widespread distribution of subsurface fluvium, it is possible that the shift of the river by the Arco flow preceded the down cutting of Box Canyon. These successive entrapment events led to intervals where

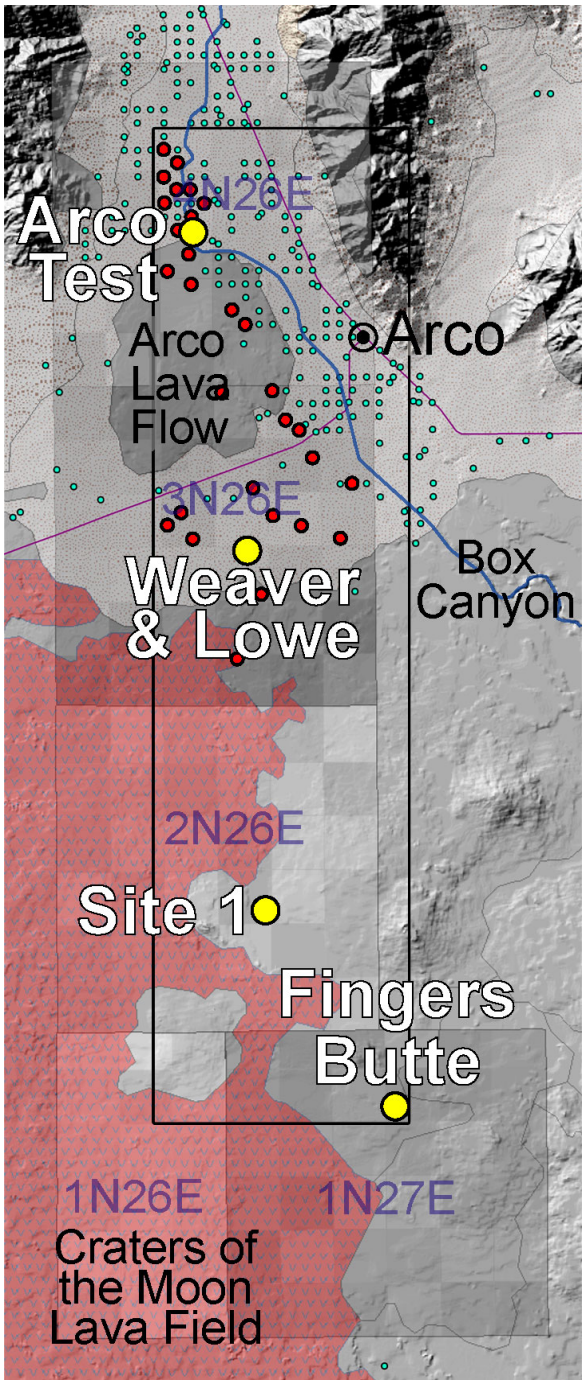

Figure 2-18. Shaded relief map of the Arco area where the Big Lost River (blue line, upper right-hand corner) exits the B&R Province and flows onto the ESRP. Major roads are in purple. Green dots are domestic water wells listed in the Idaho Department of Water Resources database. Red dots are domestic water wells whose data was used to make the cross sections shown in Figure 2-19. Yellow dots are deep wells whose data was also used to make the Figure 2 19 cross sections, for which historical water-level measurements are available. The red area is the eastern edge of the Craters of the Moon Lava Field. The black box outlines the top of the cross section boxes shown in Figure 2 19 and represents an area 18 mi long and 5 mi wide. Areas with small squares of grey shading are sections within the township-range blocks denoted by blue labels.

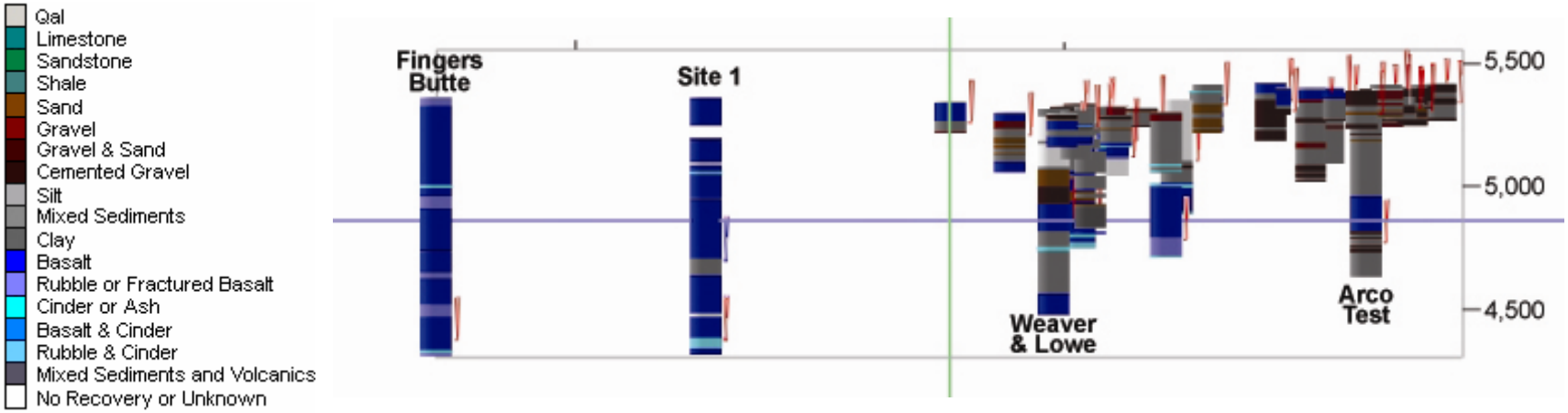

Figure 2-19a. A view from the east at a three-dimensional, 1-to-25 scale cross section of the Arco transition. This view is not tilted, so the top of the cross section box is not visible. North is to the right, and south is to the left. This view of the cross section box is 18 mi long. Elevations in feet with respect to mean sea level are shown on the right. Volcanic rocks are shown in shades of blue. Relatively permeable sediments are shown in shades of brown. Relatively impermeable sediments are shown in shades of gray. Lithified sedimentary rocks are in shades of green. The red triangular symbols are recorded static water tables. Blue symbols are either water table measurements after a well was deepened (for wells in the right half of figure) or a perched layer (for wells in the left half of figure).

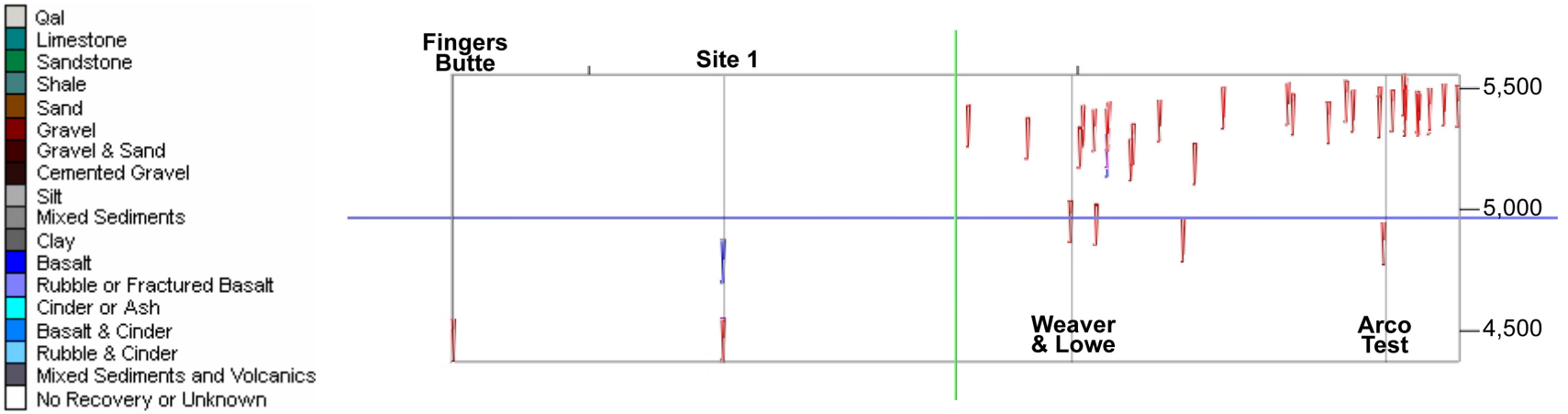

Figure 2-19b. Same as Figure 2-19a without lithology (water levels only).

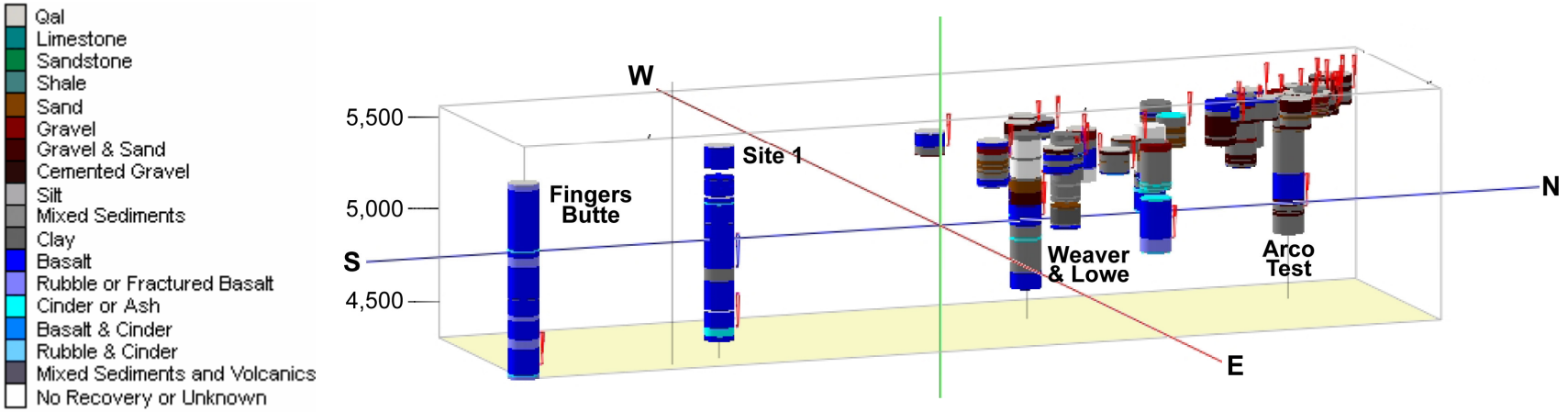

Figure 2-19c. A view at an angle of 10° above horizontal from the southeast (at an azimuthal bearing of 110°) of a 1-to-20 scale, three-dimensional cross section of the Arco transition. The cross section box represents an area 18 mi long and 5 mi wide. Elevations are in feet are with respect to MSL. All other cross section information is the same as that already described for Figure 2-19a.

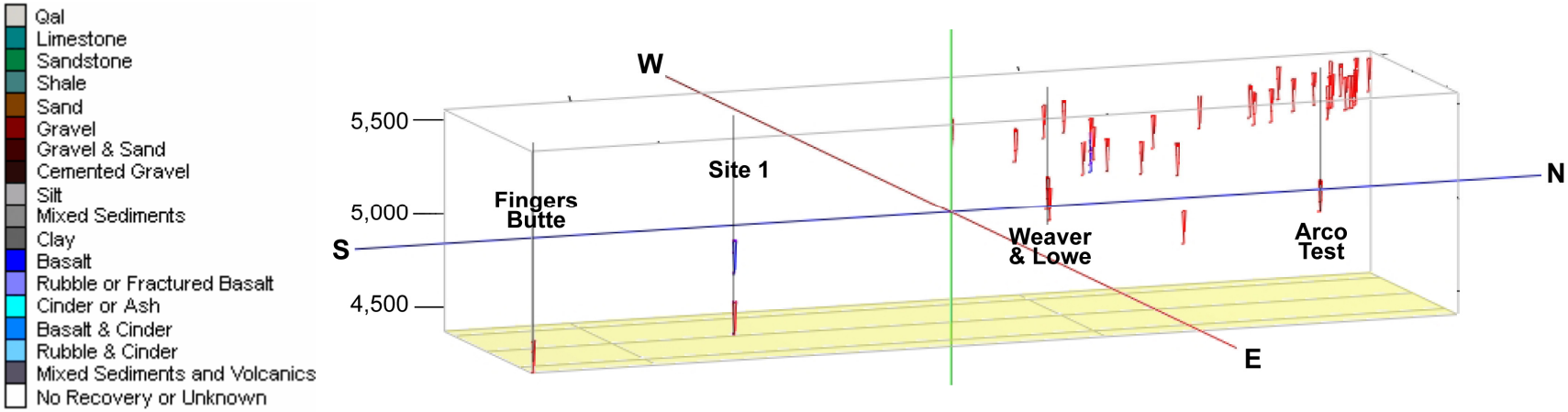

Figure 2-19d. Same as Figure 2-19c without lithology (water levels only).

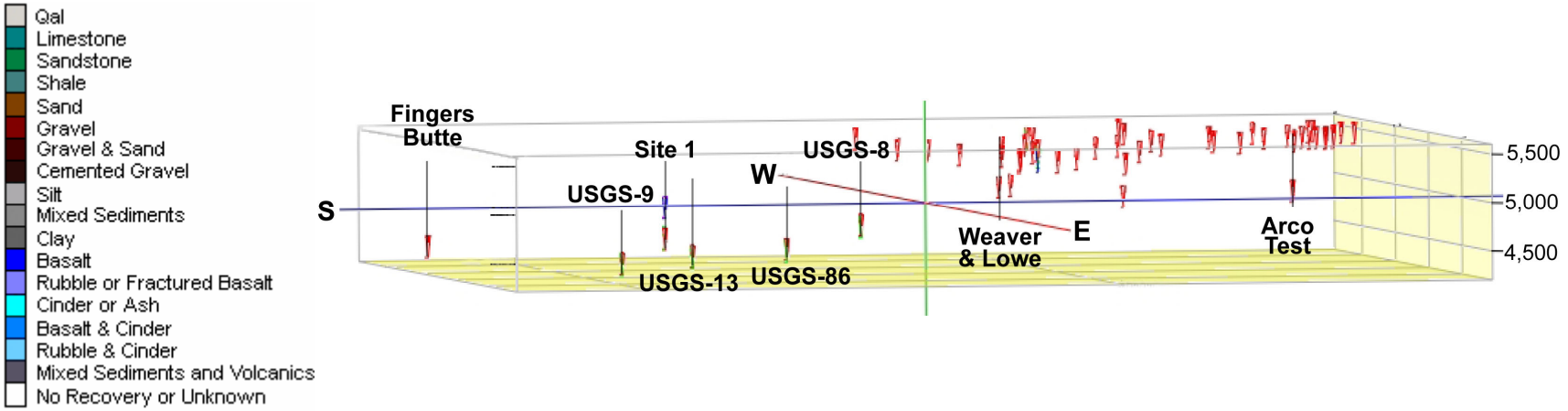

Figure 2-19e. A 1-to-15 scale, three-dimensional cross section of the Arco transition. This figure covers Townships 1N through 4N, Ranges 26E through 28E, from the town of Moore at the northwest corner of the cross section box to well USGS-009 in the south half of the INL Site at the southeast corner of the cross section box. The view is from the southeast at an azimuthal bearing of 105°, 5° above horizontal. This cross-sectional view is more than twice as wide as those shown is Figures 2-19a through 2-19d. All other cross section information is the same as that already described for Figure 2-19a. This figure shows the perched layer (blue) and water table (red) at Site 1 in the perspective of the southward deepening SRPA.

finer-grained sediments fanned outward from the mouth of the valley, forming an inland delta complex. The distance from the USGS's ARCO TEST monitoring well (Figure 2-18) to the inferred southern edge of these outwashed sediments is approximately 14.5 km (9 mi). The east-west extent of these sediments is approximately the same. This migration history of the Big Lost River is based on logs from more than 200 wells in the Arco area. Figures 2-19a through 2-19d represent an approximately north-south cross section through the middle of the outwashed sediment sequences using a small subset of these wells (the area of the cross sections is shown by the black rectangle in Figure 2-18).

Figures 2-19a and 2-19c show two different views of the three-dimensional, north-south cross section of the B&R to ESRP transition. At the beginning of the transition, many shallow water-bearing sands and gravels (shown in browns on Figures 2-19a and 2-19c) are interbedded with thick sequences of fine-grained sediments dominated by silts and clays (shown in grays). Static water levels (elongated red triangles) are initially shallow, but no wells penetrate to bedrock, so the existence of a deep basin-fill aquifer just north of the transition cannot be confirmed based on the data currently available.

Examining the strata at the ARCO TEST well (the first deep well on the right in Figures 2-19a and 2-19c), it is clear that a deep aquifer is present underneath the shallow water-bearing layers. These shallow sediments, both the channel deposits and the finer-grained ponded sediments, persist to the south far enough to be covered by the Holocene flows of the Craters of the Moon Lava Field. To the south, these sediments begin to pinch out and interbed with southward-thickening basalts.

Figures 2-19b and 2-19d show just the static water levels for the cross section. With the lithology omitted, the multi-layered nature of perched and deep aquifer layers is apparent. Our conceptual model for the path of the basin outflow is that the groundwater enters the transition zone traveling across multiple perched layers and works its way downward to the SRPA. Hydrostratigraphic evidence suggests that the deep water level measured in the ARCO TEST well represents the head in the SRPA. These data are not shown here due to space considerations but will be included in a future report dedicated to these aquifer transition zones.

The Site-1 well (02N26E22NESE), second to the left on Figures 2-19a and 2-19b, has a deep perched layer that appears to be potentially connected to the deep aquifer in the north half of the cross section. This is an artifact of the choice of wells picked for the cross section. Figure 2-19e shows a larger selection of static water levels in the environs of the Arco aquifer transition zone. By including the deep wells to the south and east of Arco, the southwesterly dip of the SRPA into the middle of the ESRP is apparent, as is the perched nature of the upper water level in the Site-1 well.

The groundwater transition between the Little Lost River tributary basin and the SRPA is similar in many ways to that of the Big Lost River, particularly with the pattern of interfingering basalts and fluvial sediments and also with the presence of multiple shallow and perched basin-fill aquifers feeding into the deeper SRPA across the width of the transition zone. The sink of the Little Lost River is in a subsiding basin. However, relative to the Lost River Range, Lemhi Range, and AVH, the amount of differential subsidence is small but sufficient to prevent the extensive ponding and lateral growth of the delta margin/lake margin sediments seen at Arco. While the intercalation, sediment types, and basalts are similar to those of Arco, the Little Lost River has not been entrapped and ponded by the rise of rift zones, so the transition between the basin fill aquifers and stratigraphy to that of the ESRP is less laterally extensive—no more than 4.8 km (3 mi) wide in a zone that stretches from the town of Howe to the northeast. The Howe transition does have one feature not seen at Arco, and that is the presence of the Lake Terreton and older pluvial sequences that approach and interfinger with transitional stratigraphy from the northeast.

The transition between the underflow in the Birch Creek drainage and the SRPA cannot be located with any certainty. Figures 2-20a and 2-20b show a three-dimensional cross section from Blue Dome in the northeast to TAN in the southwest. It is obvious from the figure that the bottoms of the Birch Creek Campground well (on the left) and the Boise State University (BSU) research well (in the middle of Figure 2-20b) are above the tops of the next nearest wells to the southeast at TAN. The distance between the BSU well and USGS-126A is approximately 9.5 km (6 mi), so the transition must occur in this interval. Compared to both the Big Lost and Little Lost transition areas, the Birch Creek transition is the simplest of the three, lacking both the entrapped and ponded sediment apron seen at Arco and the

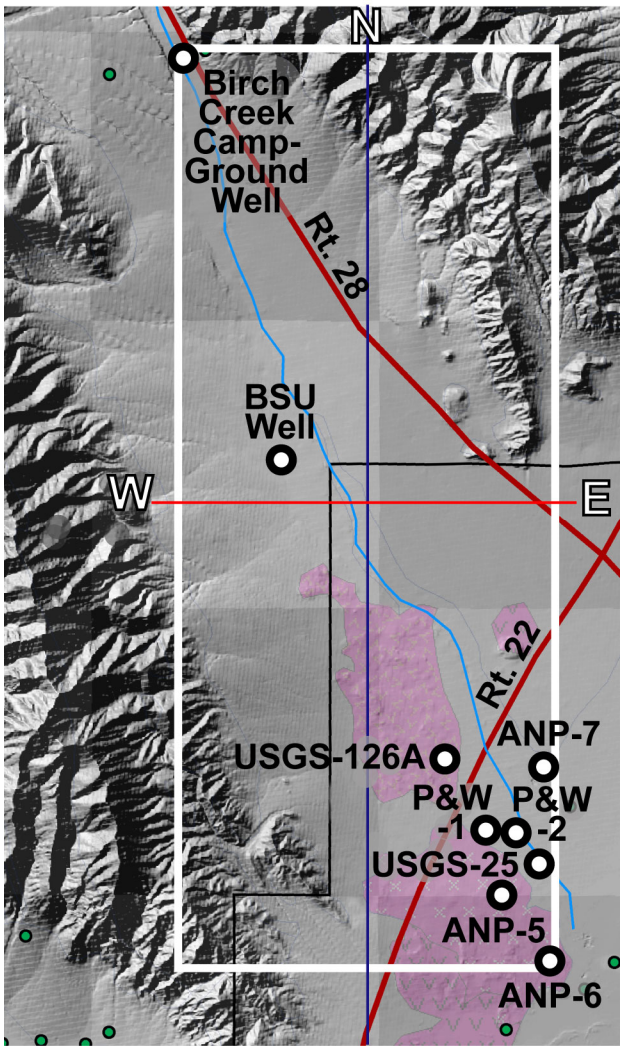

Figure 2-20a. Shaded relief map of Lower Birch Creek (light blue line) from the Bureau of Land Management Birch Creek Campground at Blue Dome to the northern portion of the INL Site just north of TAN. Major roads are in red. The black line is the north boundary of the INL Site. Green dots are water wells listed in the Idaho Department of Water Resources database. Large black-bordered white dots are water wells whose data were used to make the cross sections shown in Figure 2-20b. The pink areas are the exposed pahoehoe flows of the inactive Lava Ridge Rift Zone. The white box outlines the top of the cross section boxes shown in Figure 2-20b. The blue north-south and red east-west lines are the same as those shown in Figure 2-20b. The square areas of alternating grey shading are township-range blocks (each 6 mi to a side). The Birch Creek Campground well is in Block 9 North, 30 East. The BSU well is in Block 8 North, 30 East.

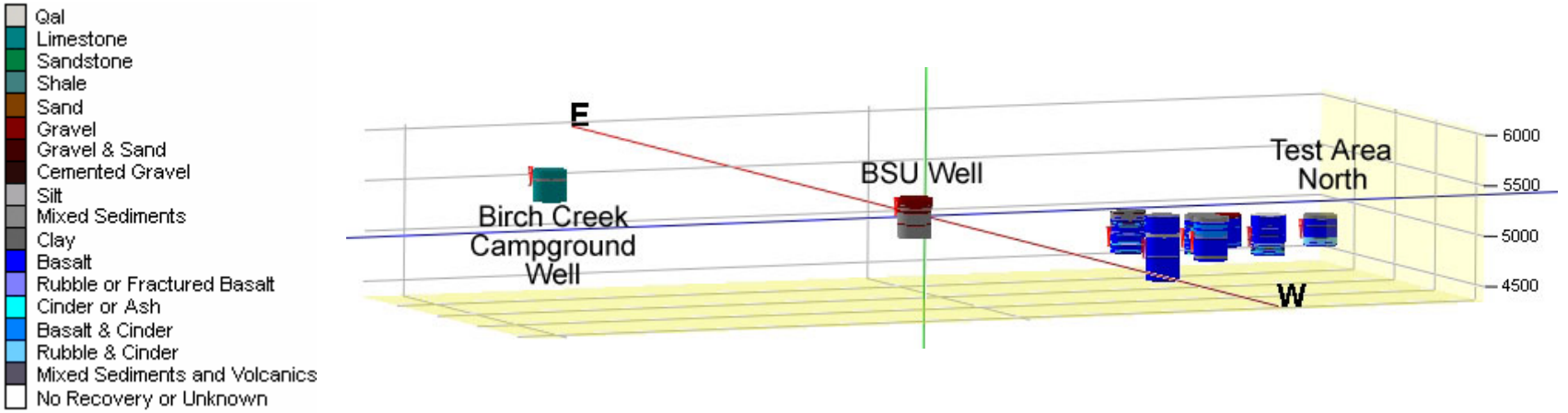

Figure 2-20b. Three-dimensional, 1-to-10 cross section of the Birch Creek transition zone viewed from the northwest. The area of the cross section box is the same as shown in Figure 2-20a. The lithography is the same as Figure 2-19. Static water levels are shown in red triangles. Elevations are in feet above mean sea level. The basalt dominated area in the south (right) half of the cross section is on the north and west side of TAN. The well to the north is at the U.S. Forest Service Birch Creek Campground at Blue Dome. The BSU research well in the center of the figure is at Township 8N, Range 30E, Section 15.

presence of interfingering pluvial beds at seen at Howe. Given the lack of any known complexity, we postulate that the Birch Creek transition will be similar in character to the other two transitions, with interfingering and with multiple shallow water layers eventually feeding into the SRPA through staggered perched zones; however, the width of the transition will be as short as or shorter than that seen at Howe.

2.2.3 Areal Recharge Derived from Direct Precipitation on the ESRP

The average precipitation over the OU 10-08 study area is approximately 20 cm (8 in.) per year. This precipitation occurs largely as winter snowfall, and most of this precipitation eventually returns to the atmosphere through evaporation and plant transpiration.

Most researchers concur that the distribution of recharge from direct precipitation is variable, depending on rock and soil type. Garabedian (1992) assumed that average annual recharge from infiltration of precipitation varied according to the amount of precipitation, the soil thickness, and the infiltration capacity of the soil cover. He distributed precipitation recharge throughout the ESRP by subdividing the area according to soil type and mean annual precipitation. Within the area encompassed by the OU 10-08 study area, Garabedian's estimated recharge for precipitation ranged from less than 1.27 cm (0.5 in.) to more than 5 cm (2 in.) per year. Larger recharge rates were associated with the Big Lost River floodplain in the vicinity of INTEC/RTC, the area of the Great Rift, and vicinity of East and Middle buttes near the southern corner of the INL Site. The State of Idaho Regional Water Resource Model utilized a similar distribution of recharge (Contor 2004). Both the Garabedian and the State of Idaho distributions of recharge from infiltration of precipitation are shown on Figure 2-21.

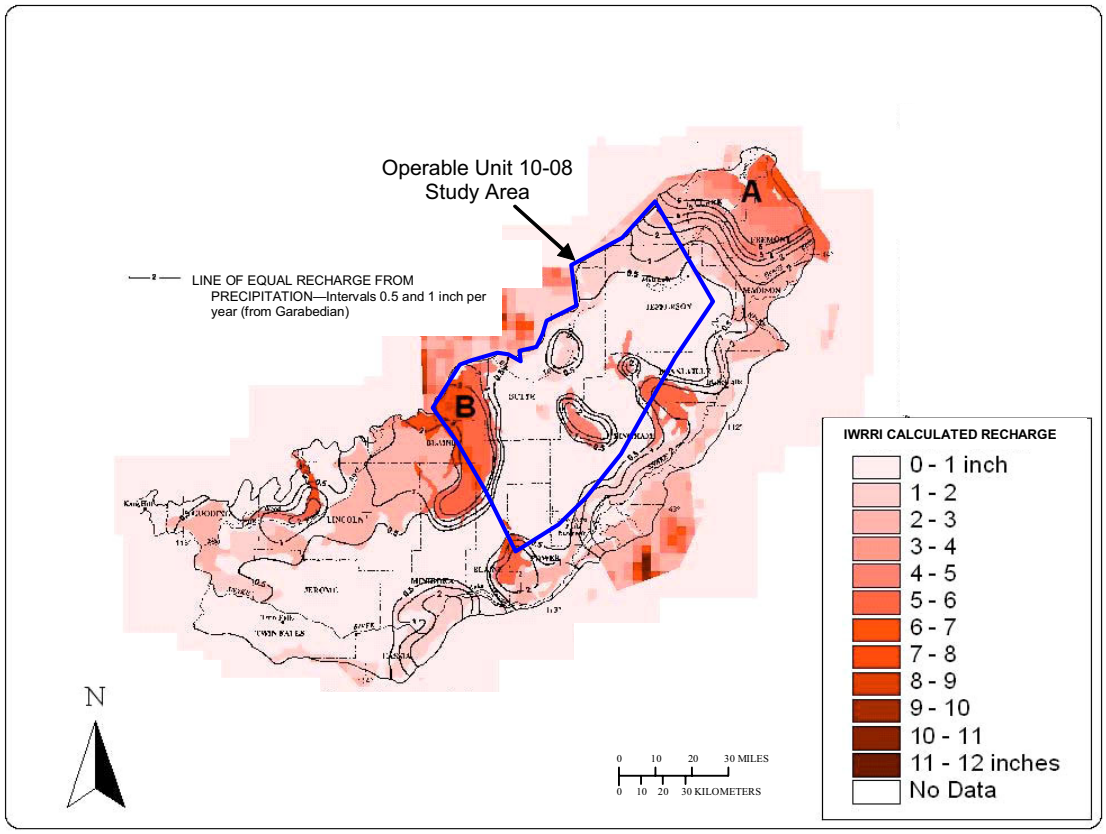

Figure 2-21. Estimates of recharge from infiltration of precipitation over the ESRP (Garabedian 1992; Contor 2004).

2.2.4 Regional Underflow out of the OU 10-08 Study Area

Regional underflow occurs across the southwestern boundary of the OU 10-08 study area. This underflow is part of the system of groundwater flow that eventually discharges to springs in the Thousand Springs area in the extreme southwestern part of the ESRP. No direct measurement of this underflow volume is possible. The estimate of underflow is derived from summation of the different inflows to the study area. Underflow out of the OU 10-08 study area ranges from 2,041 to 2,094 cfs (1,477,617 to 1,515,987 acre-ft/year), depending on the range of estimated recharge.

2.2.5 Other Sources of Inflow and Outflow

Within the OU 10-08 study area, other sources of inflow not considered in the overall water budget include recharge of applied irrigation water, possible flow upward from beneath the SRPA, and disposal of wastewater to INL Site facilities. Applied irrigation inflows occur in the Mud Lake area and contribute to the complexities of groundwater flow there. Evaluation of inflow from low-permeability rocks beneath the aquifer is not well defined and might not be essential to two-dimensional characterization of groundwater flow. The volume of wastewater disposal to INL Site facilities is minor in the context of the OU 10-08 study area.

Minor sources of outflow result from withdrawals from irrigation pumpage and from INL Site production well pumpage. Again, these sources are partially balanced by surface application of irrigation water and wastewater and are not considered in the overall water budget.

2.3 Groundwater Flow within the OU 10-08 Study Area

The following subsections discuss information pertinent to ascertaining flow directions and velocities in the SRPA within the OU 10-08 study area. This information is derived primarily from water-level data. Additionally, significant inferences about flow directions and velocity can be gained from geochemical data, including anthropogenic contaminant data and natural isotope tracer data. Lastly, temperature data, which are arguably the best data to infer flow velocities both in two- and three-dimensional interpretations, will be addressed.

2.3.1 OU 10-08 Study Area Water-level Data

Water-level data were used in the two-dimensional analysis of groundwater flow directions and velocities in the OU 10-08 study area. Water-level hydrographs showing historic trends in selected wells and water table maps from historic and recent water-level data that present the configuration of the water table at a given time were utilized in the analysis.

2.3.1.1 Long-term Water-level Trends. Historical water-level data have been collected from SRPA wells within the OU 10-08 study area for more than 50 years. More than 400 wells completed within the SRPA are routinely monitored for water levels. Most are measured by the USGS; approximately 200 are measured annually by Idaho Cleanup Project personnel.

Hydrographs were constructed for four selected wells (USGS-25, Site-14, Arbor Test, and USGS-9) to evaluate long-term trends in the configuration of the water table in the OU 10-08 study area (Figure 2-22). Water-level changes within these wells are typical of those for most of the other wells within the OU 10-08 study area. Water-level trends in all of these wells indicated a long-term decline in the elevation of the regional water table. This decline has been observed in all SRPA wells measured as part of the most recent INL sitewide water-level measurements. The decline in water levels during the past 50 years has averaged approximately 4.5 cm/year (0.15 ft/year), for a cumulative decline of approximately 2 m (7 ft). This long-term decline is attributed to increasing water consumption and reduction of recharge because of changes from flood irrigation to more efficient irrigation methods.

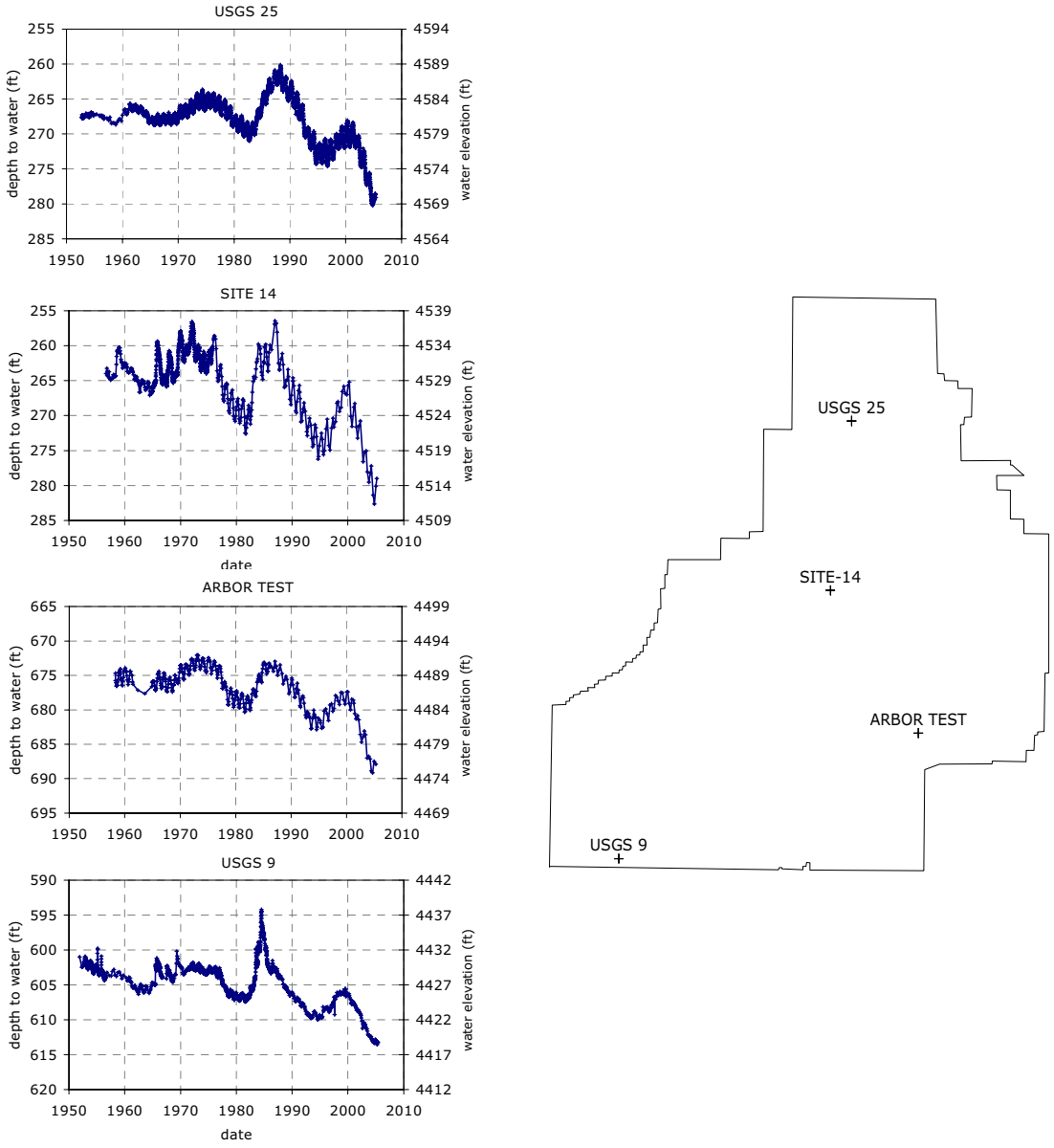

Figure 2-22. Water-level changes measured in wells USGS-25, Site-14, Arbor Test, and USGS-9 (1960 to present).

These hydrographs demonstrate intermediate-term declines and increases that correspond to drought/flood climatologic cycles (Figure 2-22). These cycles occur over an approximate interval of 10 years. Water-level fluctuations during these intervals can exceed 3 m (10 ft) or more in each direction. During the recent drought cycle, water levels within the OU 10-08 study area have declined at an average rate of about 0.6 m/year (2 ft/year).

These hydrographs also demonstrate seasonal fluctuations that are attributed to snowmelt recharge and irrigation pumping. Other observed fluctuations include those related to diurnal and synoptic barometric pressure changes and to pumping withdrawals from nearby INL Site production wells.

Hydrograph analyses were conducted to determine the recent stability of regional water-level changes. Water levels measured during a period of relatively small changes in the water table can be used to calibrate a steady-state numerical analysis. Conversely, water levels measured during a period of large water table fluctuation will not provide an accurate measure of the capability of a numerical tool to represent groundwater flow. The 1980 water table was relatively stable and provided water-level measurements that made calibration of the USGS regional groundwater flow model possible (Garabedian 1992). Most hydrographs show that water levels rose and peaked in about 1973 before declining for several years. Water levels generally remained stable for several years before and after 1980. Likewise, water levels rose again during the mid-1990s, peaking in 2000, and subsequently declining.

Based on these trends, the water table appears to be at the beginning of another relatively stable condition relative to long- and intermediate-term trends. Figure 2-23 shows detailed water-level changes in the Arbor Test well from 1960 to the present and demonstrates these periods of relatively stable water levels that occur at the bottom of intermediate drought cycles.

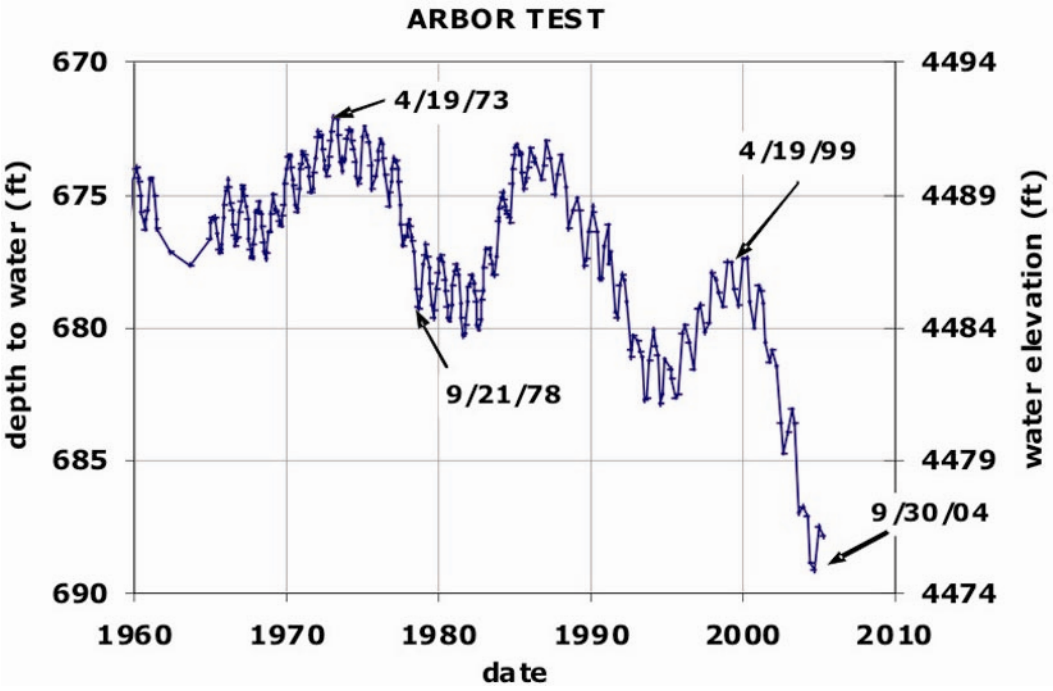

Figure 2-23. Water-level changes in the Arbor Test well (1960 to present).

2.3.1.2 Configuration of the Water Table. Mapping of the surface of the aquifer, or water table, provides an indication of the groundwater velocity or areas of contrasting permeabilities. Observed fluctuations in hydrographs, like those in Figure 2-22, have led researchers to prepare water table maps for different periods. Typically, such maps are prepared after mass water-level measurement campaigns, such those in June 2004 and 2005. The following paragraphs document preparation of the June 2004 water table for the OU 10-08 study area.

Historical Water Table Maps—Water table maps were prepared for 1980 and 1999, two periods of mass water-level measurements conducted by the USGS. The resulting USGS maps are at a regional aquifer scale and provide insufficient detail at the facility scale for the INL Site to support modeling and monitoring in these areas. As a result, the June 2004 water table map was prepared on a subregional scale

with sufficient detail to incorporate both facility-scale behavior and the broader regional picture of groundwater movement.

Initial Version of the June 2004 Water Table Map—The June 2004 sitewide water-level measurements included 254 wells within the OU 10-08 study area (Figure 2-24). The data gathered from this campaign are stored electronically in the Environmental Data Warehouse database. These measurements are primarily from on-site wells or wells immediately south of the INL Site's southern boundary. Additional water-level data from wells distributed in the model domain but outside of INL Site boundaries were obtained from the National Water Information System (NWIS), a USGS Web-based database of well information and water levels.

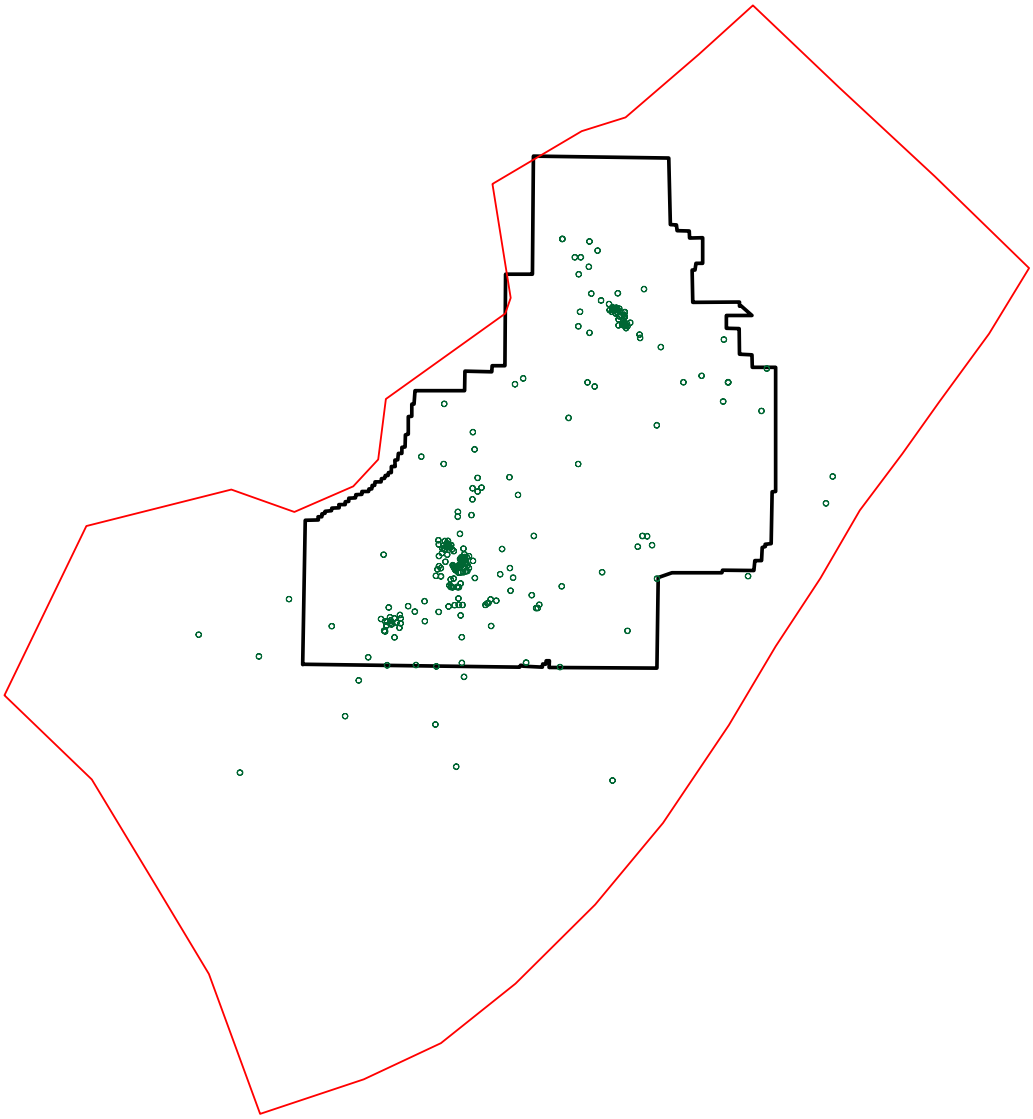

Figure 2-24. Location of wells used for the INL sitewide water-level measurement campaign (June 13 through 16, 2005).

The June 2004 measurement resulted in useable aquifer water-level measurements from 209 wells. Limitations in the spatial extent of this set required an additional collection activity in October 2004. Supplemental data were also gleaned from the NWIS database for well locations on the fringes of the OU 10-08 study area.

The initial version of the June 2004 water table map was based on water-level measurements from 282 wells (Figure 2-25). This water surface adequately supported the selection of model boundary locations and types based on the extent of the OU 10-08 study area. This version did not use the water-level measurement from well Site-2 (USGS site ID 431946113161401), because that water level appeared to be anomalously low. Deletion of that water level resulted in a linear alignment of water-level contours in the southwestern part of the study area. However, the map did not compare well with those prepared by other agencies after the 1980 and 1999 measurement campaigns, particularly in the southwest portion of the OU 10-08 study area.

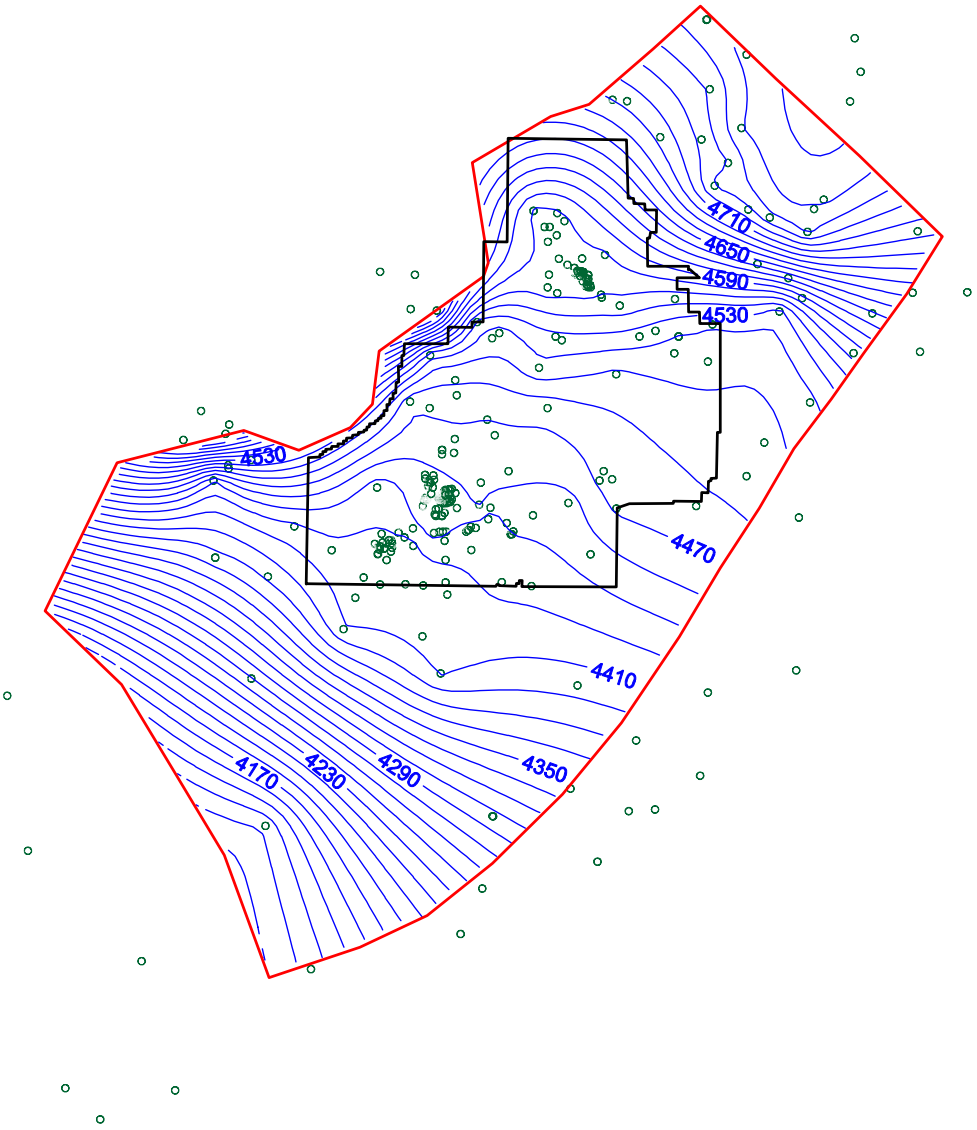

Figure 2-25. Initial cut on the June 2004 OU 10-08 water table map (elevation is feet above mean sea level, NGVD29; 15-ft contour intervals; green dots are locations of wells used in mapping).

Second Version of the June 2004 Water Table Map—A second map was constructed and included the water-level measurement from the Site-2 well (Figure 2-26). The inclusion of this point in the June 2004 map modified contours to be more consistent with 1980 and 1999 water table maps and the State of Idaho regional model simulation. Other available data, including land surface data, well locations, and water levels from prior periods, were examined in detail for the southwest portion of the study area to determine whether the single point causing the changes in contour shapes was an anomaly. The data point was found to be a valid one.

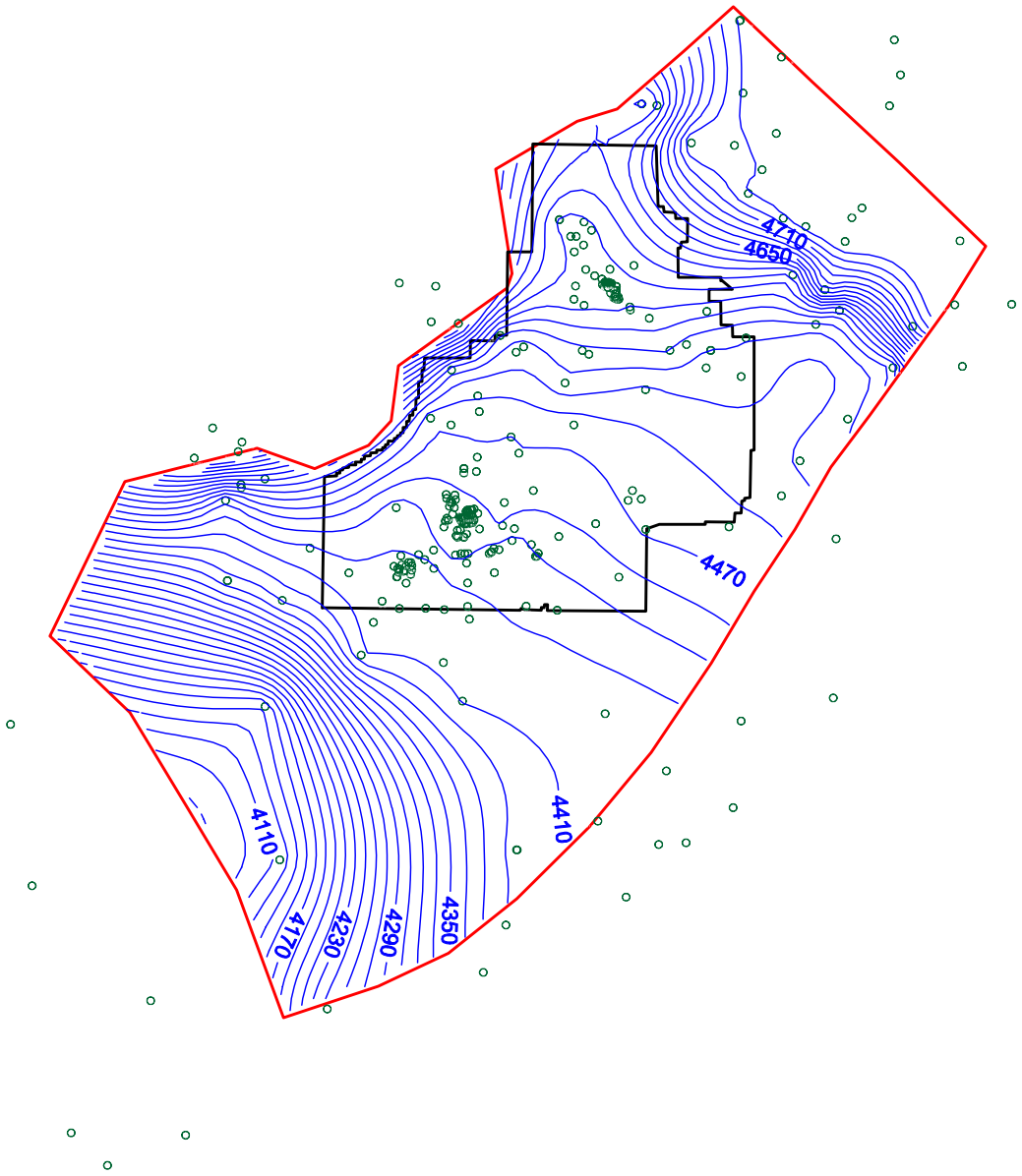

Figure 2-26. Second cut of the June 2004 OU 10-08 water-table map (elevation is feet above mean sea level, NGVD29; 15-ft contour intervals; green dots are locations of wells used in mapping).

A series of time- and space-interpolated water-level contour maps was prepared from historical water-level data. The map series was reviewed in an animated movie format to demonstrate the effects of this southwest area and the effects of short- and long-term hydrograph fluctuations on the direction and

magnitude of groundwater flow. Streamlines were superimposed on these animations, as shown in Figure 2-27; the streamlines are tangential to flow directions and perpendicular at all times to contour lines of equal hydraulic head. From the animation, these streamlines were shown to exhibit a certain pattern of converging in the southwest portion of the study area and to move across the southeast boundary, which had been selected initially as a no-flow boundary corresponding to a flow path.

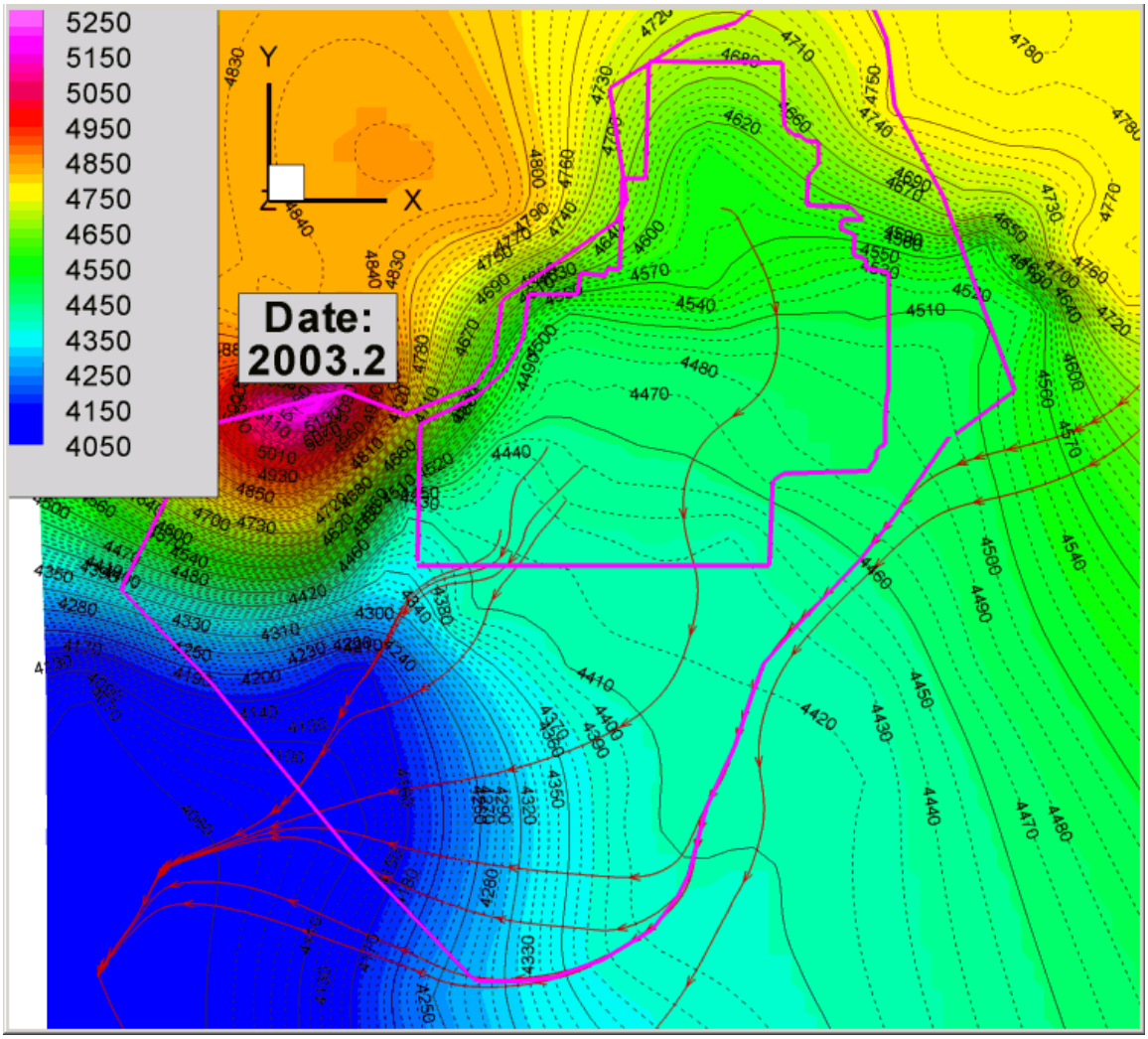

Figure 2-27. Water table map constructed from 2003 INL Site water-level data, with selected streamlines, including those emanating from major INL Site facilities. Contours are in units of feet above mean sea level.

Final Version of the June 2004 Water Table Map—From the animated water table movie, it was determined that the final model domain would likely not correspond exactly to the initial OU 10-08 study area. Further, extensive examination of all available well construction details and water table elevations in areas of the study domain near the Big Lost and Little Lost river valleys proved a layering effect occurring above the true regional aquifer in areas where significant underflow occurs at a lesser depth than the regional aquifer.

This effect is observed in six piezometer clusters in the Mud Lake vicinity near the northeast portion of the OU 10-08 study area. Initial model calibration showed the most difficulty matching heads

was in this area. As a result, only the few wells from the Mud Lake area thought to be completed at depths representative of the regional aquifer were included in the final June 2004 water table contour map shown as Figure 2-28.

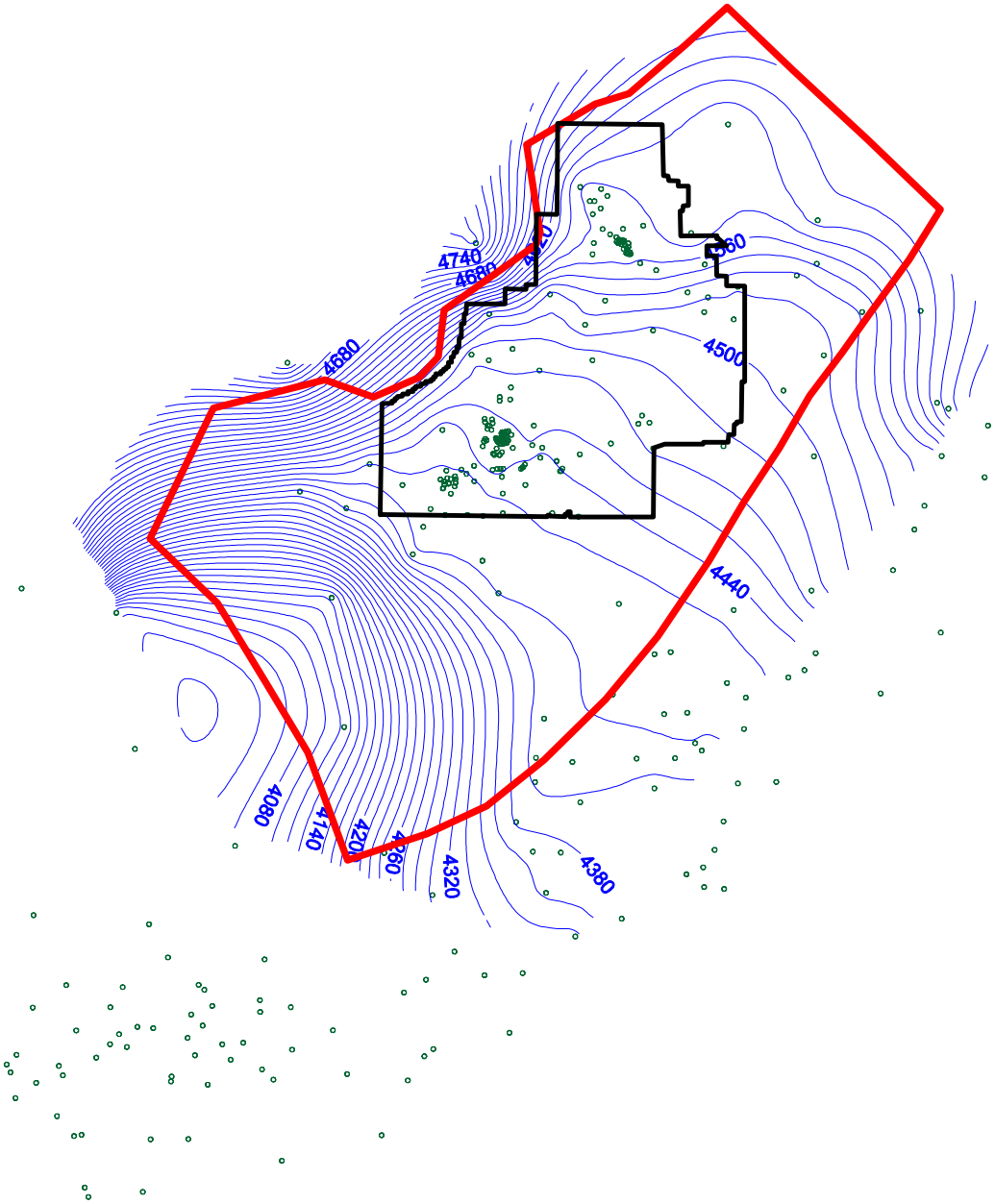

Figure 2-28. Final version of the June 2004 OU 10-08 water table map (elevation is feet above mean sea level, NGVD29; 15-ft contour intervals; green dots are locations of wells used in mapping).

The final map shown in Figure 2-28 supports the current interpretation of groundwater movement in the subregional area surrounding the INL Site. Streamlines show movement occurs generally in a southwest direction; groundwater enters the system from northeast of the OU 10-08 study area, with some appearing to enter directly from the east in the Henry's Fork region of the Snake River. Water leaves the

study area in the southwest accompanied by an increasingly steep gradient. The precipitous dropoff of nearly 61 m (200 ft) of water table elevation in the southwest causes streamlines to converge in this area.

The inclusion of NWIS data to supplement the INL-collected data provides real points to control the shape of computer-generated contour lines at the distal portions of the study area. This has led to re-thinking the model domain. Using the high-density INL-collected water levels around the facilities provides greater control of streamline direction, with results more consistent with concepts of groundwater flow arising from the interpretation of sampled contaminant concentrations in the aquifer.

June 2005 OU 10-08 Water Level Measurements—Water levels in nearly 300 wells were measured over a three-day period in June 2005 (see Figure 2-24). This represents an improvement in the sitewide collection process over June 2004. However, the June 2005 water table contour map is still under development. During the fiscal year 2005 effort, the June 2004 map was studied extensively, and minor changes were made to reflect better data and a better understanding of the groundwater flow field at or near the INL Site. A water table map not only provides a picture of groundwater movement but also provides input in the selection of the model domain, boundary types, and boundary locations.

2.3.2 Geochemistry

Geochemical data are being used to evaluate the rate and direction of groundwater flow to eventually constrain the groundwater transport model results and for comparison to simulated flow paths for the two-dimensional model described in Section 3. These geochemical data include water chemistry analyses for anthropogenic and naturally occurring constituents that serve as chemical tracers in groundwater.

2.3.2.1 Anthropogenic Tracers. Federal and state agencies, universities, and private contractors have monitored the INL Site extensively since 1949 to evaluate the distribution and transport of contaminants in groundwater. In 2003, contaminated groundwater at the INL Site has been detected at the RWMC, RTC, INTEC, TAN, and Central Facilities Area (CFA) (Figure 2-29). At TAN, trichloroethene was the primary constituent exceeding its maximum contaminant level (MCL), but cis-1,2-dichloroethene (-DCE), trans-1,2-DCE, and tetrachloroethene also exceeded their respective MCLs. Sr-90, Tc-99, and gross alpha exceeded their respective MCLs at and near INTEC. Chromium exceeded its MCL in water in two wells south of the RTC. Nitrate exceeded its MCL in two wells south of CFA. Carbon tetrachloride exceeded its MCL in groundwater beneath the RWMC.

In addition to contaminants above the MCL, several other anthropogenic contaminants form the following plumes:

- At INTEC: tritium, I-129, Tc-99, Sr-90, chloride, nitrate, and sodium
- At CFA: nitrate, chloride, tritium, and sodium
- At RTC: chromium, tritium, and sulfate
- At RWMC: carbon tetrachloride, tritium, anions (chloride and sulfate), and trichloroethene
- At TAN: trichloroethene, tetrachloroethene, DCE, Sr-90, and tritium.

Selected plumes in the RTC/INTEC/CFA/RWMC area are shown on Figure 2-30 to illustrate groundwater flow paths, the potential for commingling plumes, and the possibility of upgradient influence on the RWMC. The contaminant distributions in the SRPA generally agree with groundwater flow paths indicated by the water-level contours. However, the upgradient influences on the RWMC from the RTC and INTEC are uncertain. If there is a contribution, it is within the scope of OU 10-08 to account for the effects of commingling plumes as defined in the OU 10-08 RI/FS.

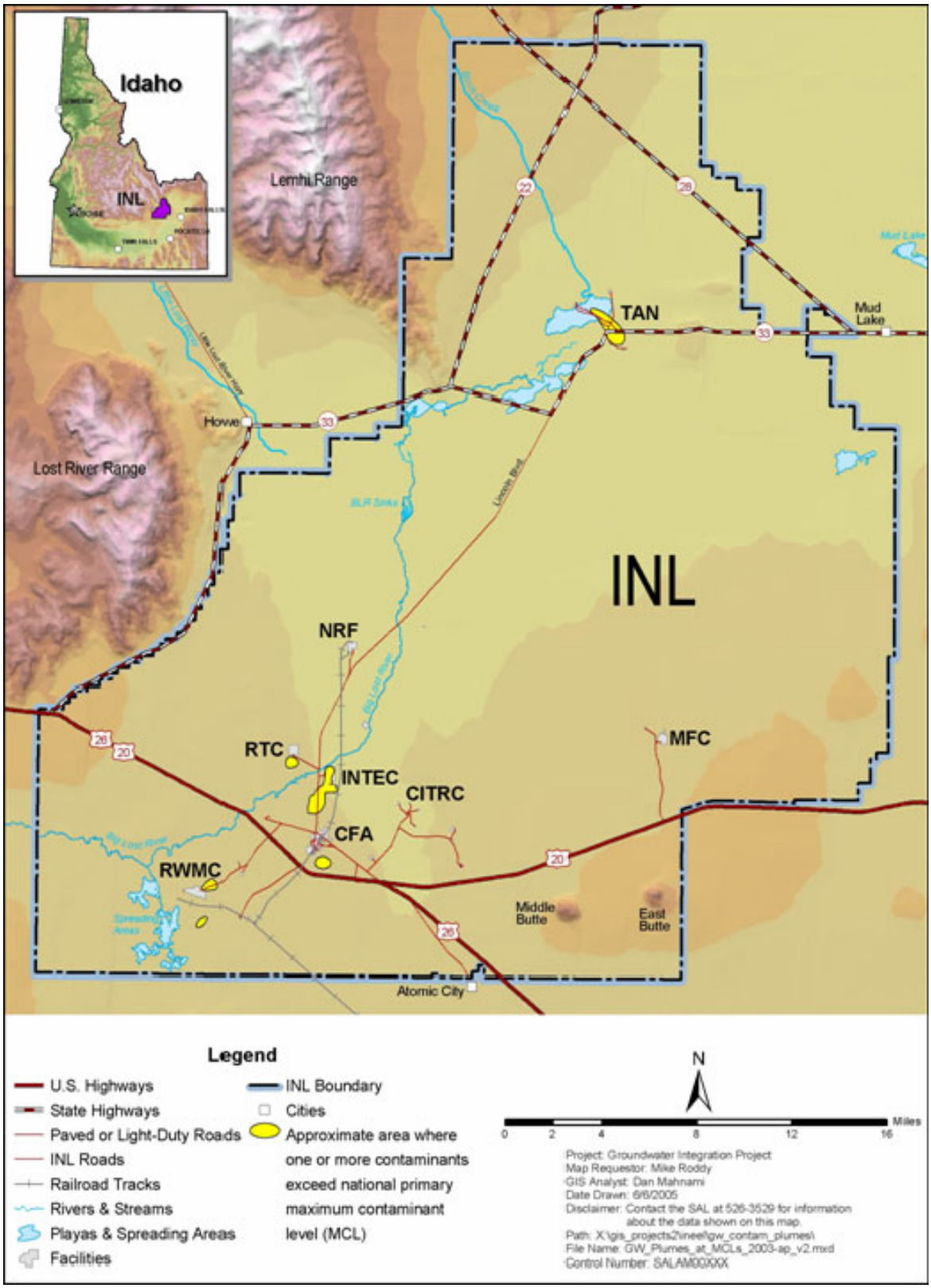

Figure 2-29. Contaminant plumes with concentrations exceeding maximum contaminant levels in 2003.

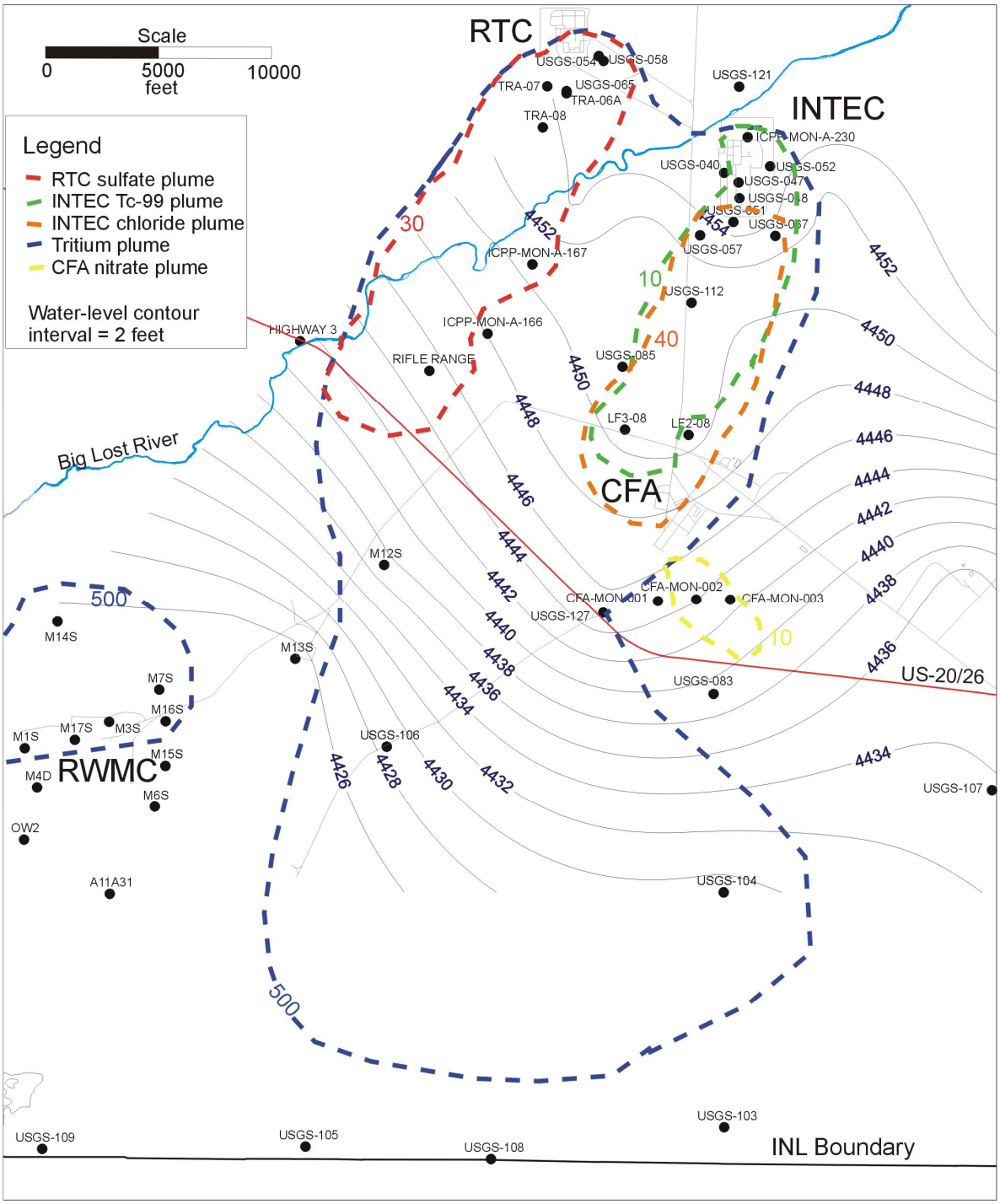

Figure 2-30. Selected contaminant plumes in the RTC/INTEC/CFA/RWMC area.

USGS Studies of Contaminant Migration and Groundwater Flow Velocities—The USGS has conducted several contaminant-transport studies that have a bearing on OU 10-08 monitoring and groundwater modeling. The primary tracers used for the USGS groundwater flow and contaminant migration studies were Cl-36 and I-129; Tc-99 was used to a lesser extent. These tracers—I-129, Cl-36, and Tc-99—are present in the SRPA as a result of past operations at the INL Site and are opportunistic groundwater flow tracers. They were not injected as part of a tracer study. Samples collected for the I-129

and Cl-36 studies were analyzed using the low-detection limit accelerator mass spectrometry method; samples collected for Tc-99 studies were analyzed using the thermal ionization mass spectrometry method. The results are described below. I-129 and Cl-36 are excellent tracers for groundwater flow and contaminant migration paths. Cl-36 is an excellent tracer, because it is a conservative anion, and I-129 is an excellent tracer in anion form. In addition, I-129 and Cl-36 can be tracked over great distances.

A Cl-36 plume extending from the RTC and INTEC to the southern INL Site boundary is described in two studies (Beasley et al. 1993; Cecil et al. 2000). A comparison of tritium and Cl-36 data indicated that the Cl-36 plume extended beyond the area of the tritium plume defined by the 500-pCi/L concentration for tritium. Cl-36 was also detected in a well at the RWMC (Beasley et al. 1993). Based on the first detection of Cl-36, contaminant/groundwater flow velocities of approximately 1 m/day (3 ft/day) were estimated for two wells south of the INL Site boundary (Cecil et al. 2000).

Sampling done in 1991 and 1992 identified an I-129 plume extending from INTEC to south of the INL Site boundary (Mann and Beasley 1994). It should be noted that the I-129 concentrations south of the INL Site boundary are low (at least two orders of magnitude below the MCL of 1 pCi/L). Groundwater flow velocity from INTEC past the southern boundary of the INL Site was estimated at 1.8 m/day (6 ft/day) based on movement of I-129 (Mann and Beasley 1994). I-129 was also detected at low concentrations in USGS-90, which is located near the RWMC (Mann and Beasley 1994). The occurrence of a low I-129 concentration near the RWMC suggests that a groundwater flow path from INTEC exists and that INTEC/RWMC plumes could be commingling. The interpretation of flow paths is complicated, because I-129 is also present in the wastes emplaced in the RWMC. Sampling of Magic Valley wells and springs south of the INL Site from 1992 to 1994 indicated background I-129 concentrations (Cecil et al. 2003). Although a Cl-36 plume originates from both the RTC and INTEC, I-129 appears to originate from INTEC but not from the RTC (Mann and Beasley 1994). In addition to samples collected during the Mann and Beasley study, I-129 samples were collected south of INTEC in 1977, 1981, 1986, and 1990.

Sampling and analysis for Tc-99 using the low-detection limit thermal ionization mass spectrometry method indicated a plume from INTEC extending past the southern boundary of the INL Site (Beasley et al. 1998). Tc-99 was detected in the RWMC production well, which is consistent with the low-detection limit I-129 data. This suggests that a groundwater flow path extends from INTEC to the RWMC and that commingling of INTEC and RWMC contaminant plumes is possible. The interpretation of flow paths is complicated, because Tc-99 is also present in the wastes emplaced in the RWMC.

In addition to the radiological analytes discussed above, the USGS has mapped concentrations of chlorofluorocarbons (CFCs) in the SRPA (Busenberg et al. 2001). The CFC analyses were done to estimate the age of groundwater beneath the INL Site, but they indicated the presence of several CFC anomalies that could potentially be used as groundwater flow tracers. The CFC study indicated a plume of dichlorodifluoromethane (F-12) originating from INTEC and a 1,1,2-trichloro-1,2,2-trifluoroethane (F-113) plume originating at the RWMC. However, the CFC concentrations were very low and required special detection methods (Busenberg et al. 2001).

OU 10-08 Geochemical Study—A geochemical study in progress will attempt to resolve the source of the tritium in the aquifer at the RWMC, identify flow paths of contaminants from INTEC and the RTC, determine the source of the anion anomaly south of the RWMC, and identify flow paths and evaluate contaminant influence south of the southern INL Site boundary (Figure 2-31). Identification of groundwater flow paths is essential for development and calibration of the SWGM. In addition, data from the geochemical study will be used to evaluate the potential for commingled plumes, which might elevate the cumulative risk above levels calculated for each plume individually.

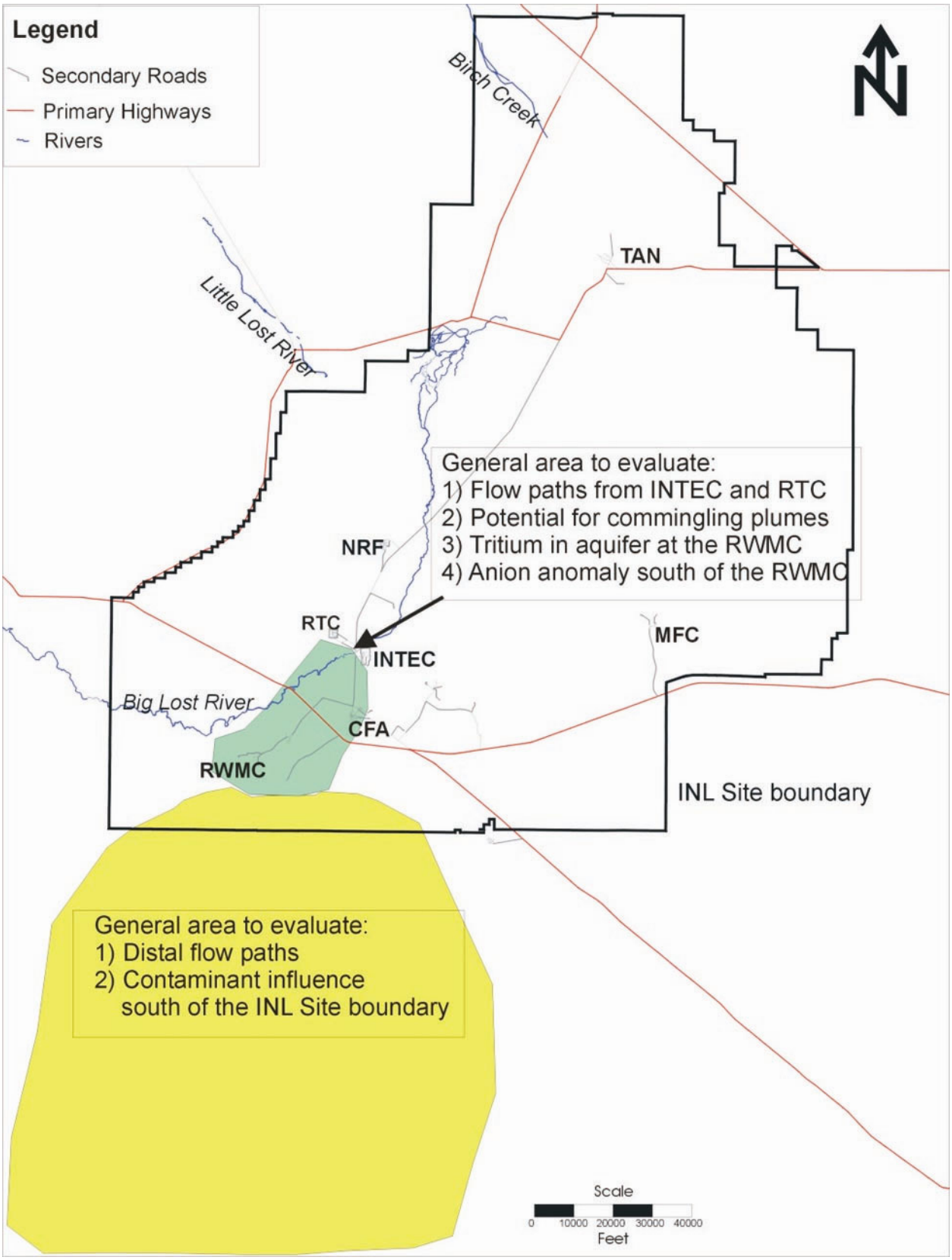

Figure 2-31. Geochemical study areas.

2.3.2.2 Preferential Flow. Since the earliest studies of the SRPA, researchers have recognized that aquifer temperature and the chemical signature of groundwater are useful tools in characterizing the aquifer flow system (Olmsted 1965). As the number of studies and available data have increased, more insight into the nature of the aquifer system has been gained. Specifically, beginning in 1997, a series of investigations has been conducted to characterize groundwater flow in the context of the regional geologic framework that hosts the aquifer. These studies investigated aquifer temperature distribution, natural groundwater isotopes, and chemistry as indicators of preferential flow paths. Aquifer isotope signature, major element geochemistry, and temperature distribution have revealed the presence of zones in the aquifer that have been interpreted as preferential flow corridors that are surrounded by zones of slower flow. Because of the INL Site's proximity to the northwestern boundary of the ESRP, a number of sources and types of water contribute recharge to the system. These sources include infiltrated irrigation water, the Big Lost River Valley, the Little Lost River Valley, the Birch Creek Valley, the Mud Lake basin, and, the largest contributor, the Yellowstone Plateau. Another source of water is upwelling of thermal water emanating from deep within the ESRP (McLing et al. 2002; Mann 1986). Because of the distinct chemical and thermal signature of these recharge waters, they can be used as natural tracers to elucidate regional groundwater flow and, therefore, as calibration targets for flow and transport models.

Isotope Delineated Flow Paths—Isotope and chemical tracer studies have addressed the primary concern that, within the aquifer, long-range (tens to hundreds of kilometers) "fast paths" exist that could transport contamination downgradient faster than expected. Isotopes of heavy elements such as those in the uranium and thorium series are powerful tools that can be used to elucidate physico-chemical, geologic, and hydrologic variables of groundwater systems. Because of their high atomic mass, these elements do not fractionate in aquifer systems. These isotopes are very useful, because, in rocks older than a few hundred ka, the ratios of U-234/U-238 are generally close to the secular equilibrium value of 5.49×10^{-6}. In recently recharged groundwater, however, U-234 is typically enriched relative to U-238 by factors most commonly ranging from 1.5 to 10 because of preferential dissolution of U-234 from crystallographic defects created by alpha recoil and because of direct ejection of U-234 into groundwater by recoil (Osmand and Cowart 1992). Variations in U-234/U-238 in short-residence waters (ten to a few hundred years), such as those in the SRPA, reflect the competing effects of aquifer residence time and host rock dissolution. The longer a recharged water with an elevated U-234/U-238 ratio is in contact with the aquifer host rock, the closer to equilibrium it will be.

Strontium isotope (Sr-87/Sr-86) ratios in groundwater reflect the water-rock reaction histories and flow pathways of the water. Groundwater Sr-87/Sr-86 ratios are inherited from soil or rock through which the water passes. Both Sr-87 and Sr-86 are stable isotopes, but because Sr-87 is produced by radioactive decay of Rb-87 ($t1/2 = 4.8 \times 10^{10}$ yr), the Sr-87/Sr-86 ratios of rocks and soil depend on their original rubidium concentrations and their ages. For this reason, strontium isotopes are useful as groundwater tracers in a system like the ESRP, because the rock types in the recharge regions are different than the aquifer host rock. Like U-234/U-238, the strontium isotope ratio inherited from the recharge region will evolve toward isotopic equilibrium with the aquifer host rock. The rate at which this equilibration will occur is largely a function of the amount of time that the groundwater is in contact with the aquifer host rock.

Contour plots of uranium and strontium isotope ratios (Figure 2-32) show that water entering the aquifer from the river valleys to the northwest has high ratios of Sr-87/Sr-86 (> 0.71100) and U-234/U-238 and elevated concentrations of thorium. In some areas, the high isotope ratios of this water persist 19 to 30.5 km (12 to 19 mi) downgradient in the aquifer along zones of preferential flow. In contrast, two zones have relatively low Sr-87/Sr-86, U-234/U-238, and Th-234/Th-238 ratios in the central part of the INL Site, one near the southern extent of the Lemhi Range and one near the western boundary of the site near the southern end of the Lost River Range (Figure 2-32).

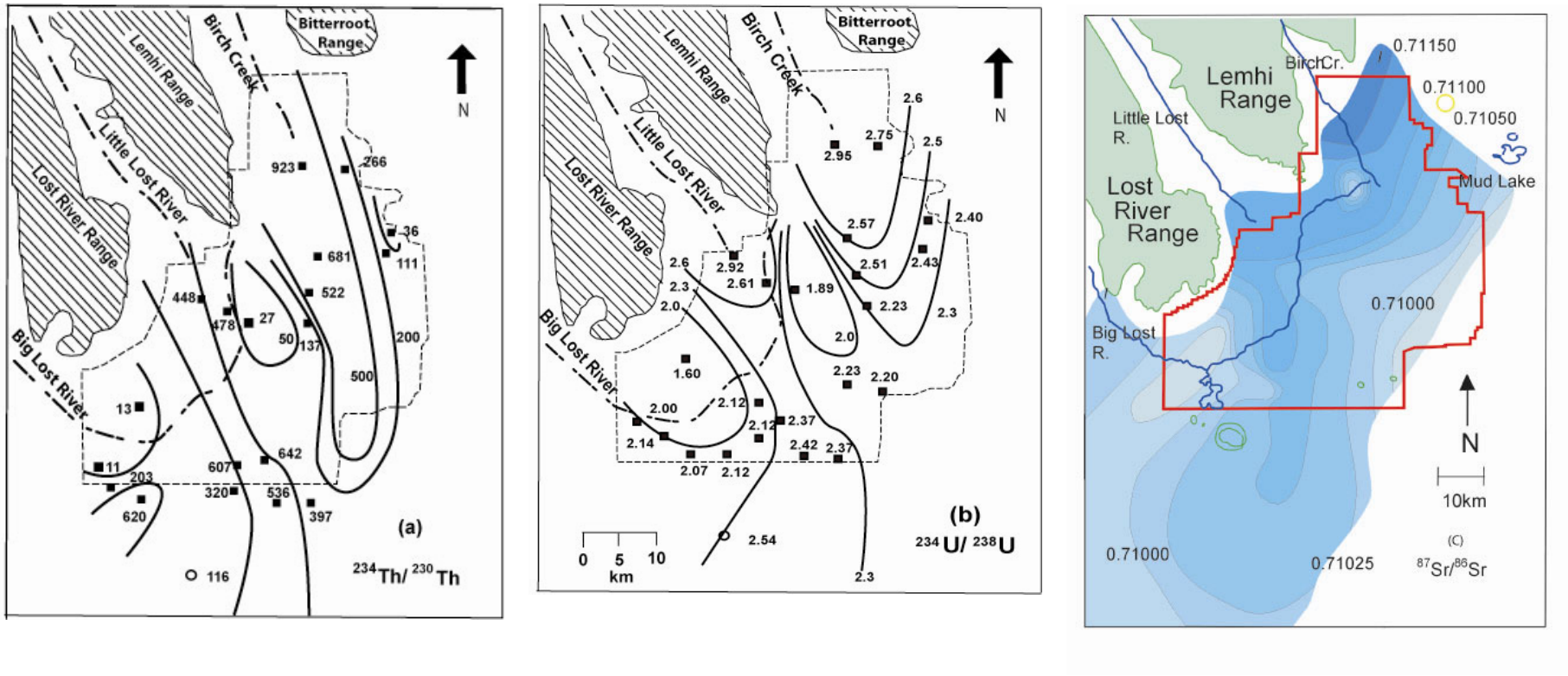

Figure 2-32. Distributions of (a) 234Th/230Th, (b) 234U/238U, and (c) 87Sr/86Sr activity rations in INL Site groundwater, all showing southward decreases along two preferential flow paths with minimum values occurring just south of the Lost River and Lemhi ranges. The general similarities among the three plots reflect a linkage between the age of water and areas of preferential flow and stagnant flow. The plot shows that the observed isotopic compositions cannot be explained by mixing of the water masses (after Luo et al. 2000).

Preferential flow of groundwater through the high-ratio zones and relatively long residence time or slow flow through the low-ratio zones can account for the observed isotope-ratio pattern. In this scenario, the high-ratio zones are fast-flow zones, where high-ratio isotopes originating in the recharge zones north of the INL Site persist far into the regional aquifer system, because the groundwater in these preferential flow corridors is moving fast and has had less time to react with the aquifer host rock. In contrast, groundwater in the low-isotope ratio zones evolves closer to the isotopic composition of the host rock—Sr-87/Sr-86 = 0.7070 ± 0.0003 (Leeman and Manton 1971; Morse and McCurry 1997) and U-234/U-238 ~5.49×10^{-5} (Roback et al. 2001)—due to slower groundwater flow, longer residence times, and subsequent dissolution of the basalt host rock. Geochemical modeling and temperature profiles supporting this conclusion suggest that groundwater located at the toes of the Lost River and Lemhi ranges is moving slower relative to flow through the rest of the aquifer (Luo et al. 2000), with calculated residence times for water in these "stagnant" zones being two to 10 times longer than in the high-isotope ratio zones (Figure 2-32).

Hydraulic Head versus Chemically Defined Flow Paths—Since the SRPA was first characterized in the mid-1900s, little has changed with respect to the generally accepted northeast-to-southwest flow direction in the SRPA. However, as more wells have been drilled and more studies have been conducted, especially at the INL Site, it has become apparent that the regional potentiometric surface may not have enough resolution in areas with sparsely populated wells to reveal the preferential flow pathways identified by recent geochemical studies. These preferential flow paths indicate that there is a strong geologically based hydraulic anisotropy in the aquifer. Isotope-delineated flow pathways are generally oriented in a northwest-to-southeast direction, which is consistent with the orientation of primary volcanic features on the ESRP (Rodgers et al. 1990). In addition, it is consistent with the Welhan and Reed (1997) predictions of preferred northwest-to-southeast hydraulic conductivity. However, because of the assumptions made in the definition of the preferential flow corridors (i.e., water samples are representative of the entire thickness of the aquifer, and well density is sufficient to define flow corridors), it is not possible to make definitive statements about the cause or exact boundaries of the preferential flow corridors.

Groundwater temperatures and borehole temperature profiles provide another useful tool for ascertaining the geometry of the SRPA and generally support the conclusions of the isotope-preferred flow path studies (Roback et al. 2001; Johnson et al. 2000; Luo et al. 2000). For example, groundwater temperature at the top of the SRPA beneath the INL Site ranges from less than 8°C to more than 18°C (Figure 2-33). The coldest of this water correlates with the preferential flow corridors identified by Roback et al. (2001) and is associated with areas where cold recharge moves rapidly through the system. In contrast, regions with warmer water temperatures generally correlate with the slower flow regions identified by the previous studies (Lou et al. 2000; Roback et al. 2001). This supports the conclusion that areas where water temperature is higher groundwater flow is slow enough that the thermal gradient of the ESRP overwhelms flow velocity.

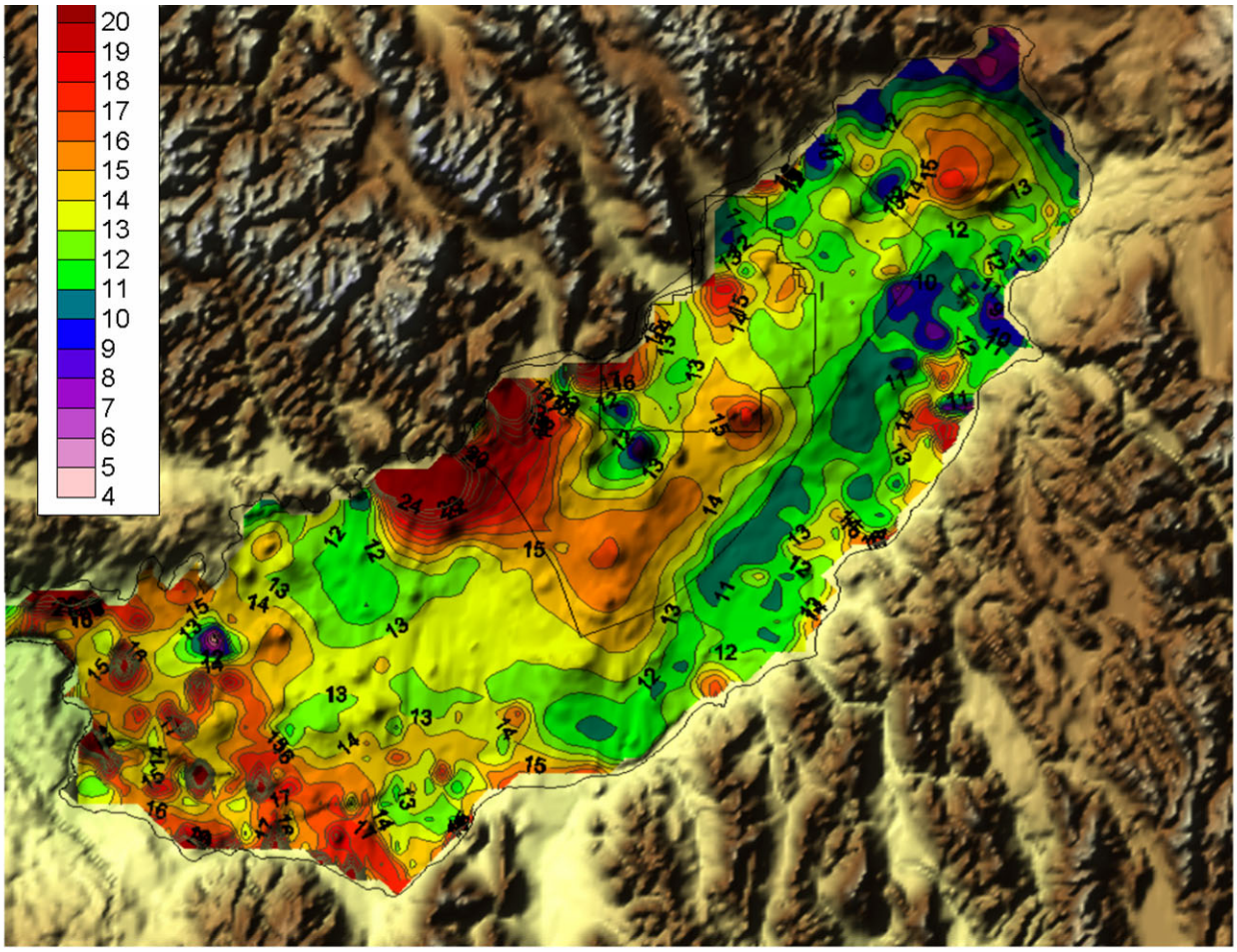

Figure 2-33. Groundwater temperature (°C) in the eastern SRPA, based on groundwater temperature data obtained from the NWISWeb Data for Idaho (http://nwis.waterdata.usgs.gov/id/nwis/nwis).

Although the use of natural flow indicators (e.g., chemistry, isotopes, and temperature) are powerful tools for the interrogation of aquifer flow properties, one limitation of this type of data is the lack of spatially distributed data. At the INL Site, most of the wells available for sampling are located near major facilities and are completed in the uppermost part of the SRPA. The same types of problems are encountered using anthropogenic contaminants as tracers. This property of the aquifer-monitoring system at the INL Site creates a data set with a high density of wells in some areas and a paucity of wells in others. As a result, flow fields or pathways based on non-anthropogenic and anthropogenic flow indicators often require significant smoothing or extrapolation on the distal or edge portions of the data set. In some places, this generates significant discrepancies between anthropogenic plume geometries and naturally occurring isopleths. Potential solutions for this problem include more spatially located sampling wells and wells that sample more than just the top of the aquifer. Additionally, it would be beneficial to integrate the natural and anthropogenic data sets such that each set of conclusions is considered in the context of both (a) short-term migration (< 60 years using contaminant plumes) and (b) long-term migration (> 60 years using naturally occurring chemical tracers).

The spatial distribution of water temperature at the top of the SRPA indicates that locally recharged water is not vertically mixed within aquifer but is spread laterally over the upper part of the aquifer (for example, cool water beneath the INL Site spreading areas and the Big Lost River). The effect of locally layered water on the three-dimensional geochemistry of the active SRPA is not well defined.

There is some indication that current well completions at the INL Site result in water samples that are representative of only the most conductive horizon in the completed interval. This has resulted in the assumption that the SRPA is homogeneous vertically and chemically. The need for wells that can be sampled at multiple intervals to provide insight into the vertical chemical stratigraphy of the aquifer is significant.

2.3.3 Temperature

One of the goals of the OU 10-08 modeling program is to use nontraditional data sets to help constrain hydraulic properties in the aquifer. Temperature data, for example, can be used to trace groundwater movement, because the mechanisms of energy transport are essentially the same as those that transport solutes. So if water with a temperature different than the background temperature of an aquifer is introduced at a known location, then the attenuation of that thermal energy difference with time or distance can be modeled just as attenuation of a solute injection can be modeled. Temperature data for the SRPA are thus being collected to attempt to identify the heat sources and sinks and the downstream temperature distributions that may be used to quantitatively estimate groundwater flow velocities using a numerical heat transport simulator.

To map temperature distribution in the SRPA in the vicinity of the INL Site, we rely primarily on two types of data: (1) groundwater temperature measurements that have been collected during water-quality sampling or other monitoring programs and generally represent an integrated temperature for the well and (2) temperature profiles collected during geophysical well logging. The first type, which is far more abundant, is used to define the general two-dimensional (in the horizontal plane) temperature distribution. The second type is used in conjunction with the two-dimensional data to attempt to define the three-dimensional temperature distribution of the system.

2.3.3.1 Spatial Distribution—Horizontal Plane. Groundwater temperature measurements are relatively abundant in the SRPA. The USGS NWISWeb (http://nwis.waterdata.usgs.gov/id/nwis/nwis) contains temperature measurements for approximately 5,700 locations in the eastern SRPA. Those data typically contain multiple measurements, at different times, for each well or surface water location. To date, we have used the average of each time series to construct a map of groundwater temperature for the aquifer (Figure 2-33), based on the fact that temperatures respond relatively slowly to changes at the boundaries of the system. Subsequent efforts will focus on examining the variability of temperatures in the SRPA as a means of identifying potential errors and identifying temperature variations characteristic of a seasonal groundwater recharge signal.

The groundwater temperature map produced from the NWIS data illustrates several characteristics that have been noted in several previous studies (Blackwell et al. 1992; Brott et al. 1981). First, temperatures generally increase in the direction of groundwater flow. Recharge temperatures along the edge of the Yellowstone Plateau are approximately 5 to 9°C, while temperatures at the other end of the system, in the vicinity of Thousand Springs, are approximately 15°C. The increase is, however, not a gradual trend with distance. Temperatures increase dramatically over relatively short distances in the northeast part of the system, with a localized warm anomaly located approximately at Grassy Ridge near the Saint Anthony sand dunes. Horizontal temperature gradients around that high temperature anomaly are much greater in the southwesterly direction, perhaps due to agricultural introduction of cold water recharge to the southwest. Groundwater temperatures southwest of that location appear to reflect mixing of water heated by local geothermal effects with water recharged through irrigation or losing streams.

Groundwater temperatures along the northern boundary of the INL Site are approximately 12 to 13°C, and that range is also prevalent throughout parts of the site, to the southeast of the site, and to the southwest of the WAG 10 study area southeast of the Wood River Valley. On, and to the southwest of,

the INL Site, temperatures are locally both higher and lower than that apparent background range. Warm anomalies at several locations appear to reflect local heating, presumably due to areas with greater upward flux of geothermally heated groundwater. Localized hot spots are evident below Craters of the Moon National Monument, along the AVH southwest of the INL Site, and around CH-1 near Middle Butte, where shallow groundwater temperatures reach ~19°C. Two localized cold water anomalies exist in two places in the southwest portion of the INL Site, one located approximately under the Big Lost River spreading areas and a second located directly below Big Southern Butte.

2.3.3.2 Vertical Heat Flux. Vertical heat fluxes above the SRPA provide evidence of the effect of groundwater flow on geothermal heat flow and provide a useful boundary condition for heat flow modeling of the system. To calculate the vertical heat flux distribution over the ESRP, we apply Fourier's steady-state law of heat conduction, as follows:

$$J = -\kappa_{eff} \frac{\Delta T}{\Delta Z} \tag{2-1}$$

where

J	=	heat flux
κ_{eff}	=	effective thermal conductivity
ΔT	=	temperature difference (mean annual air temperature minus groundwater temperature)
ΔZ	=	elevation difference (ground-surface elevation minus water table elevation).

The heat flux calculation, therefore, requires spatial distributions of groundwater temperature, surface temperature, water table elevation, and ground surface elevation. For this system, we assumed a ground surface temperature equal to the mean annual air temperature for the area (using gridded data obtained from the Spatial Climate Analysis Service [2005], Oregon State University), estimated groundwater elevations from the 1980 water table map developed by Garabedian (1992), and ground surface elevations from a USGS digital elevation model for the region. We assumed an effective thermal conductivity of 2 watts m^{-1} K^{-1}, a reasonable approximation for basalt (e.g., Brott et al. 1981).

Resultant heat fluxes are generally upward across the ESRP, even in the recharge areas at the edge of the Yellowstone Plateau (Figure 2-34). The persistence of upward heat fluxes throughout the northeastern portion of the ESRP contradicts the conclusions of some previous studies (Brott et al. 1981; Blackwell et al. 1992) that described heat fluxes as positive in that vicinity. This suggests that mountain-front recharge is generally warmer than the mean annual air temperature. With one exception, calculated heat fluxes were negative only where the water table elevation exceeded the ground surface elevation, indicating errors in the elevation data used. The high positive heat fluxes surrounding those areas may thus, to some extent, reflect errors in the groundwater elevation data if the thickness of the vadose zone is substantially underestimated. In this case, the groundwater elevation data are based on a water table map developed by Garabedian (1992) for 1980 water levels. The sensitivity of the calculated heat flux to elevation differences suggests that further effort should be made to develop a more accurate water table map for the aquifer.

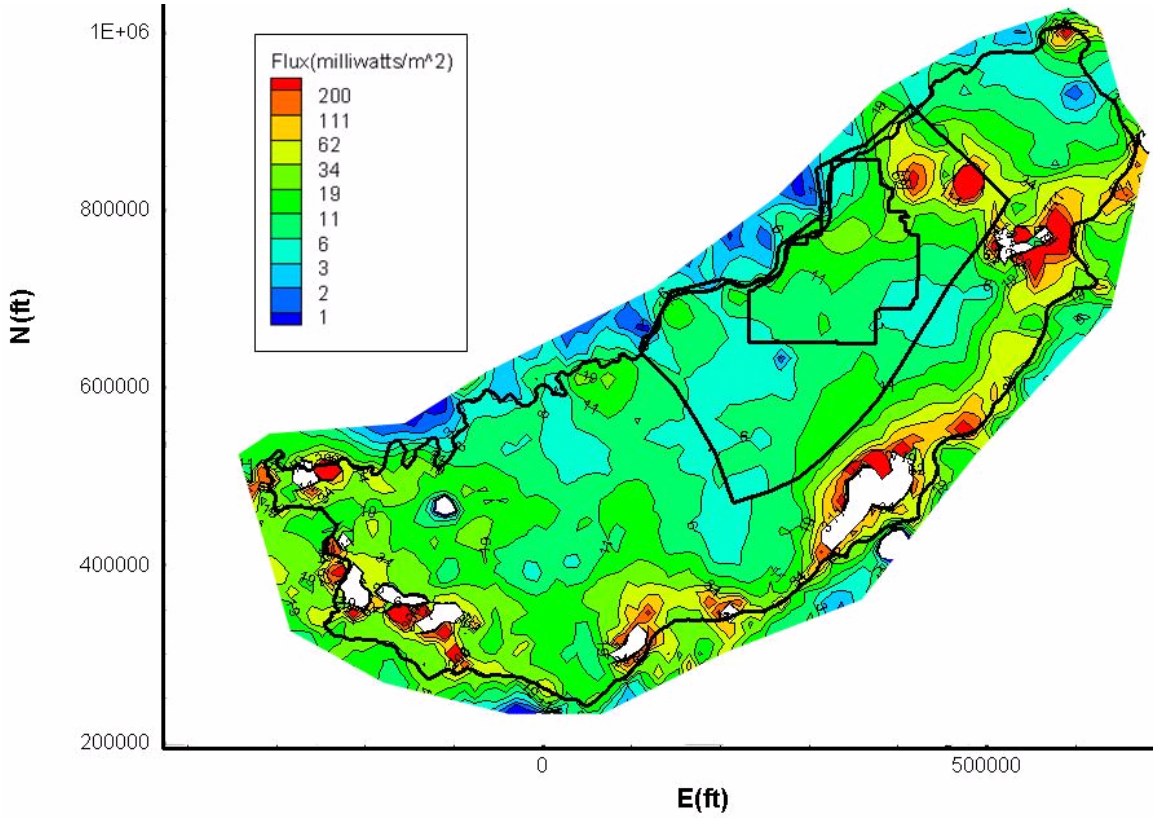

Figure 2-34. Heat flux above the eastern SRPA, based on the groundwater temperature map presented as Figure 2-33 and mean annual air temperatures obtained from the Spatial Climate Analysis Service. Contour scale is exponential because of several anomalously high heat flux values (red areas). Areas shown in white had negative heat fluxes. With one exception, negative fluxes occurred where the estimated groundwater elevation exceeded the surface elevation that was based on the digital elevation model. Heat flux estimates around those areas should, therefore, be considered uncertain, because small errors in elevations at those locations would produce large differences in the calculated heat flux. Solid lines indicate the boundaries of the INL Site, the OU 10-08 study area, and the eastern SRPA.

The heat flux map provides a better indication of the effect of groundwater movement and local recharge on the temperature field than the temperature map itself, because the calculation reflects the effect of the overlying material on the groundwater temperature. Warm anomalies to the northeast of the site, where the unsaturated zone is relatively thin, thus indicate pronounced heat fluxes, while the warm anomaly along the AVH to the south of the site, where the thickness of the unsaturated zone locally exceeds 400 m, produces only minor upward heat flux. The heat flux map also underscores the large difference in heat transfer above and below the aquifer. Below the aquifer, measured heat fluxes are approximately 110 milliwatts m^{-2} (Blackwell et al. 1992). With the exception of several anomalously high values in regions that appear to be affected by local recharge, calculated heat fluxes above the aquifer are less than 35 milliwatts m^{-2}. This underscores the strong influence of the rapidly moving and rapidly replaced groundwater on heat flow through the system. Finally, while this map provides a useful means of examining the spatial distribution of vertical heat flux, the map also provides data necessary for development of a three-dimensional thermo-hydraulic model. The upper boundary of the thermo-hydraulic model will likely be the top of the aquifer. The vertical heat flux map thus provides the upper boundary condition for heat flow in that model.

2.3.3.3 Apparent Sources and Sinks. The groundwater temperature map suggests that temperatures in several locations in the vicinity of the INL Site might greatly aid in constraining groundwater velocities. The most prominent temperature anomalies in the vicinity of identified contaminant plumes are the cold water anomalies located near the spreading areas and beneath Big Southern Butte. The latter might reflect either cold water recharge from the nearby spreading areas or cold water recharge through Big Southern Butte. Using estimates of the likely recharge in the microclimate associated with the butte, as well as information about the spreading areas, we anticipate that we will be able to identify the most likely source. Because we can estimate the recharge flux and the groundwater temperature reasonably well for both sources, heat transport modeling of those effects should provide valuable information about groundwater flow in that area.

Other areas where both recharge fluxes and recharge temperatures should be reasonably well constrained include areas where tributary stream leakage appears to heavily influence groundwater temperature, for example, near the confluence of the North and South forks of the Snake River and along the boundary of the study area where streams flow onto the ESRP.

2.3.3.4 Vertical Temperature Profiles. Temperature data are one of the few existing sources of information about the three-dimensional nature of flow in the eastern SRPA, because temperature logs have been obtained from numerous boreholes that penetrate well below the water table. As part of the OU 10-08 effort to use temperature data to help constrain aquifer velocities, these profiles have been combined with the previously described two-dimensional temperature distribution to develop a three-dimensional picture of temperature distribution below the ESRP. A preliminary fence diagram illustrating the three-dimensional temperature distribution (Figure 2-35) has been generated from about 150 temperature logs, most of which were conducted by Dr. David Blackwell as part of geothermal studies of the area. This fence diagram depicts the approximate extent of the three-dimensional data set available as a target for the three-dimensional heat flow modeling study. Because relatively few wells penetrate to great depth and most of those wells are located on the INL Site, the data density is greatest in that area. INL Site cross sections describing general characteristics of heat flow along and perpendicular to the direction of groundwater flow have previously been described by Smith et al.[c]

Temperature profiles have also been used to help identify the bottom of the active portion of the aquifer at the INL Site,[c] because vertical temperature gradients within the active flow system are generally much less than those in the subaquifer or in the overlying vadose zone.

The temperature log of the Middle-1823 well illustrates several features common to temperature profiles at the INL Site (Figure 2-36). Immediately above the water table, temperature gradients are relatively steep and appear to reflect diffusive heat transport. Closer to the surface, reversing gradients are frequently observed, probably reflecting seasonal temperature changes that can propagate to a relatively great depth in the fractured basalt stratigraphy. Below the water table, and often extending several hundred yards below, temperature gradients are typically very small. Morse and McCurry (2002) described this as the effect of actively circulating water on the temperature profile. Below this "isothermal" region, the temperature gradient becomes relatively steep and constant to depth. Based on measured values of the thermal conductivity of basalt, this lower regime clearly reflects diffusive heat transport. Based on the measured gradients in such subaquifer sections, the average geothermal heat flux is approximately 110 milliwatts m^{-2} (Blackwell et al. 1992).

c. Smith, R. P., T. McLing, and, M. Rohe, 2000, *Implications of Water Temperature, Water Chemistry, and Regional Geophysical Setting for Flow Characteristics of the Snake River Plain Aquifer beneath the INEEL Area*, INL Internal Report.

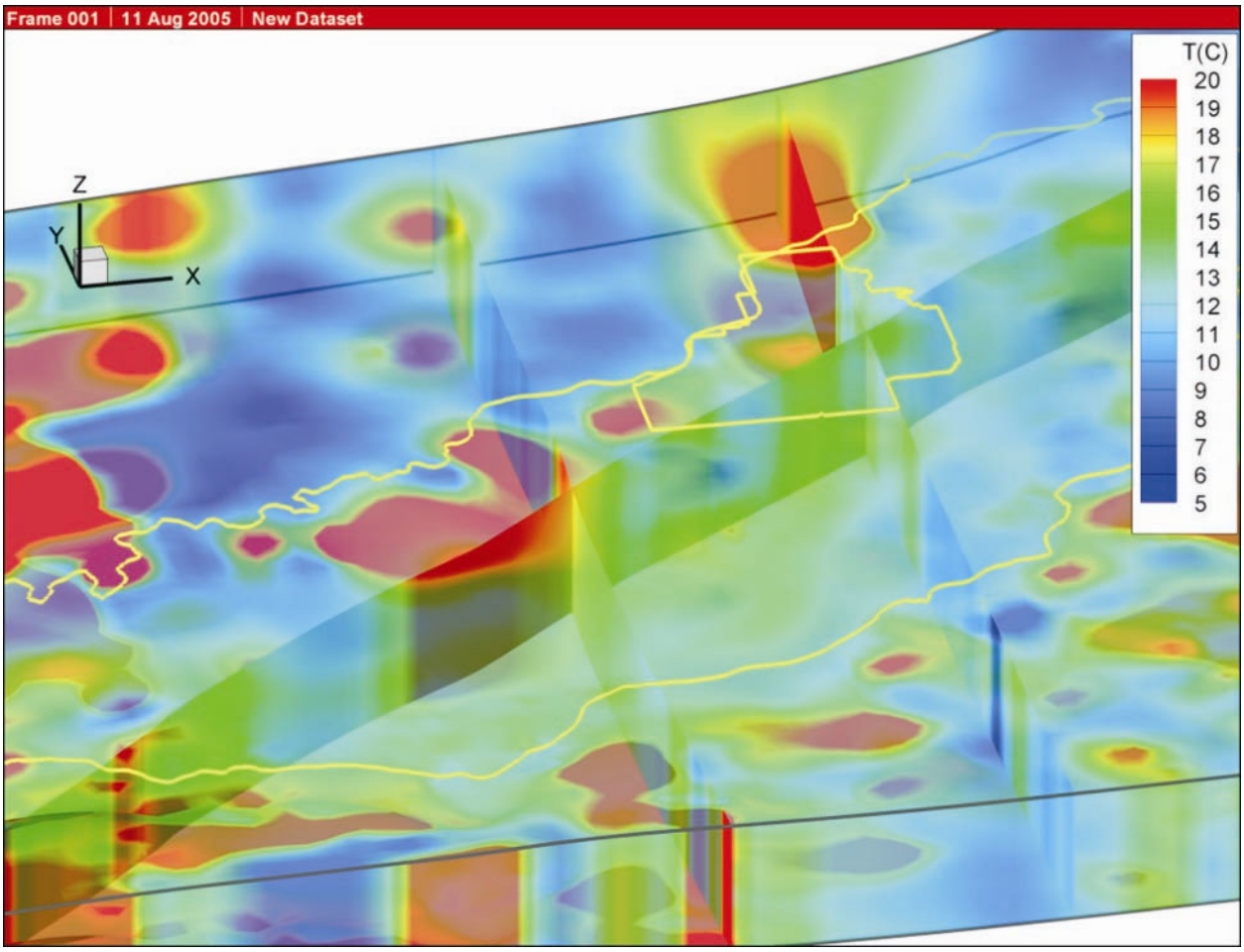

Figure 2-35. Three-dimensional contour plot with vertical cross sections displayed at three arbitrary locations, illustrating the nature and extent of three-dimensional temperature data in the eastern SRPA. The surface of contoured domain is the water table. The thickness of the contoured domain is 610 m (2,000 ft). Interpolated data combine temperature profiles from approximately 150 temperature profiles with the estimated water surface temperature map included as Figure 2-33.

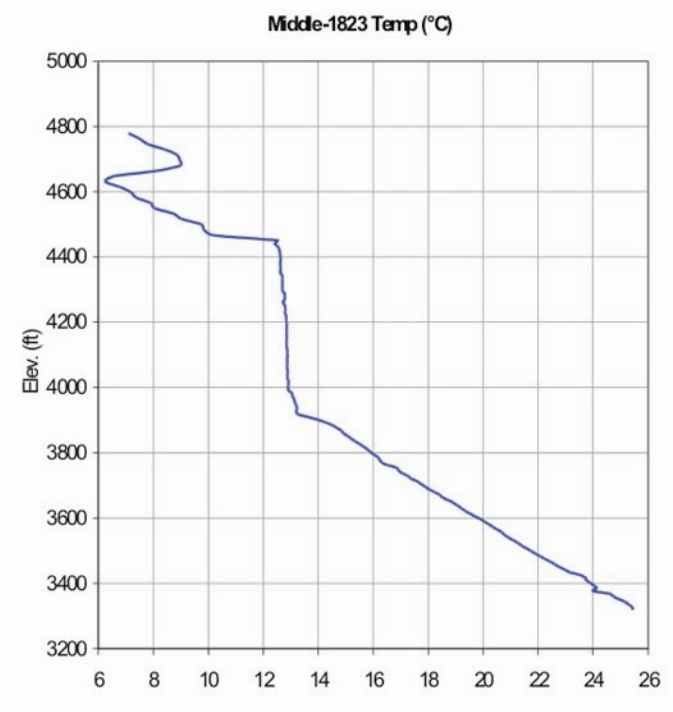

Figure 2-36. Temperature profile obtained in February 2003 from the Middle-1823 corehole.

As part of an effort to further define the large-scale hydrostratigraphy, temperature profiles are currently being reviewed to separate intra-borehole flow effects from the effects of natural groundwater flow on temperatures. Within the isothermal section of several INL Site wells, changes in gradient are commonly observed, and, in some cases, these changes might be indicative of hydrostratigraphic breaks. Intra-borehole flow can produce similar effects in uncased wells. For example, water is free to enter or exit the open borehole in response to variations in vertical head differences across hydrogeologic units and fracture networks (Figure 2-37). In this manner, the natural groundwater flow system can be short-circuited by flow within the borehole. The velocity of water flowing in the open borehole is likely to be fast enough so that diffusive heating is insufficient to bring the moving water into equilibrium with the natural system. Thus, intra-borehole flow can create an isothermal interval in the temperature log that is not representative of the actual temperature profile of the aquifer. Several interpretative techniques are employed to evaluate the effects of intra-borehole flow.

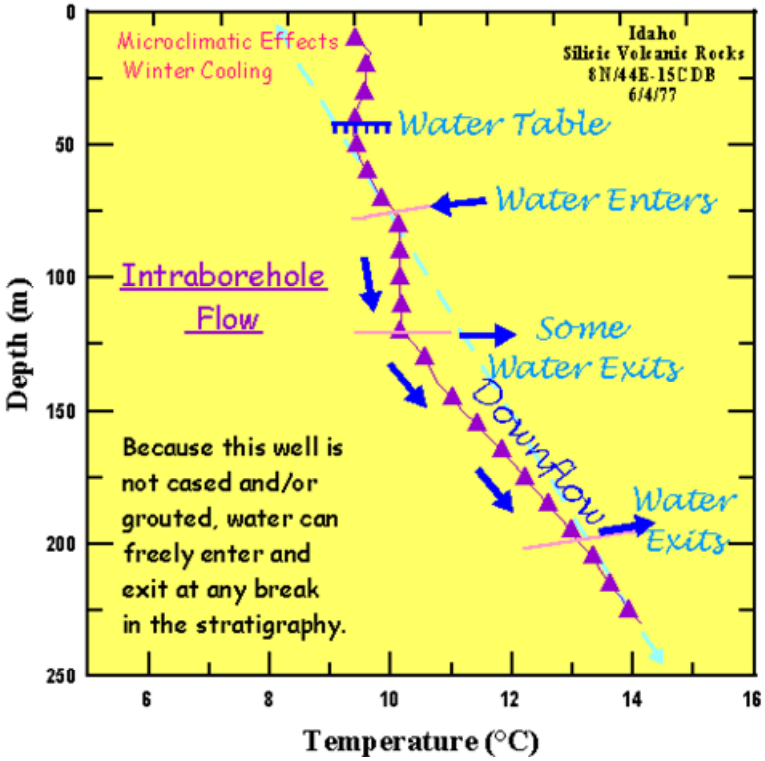

Figure 2-37. Illustration of the effects of intra-borehole flow on the temperature profile of an uncased borehole (from Southern Methodist University [2005]).

3. TWO-DIMENSIONAL NUMERICAL MODELING ACTIVITIES

3.1 Flow Model Development

During fiscal year 2005, the conceptual model described in Section 2 was implemented in a two-dimensional, steady-state numerical flow model. The computer codes used to develop the two-dimensional flow model were the MODFLOW-2000 (Harbaugh et al. 2000) groundwater flow simulation code, the PEST (Doherty 2005) parameter estimator, and the Groundwater Modeling System (GMS) (BYU 2003) pre- and post-processor and data analyzer. MODFLOW is an industry standard groundwater flow simulation code developed by the USGS. MODFLOW-2000 is the latest version and incorporates many new features.

PEST is a robust parameter estimator that is designed to automatically adjust the parameters in any model over a series of runs until model-generated results fit a set of observations as closely as possible. PEST also provides information about the sensitivity of the results to changes in the selected parameters, the correlation (a measure of non-uniqueness) among parameters, and the resolution of the parameters.

GMS is a widely used software package developed for the Army Corps of Engineers. GMS integrates and facilitates implementation of the conceptual model, interpretation of the output, and visualization of the results for all of the codes used in this effort. GMS also provides a convenient interface to link MODFLOW-2000 and PEST.

The overall objective of developing the two-dimensional flow model is to better understand both the regional- and local-scale features, investigate the validity of various calibration approaches, and investigate the feasibility of using all of the aquifer wells available inside the INL Site boundaries and the rest of the model domain as calibration wells. Another objective is to investigate the sensitivities of important model input parameters, such as hydraulic conductivity, underflow recharge rates from tributary drainage basins and the precipitation recharge rate, and their influence on the simulated head field at the local and subregional scale. Transient effects of the flow field on contaminant transport will be investigated in the next phase of the OU 10-08 modeling project. This could lead to a revision of the two-dimensional flow model.

The following subsections summarize the implementation of the conceptual model into a two-dimensional, steady-state numerical flow model using GMS/MODFLOW-2000. Topics discussed include domain selection, grid design and orientation, depth scenarios, boundary assignments, calibration approaches, calibration results, and limitations of the two-dimensional integrated model.

3.1.1 Model Domain Selection

This subsection discusses the domain size selection, domain boundary locations, and effective aquifer thickness scenarios. The physical extent, or domain, of any groundwater numerical model should be beyond the institutional boundaries of the subject facility being studied such that the simulated groundwater flow at the facilities is not affected by the model boundaries. Typically, physical boundaries, such as impermeable barriers, are used as model boundaries. But hydraulic boundaries, based on groundwater divides or streamlines, are also often used.

For the OU 10-08 model, groundwater flow is principally in a southwest direction. Model boundaries, therefore, generally lie to the northwest, southeast, northeast, and southwest. For the OU 10-08 project, the spatial extent of the model was chosen to correspond to natural physical boundaries to the northwest of the INL Site; hydraulic boundaries, based on streamlines, along the southeast; and hydraulic boundaries to the northeast and southwest.

The distance from the institutional boundaries of the INL Site to the natural boundaries northwest of the site is predetermined by the geologic nature of the mountain ranges intersecting the ESRP. The other boundaries, however, are open to interpretation. Factors influencing the location of the hydraulic boundaries include the need to provide adequate downgradient extent for risk assessment, a need to minimize overall domain size for computational efficiency, and interpretation of hydraulic head maps to determine fixed-head or no-flow conditions.

The initial model domain was selected based on then-current hydraulic head maps and the need to extend the model sufficiently downgradient. This domain is depicted in Figure 3-1. This domain covers nearly 7,770 km^2 (3,000 mi^2), as proposed initially in the OU 10-08 modeling strategy report (Arnett and Smith 2001). The domain is approximately 143 km (89 mi) along the general direction of groundwater flow, between 43 and 61 km (27 and 38 mi) in the transverse direction, and oriented along the principal axes of the Snake River Plain. This domain was incorporated into both the preliminary two-dimensional flow and two-dimensional transport models experimented with during fiscal year 2005.

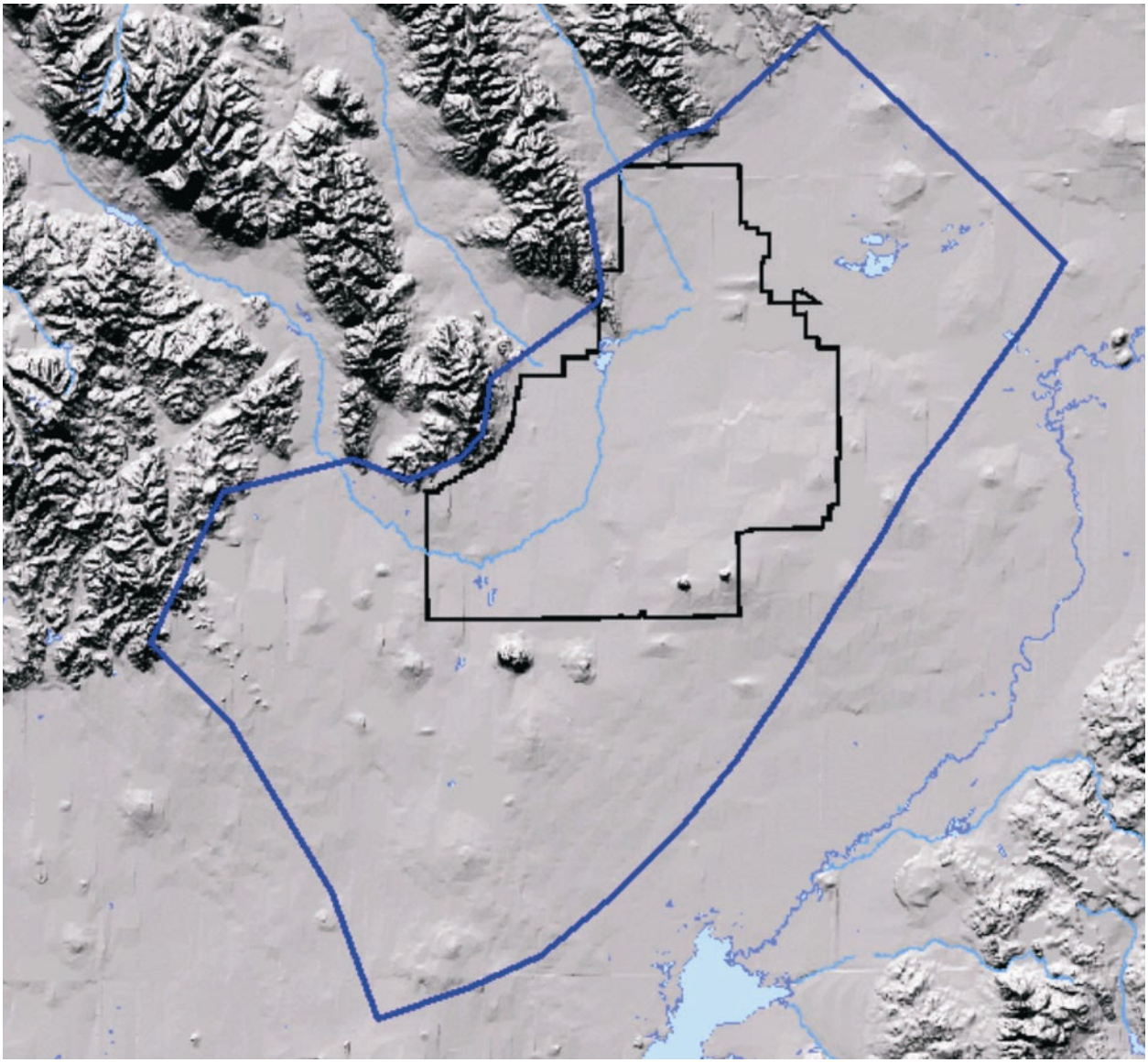

Figure 3-1. Initial OU 10-08 model domain.

The Mud Lake area in the northern part of the initial model domain is known to have very seasonally dependent head conditions with significant fluctuation. The available head measurements indicate a much higher groundwater elevation than the regional aquifer. Much of the groundwater in this area appears to be basically a perched water body. As a result, the placement of the northeast boundary was brought closer to the INL Site institutional boundary.

Additionally, inclusion in head maps of certain wells to the southwest of the OU 10-08 initial model domain demonstrated that a significantly steepening hydraulic gradient occurs in this area. However, this gradient is based on a very limited number of aquifer wells. Furthermore, analysis of streamlines resulting from the final mapping of June 2004 water levels indicates a somewhat different streamline near the southern end of the southeast boundary. As a result, the southwest boundary was slightly modified by truncating the southeastern corner of the original model domain.

The resulting new model domain is shown in Figure 3-2. This domain now covers approximately 2,500 mi^2, with boundary lengths of 101, 51, 109, and 68 km (63, 32, 68, and 42 mi) along the southeast, northeast, northwest, and southwest sides, respectively.

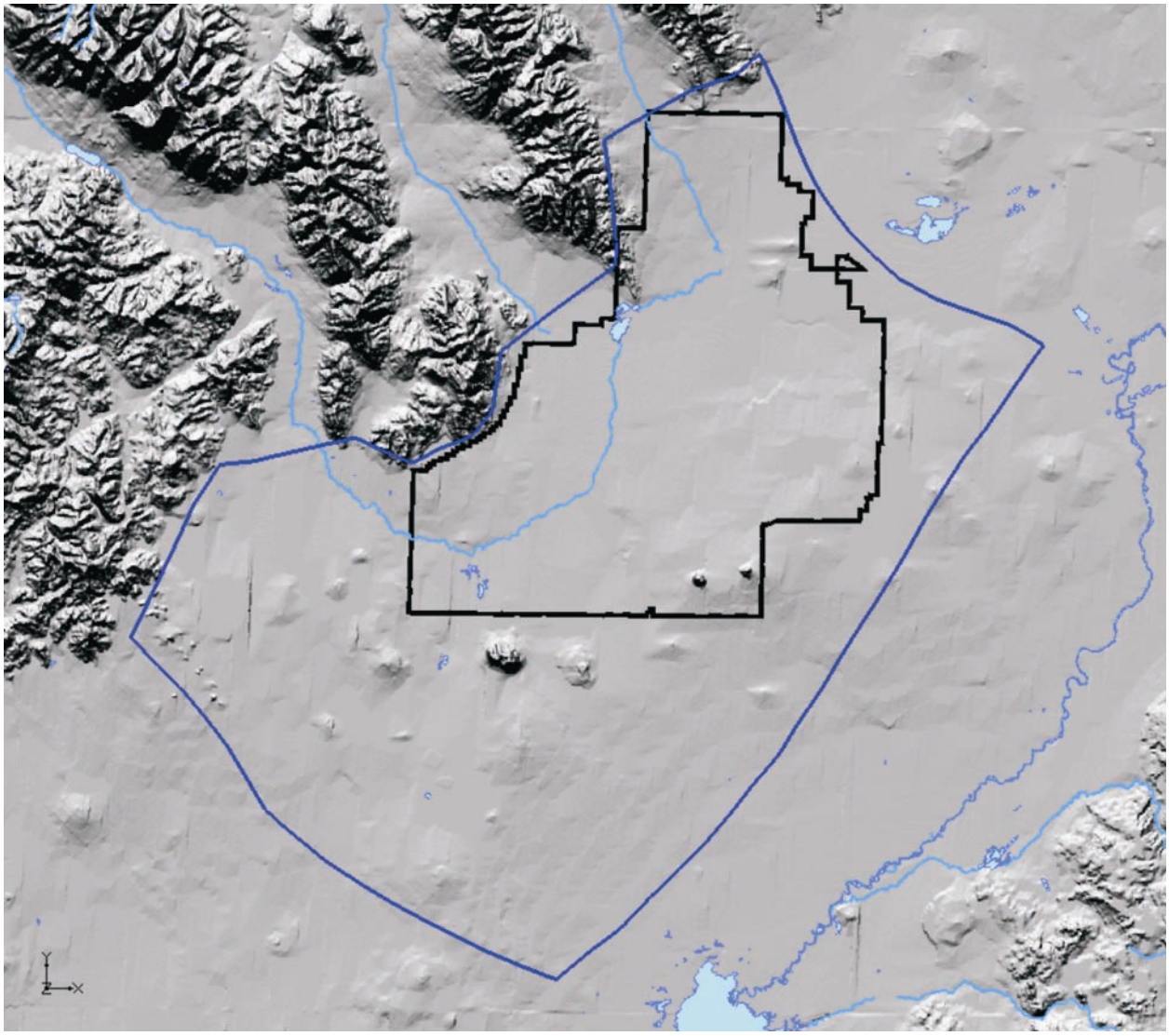

Figure 3-2. New two-dimensional flow model domain.

In the vertical direction, the model domain extends to the top of the aquifer, or water table surface, as determined from aquifer well water-level measurements such as those obtained in June 2004 and June 2005. This elevation and surface configuration are described in detail in Section 2, with a final elevation contour map provided in Figure 2-28.

The lower surface of the model domain is defined by the thickness of the active portion of the aquifer. The aquifer thickness has been previously determined from an integration of temperature-profiling and electrical-resistivity studies. As described in the OU 10-08 work plan (DOE-ID 2004), two thickness scenarios have been considered for the flow and transport modeling activities of fiscal year 2005. The thickness scenarios include both a thick and a thin version. They are based on different interpretations of trends observed in electrical-resistivity and thermal-profile data that are used to delineate the bottom of the aquifer. Both use the limited direct evidence of the aquifer base from the eight deep wells in the south-central part of the study area and extrapolate differently to the perimeter of the model domain using electrical-resistivity data and water temperature at the top of the aquifer. The thick interpretation uses colder water temperatures to infer thicker areas of the aquifer toward the north of the model domain and electrical-resistivity observations of a very thick aquifer section downgradient of the INL Site. The thin scenario only infers a general tendency for the aquifer to thicken toward the center of the Snake River Plain. Images depicting these two thickness scenarios are presented later in Subsection 3.1.4 (Figures 3-4 and 3-5).

3.1.2 Boundary Conditions

Figure 3-3 shows the locations and types of boundary conditions implemented in the two-dimensional flow model. The northern and southern boundaries of the OU 10-08 model domain are currently treated as specified head boundaries. The contour map of the June 2004 water table map shown in Figure 2-28 was used to assign head values along these two specified head boundaries.

The eastern boundary of the OU 10-08 model domain extends in a northeast-to-southwest direction and corresponds to an estimated groundwater flow line across which there is no groundwater flow. The preliminary model domain is bounded on the west by a Type 2 boundary (part no-flow and part specified-flux) that represents mountain ranges and the mouths of important tributary drainages. The toes of mountain ranges are assumed to minimize groundwater movement in and out of the model domain and are, therefore, modeled as no-flow (zero-flux) boundaries. Between these mountain ranges, specified-flux boundary conditions are used to model the underflow recharge from tributary drainage basins. The flux estimates were derived from the USGS regional aquifer model studies (Kjelstrom 1986; Garabedian 1992) and subjected to sensitivity study. Table 3-1 summarizes the underflow recharge fluxes implemented in the two-dimensional flow model. These estimated fluxes are highly uncertain, and a comprehensive sensitivity study discussed later in this report will be carried out.

Table 3-1. Underflow recharge flux from tributary drainage basins.

	Estimated Mean Underflow Flux		
Basin Name	m^3/d	m^3/s	ft^3/s
Big Lost River	882,122	10.2	361
Little Lost River	554,284	6.4	227
Birch Creek	250,104	2.9	102

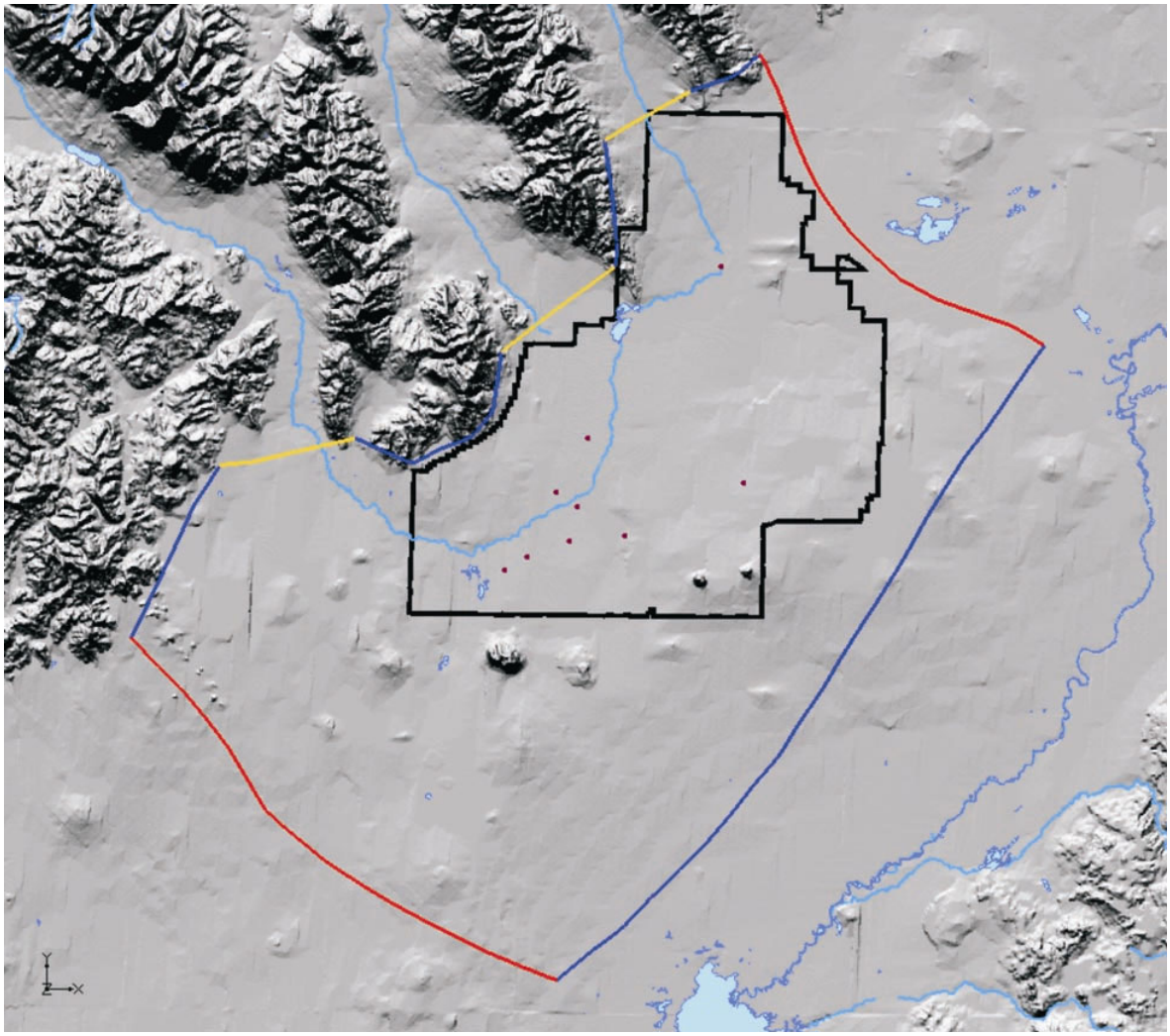

Figure 3-3. Boundary types of the two-dimensional flow model. (Red indicates the specified head boundary, blue indicates the no-flow boundary, and yellow indicates the specified-flux boundary.)

3.1.3 Sources and Sinks to the Flow Model

Within the new model domain described in Subsection 3.1.1, several sources and sinks of groundwater exist. Sinks are limited to pumping well discharge. Within the model domain, approximately 30 production or potable water wells are active. For potable water wells, it is assumed that the pumping rates are minor and groundwater consumption is minimal. For the production wells at major facilities, pumping can be quite significant, up to 0.044 m^3/s (1E + 6 gal/d). However, the pumping rates and times of pump operation for these wells are not well recorded; furthermore, it is assumed that all of the groundwater produced by these wells returns to the aquifer, because the production well water is, in all cases, discharged to disposal ponds. As such, no sinks are included in the numerical two-dimensional flow model at this point.

Sources include infiltration recharge from the Big Lost River, an ephemeral surface water feature that flows into areas simulated within the new two-dimensional model domain. For this version of the two-dimensional flow model, the Big Lost River was simulated as a specified-flow boundary with a constant flux of 243,344 m^3/d (100 cfs) that was variably distributed along the entire reach, which enters

the new model domain along the west boundary in the vicinity of Arco and terminates in the Big Lost Sinks southwest of TAN.

Areal precipitation falling within the new model domain constitutes another source of recharge. For this source, the two-dimensional model receives across the top boundary (water table) a constant flux of 1.95E-5 m/d (0.28 in./yr) of infiltration to represent the average of the 2 to 5% of precipitation estimated by Cecil et al (1992). This is currently uniformly distributed across the new model domain.

3.1.4 Construction of the Numerical Grid

The size of the nodal spacing in the horizontal dimension is a function of the expected curvature in the water table or potentiometric surface (Anderson and Woessner 1992). Finer nodal spacing is required for highly undulated water tables. Spatial variation of the hydraulic parameter should also be considered in the selection of node spacing. Currently, the minimum base node spacing used in any of the three existing individual WAG models is 305 m (1,000 ft) in the WAG 7 groundwater model, but each WAG model also has local refinements with smaller node spacing.

For instance, the WAG 7 model is refined near the Subsurface Disposal Area of the RWMC with a grid spacing of 152 m (500 ft). The WAG 3 groundwater model has a base grid spacing of 400 m (1,312 ft) and is refined to 200 m (656 ft) within facility boundaries. The WAG 1 groundwater model has a 1,600-m (5,249-ft) base grid spacing and 25-m (82-ft) refined spacing, resulting from a six-layer telescopic refinement scheme. Some optimization will be required to find the ideal grid spacing; spacing that is too coarse will fail to capture groundwater flow, but spacing that is too fine will result in an unwieldy number of grid cells and reduced computational efficiency.

It is anticipated that a variable grid spacing scheme will be required. Toward the margins of the model, the grid spacing will be largest, because these areas are farthest from the individual WAGs. Local refinements will be made at the portions of the model corresponding to the individual WAGs. Figures 3-4 and 3-5 show the two-dimensional, single-layer grid that we implemented in the two-dimensional numerical model for the two thickness scenarios. The grid has a minimum size of 492 ft (150 m) near nine individual WAGs and a maximum size of 2,460 ft (750 m) elsewhere inside the model domain. Such discretization results in a total of 53,658 grid cells. MODFLOW uses a structured grid discretization. As a result, local refinements made at individual WAGs must be carried throughout the model in both grid alignment directions. The grid is rotated by 45° to align with the main flow direction in order to save computational time.

3.1.5 Selection of the Calibration Targets

The OU 10-08 flow model will provide regional- and local-scale groundwater flow fields for the integration of groundwater flow and transport modeling results from individual WAGs. The flow velocity is the primary parameter of importance. Typically, measured heads and head gradients are the targets used to calibrate flow models.

The primary calibration target for this two-dimensional flow model is hydraulic head (i.e., hydraulic potential) measured in aquifer wells. Ideally, the set of primary calibration targets or head values should represent the same period in time. This is due to head values being subject to barometric fluctuations and changes due to recharge or discharge. The data collected from the June 2004 water-level measurements were used for the fiscal year 2005 two-dimensional flow model calibration.

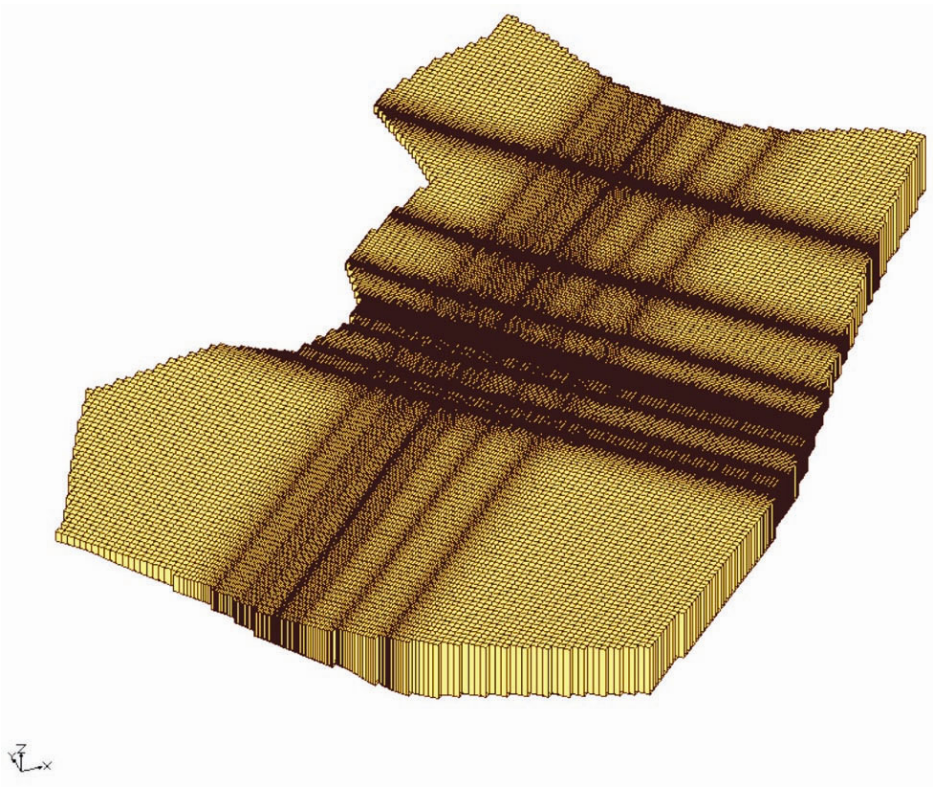

Figure 3-4. The two-dimensional, single-layer grid for the “thick” aquifer scenario.

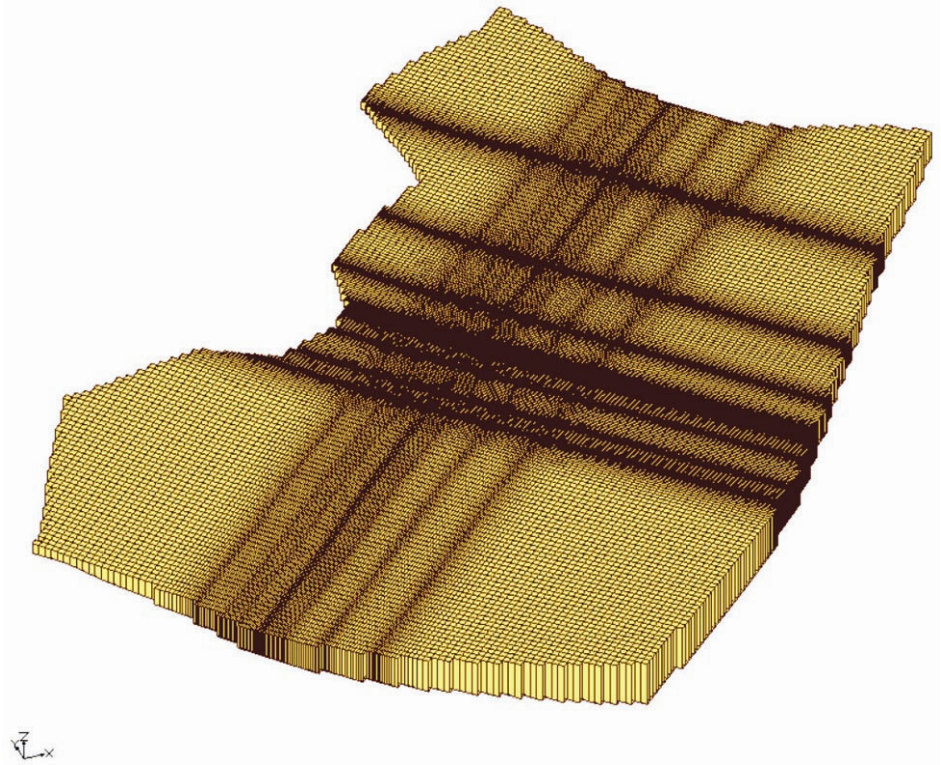

Figure 3-5. The two-dimensional, single-layer grid for the “thin” aquifer scenario.

The previous WAG 10 SWGM (McCarthy et al. 1995) used a limited subset of available spring 1980 water-level data. A total of 21 key wells were selected and supplemented by an additional 27 wells that were weighted less in that model's calibration scheme. Initially, all aquifer water-level measurements collected by Idaho Cleanup Project personnel in June 2004 from wells within the model domain were considered as calibration targets for the fiscal year 2005 two-dimensional flow model. The June 2004 water-level measurement effort included 229 aquifer wells; however, 15 of these were found to be completed at significantly deeper depths than the mean completion depth of the aquifer well set. Although the data are useful for examining the potential for vertical gradients, they were not included as part of the calibration set for the two-dimensional flow model.

Of the remaining 214 wells measured by INL Site contractors in June 2004, seven water-level measurements were replaced with USGS measurements, because inaccuracies were found in some of the INL-collected data points. Furthermore, this set of 214 wells was supplemented with additional USGS wellhead data that were collected from 10 wells; these wells are located along the outer edges of the model domain and are not typically measured by INL Site contractors. Though not used in calibrating the model, an additional 119 water levels from wells located outside the model domain were used for controlling contour lines in the creation of the water table map presented in Figure 2-28.

The new domain is smaller than the initial domain, so the 214-well set used to calibrate the two-dimensional flow model within the new model domain (described in Subsection 3.1.4) is smaller than the 253-well set used to calibrate the two-dimensional flow model with the initial domain. The land-surface elevation of the 214-well calibration set ranges over 565 ft (172 m) from a minimum of 4,112 ft (1,243 m) to 4,677 ft (1,425 m). These elevations are feet above mean sea level (National Geodetic Vertical Datum of 1929). Figure 3-6 illustrates the location of the 214 wells relative to the new model domain.

Figure 3-7 illustrates an important sensitivity of the model to the number of wells that are used in the calibration process. Similar to the previous WAG 10 model (McCarthy et al. 1995), the fiscal year 2005 two-dimensional flow model was initially calibrated using a smaller subset of 70 key wells. This resulted in very minimal overall error between simulated and observed heads. However, the model was later calibrated with the initial model domain using 253 wells. Particle tracking using the MODPATH feature of GMS allowed examination of resulting flow paths. Figure 3-7 shows that adequate approximation of the flow field is achieved with the 253-well calibration. The resulting flow paths in the vicinity of INTEC are oriented more to the south and are more consistent with those obtained from the local-scale OU 3-14 groundwater model. Additional model sensitivities are discussed in Subsection 3.1.10.

The use of more than four times as many calibration targets represents the difference in two important calibration approaches, zonation versus pilot point. In this study, three calibration techniques have been explored and applied. The three calibration techniques are zonation with automated parameter estimation, automated parameter estimation using the "pilot-point" approach, and a combination of these two methods. Each method has advantages and disadvantages. All three methods were applied, and the method that produced the best results was selected as the final calibration method. These approaches and their results are described briefly in the following subsections.

3.1.6 Zonation Approach for Groundwater Flow Model Calibration

The zonation approach is the traditional method of calibration; this approach divides the model domain into zones of constant property value. The main steps in the process are as follows:

- The model domain is divided into zones of equal hydraulic conductivity. Each zone of hydraulic conductivity is defined by a different parameter with a constant model parameter value.

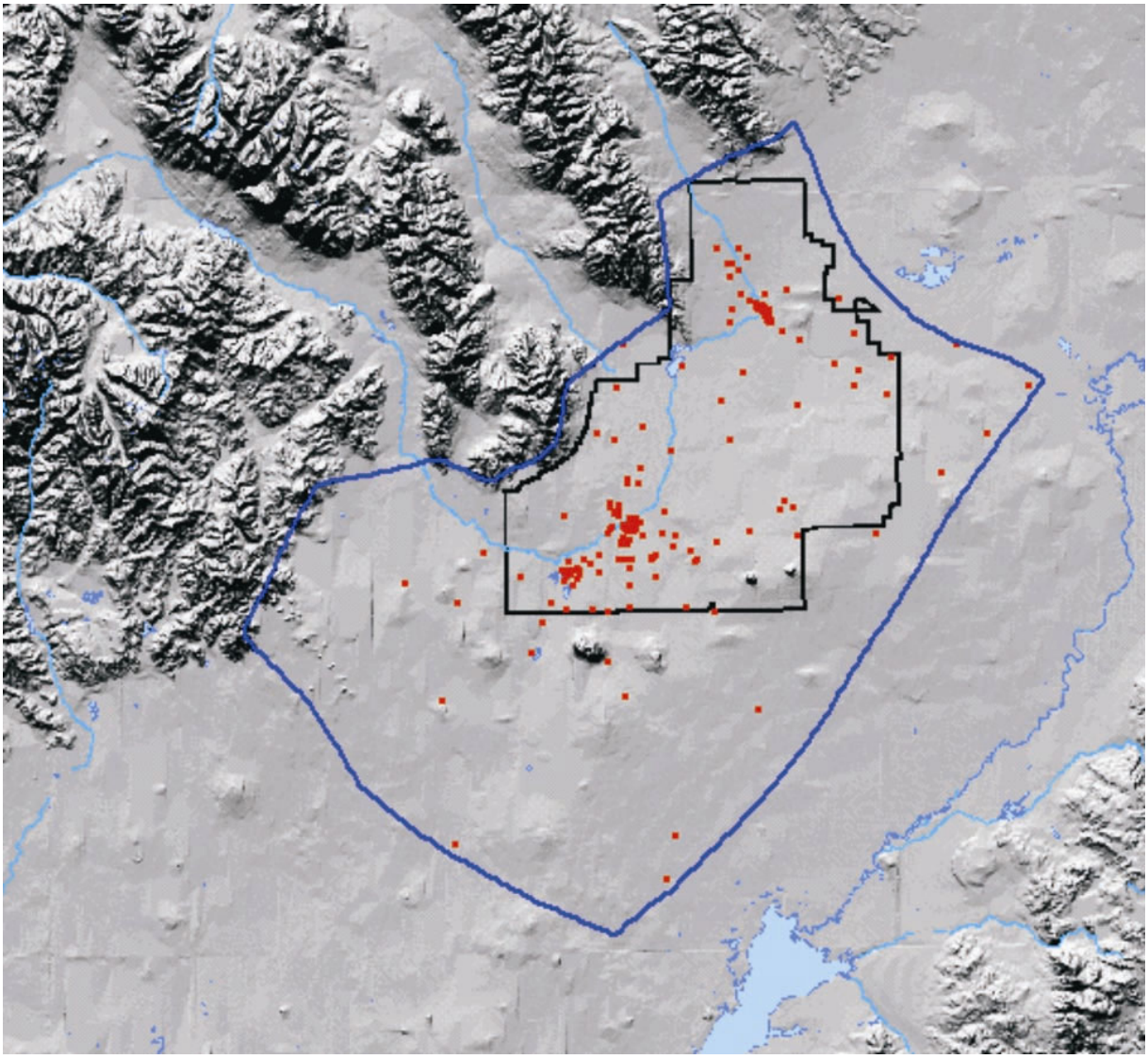

Figure 3-6. New model domain showing the locations of 214 aquifer wells (red dots) that were used as calibration targets in fiscal year 2005.

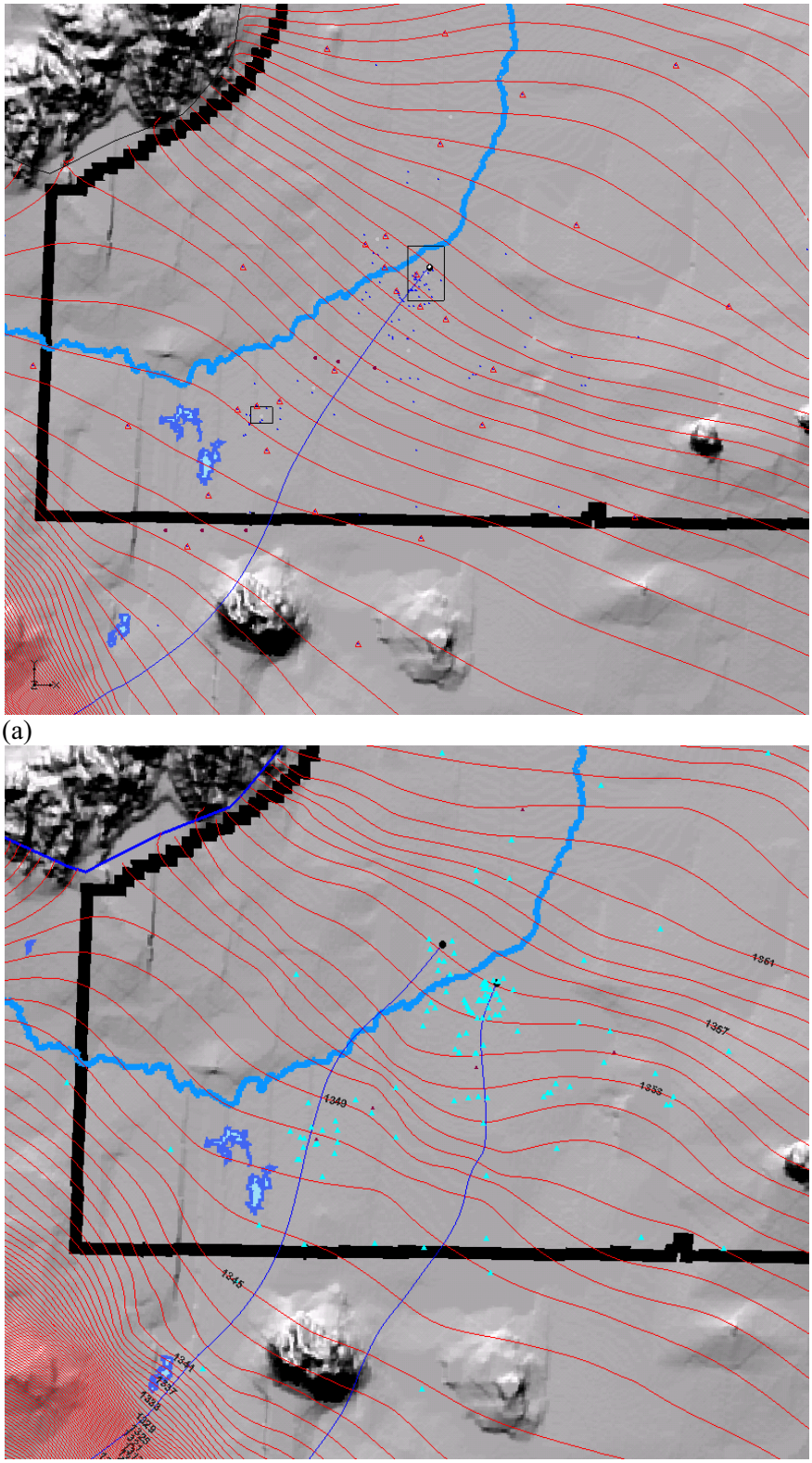

(a)

(b)

Figure 3-7. Comparison of simulated flow paths that are the result of two-dimensional flow model calibration using head data from (a) only 70 wells (red dots) and (b) 253 wells (light blue dots).

- Initial hydraulic conductivity estimates are made for each zone.
- PEST is utilized to automatically adjust the hydraulic conductivity values of a selected set of hydraulic conductivity zones and, therefore, minimize the weighted sum of the squared simulation errors over all of the hydraulic head measurements.

The zonation approach was applied to the two-dimensional flow model calibration process in fiscal year 2005 with limited success. The results of this approach, as well as the results of other approaches, are discussed in a Subsection 3.1.9.

3.1.7 Pilot-point Approach for Groundwater Flow Model Calibration

The pilot-point approach also utilizes PEST automated parameter adjustment, but instead of beginning with zones of constant parameter value, the approach uses arbitrarily positioned pilot points. The steps in this approach are as follows:

- A set of points is selected inside the model domain as pilot points.
- Initial estimates of hydraulic conductivity are assigned for each pilot point.
- PEST is used to automatically adjust the hydraulic conductivity values of pilot points to minimize the weighted sum of the squared simulation errors over all of the hydraulic head measurements. The results of a PEST run consist of a set of optimal hydraulic conductivity values at pilot points that provide the best fit of the flow model to the hydraulic head measurements being used for calibration. The hydraulic conductivity values of the rest of the model domain are obtained by interpolating those optimal conductivity values at pilot points.

One advantage of the pilot-point approach is that it provides a smoothly varying and heterogeneous conductivity map without arbitrarily defining hydraulic conductivity zones. Another advantage is that this method can directly incorporate aquifer test data as a subset of pilot points, with fixed hydraulic conductivity values inferred from those tests.

The disadvantage of the pilot-point approach is that it is difficult to incorporate lithologic information when available. Therefore, we planned to use the following coupled pilot-point/zonation calibration approach, which has advantages of both approaches.

3.1.8 Coupled Pilot-point/Zonation Approach for Groundwater Flow Model Calibration

Another calibration method implemented in fiscal year 2005 for the two-dimensional flow model is a combination of the two previously discussed approaches. The coupled pilot-point/zonation calibration approach bounds upper and lower limits of possible pilot-point values via the zonation approach, thus taking advantage of known geologic features. The steps in this method are as follows:

- Hydraulic conductivity zones are defined according to available lithology and hydrostratigraphic information.
- Zones are selected where additional variation within zones is desired, and pilot points are set up within them. The hydraulic conductivity values at pilot points of a particular zone are bounded by the range of hydraulic conductivity appropriate for that particular zone's lithology.
- Uniform hydraulic conductivity values are assigned to zones without pilot points.
- Hydraulic conductivity values are assigned to pilot points.

- PEST is utilized to adjust the hydraulic conductivity values of each pilot point and for zones without pilot points.

The output of PEST will be a conductivity map that consists of zones with a constant hydraulic conductivity value and zones with varying hydraulic conductivity values. This feature may be important for the transport model to reproduce the observed plume migration behaviors, because local-scale heterogeneity largely affects plume migrations. The coupled pilot-point/zonation approach provides a good combination of the large-scale heterogeneity (from zone to zone) and local-scale heterogeneity (inside a zone). For the OU 10-08 numerical model, we started with the zonation approach followed by the pilot point and coupled pilot-point/zonation approaches. The approach that is most efficient and most realistically reflects field hydrogeological settings will then be used for the future three-dimensional model calibrations.

3.1.9 Calibration Results

The following subsections provide the hydraulic head mismatch, parameter value ranges, and a discussion on parameter reliability. The calibration results from all three approaches are compared and discussed below.

3.1.9.1 Zonation Approach. The fiscal year 2005 modeling effort considered two different aquifer thickness scenarios, thick (Figure 3-4) and thin (Figure 3-5), within this calibration effort. Figure 3-8 shows the hydraulic conductivity zones derived mainly from the large-scale geological settings. Table 2-1 summarizes the large-scale geologic features associated with each zone and the conductivity value ranges based on pumping test data.

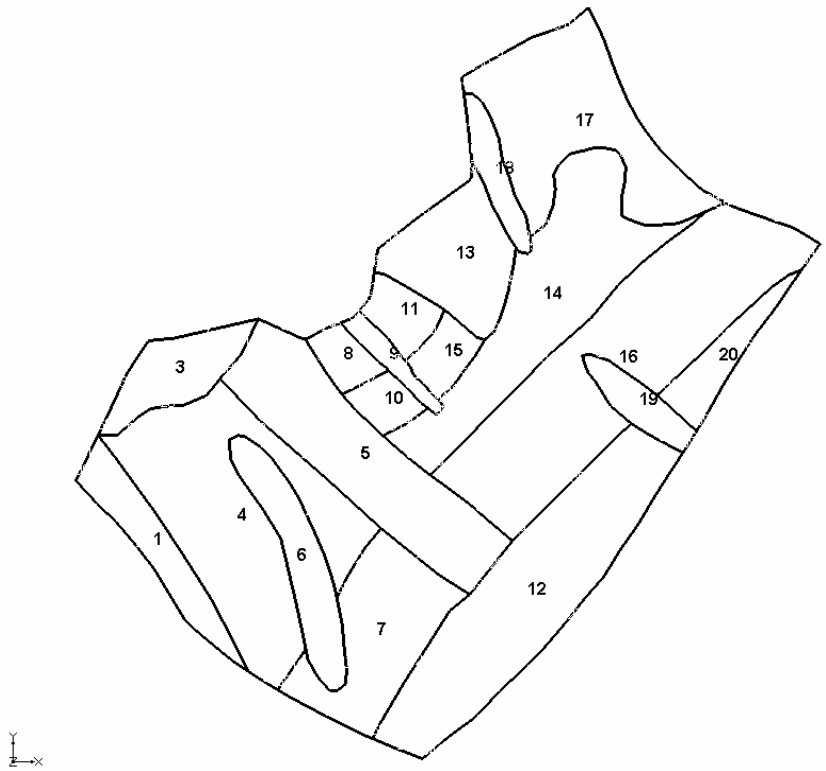

Figure 3-8. Hydraulic conductivity zone map implemented in the two-dimensional flow model.

Such a hydraulic conductivity zone map caused very irregular head distributions near the southern portion of the model domain, particularly in Zones 4, 6, and 7, so they were combined during the calibration process. The following results indicate that such treatment yields a better head contour map that is much closer to the measured groundwater table.

Figure 3-9 shows the simulated hydraulic head contour map and residuals at all observation wells for thick and thin aquifer scenarios. Figure 3-10 shows the residuals for wells near facilities for both scenarios. As shown in these figures, large mismatches occurred at wells in the northern and southern portion of the model domain, wells near INTEC, and wells in the central portion of the INL Site. Despite large residuals for both scenarios, the simulated head fields are able to reproduce the large-scale features of the measured water table, as shown in Figure 2-28.

For both aquifer thickness scenarios, a number of observation wells south of INTEC, north of TAN, and near the central portion of the INL Site have large mismatches; some of them are quite high. Figure 3-11 shows the plots of residuals versus observed heads for both aquifer thickness scenarios. For both scenarios, residuals are randomly distributed, and no systematic bias is observed in these two plots. The large residuals are unacceptable in terms of accurate description of the flow field inside and near the INL Site.

Figure 3-12 shows the comparison of the estimated hydraulic conductivity maps between the two aquifer thickness scenarios. Visual comparison between the two maps reveals some differences in the magnitude of the estimated K values for a number of zones. However, the overall K value distribution patterns are similar for both scenarios.

Because two different thickness scenarios are considered, it is interesting to see the transmissivity field for both scenarios. Figure 3-13 shows the transmissivity fields by multiplying the estimated K field with the effective aquifer thickness. Despite some differences between the estimated K maps, the transmissivity fields for both scenarios look similar. This indicates that, from a perspective of inverse modeling for a two-dimensional flow model, the thickness of the aquifer does not really matter. Although the fiscal year 2005 two-dimensional model includes variable aquifer thickness, only transmissivity really matters in terms of affecting simulated head contour maps.

PEST also automatically calculates the confidence bounds of the estimated parameters as an indicator of parameter uncertainty. Tables 3-2 and 3-3 show the estimated K value for each zone and the associated 95% confidence bounds of each estimate for the thick and thin scenarios, respectively. As shown in these tables, the confidence bounds for most estimated parameters span two to seven orders of magnitude, an indicator of large uncertainty associated with the estimated parameter values. The largest uncertainty occurs in Zones 1 and 3, where no observation wells are located. Other results, including the sensitivities of the parameters, will be further discussed in Subsection 3.1.10.

In summary, the current zonation approach based on the knowledge of large-scale geological features is able to reproduce the large-scale features of the measured water table. However, the current zonation approach is unable to produce satisfactory matches to the measured heads, particularly the heads measured near facilities. In addition, the estimated parameters for both aquifer thickness scenarios exhibit large uncertainties, indicating that the estimated parameter values are poorly resolved during the inversion process. Further refinement of the current K zone map is necessary to obtain more satisfactory matches to the measured heads, which is critical in accurately predicting the flow path of contaminant.

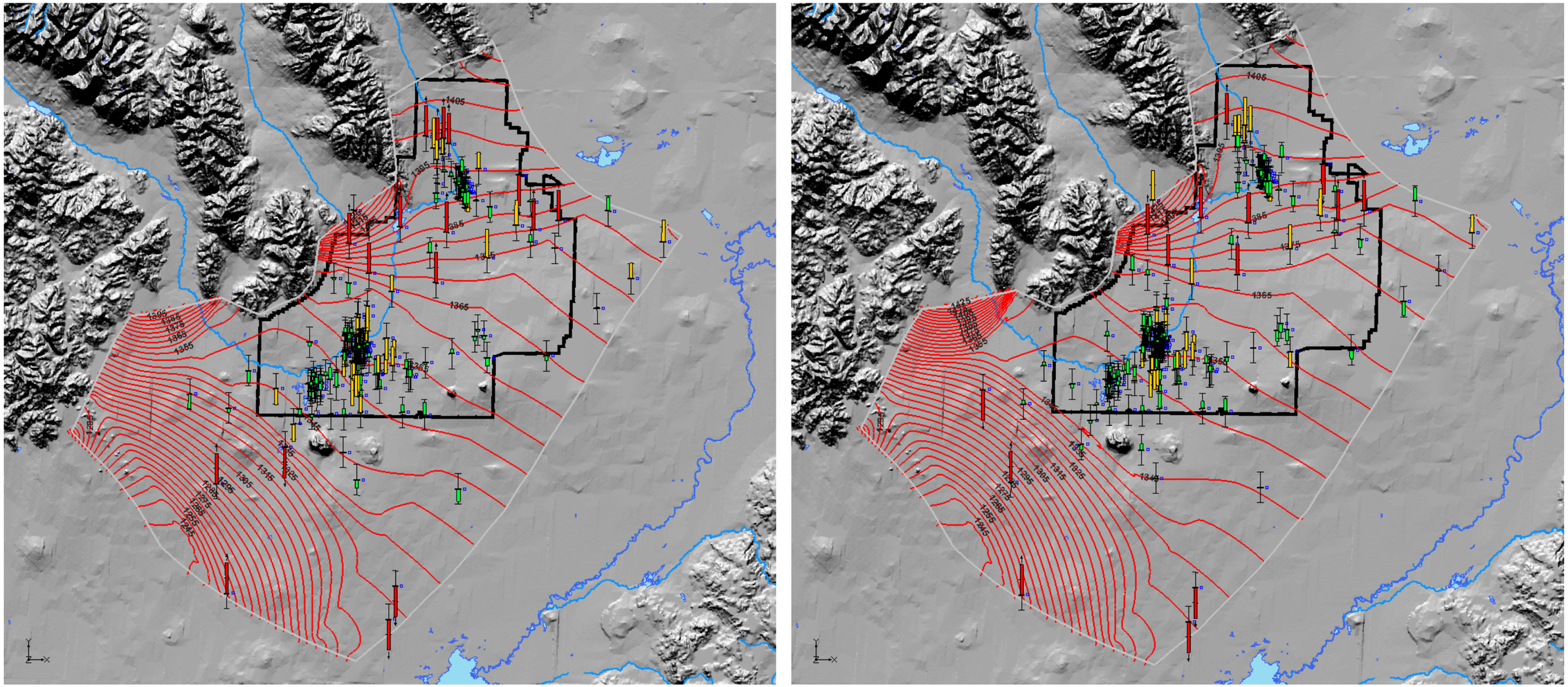

(a) (b)

Figure 3-9. Simulated head contour map and simulation residuals at observation wells for (a) the thick aquifer scenario and (b) the thin aquifer scenario (red is > 3 m, yellow is 2 to 3 m, and green is < 2 m).

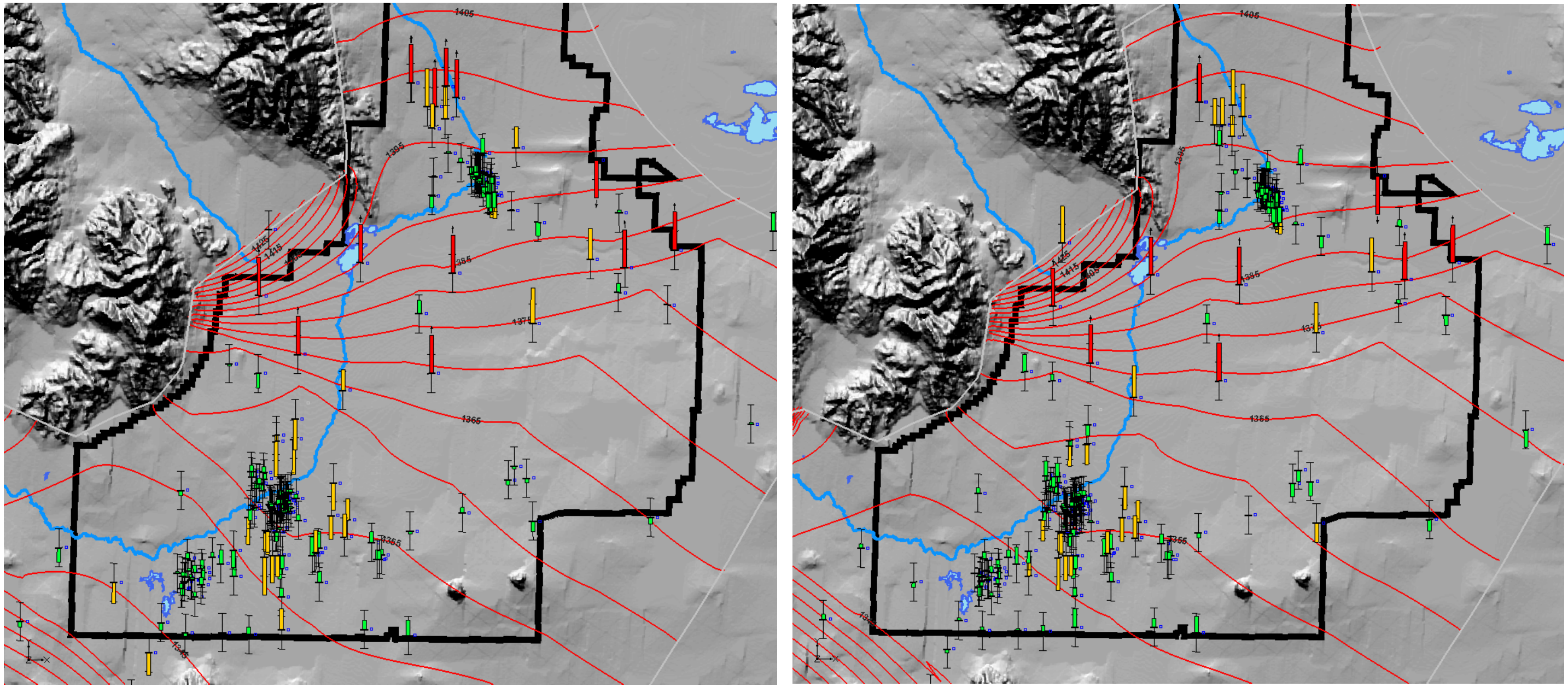

(a) (b)

Figure 3-10. Simulated head contour map and simulation residuals at observation wells inside the INL Site for (a) the thick aquifer scenario and (b) the thin aquifer scenario (red is > 3 m, yellow is 2 to 3 m, and green is < 2 m).

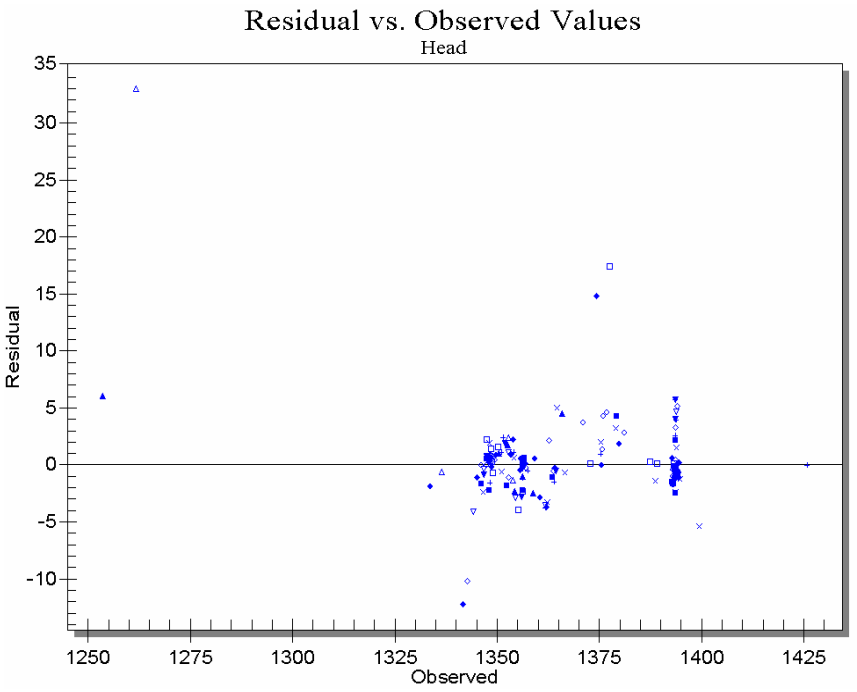

Mean Error: 0.285 m
Mean Abs. Error: 1.543 m
Root Mean Sq. Error: 3.363 m

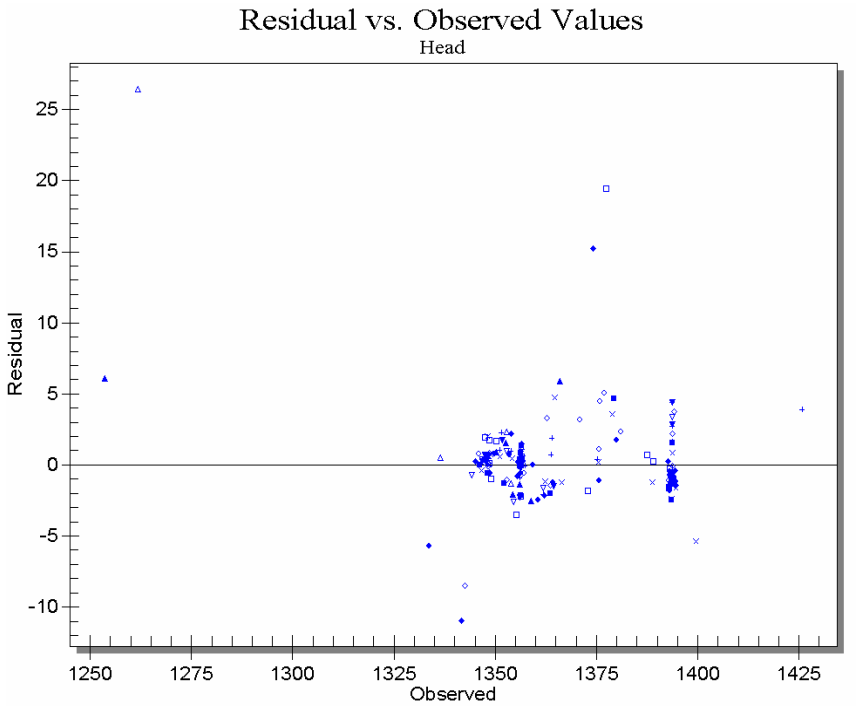

Mean Error: 0.240 m
Mean Abs. Error: 1.521 m
Root Mean Sq. Error: 3.069 m

Figure 3-11. Residual versus observed head values for the thick aquifer scenario (top) and the thin aquifer scenario (bottom).

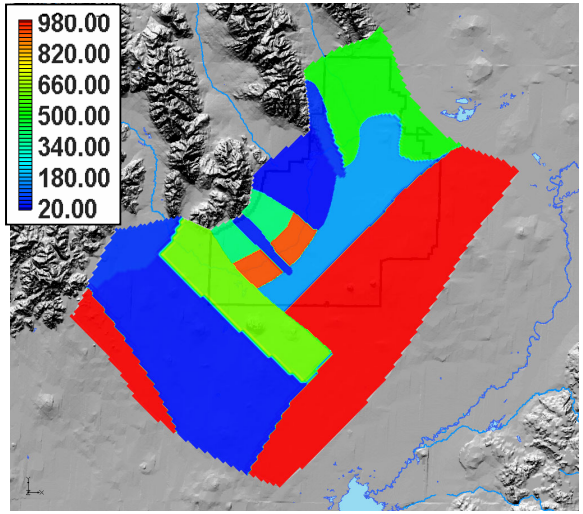

(a)

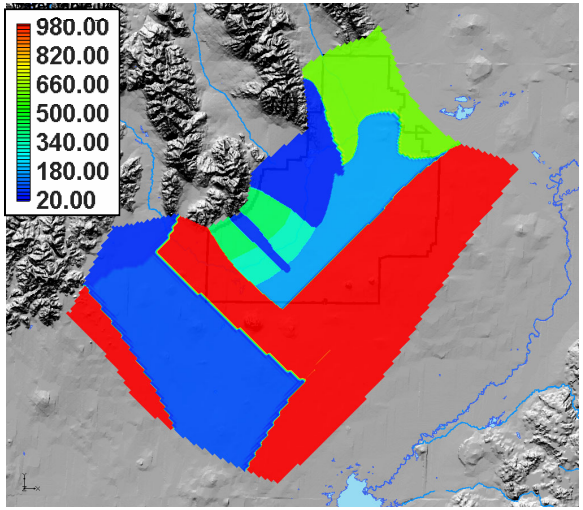

(b)

Figure 3-12. The estimated hydraulic conductivity field (in m/d) for (a) the thick scenario and (b) the thin scenario.

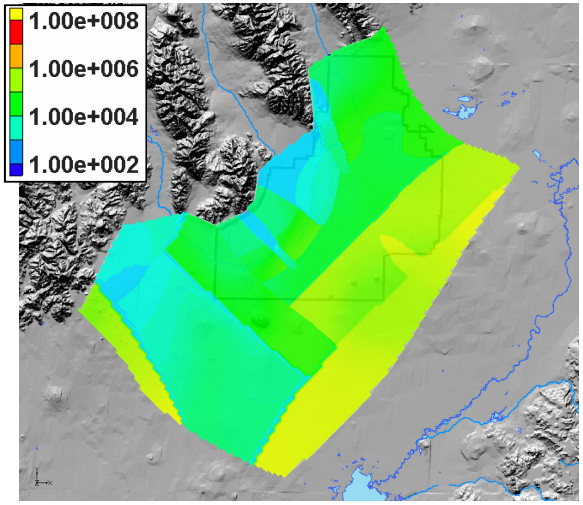

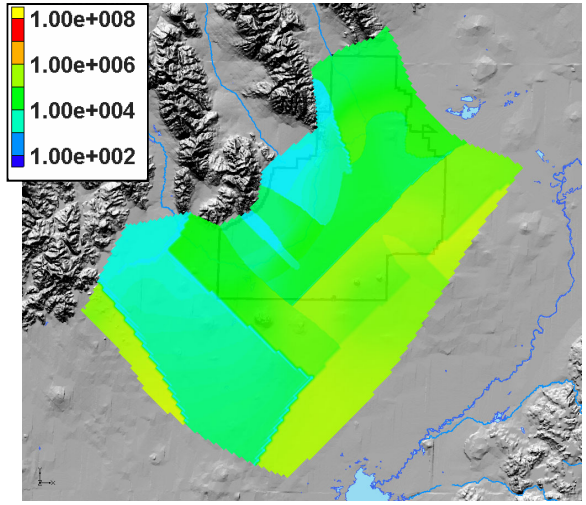

Figure 3-13. The estimated transmissivity field for the thick scenario (left) and the thin scenario (right).

Table 3-2. Estimated K values and associated 95% confidence bounds for the thick aquifer scenario.

Parameter[a]	Estimated Value (m/d)	Lower limit (m/d)	Upper limit (m/d)
Zone 3	8.73E+01	6.63E-05	1.15E+08
Zone 1	8.00E+03	4.05E-01	1.58E+08
Zone 4	6.01E+01	2.43E+01	1.49E+02
Zone 17	5.32E+02	6.70E+01	4.22E+03
Zone 18	8.90E+01	2.61E+00	3.04E+03
Zone 5	6.24E+02	2.30E+02	1.69E+03
Zone 13	4.87E+01	4.24E+01	5.59E+01
Zone 8	4.06E+02	1.91E+02	8.66E+02
Zone 9	7.15E+01	2.79E+01	1.83E+02
Zone 14	1.95E+02	3.06E+01	1.25E+03
Zone 10	9.23E+02	2.90E+01	2.94E+04
Zone 16	2.96E+03	3.83E+02	2.29E+04
Zone 19	6.56E+03	2.81E+02	1.53E+05
Zone 12	6.25E+03	7.73E+02	5.05E+04
Zone 20	6.10E+03	2.25E+02	1.65E+05

a. Zones 6 and 7 are tied with Zone 4; Zone 11 is tied with Zone 8; and Zone 15 is tied with Zone 10.

Table 3-3. Estimated K values and associated 95% confidence bounds for the thin aquifer scenario.

Parameter[a]	Estimated Value (m/d)	Lower Limit (m/d)	Upper Limit (m/d)
Zone 3	5.60E+01	2.04E-04	1.54E+07
Zone 1	8.00E+03	5.41E-03	1.18E+10
Zone 4	8.89E+01	4.05E+01	1.95E+02
Zone 17	6.19E+02	1.19E+02	3.21E+03
Zone 18	4.86E+01	3.59E+00	6.58E+02
Zone 5	1.15E+03	3.26E+02	4.06E+03
Zone 13	4.87E+01	4.37E+01	5.42E+01
Zone 8	4.05E+02	2.15E+02	7.63E+02
Zone 9	6.13E+01	1.39E+01	2.70E+02
Zone 14	1.75E+02	4.59E+01	6.70E+02
Zone 10	3.13E+02	3.74E+01	2.62E+03
Zone 16	2.02E+03	3.84E+02	1.07E+04
Zone 19	2.98E+03	1.06E+02	8.43E+04
Zone 12	3.27E+03	5.94E+02	1.79E+04
Zone 20	5.69E+03	3.42E+02	9.45E+04

a. Zones 6 and 7 are tied with Zone 4; Zone 11 is tied with Zone 8; and Zone 15 is tied with Zone 10.

3.1.9.2 Pilot-point Calibration Approach. An alternative inverse modeling approach, namely the pilot-point approach, was also implemented to calibrate the two-dimensional flow model using the same June 2004 head data. Figure 3-14 shows the distribution of the pilot points. The overall strategy of selecting the pilot points is to distribute the pilot points uniformly first and then refine the distribution in areas with a large head gradient. We also refine the distribution of pilot points near facilities such as INTEC, TAN, and RWMC, where observation wells are highly concentrated. A total of 265 pilot points is distributed within the domain. PEST estimates the K values at these pilot points and then interpolates the estimated K values to each active grid cell within the domain.

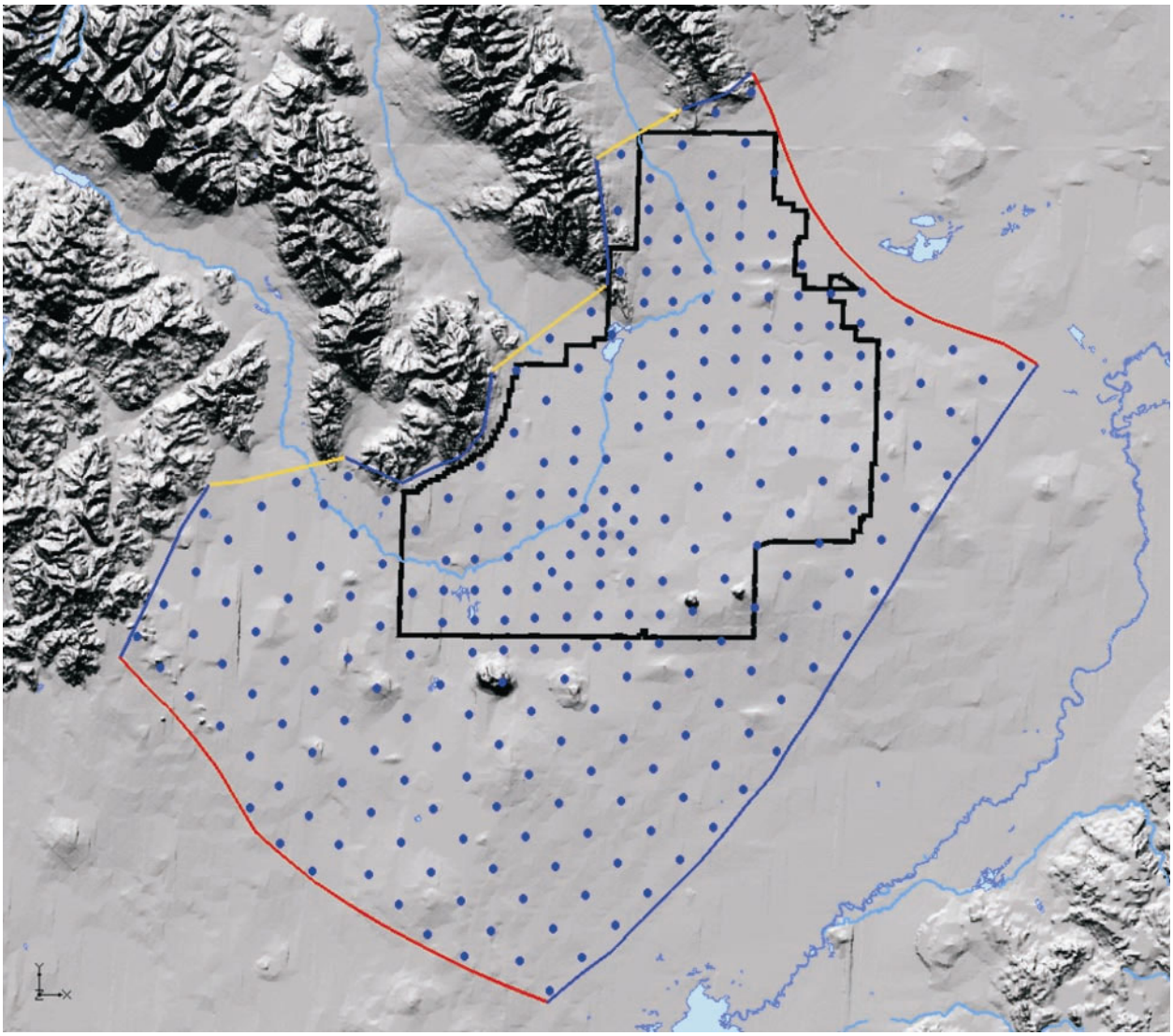

Figure 3-14. Distribution of pilot points.

Like the zonation approach, we have implemented the pilot-point method to both thick and thin aquifer scenarios. Initially, we planned to use the pumping test data shown in Figure 2-13 as a subset of pilot points with fixed K values in our two-dimensional flow model. However, we quickly realized that all of those pumping test were performed through limited intervals of wells and did not necessarily represent the averaged K values across the entire aquifer thickness. Furthermore, most tests are just single-well tests and have a limited influence area. Therefore, these test data also have a scale discrepancy

with the model grid size. For these reasons, we decided not to directly use these pumping test data as prior information during the calibration process. Instead, the range of K values inferred from pumping tests was used to set up the upper and lower limits of K value at each pilot point.

We tried to use the pumping test data to infer the variogram of the K field. However, the test data provide a poor estimate of the variogram or correlation structure. We also experienced some numerical instability problems during inversion when an arbitrary variogram was used to krige the K values at pilot points to each grid cell. Therefore, we decided to use a simpler inverse distance method to interpolate K values at pilot points. The nearest five points were selected for interpolation. Such an interpolation scheme yields stable solutions for the thick and thin aquifer scenarios.

Figure 3-15 shows the simulated hydraulic head contour map and residuals at all observation wells for thick and thin aquifer scenarios. Figure 3-16 shows the residuals of observation wells near INTEC and RWMC. As shown in these figures, most observation wells have mismatches less than 2 m (6.5 ft). Only a limited number of wells have mismatches over 2 m (6.5 ft) but still less than 3 m (9.8 ft). Compared with the previous zonation approach, the pilot-point approach not only reproduces the large-scale features of the measured groundwater table but also provides much more satisfactory matches to all measured heads. Figure 3-17 shows the residuals more clearly.

Figure 3-17 shows the residual distributions for the thick and thin aquifer thickness scenarios. Most observation wells have residuals less than 1 m (3.3 ft); only a limited number of wells have residuals greater than 1 m (3.3 ft). The thin aquifer scenario provides slightly better matches (smaller residuals) than the thick aquifer scenario, as manifested by the statistics of residuals shown in this figure.

Figure 3-18 shows the comparison of the estimated hydraulic conductivity maps between two aquifer thickness scenarios. Visual comparison between the two maps reveals some differences in the magnitude of the estimated K values for a number of zones. However, the overall K value distribution patterns are similar for both scenarios. Compared with the zonation approach, the estimated conductivity field using the pilot-point approach looks more realistic and varies more smoothly while still allowing variations at different scales. One interesting point is that the estimated field starts to reflect some known large-scale geological structures.

Figure 3-19 shows the transmissivity fields that result from multiplying the estimated K field by the effective aquifer thickness. Like the zonation approach, the transmissivity fields for both aquifer thickness scenarios look rather similar. This is in agreement with the fact that for a horizontal two-dimensional flow model, the transmissivity field is the primary parameter that determines the head distributions. Although we have used a two-dimensional model with variable aquifer thickness, only transmissivity really matters in terms of affecting simulated head contour maps.

Like the zonation approach, PEST also automatically calculates the confidence bounds of the estimated K value for each pilot point, an indicator of parameter uncertainties. Figure 3-20 shows the estimated K value and corresponding 95% confidence bound of each pilot point for both thick and thin aquifer thickness scenarios. Compared with the zonation approach, the confidence bounds of the estimated K values are much narrower, a strong indicator that the estimated parameter field is well resolved during the inversion process.

In summary, compared with the previous zonation approach, the pilot-point approach is not only able to provide satisfactory matches to all of the measured heads and reproduce large- and local-scale features of the measured groundwater table but is also able to extract more heterogeneity information at various scales using the same amount of measured information. The ability of the model to accurately reproduce both large- and small-scale features of the measured groundwater table is particularly critical to

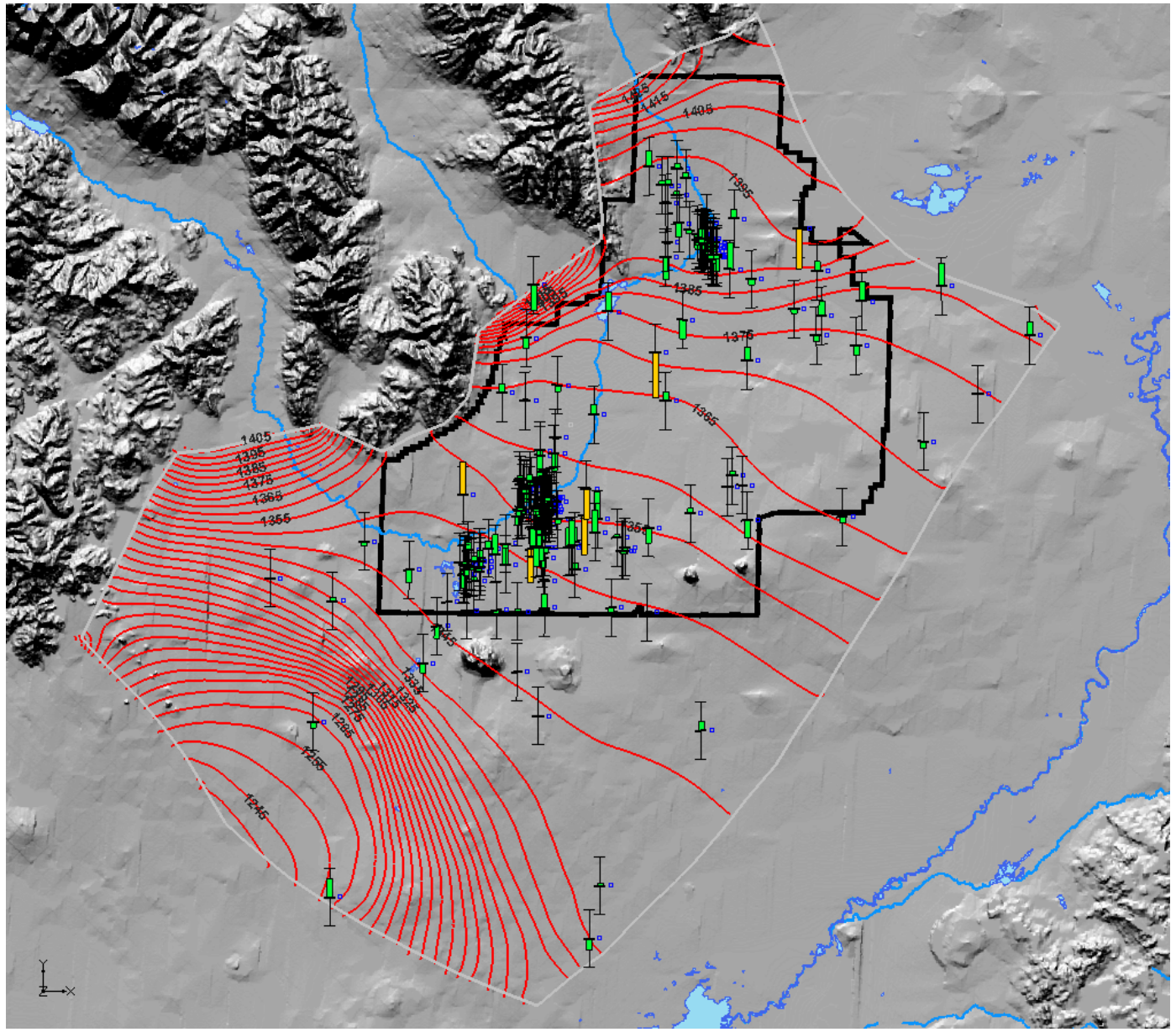

(a)

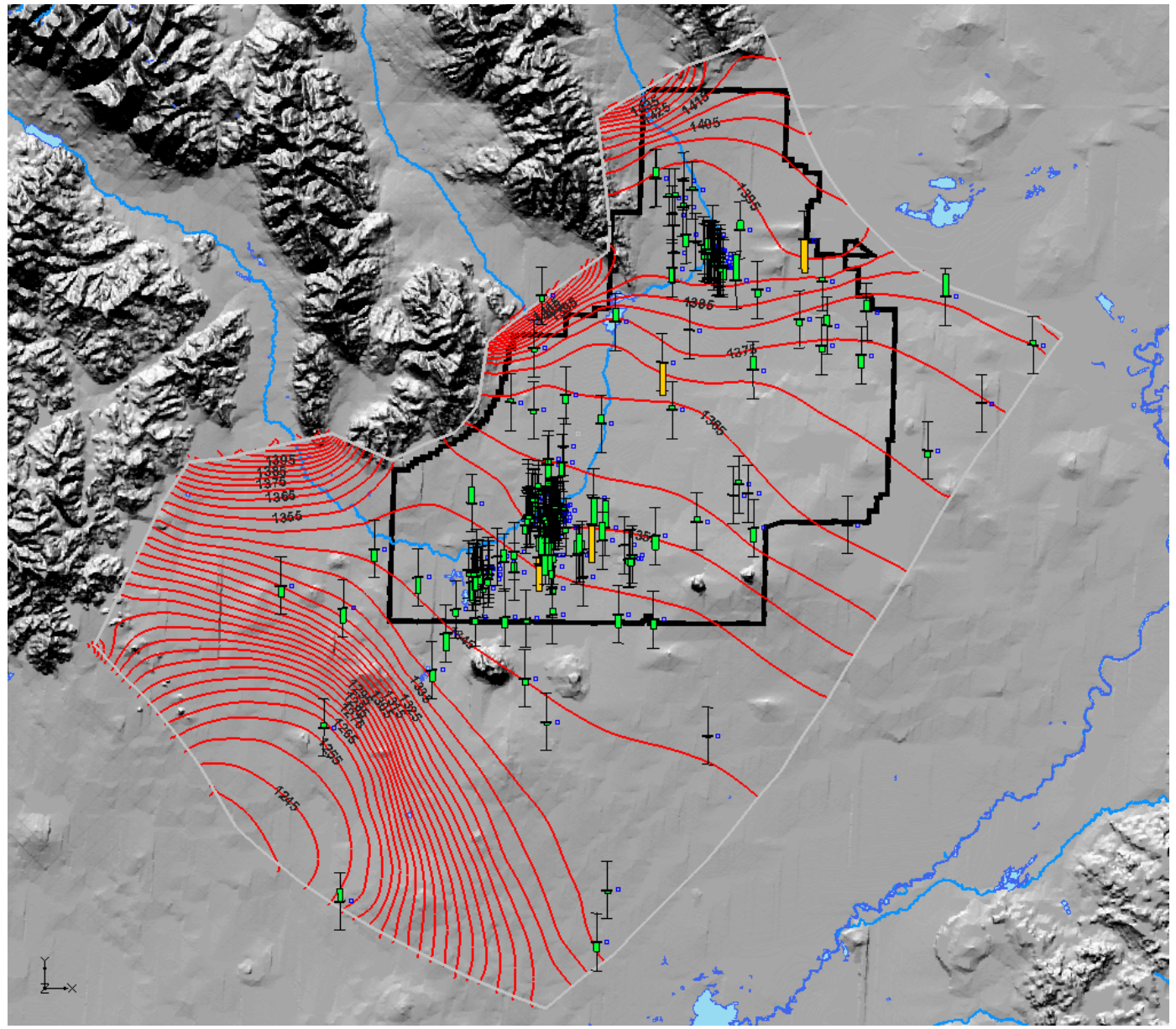

(b)

Figure 3-15. Simulated head contour map and simulation residuals at observation wells for (a) the thick aquifer scenario and (b) the thin aquifer scenario (red is > 3 m, yellow is 2–3 m, and green is < 2 m).

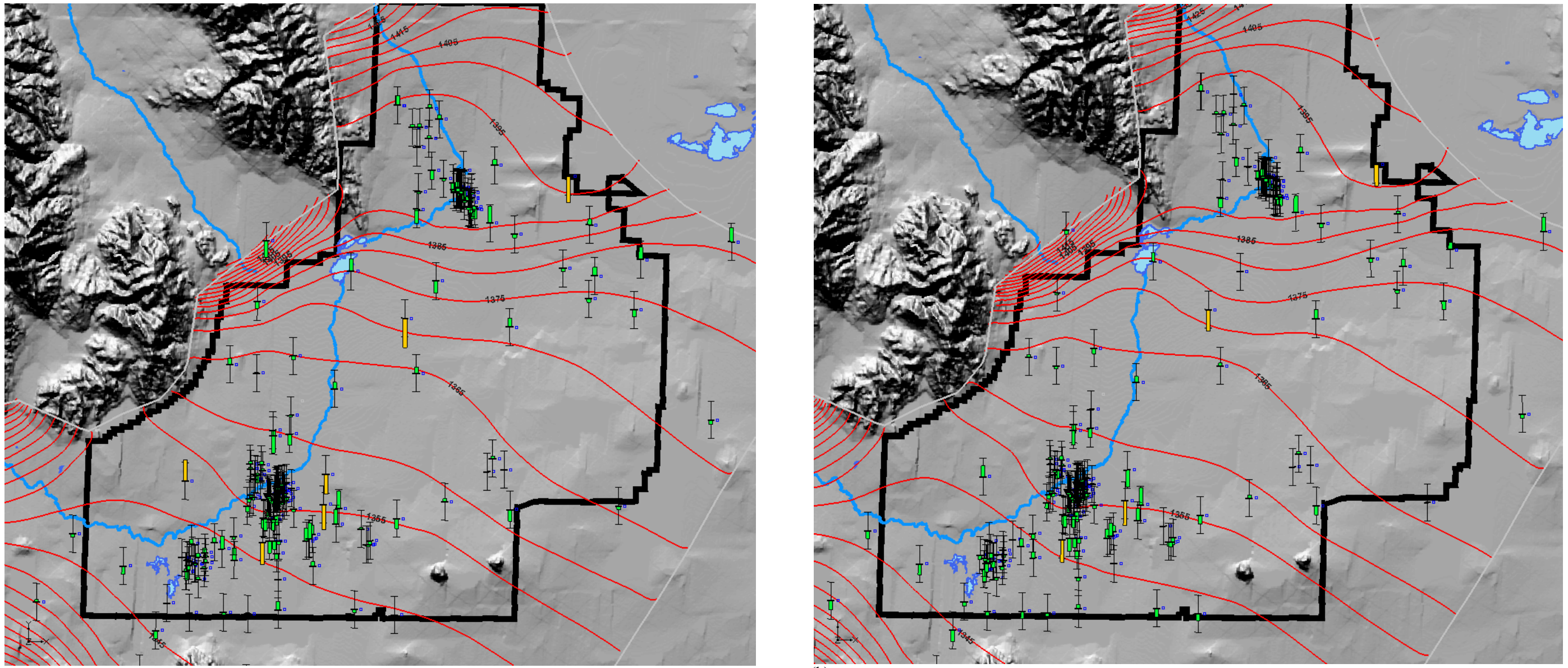

(a) (b)

Figure 3-16. Simulated head contour map and simulation residuals at observation wells inside INL Site for (a) the thick aquifer scenario and (b) the thin aquifer scenario (red is > 3 m, yellow is 2–3 m, and green is < 2 m).

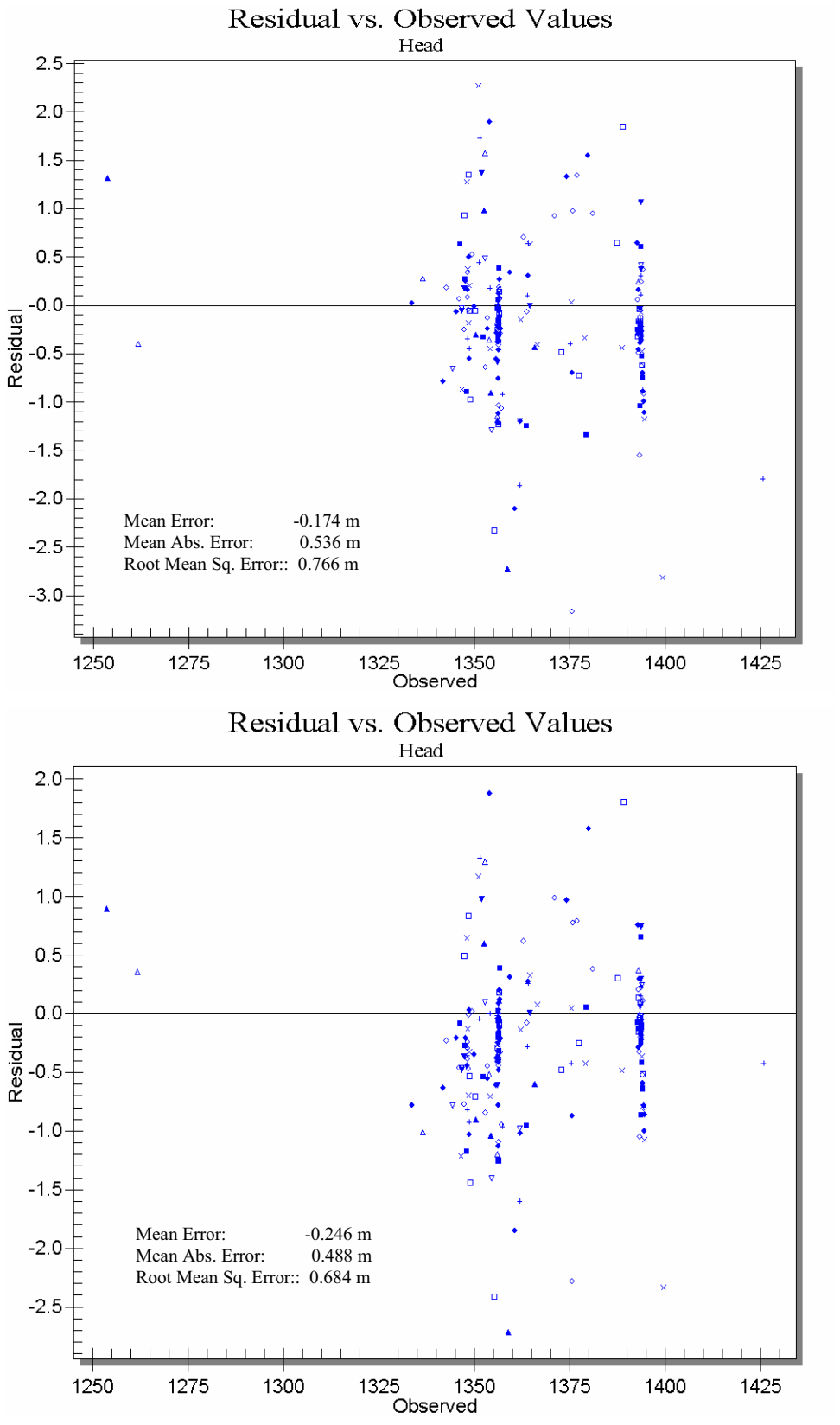

Figure 3-17. Residual versus observed head values for the thick aquifer scenario (top) and the thin aquifer scenario (bottom).

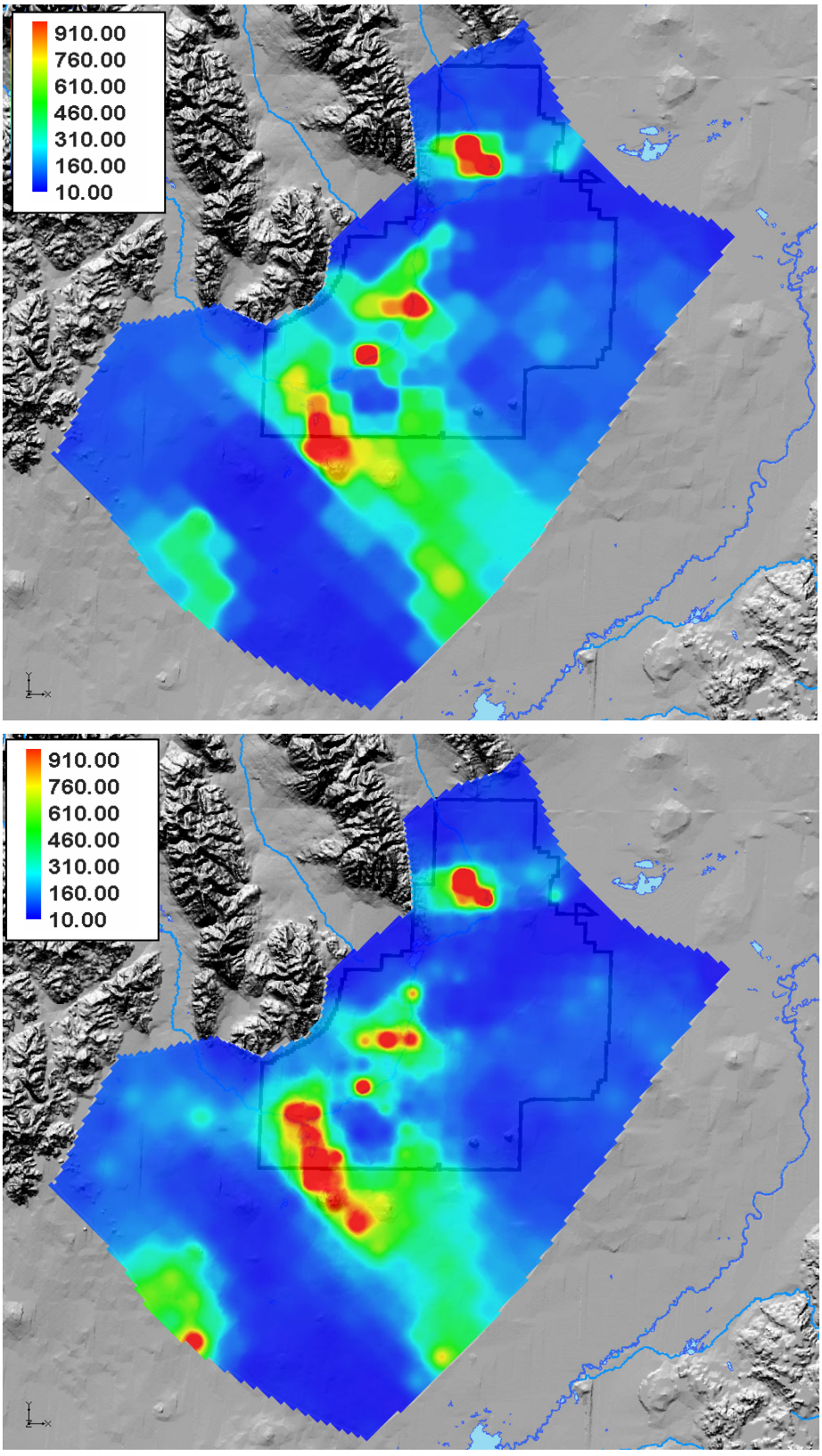

Figure 3-18. The estimated hydraulic conductivity field (in m/d) for the thick scenario (top) and the thin scenario (bottom).

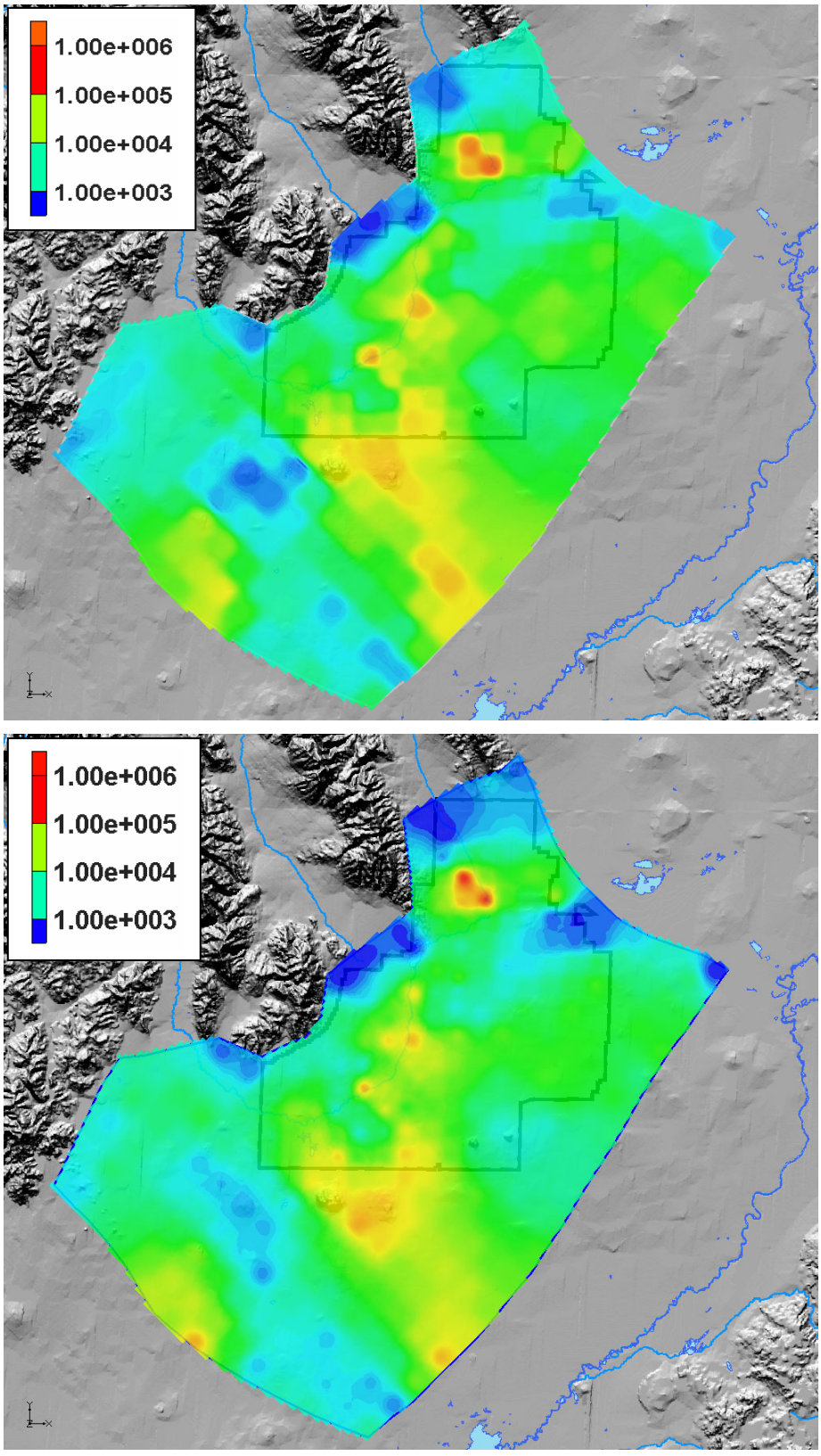

Figure 3-19. The calculated transmissivity field for the thick scenario (top) and the thin scenario (bottom).

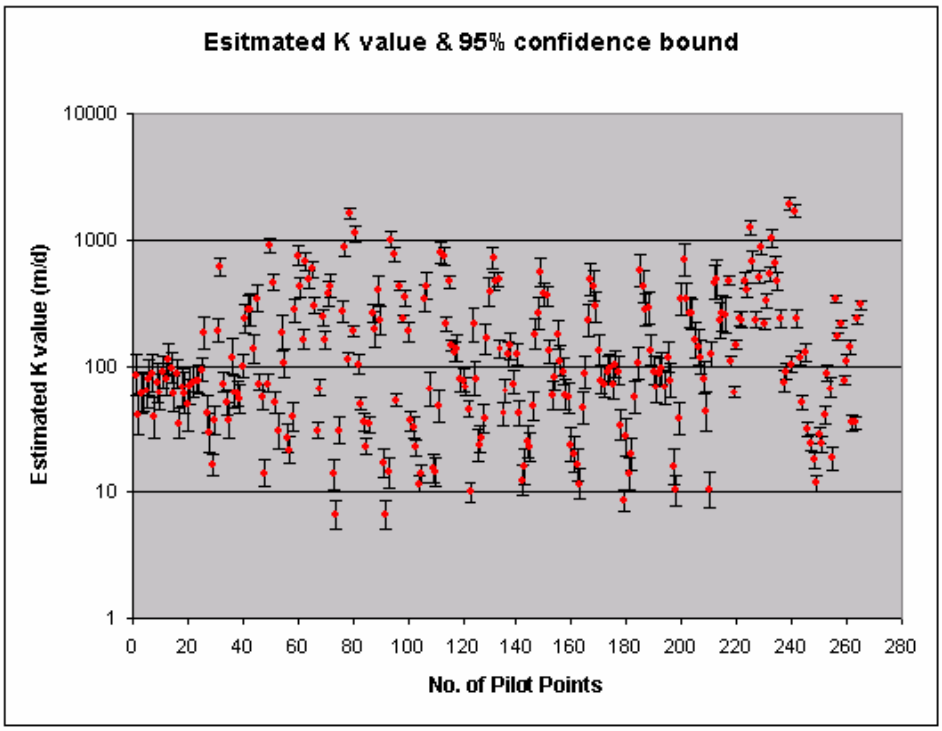

(a)

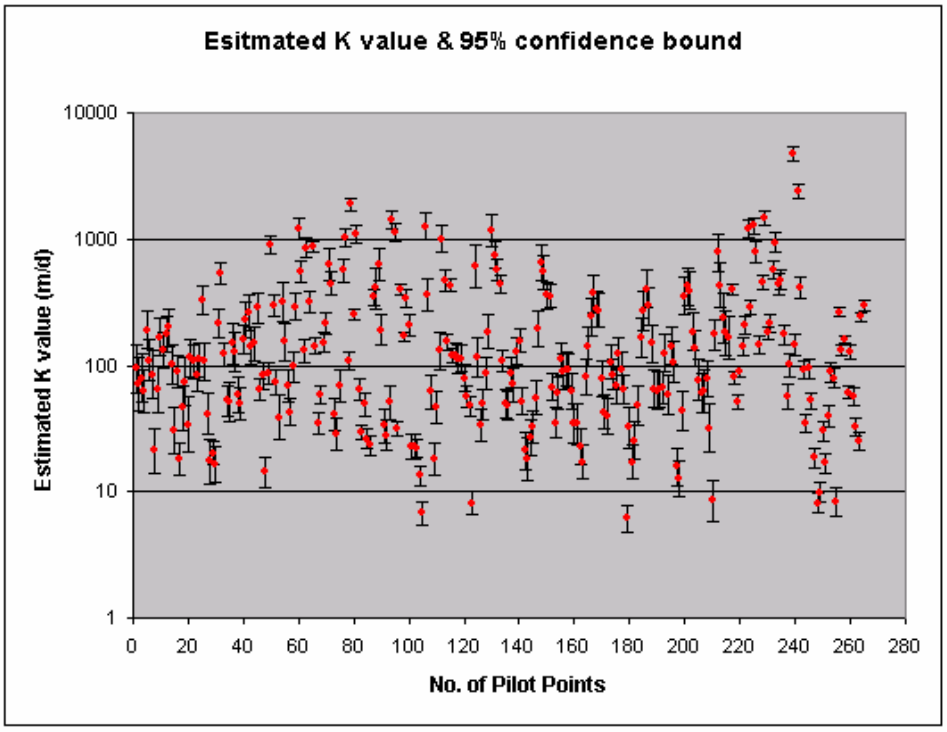

(b)

Figure 3-20. The estimated K values and corresponding 95% confidence bounds of pilot points for (a) the thick aquifer scenario and (b) the thin aquifer scenario.

accurately predict the contaminant migration path inside the INL Site boundaries. In addition, the estimated parameter fields for both aquifer thickness scenarios exhibit low uncertainties, indicating the estimated parameter values are well resolved during the inversion process. All of the results shown previously indicate that the pilot-point approach outperforms the zonation approach.

3.1.9.3 Coupled Zonation/Pilot-point Calibration Approach. The pilot-point approach provides satisfactory results in terms of a better match to the observed heads and more reliable estimates of the parameter field, but this approach is often criticized for not honoring the large-scale geological features. Reliability in this context means the likelihood of being a unique solution. Therefore, we also implemented the coupled zonation/pilot-point approach to calibrate the two-dimensional flow model. In this approach, we still use zones to honor the large-scale geological features and then distribute an independent set of pilot points to each zone to allow sub-zone heterogeneity to be modeled. Ideally, the coupled approach should provide a better result than those for either the zonation approach or pilot-point approach.

A simulation with the coupled zonation/pilot-point approach was carried out in which the geologic subdomains were significantly simplified. The lumping of the subdomains was determined by comparing the June 2004 water table map with the full set of subdomains. Areas where the water table showed no significant response to the subdomain boundaries were found to be hydrogeologically indistinguishable from the surrounding subdomains and were therefore lumped together. Figure 3-21a shows the subdomain map overlain with the interpolated water table contours. One can see that a number of the geologic subdomains are, in effect, invisible to the head contours. Figure 3-21b shows the geologic subdomains lumped into five hydrogeologic complexes. The major geologic features are preserved in the hydrogeologic complexes, such as the Arco Rift, which is contained in the Arco Rift complex that runs completely across the center of the model domain. Each lumped zone contains at least a number of observation wells. In this manner, we honor the geologic constraints on the flow system while numerically capturing the complex hydrogeology. Figure 3-21c shows the individual sets of the pilot points for individual lumped zones. Each zone clearly has its own population and density of pilot points. Interpolation of K values is allowed within each zone but not across zone boundaries. Due to the time limit, we only implemented this approach for the thin aquifer scenario. We expect the thick scenario will yield similar results, as shown previously for the zonation approach and pilot-point approach.

Figure 3-22a shows the simulated hydraulic head contour map and residuals at all observation wells, and Figure 3-22b shows the residuals of observation wells inside the INL Site. As shown in these figures, most observation wells have mismatches of less than 1 m. A few wells have mismatches of about 2 m. Compared with the previous zonation approach and pilot-point approach, the coupled approach seems to provide the best matches to the observed heads, particularly near INTEC.

Figure 3-23 shows the residual distributions. Most observation wells have residuals of less than 1 m (3.3 ft); only a limited number of wells have residuals greater than 1 m (3.3 ft). The statistics of residuals shown in this figure reveal that the coupled approach does provide a slightly better match to the measured heads compared with the pilot-point approach.

Figure 3-24 shows the estimated hydraulic conductivity field generated by the coupled zonation/pilot-point approach. The estimated K field shows overall patterns similar to those shown in the K field estimated by the pilot-point approach. However, a number of discontinuities in the K value exist across the zone boundaries. Sharp changes in the K value across those zone boundaries are clearly shown across the entire domain. Compared with the K field estimated by the pilot-point approach, in which the K value varies smoothly, it is difficult to judge which parameter field is more reliable (or realistic) via visual comparison.

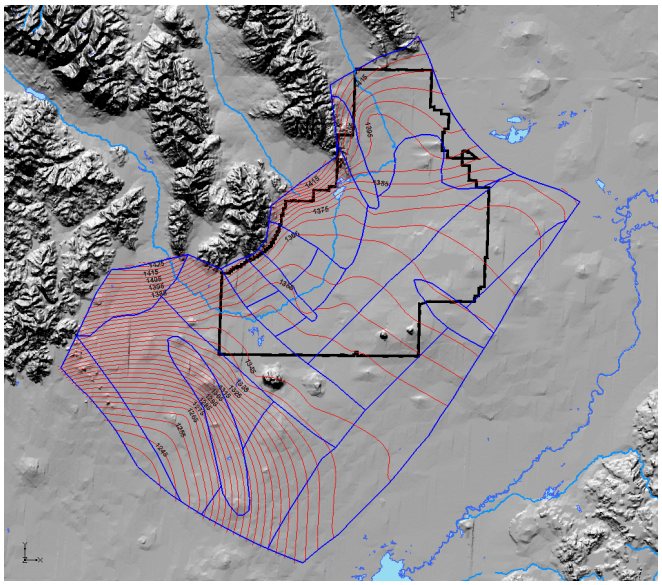

(a)

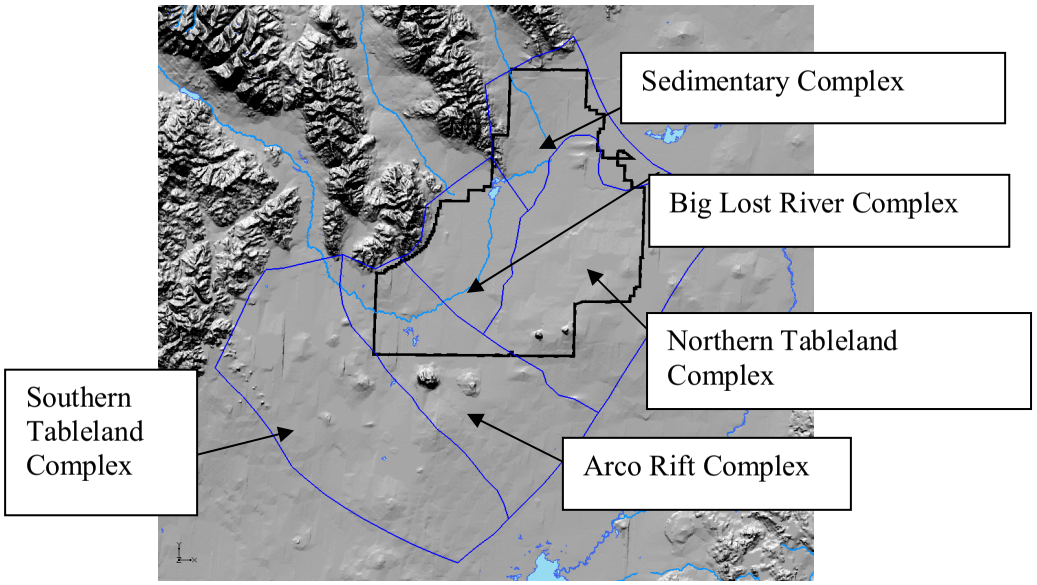

(b)

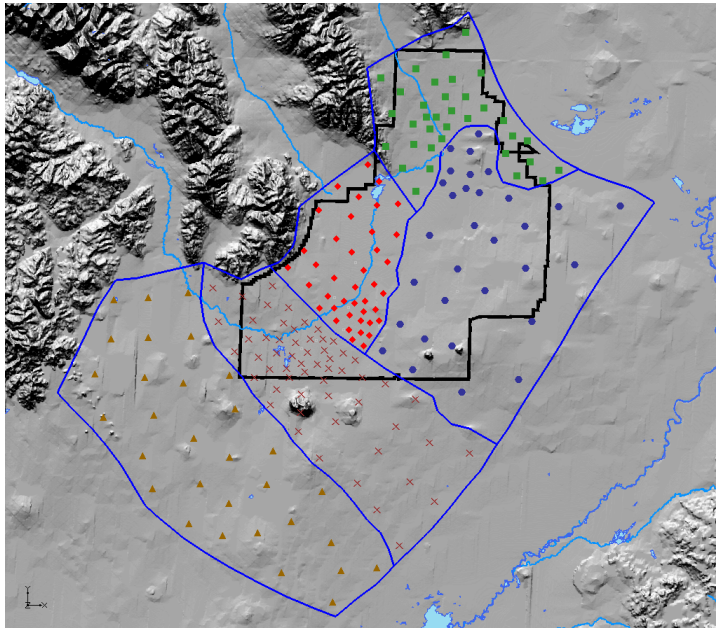

(c)

Figure 3-21. (a) Geologic subdomains overlain with the June 2004 water table (5-m contour interval), (b) the resulting "lumped" subdomains or hydrogeologic complexes, and (c) the pilot-point distributions for individual zones.

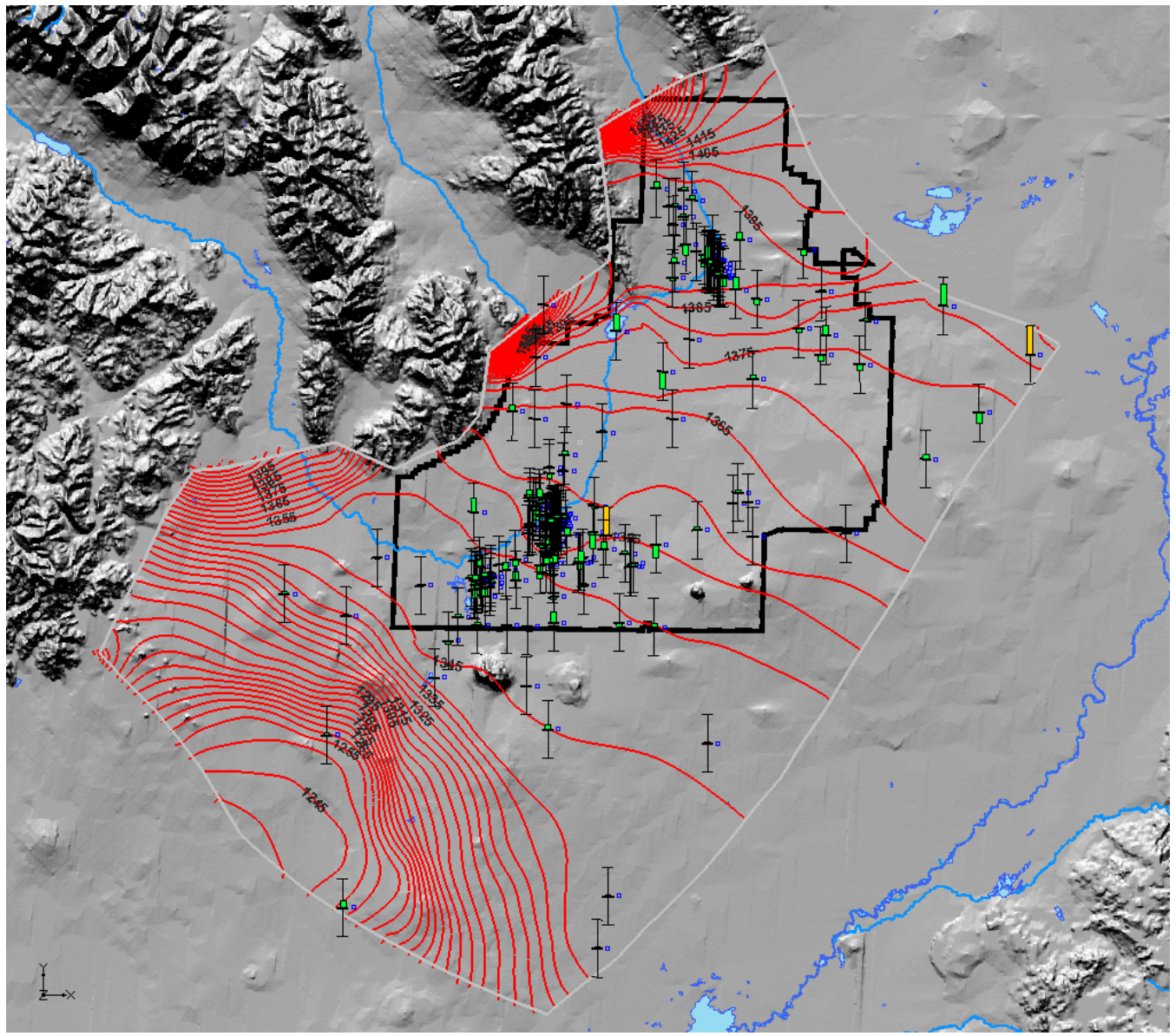

(a)

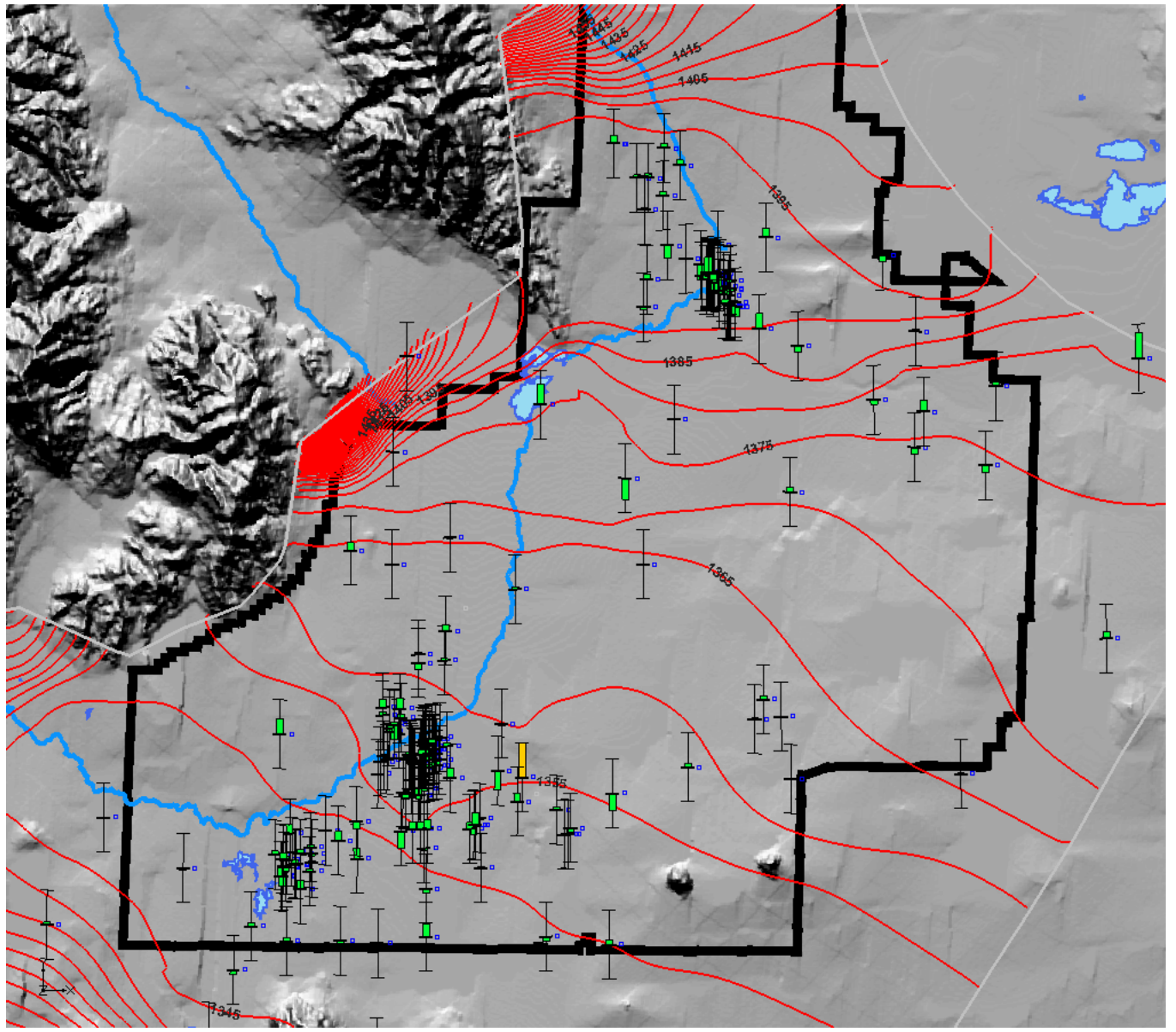

(b)

Figure 3-22. Simulated head contour map and simulation residuals at observation wells for the “thin” aquifer scenario for (a) the whole domain and (b) the central portion of the domain (red is > 3 m, yellow is 2–3 m, and green is < 2 m).

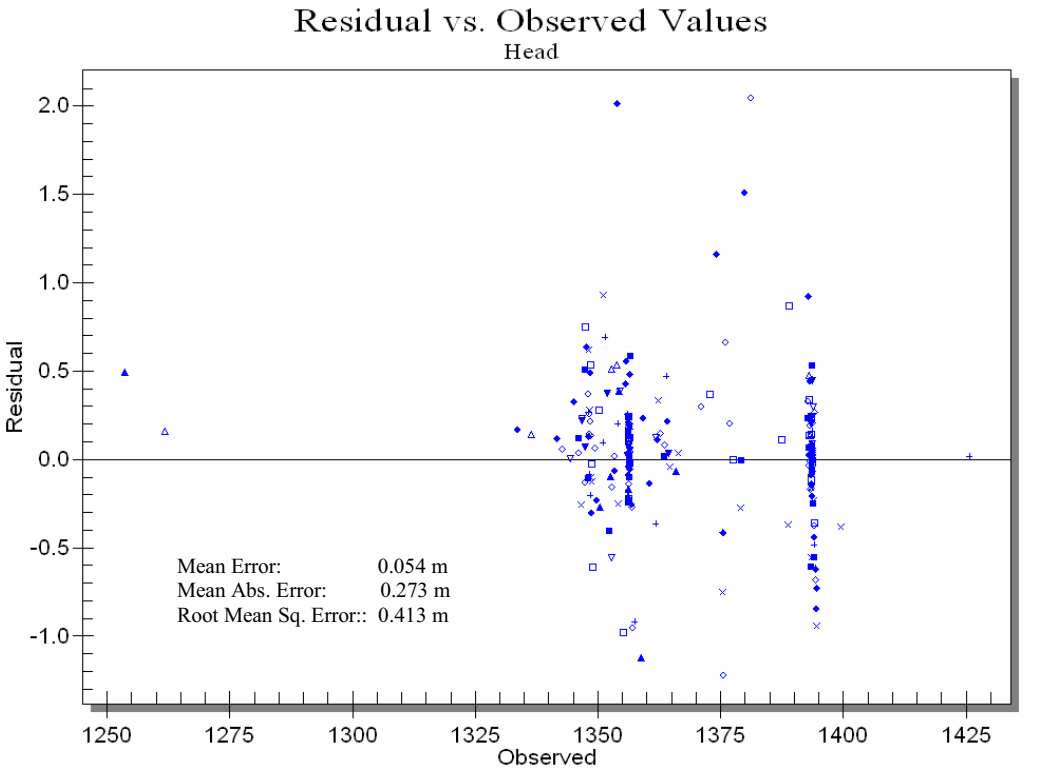

Figure 3-23. Residual versus observed head values.

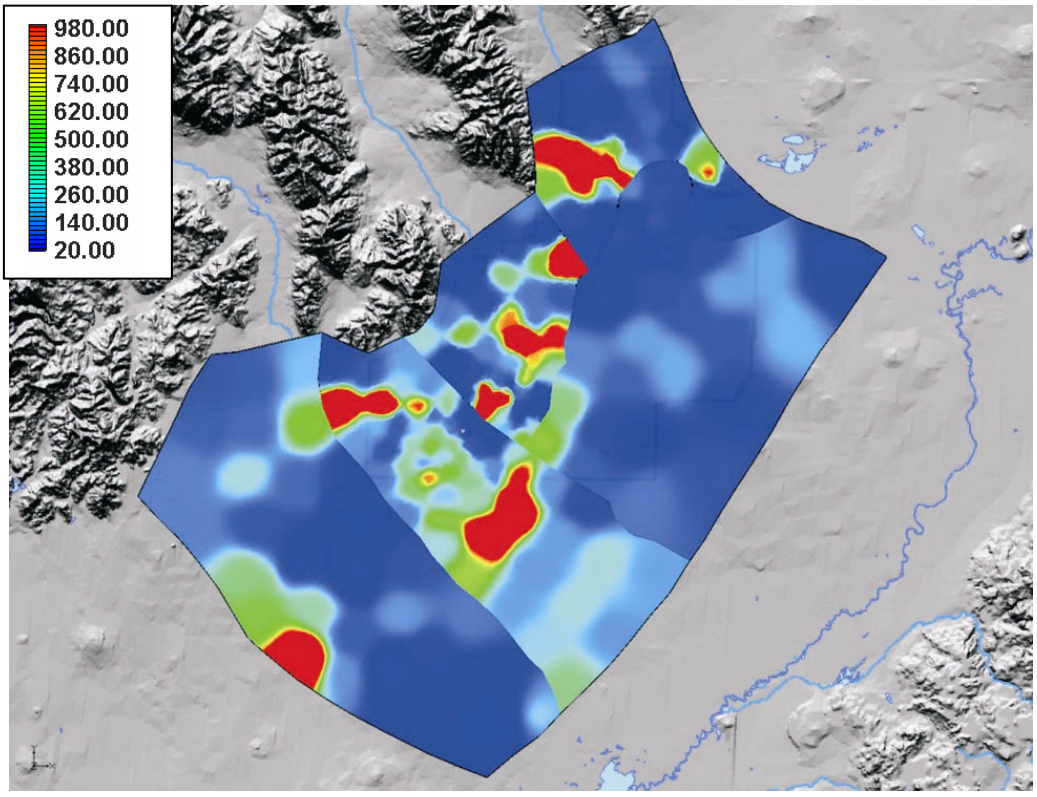

Figure 3-24. The estimated hydraulic conductivity field (m/d).

Like the previous two approaches, we also investigated the reliability of the estimated K field through the parameter confidence bounds (or uncertainty). PEST also automatically calculates the parameter confidence bounds for the coupled zonation/pilot-point approach. Figure 3-25 shows the 95% confidence bounds of the estimated parameter at each pilot point. Many parameters have confidence bounds spanning two to six orders of magnitude. Some parameters have even higher confidence intervals, a strong indicator that the estimated parameter field is much less resolved than that estimated by the pilot-point approach. The large confidence intervals shown in Figure 3-25 also indicate that it is highly likely that the inverse procedure tends to have a non-unique solution. Although the coupled approach provides the best match to the observed heads among all three calibration approaches, the estimated hydraulic conductivity is much less reliable than that obtained by the pilot-point approach.

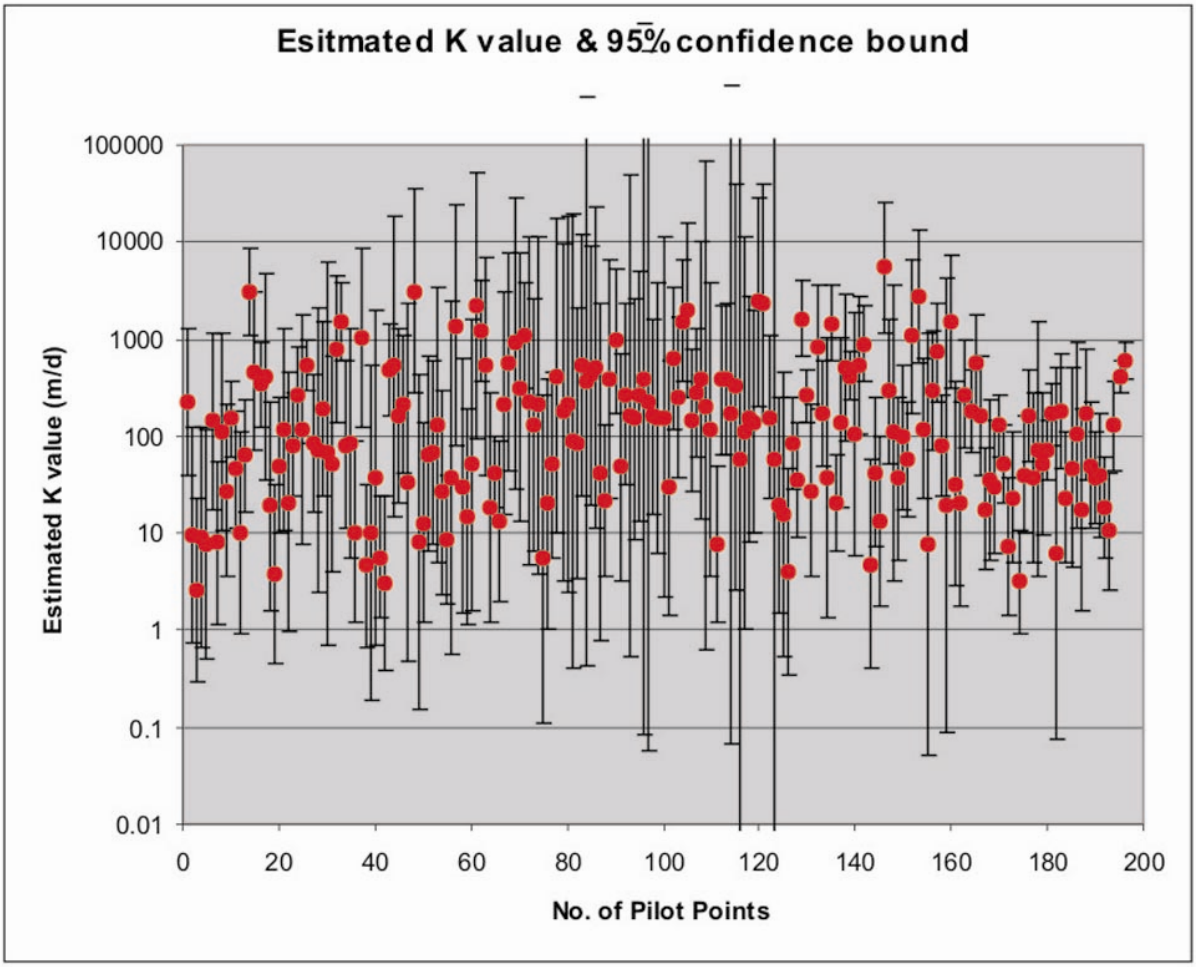

Figure 3-25. The estimated K values and corresponding 95% confidence bounds of pilot.

3.1.10 Sensitivity Analysis

The following subsections summarize the sensitivity studies of the model with respect to hydraulic conductivity values, boundary conditions (tributary underflows), and recharge (including homogeneous and inhomogeneous infiltration of precipitation).

The two-dimensional groundwater flow model is a useful tool for evaluating regional flow in the vicinity of the INL Site, but results inferred from the model must be evaluated with respect to their

sensitivity to various parameters, primarily the hydraulic conductivity, the tributary groundwater underflow rate, and the precipitation recharge rate. Large variations in the hydraulic conductivity field, the underflow rate, and spatial distribution of precipitation recharge rate have been observed or inferred. In the subsections below, we report the sensitivity study of the two-dimensional flow model with respect to the following important model inputs:

- Hydraulic conductivity values
- Estimated underflow rates from the tributary drainage basins
- Homogeneous versus heterogeneous precipitation infiltration.

Because we concluded that the pilot-point approach provides the best results in terms of smallest residuals and most reliable parameters, we used the pilot-point approach for the thin aquifer scenario as our base case for sensitivity studies.

3.1.10.1 Sensitivity Study for the Hydraulic Conductivity. The traditional sensitivity study of the flow model with respect to the hydraulic conductivity is to change the K value by a small amount (i.e., 1%) and then rerun the model and calculate a so-called coefficient of variation by dividing the changes of the simulated heads with the changes of the K value. In our pilot-point approach, however, a total of 265 pilot points were used. Thus, the traditional way to carry out the sensitivity study requires a tremendous amount of effort. We propose an alternative way to carry out the sensitivity study. The composite sensitivity, which basically measures the sensitivity of the objective function (sum of weighted residuals), is calculated with respect to the K value at a particular pilot point. PEST automatically calculates the composite sensitivities during the inversion process.

Figure 3-26 shows the composite sensitivity map of hydraulic conductivity to the objective function. The hydraulic conductivity values in the southern portion of the domain, south of the INL Site boundary, are most sensitive to the simulated heads. One possible reason for the higher composite sensitivity near this area is that this area functions like a gate close to the groundwater exit of the model domain; therefore, small changes in K values in this area will have large impacts on the simulated heads in the central and northern portions of the model domain. Unfortunately, this area only has a few wells to constrain the inversion process. Large uncertainties of K values exist in this area, which eventually will propagate to uncertainties associated with contaminant transport prediction. Inside the INL Site boundaries, the composite sensitivity is fairly uniformly distributed, except for a relatively more sensitive area near the Little Lost River tributary basin.

3.1.10.2 Sensitivity Study for the Underflow Recharge Rate. The two-dimensional flow model includes three underflow recharge boundaries along the west boundary of the model domain. As discussed previously, large uncertainties associated with these estimated fluxes are also expected. We carried out sensitivity studies on these estimated fluxes by changing the estimated flux with a small amount (1%) and calculating the sensitivity coefficients by dividing the corresponding changes of the simulated heads in all grid blocks with the change of the underflow rate. Figures 3-27 through 3-29 are the sensitivity coefficient maps of the simulated heads to the underflow rates from the Big Lost River, Little Lost River, and Birch Creek drainage basins, respectively. All three sensitivity maps are plotted using the same color scale for convenience of comparison.

Visual comparison among these sensitivity maps (using the same color bar scale) immediately reveals that the simulated heads near Birch Creek drainage basin are mostly sensitive to the underflow recharge rate of that basin. In addition, all underflow rates are relatively more sensitive to the heads near drainage basins, but the sensitivity quickly fades away inside the domain. The underflow rate of the Little Lost River drainage basin has slightly higher sensitivity inside the INL Site boundaries than those

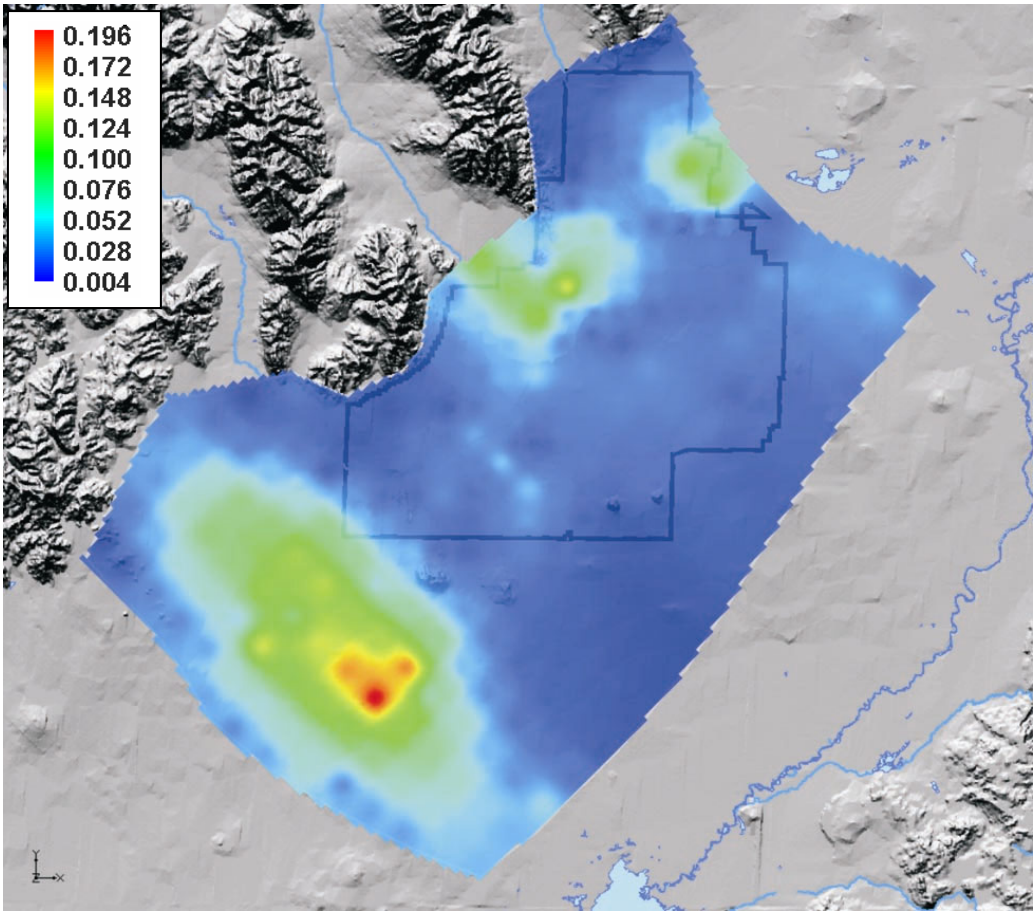

Figure 3-26. Spatial distribution of the composite sensitivity of hydraulic conductivity to the simulated heads.

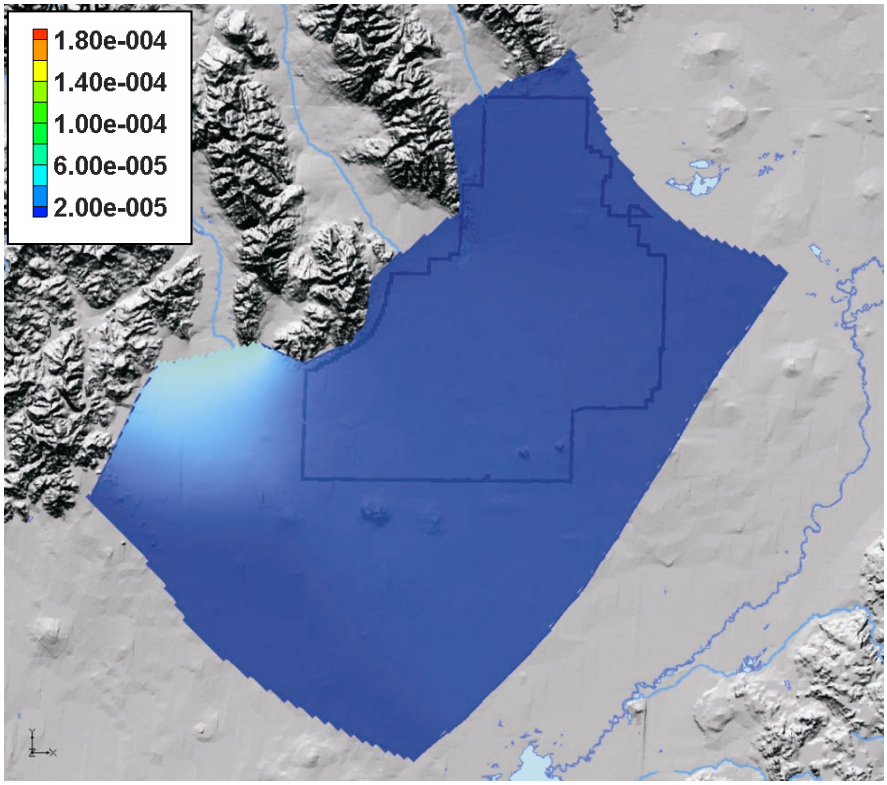

Figure 3-27. Sensitivity of the simulated heads to the underflow rate of the Big Lost River drainage basin.

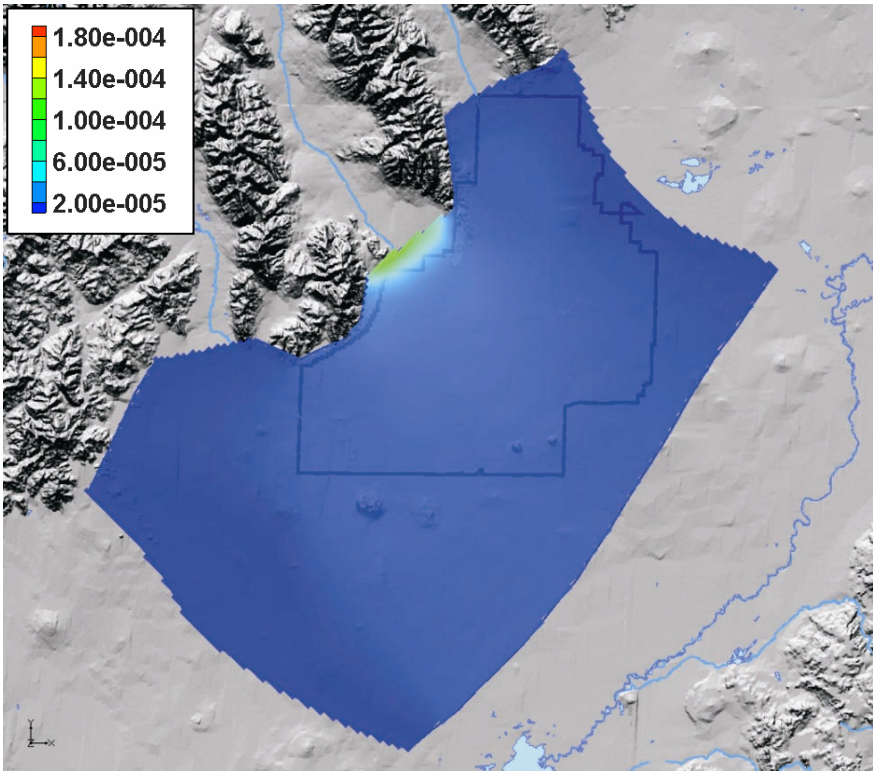

Figure 3-28. Sensitivity of the simulated heads to the underflow rate of the Little Lost River drainage basin.

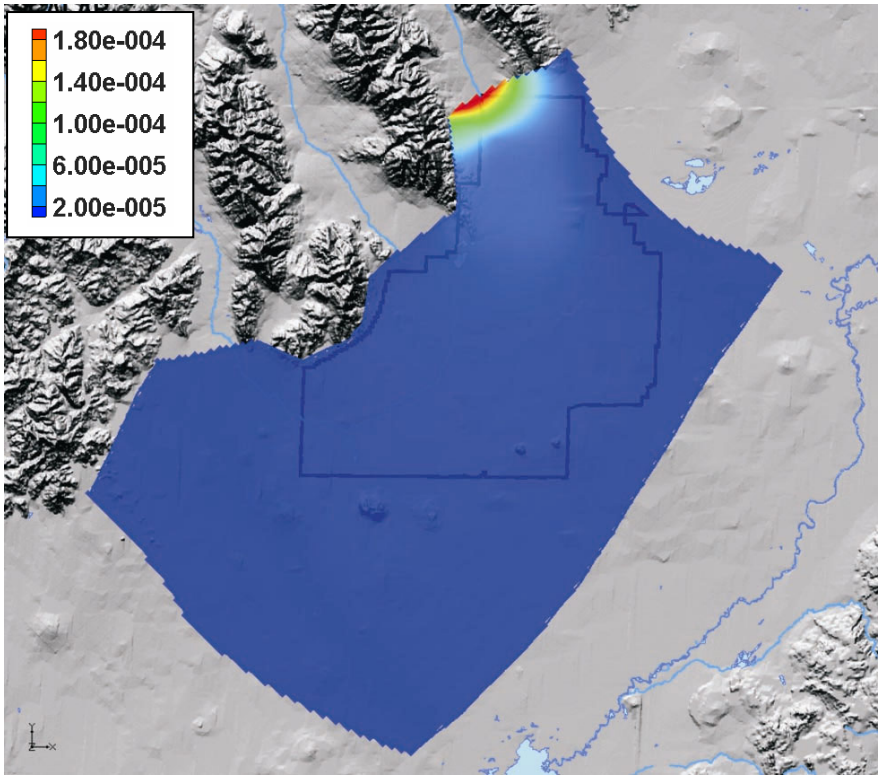

Figure 3-29. Sensitivity of the simulated heads to the underflow rate of the Birch Creek drainage basin.

of the Big Lost River and Birch Creek drainage basins. Visual comparison of these sensitivity maps also indicates that the simulated heads inside the INL Site boundaries, particularly the heads in the southern portion of the site, are relatively insensitive to the underflow rates. More importantly, these heads are almost equally sensitive to all three underflow rates. This has an important implication for the future transport simulations: the uncertainties associated with the flux estimates will not affect (or propagate to) transport predictions, because the simulated heads inside the INL Site, particularly in the southern portion of the site, will rise or fall in a uniform way when the estimated fluxes increase or decrease.

As shown in Figure 3-29, the simulated heads in the northern portion of the INL Site, particularly in the TAN area (or WAG 1), are more sensitive to the underflow rate of the Birch Creek drainage basin than are the heads in the southern portion of the site. However, the simulated heads in the southern portion of the site are almost equally sensitive to the underflow rate of the Birch Creek drainage basin.

To more quantitatively investigate the sensitivity of the underflow rates to the simulated heads inside the INL Site boundaries, we present Table 3-4, which shows the sensitivity coefficient of the heads at the approximate centers of all nine INL Site facility areas. The numbers in this table are consistent with the previous sensitivity maps and support our previous conclusions regarding the sensitivity of the underflow rates.

3.1.10.3 Study of Sensitivity to the Precipitation Recharge. In the current two-dimensional flow model, a uniform precipitation recharge rate of 1.95×10^{-5} m/d (6.39×10^{-5} ft/d) was applied to the entire domain. This subsection presents the results of the sensitivity study on the precipitation rate.

We focus on the heterogeneous infiltration scenario by correlating the infiltration rate with the surface soil/rock types and record the changes of the simulated heads. Figure 3-30 shows the surface

Table 3-4. The sensitivities of heads at the facility centers to the underflow rates.

	WAG 1 (TAN)	WAG 2 (RTC)	WAG 3 (INTEC)	WAG 4 (CFA)	WAG 5 (PBF/ARA)	WAG 6 (EBR/BORAX)	WAG 7 (RWMC)	WAG 8 (NRF)	WAG 9 (MFC)
Big Lost River	2.64e-6	8.75e-6	8.65e-6	8.83e-6	8.51e-6	1.0e-5	1.1e-5	7.75e-6	6.56e-6
Little Lost River	1.1e-5	1.6e-5	1.6e-5	1.5e-5	1.5e-5	1.4e-5	1.4e-5	1.8e-5	1.4e-5
Birch Creek	1.5e-5	6.0e-6	5.95e-6	5.78e-6	5.76e-6	5.27e-6	5.12e-6	6.59e-6	5.91e-6

CFA = Central Facilities Area
EBR/BORAX = Experimental Breeder Reactor/Boiling Water Reactor Experiment
INTEC = Idaho Nuclear Technology and Engineering Complex
MFC = Materials and Fuels Complex
NRF = Naval Reactors Facility
PBF/ARA = Power Burst Facility/Auxiliary Reactor Area
RTC = Reactor Technology Complex
RWMC = Radioactive Waste Management Complex
TAN = Test Area North

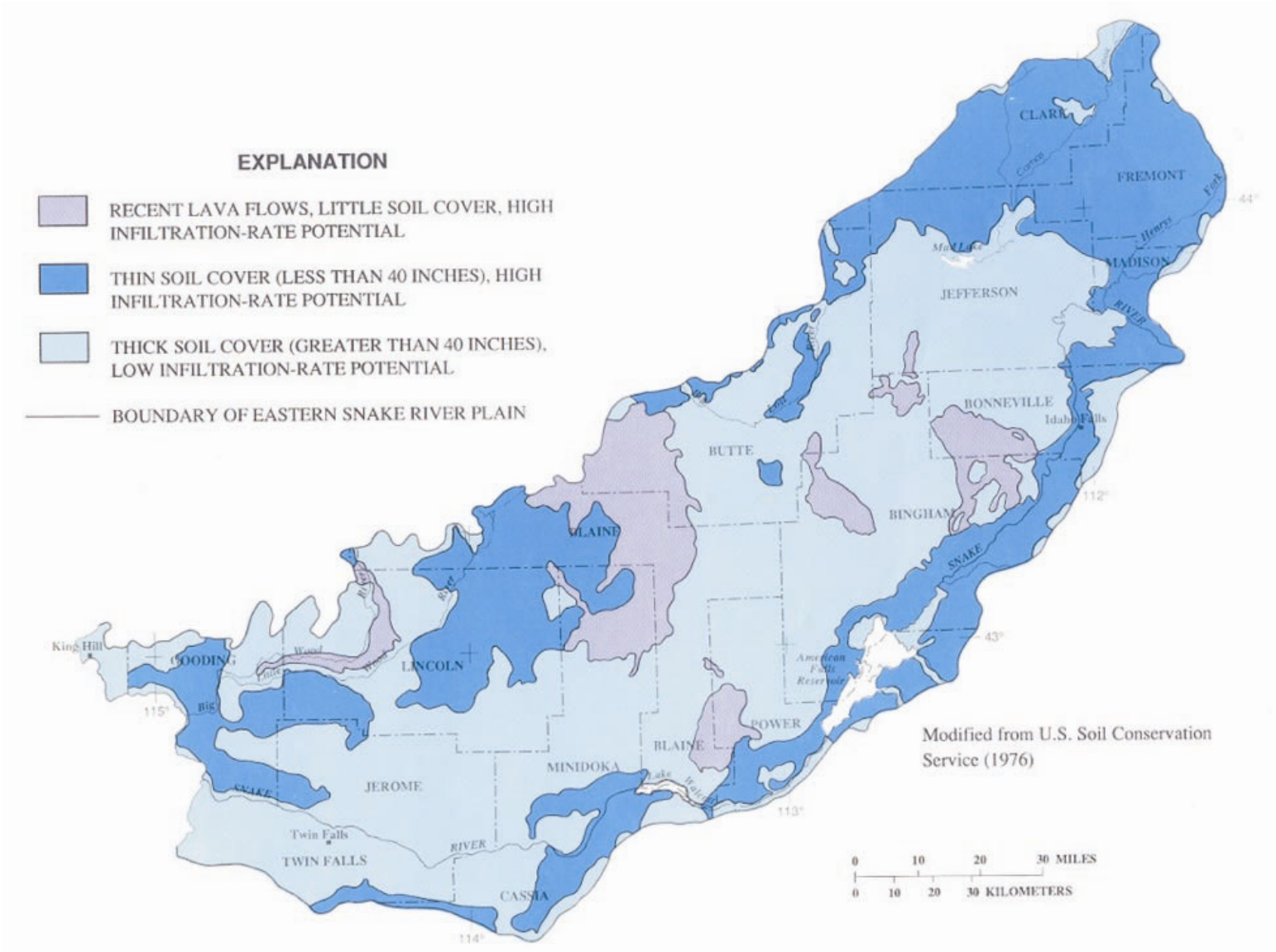

Figure 3-30. Surface soil/rock distribution map across the Snake River Plain.

soil/rock distribution across the entire Snake River Plain, which was used to derive the precipitation infiltration rates for Garabedian's (1992) flow model and the IWRRI model (IWRRI 2005). On the basis of the surface soil/rock distribution, we developed a heterogeneous precipitation infiltration rate map as show in Figure 3-31. The heterogeneous infiltration rate scenario was implemented in the two-dimensional model, and the head change for each grid block was calculated to evaluate the sensitivity of the simulated heads to the infiltration rate heterogeneity. Figure 3-32 shows the changes of simulated heads between the heterogeneous infiltration scenario and the homogeneous infiltration scenario.

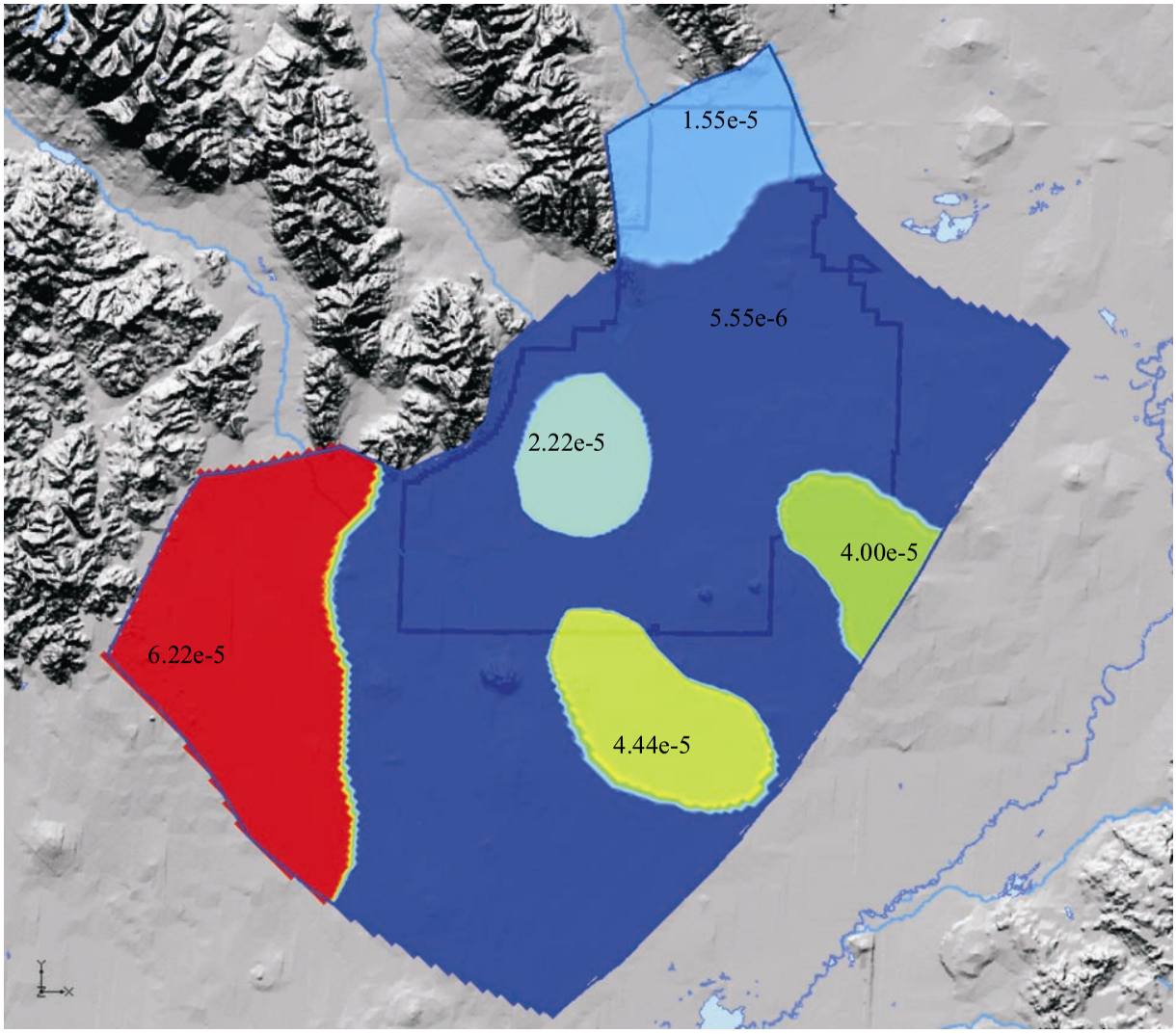

Figure 3-31. The heterogeneous precipitation infiltration rate (m/d) implemented in the two-dimensional model domain for sensitivity study.

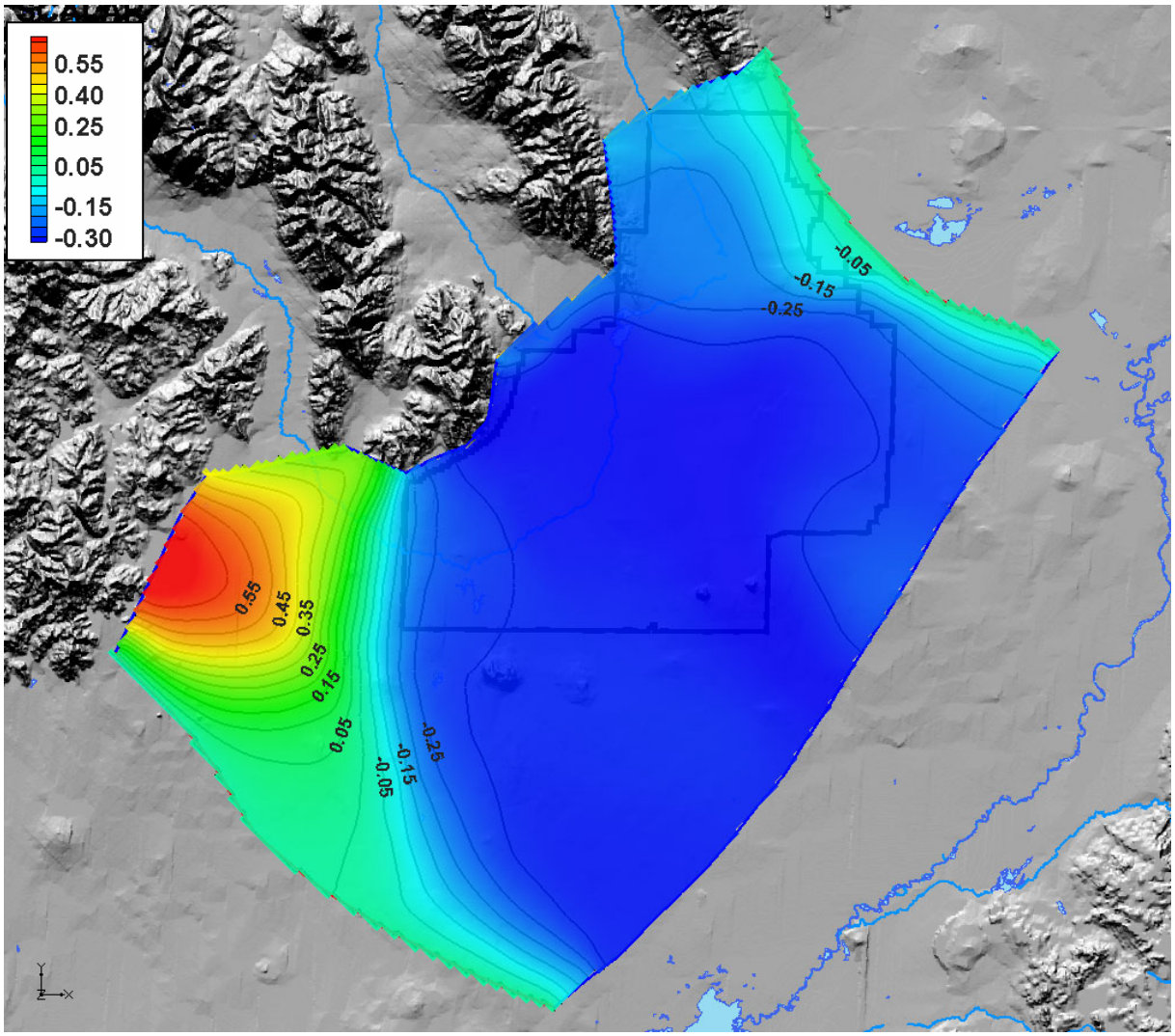

Figure 3-32. Changes (in meters) of simulated heads between heterogeneous and homogeneous infiltration scenarios.

Sensitivities of the simulated heads were highest in the southwestern part of the model domain, where the highest heterogeneous infiltration rate was used. Sensitivities of the simulated heads were lowest in the middle of the domain, where a small infiltration rate of 5.55e-6 m/d (1.8e-6 ft/d) was applied to a large portion of the model domain. However, the maximum absolute change of the simulated heads for both infiltration scenarios was only about 0.6 m (2 ft), still within the acceptance range of the simulation residuals (1 m [3.3 ft]). More importantly, the changes of heads inside the INL Site boundary, particularly changes in the southern portion of the site, are fairly uniform, as manifested by the large separation distance between the contour lines of head changes. This is particularly important for transport simulation, because such uniform changes of heads will not affect the gradient.

3.1.10.4 Particle Tracking Simulation of the Potential Contaminant Travel Paths. To further evaluate the potential travel paths of possible contaminants initiated from individual facilities, we conducted particle tracking simulations by using our two-dimensional simulated flow field. We considered both thick and thin aquifer scenarios and compared the particle tracking simulation results using the simulated head fields as input from both the zonation approach and pilot-point approach,

respectively. Figures 3-33 and 3-34 show the possible flow paths of contaminants initiated from some facilities. One interesting point is that the flow field calibrated by the pilot-point approach provides more realistic travel paths than does the zonation approach. In particular, the predicted travel path initiated from INTEC by the pilot-point approach is more consistent with the measured plume spreading. This result clearly demonstrates the need to accurately reproduce the flow field at both large and local scales in order to make reliable transport predictions.

An interesting result shown in Figures 3-33 and 3-34 is that the simulated travel paths are not necessarily consistent with the flow paths inferred from geochemical and isotope studies, as shown in Figure 2-32, where the inferred flow path from INTEC is more southeasterly. The simulated travel path from INTEC is more southerly.

Although the Figures 3-33 and 3-34 show the potential travel paths of contaminants, the travel paths have no information available with respect to travel time. In order to accurately depict and predict contaminant transport, a truly three-dimensional model is needed.

3.1.11 Limitations of the Two-dimensional Flow Model

The objectives of developing the current two-dimensional flow model are to better understand both the regional- and local-scale features, investigate the validity of various calibration approaches, and investigate the feasibility of using all aquifer wells available inside the INL Site boundaries and the rest of the model domain as calibration wells. The two-dimensional modeling results (primarily the pilot-point approach) are satisfactory in terms of meeting the above objectives.

Although we have used variable thickness, the two-dimensional model assumes the hydraulic conductivity and head are the same along the vertical direction. So the estimated hydraulic conductivity field and simulated head are the averages across the entire aquifer thickness. However, there is strong evidence that the vertical heterogeneity of the aquifer could lead to potential vertical flow within the system. Vertical flow will have important impacts on subsequent contaminant transport predictions. Where significant vertical flow exists in the aquifer, the two-dimensional flow model is inadequate for simulating transport.

Another limitation of the steady-state two-dimensional model is that it does not consider the dynamic nature of aquifer recharge (e.g., wet and drought periods). The model only considers a snapshot in time for its calibration. Calibrating flow ***and*** transport to long-term anthropogenic plumes and stable-isotope geochemistry plumes will be accomplished during the next phase of the OU 10-08 modeling project. The remainder of this subsection discusses limitations of a vertically integrated two-dimensional model for simulating transport.

First and foremost, transport is inherently three-dimensional within the aquifer. Contaminants from the vadose zone are introduced to the top of the aquifer and then begin mixing vertically along flow paths. In addition, contaminants are injected at depth. A two-dimensional model assumes constant concentration across the entire thickness of the aquifer, implying that whenever contaminant flux enters into the aquifer across the water table, the contaminants immediately mix (or dilute) along vertical directions within the whole aquifer. This assumption leads to significantly underestimated simulated contaminant concentrations within the aquifer.

Another limitation of the two-dimensional model is its inability to reproduce the “preferential” flow path identified through geochemical and isotope studies in the INL Site. This is based on the observations described in Subsection 3.1.10.4 regarding the divergence between simulated flow paths from INTEC compared to flow paths interpreted from sparse geochemical data. One hypothesis is that

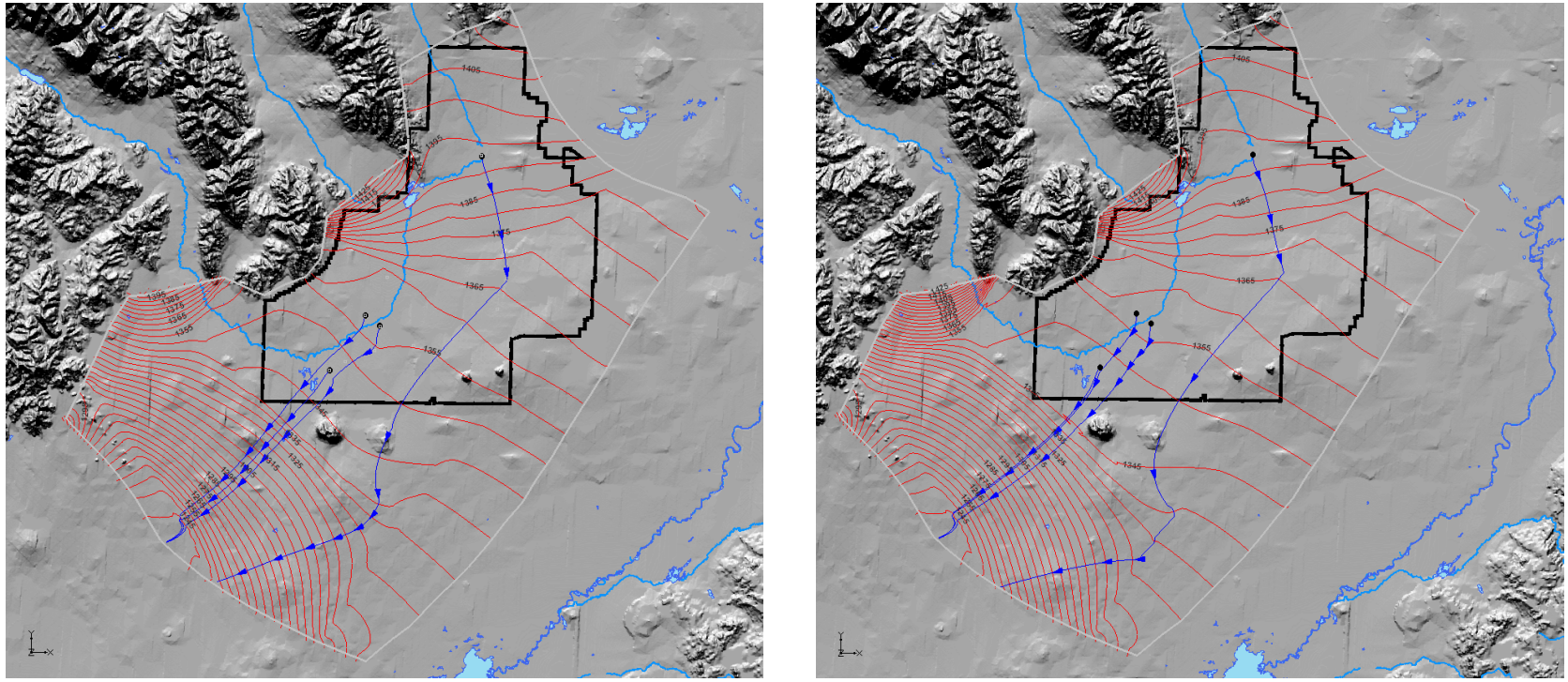

Figure 3-33. Simulated flow paths from individual WAGs using the head field calibrated by the zonation approach for the thick scenario (left) and the thin scenario (right).

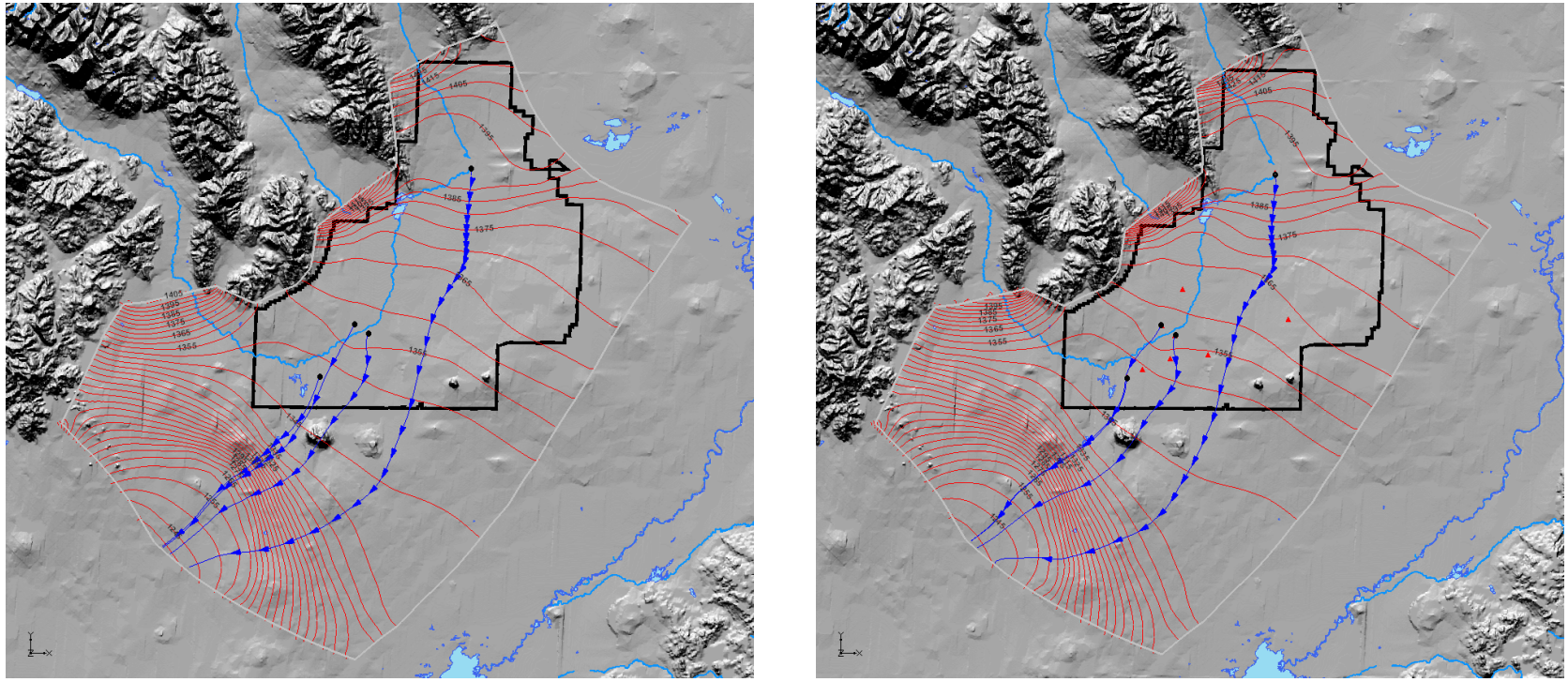

Figure 3-34. Simulated flow paths from individual WAGs using the head field calibrated by the pilot-point approach for the thick scenario (left) and the thin scenario (right).

this preferential flow path might be a feature only within the upper portion of the aquifer. A two-dimensional model can only address the lumped (averaged) effect across the entire thickness of the aquifer. A three-dimensional model is required to test this hypothesis by incorporating vertical heterogeneity. If the preferential flow exists, it will lead to much faster contaminant transport than we expected, and a three-dimensional model is required to test this hypothesis.

Due to the limitations of the two-dimensional flow model, we conclude that a fully three-dimensional model that incorporates both horizontal and vertical heterogeneities at various scales is required in order to accurately depict and predict the contaminant transport in the SRPA.

3.2 Thermo-hydraulic Two-dimensional Modeling Activities

The reliability of a flow and transport model relies entirely on its ability to mimic the system it represents. Thus, confidence in a model depends on how well it reproduces observed behavior. In general, the process of refining a model to match different sets of observations is termed calibration, and calibration to several data sets is preferred. In the SRPA, one of the calibration targets is the abundant temperature data available from boreholes and wells. Accordingly, a groundwater heat flow modeling study is being conducted to provide a quantitative means of relating observed groundwater temperature distribution to groundwater flow. Results of this effort will be used to constrain aquifer properties in a refined model calibration effort. A three-dimensional thermal model, calibrated to the areal and vertical distribution of subsurface temperature, is planned for completion in fiscal year 2006.

One of the principal questions that can be addressed via heat flow modeling is related to the isothermal nature of temperature profiles in the active portion of the aquifer. The homogenization of temperature in those sections clearly represents either significant vertical mixing or a horizontal rate of groundwater movement sufficiently fast to prevent significant heating from below. Vertical mixing may be occurring via vertical flow or via dispersion transverse to the principal direction of groundwater flow. Vertical flow, in turn, may be driven by pressure gradients or by free convection if temperature gradients are large enough to create significant buoyant forces.

The potential for free convection in groundwater systems can be assessed by calculating the Rayleigh number, a dimensionless number that essentially represents the ratio of buoyant forces, promoting vertical flow, to viscous and diffusive forces that inhibit vertical flow. The Rayleigh number, N_{Ra}, is as follows:

$$N_{Ra} = \frac{g \cdot \rho_0 \cdot c_w \cdot \rho_w \cdot L \cdot k \cdot \alpha_w \cdot \Delta T}{\mu_w \cdot \kappa_{eff}} \tag{3-1}$$

where

g	=	gravitational acceleration constant
ρ_0	=	water density at a specified background temperature
c_w	=	the specific heat of water
ρ_w	=	water density
L	=	aquifer thickness
k	=	intrinsic permeability
α_w	=	coefficient of volume expansion
ΔT	=	temperature difference across the system
μ_w	=	dynamic viscosity of water
k_{eff}	=	effective thermal conductivity.

Theoretical analysis indicates that free convection in groundwater does not occur until the Rayleigh number exceeds ~40 (Lapwood 1948). To estimate the potential for free convection in the eastern SRPA, we can thus determine whether the estimated Rayleigh number for the system exceeds that value. Assuming a temperature gradient similar to that observed in the subaquifer at the Middle-1823 well (~0.07°C m^{-1}), and assuming an aquifer thickness (L in Equation 3-1) of 200 m (~656 ft), the potential temperature difference across the system, ΔT, is about 13°C. Under these assumptions, the Rayleigh number depends primarily on the intrinsic permeability, k, of the system. Based on estimates of Ackerman (1991), the transmissivity of the SRPA ranges from 0.1 to 70,606 m^2 day^{-1} (1.1 to 760,000 ft^2 day^{-1}). Again, assuming an aquifer thickness of ~200 m (656 ft) implies that the intrinsic permeability of the aquifer ranges from approximately < 10^{-15} to 10^{-10} m^2. The Rayleigh number for that k range is then readily calculated by assuming that other variables in Equation 3-1 vary little from their values at ~15°. Results indicate that free convection is possible but unlikely, because the combination of temperature and permeability provides the necessary conditions only at the maximum estimated permeability for the system (Figure 3-35).

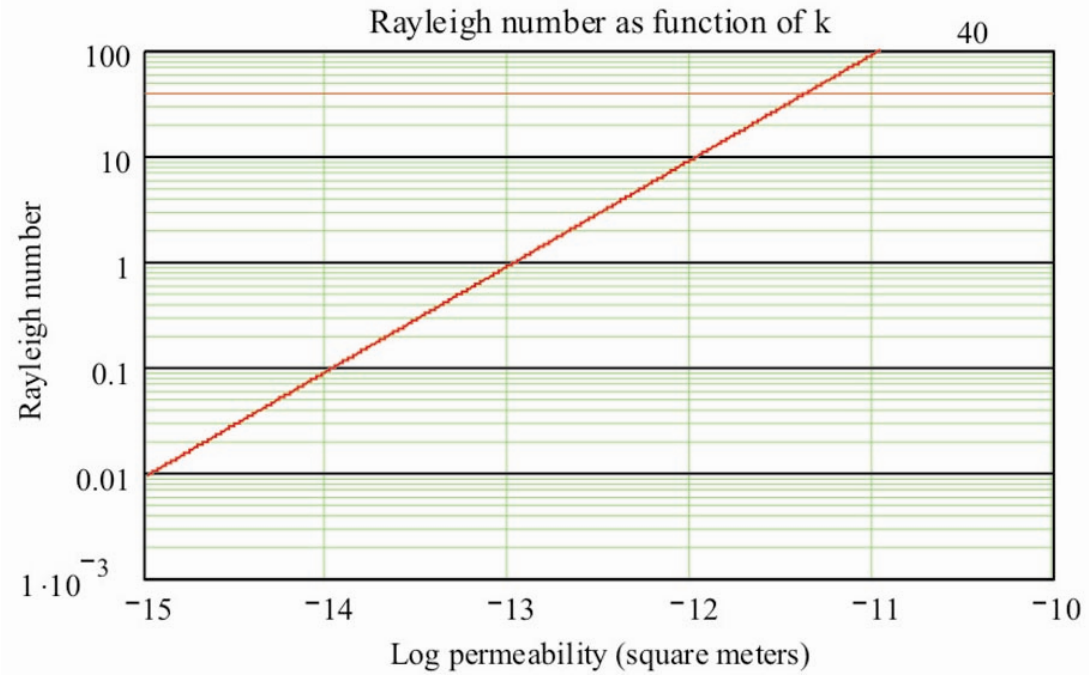

Figure 3-35. Rayleigh number versus intrinsic permeability, k, for an assumed aquifer thickness of 200 m (656 ft) and temperature difference of ~13°C. The estimated range for k is based on transmissivity estimates of Ackerman (1991). The red line indicates the threshold value (~40) for free convection in groundwater (Lapwood 1948).

Other plausible mechanisms for producing the isothermal profiles in the aquifer are high horizontal groundwater velocities and strong mechanical dispersion in the vertical direction induced by flow in the horizontal plane. As a preliminary exploration of how these effects might be explored in a heat flow model, we conducted a set of simple modeling experiments with a two-dimensional block model scaled to reflect average dimensions of the eastern SRPA. Using MATLAB and the MATLAB PDE Toolbox, we constructed a three-layer model of the system comprised of a 200-m (656-ft) thick vadose zone, a 200-m (656-ft) thick aquifer, and a 100-m (328-ft) thick subaquifer (Figure 3-36). Assuming that groundwater flow and heat transport are uncoupled, the steady-state convection-dispersion equation that follows is solved for the entire system, with stratigraphic differences represented by differences in effective thermal

conductivity, advective velocity, and boundary conditions. The equations are solved using the finite element method, using the Gauss-Newton iteration to solve the prescribed non-linear set of elliptic equations.

$$\left[\frac{\partial}{\partial x}\left(k_{eff}\frac{\partial T}{\partial x}\right)+\frac{\partial}{\partial y}\left(k_{eff}\frac{\partial T}{\partial y}\right)\right]-\left[\frac{\partial}{\partial x}\left(C_w q_x T\right)+\frac{\partial}{\partial y}\left(C_w q_y T\right)\right]=0 \qquad (3\text{-}2)$$

where the effective thermal conductivity, $\kappa_{eff,}$ is defined as

$$\kappa_{eff}=\kappa+\alpha_i q_x C_{eff} \qquad (3\text{-}3)$$

where

κ = thermal conductivity of the solid matrix
α_i = dispersivity, in direction i (longitudinal or transverse)
q_x = flux density of water in the x direction
C_{eff} = effective heat capacity of the solid/water matrix.

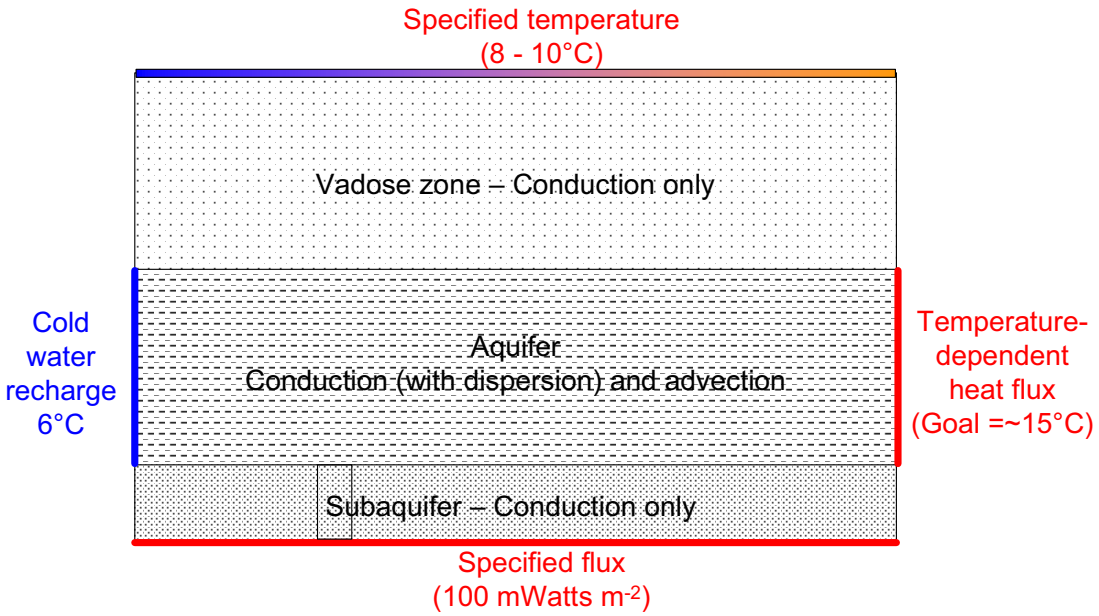

Figure 3-36. Schematic representation of the two-dimensional heat transport model.

We assumed a thermal conductivity of the solid/water matrix, κ, of 1.9 J m^{-1} sec^{-1} K^{-1}; an effective heat capacity, $C_{eff,}$ (solid + water), of 2.3×10^6 J m^{-3} K^{-1}; and a heat capacity for water, C_w, of 2.1×10^6 J m^{-3} K^{-1}. The flux density, q_x, was calculated from the average groundwater velocity assuming a porosity of 0.05. The dispersion coefficients, α_i, for dispersion of heat in the i directions are described below, and further details of notation and parameter values used in the calculations are included in Appendix B.

The model is designed to broadly represent a vertical cross section along a flowline through the ESRP, with flow from left to right. Thus, horizontal distance represents distance along a flow line extending from the edge of the Yellowstone Plateau to the Snake River near Thousand Springs,

approximately ~200 km (124 mi). This length is much greater than the thickness of the system. To scale the system appropriately, without requiring either a large number of elements or triangular elements with high aspect ratios, horizontal derivative terms in the equation matrices were multiplied by the appropriate constant.

In the aquifer layer, a uniform groundwater velocity of 3 m day^{-1} (~10 ft day^{-1}) is assumed. The advective term is zero in the other layers. A heat flux of 100 mWatts m^{-2} is specified along the bottom boundary of the system, and temperature along the top boundary is fixed, varying from 8°C on the left to 10°C on the right, representing ground temperatures on the ESRP. Temperature on the left, or recharge, boundary is fixed at 6°C, slightly colder than the overlying ground surface. The right, or discharge, boundary is a zero-gradient condition, so that the heat flux equals that advected across the boundary. All other boundaries are zero-flux boundaries.

In the eastern SRPA, temperatures along the discharge boundary are about 14 to 15ºC, and if the two-dimensional model described in this report adequately describes the geometry of the system and controls on heat flow in the system, the temperatures on the right-hand boundary of the model would be in that range. This model, however, is intended only to examine the basis sensitivity of the system to primary controls and should not be expected to accurately portray heat flow along a flow line to that level of detail. The discharge temperature is, therefore, provided only as a reference to illustrate how the model sensitivity to various parameters compares to the overall accuracy of the calculated temperature distribution. Note also that the temperatures specified along the boundaries do not exactly match observed ranges and are intended only to reflect the general trends within the system.

A base case simulation that includes longitudinal and transverse (vertical mixing) dispersivities of 1 m (3.3 ft) and 0.1 m (4 in.) describes a temperature distribution (Figure 3-37a) with several similarities to previous descriptions (Brott et al. 1981) of temperature trends along a flowline in the eastern SRPA. First, vertical temperature gradients in the recharge area are negative (temperature increasing with elevation), because the specified recharge temperature is colder than the mean annual air temperature at that location. Second, the flux of heat from below quickly effects a reversal in the vertical gradients, so that downstream (to the right) vertical gradients are positive and increasingly steeper with distance.

The modeled temperature distribution also exhibits several substantial differences from that observed in the SRPA. Near-isothermal vertical gradients exist only very near the recharge zone, for example, and little contrast exists in the gradient between the aquifer and subaquifer anywhere in the system. This contrasts markedly with the large difference in temperature gradient found between the active aquifer and subaquifer in wells that penetrate both systems. Discharge temperatures in this base case simulation (~25 to 30°C) are also considerably warmer than observed temperatures (approximately 15°C) at the recharge area. These differences suggest either that the included heat transport parameters (boundary conditions, thermal conductivities, advective velocity, and dispersivities) are incorrect or that this highly simplified model does not adequately capture the processes important to temperature control along a flowline through the aquifer. While the latter may be true, the sensitivity of the system to first-order heat flow processes should still be instructive, and we examine now how changes to some of these parameters affect the simulated temperature distribution.

Previous studies (Robertson 1974; Goode and Konikow 1990b) have indicated that longitudinal dispersivities in the system are on the order of 90 m (295 ft) in the aquifer beneath the INL Site. While large, dispersivity of that magnitude has only a minor effect (Figure 3-37b) on the large-scale temperature distribution here, primarily because the mixing scale is still relatively small compared to the length of the system, 200 km (124 mi). The advective velocity is an important control on the heat distribution, because it acts to alter the direction of heat transport from upward to sideways. In this system, the base case temperature distribution demonstrates that the advective velocity is insufficient to erase the effects of

heating along a flowline; temperatures increase by approximately 20°C across this system. A 5x increase in the advective velocity (Figure 3-37c) demonstrates that the system is quite sensitive to that velocity, and that temperature changes along a flowline might be diagnostic of velocity. The simulation also suggests that the observed nearly isothermal vertical profiles are not readily explained by the relatively fast advection in the system. In the base case scenario, vertical gradients across the aquifer are not much different than in the subaquifer, and the increase in velocity primarily acts to increase the gradient in both the subaquifer and aquifer, rather than increase the contrast between the two.

Vertical mixing within the aquifer could be the result of mechanical dispersion along a flowline. In the base case simulation, the transverse dispersivity is set to 0.1 m (3.3 ft), one tenth of the longitudinal dispersivity. If we again increase the longitudinal dispersivity to that estimated from previous studies, 90 m (295 ft), but also maintain the 10:1 ratio of longitudinal to transverse dispersivity, we see that the vertical gradients are very sensitive to that parameter (Figure 3-37d). In this example, temperature gradients in the aquifer are nearly isothermal along the entire flowline, and they contrast markedly with the underlying and overlying vertical gradients. This latter example demonstrates that the isothermal profiles commonly observed in SRPA wells might be excellent indicators of the degree of vertical mixing occurring along a flow path and thus provide a sound means of constraining longitudinal dispersivity in the system.

Note that the advantages gained from a better understanding of vertical mixing behavior might extend beyond those associated with constraining transport parameters. Development of a three-dimensional model for the SRPA requires a knowledge of the subsurface, and acquiring this knowledge can be very expensive to obtain. As discussed above, the isothermal temperature profiles suggest that vertical mixing in this system might be relatively rapid, and where vertical mixing is rapid, the system might well be described by a two-dimensional flow model. Thus, the temperature data might provide a robust means of identifying areas where the planned three-dimensional flow and transport model might reasonably assume homogeneity in the vertical direction and allow more focused effort on three-dimensional structure in areas with less pronounced vertical mixing.

One of the difficulties in parameterizing a heat flow model is that the geothermal heat flux is generally only roughly known. In the eastern SRPA, for example, results of an energy budget analysis of the system (Brott et al. 1981) indicate that the average geothermal heat flux is approximately 200 mWatt m^{-2}, while analysis of deep temperature profiles in the same region suggests that the flux is approximately 110 watts m^{-2}. Experiments with the two-dimensional model can provide insight to the sensitivity of temperature distribution to that value. As a simple example, doubling the heat flux across a 1-km (0.6-mi) length of the system has little impact on the temperature distribution (Figure 3-38), even near the bottom of the aquifer. This suggests that local hot spots in the temperature field might be the result of vertical movement of deep water, rather than simply variations in the underlying geothermal gradient.

3.3 Summary

The two-dimensional vertical profile model developed during the OU 10-08 two-dimensional modeling effort provides several insights as to how temperature data might be used to better constrain aquifer properties. First and foremost, the temperature data are one of the few parameters that have been obtained along the vertical dimension of the aquifer, and preliminary heat flow studies indicate that those temperature profiles can provide a quantitative means of constraining horizontal groundwater velocity and vertical mixing behavior.

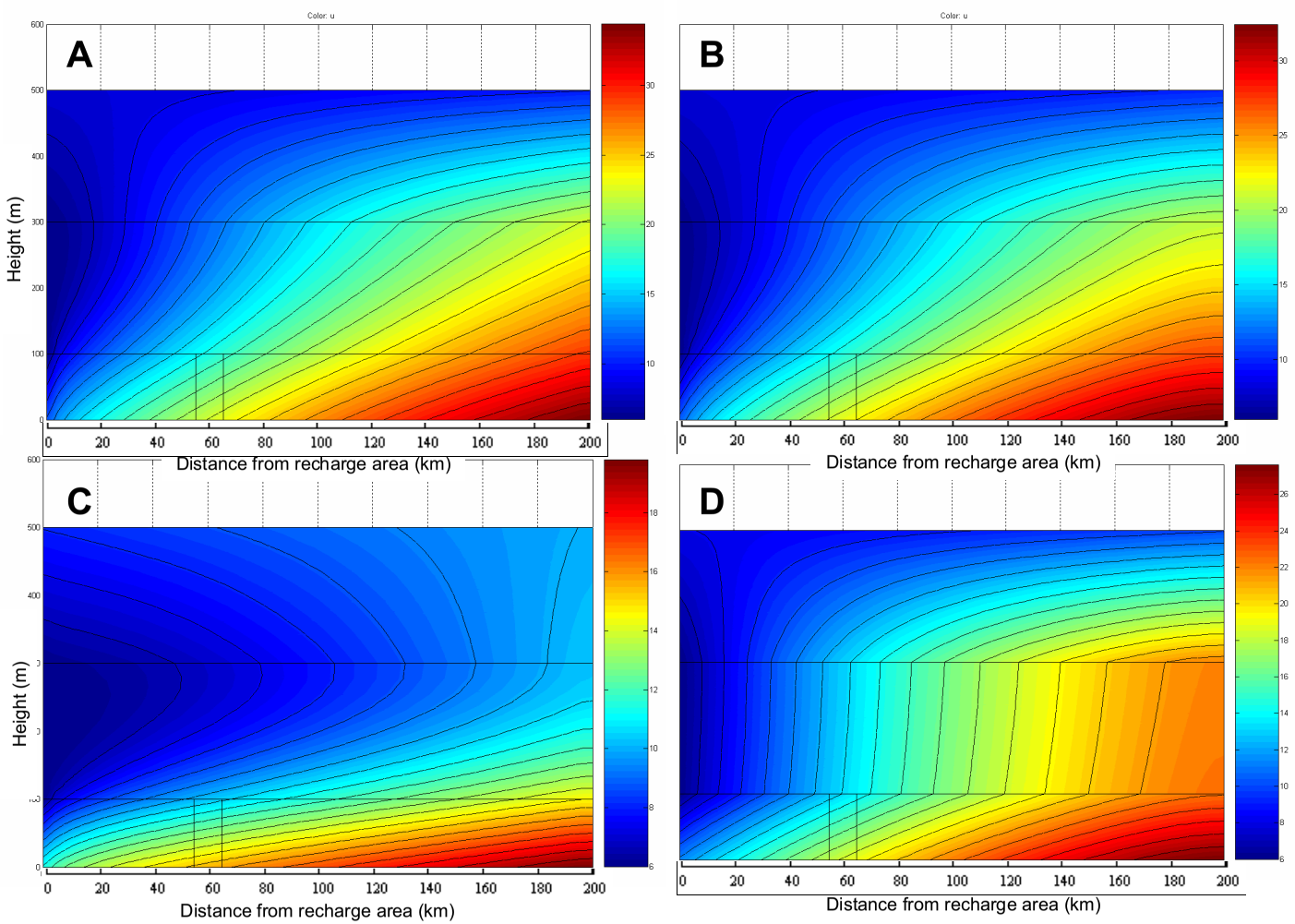

Figure 3-37. Simulated temperature distributions for the model depicted in Figure 3-36 for four scenarios described in the text: (a) simulated temperature distribution for the base case simulation described in the text, with α_L = 1 m, α_T = 0.1 m, ν = 3 m s^{-1}; (b) effect of increased longitudinal dispersivity on temperature distribution, base case condition with α_L = 90 m; (c) effect of a 5x increase in advective velocity, base case condition with ν = 15 m s^{-1}; and (d) effect of increased longitudinal dispersivity on temperature distribution, base case condition with α_L = 90 m and α_T = 9 m. Temperature scales are shown to the right of each plot. Vertical axes are meters, and horizontal axes are kilometers.

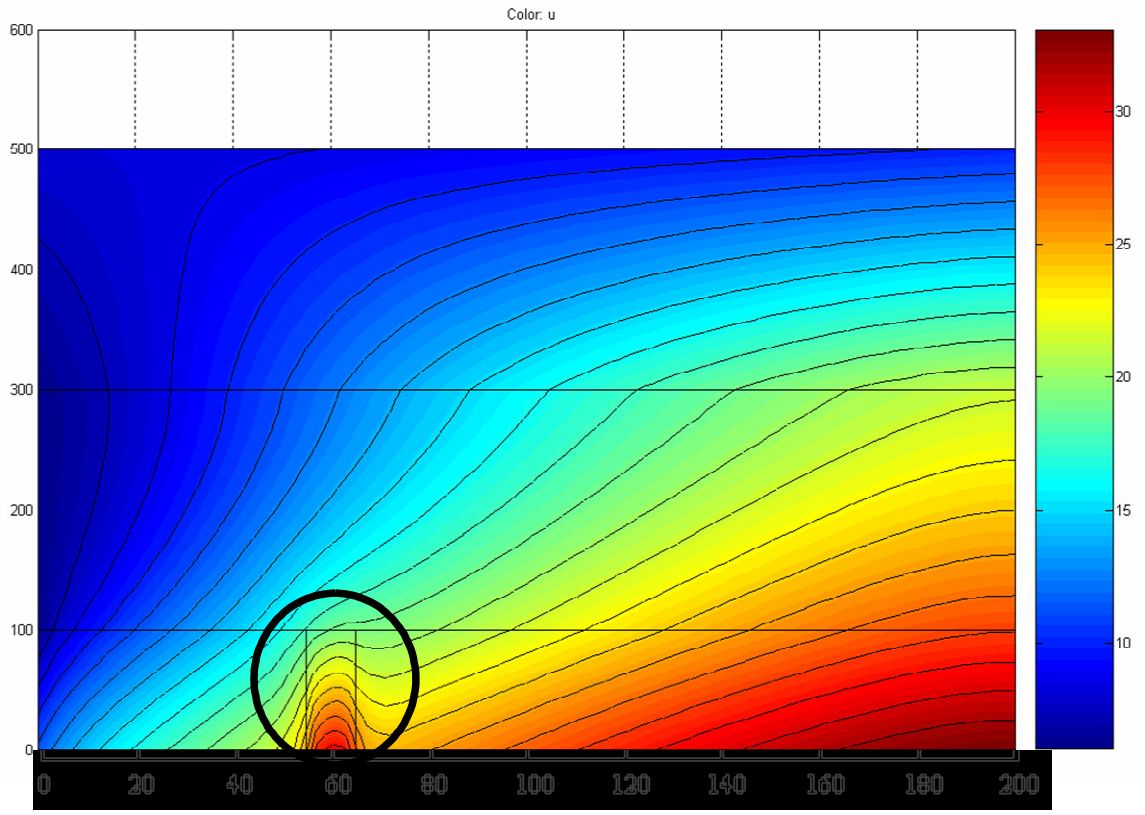

Figure 3-38. Simulated temperature distributions for the model depicted in Figure 3-36, for base case conditions, but with vertical heat flux doubled along the lower boundary of the circled rectangle.

In addition, the two-dimensional temperature distribution of the system is relatively well defined, the heat flux at the bottom of the aquifer can be obtained from approximately 10 deep wells, and the heat flux from the aquifer to the ground surface can be readily obtained at relatively high resolution. Thus, the preliminary heat flow studies conducted during fiscal year 2005 strongly support the argument that more detailed, three-dimensional heat flow modeling will greatly aid in constraining aquifer hydraulic properties, thereby providing increased confidence in predictions using the OU 10-08 groundwater flow and contaminant transport model.

Finally, the value of a heat flow study of the eastern SRPA is not limited to better constraining transport parameters. Preliminary results suggest that the nearly isothermal profiles commonly observed in deep boreholes might reflect strong vertical mixing that effectively results in vertically integrated transport behavior. Analysis of the temperature profiles might thus provide a means of identifying areas where the three-dimensional model might be considerably simplified to reflect, in essence, a homogeneous layered system.

4. SUMMARY AND CONCLUSIONS

The conceptual model and the numerical model are inextricably intertwined. The two-dimensional (and eventually the three-dimensional) groundwater models are based on the conceptual model—directly for boundary conditions and indirectly for hydraulic property distributions. Inverse modeling methods, including the pilot-point approach, result in an estimated hydraulic property field. The conceptual model is used indirectly to provide a constraint to ensure the reasonableness of the property field estimated from the inverse model results.

Completion of the two-dimensional groundwater flow model is an important step in developing a three-dimensional, subregional-scale groundwater flow and transport model for OU 10-08. The two-dimensional model sets the stage for the three-dimensional model. Because transport within the aquifer is inherently three-dimensional, it was important to have the domain initially defined in two-dimensions, which is computationally easier to solve. The two-dimensional effort has defined the boundary for the eventual three-dimensional modeling study, many of the necessary boundary conditions, and an approximate distribution of hydraulic conductivity that will serve as a constraint or cross-check on the three-dimensional simulation. This effort has also established the methodology for calibrating the three-dimensional model.

Numerous results and conclusions can be drawn from the activities that were completed to support development of the two-dimensional conceptual and numerical models. These primary conclusions are summarized below for the conceptual model and the numerical model.

4.1 Conceptual Model of the OU 10-08 Study Area

The primary conclusions reached for the conceptual model are as follows:

- The 7,770-km^2 (3,000-mi^2) OU 10-08 study area extends beyond INL Site boundaries and is bounded by natural geohydrologic boundaries and selected boundaries located to most efficiently define active groundwater flow within the INL Site boundary.
  - Natural groundwater flow boundaries in the northwest portion of the study area consist of mountain ranges and intervening valleys of the B&R Province. These mountainous areas also consist of tributary drainages that provide a source of inflow to the SRPA.
  - A groundwater flow line to the southeast forms a natural hydraulic boundary to flow.
  - The study area extends upgradient and downgradient to cross-sectional boundaries that are normal to the general direction of groundwater flow.
- Two bounding estimates of thickness (“thick” and “thin”) were developed for the SWGM domain. The thick aquifer and thin aquifer alternative interpretations are equally likely, and both are being considered in the SWGM. Both use the limited direct evidence of the aquifer base from the eight deep wells in the south-central part of the study area and extrapolate differently to the perimeter of the model domain using electrical resistivity data and water temperature at the top of the aquifer. The thick interpretation uses colder water temperatures to infer thicker areas of the aquifer toward the north of the model domain and electrical resistivity observations of a very thick aquifer section downgradient of the INL Site. The “thin” scenario only infers a general tendency for the aquifer to thicken toward the center of the Snake River Plain.

- The OU 10-08 study area can be divided into five general geologic types: active volcanic rift zones, inactive volcanic rift zones, floodplains, sedimentation areas, and volcanic tablelands. These geologic types are further divided into 17 subdomains that might exert some control over groundwater flow.
- A total of 306 aquifer tests were identified for 182 wells. The calculated hydraulic conductivity ranged over seven orders of magnitude, with a mean value of 0.94×10^{3} m/day (3.1×10^{3} ft/day) and a range from 0.49×10^{-2} to 0.33×10^{5} m/day (1.6×10^{-2} to 1.1×10^{5} ft/day). This range equates to values representative of dense basalts and loess to highly fractured basalts, interbeds, and coarse gravels.
- Major inflows to the SRPA within the OU 10-08 study area consist of regional underflow across the northeastern study area boundary, inflows derived from tributary basin underflow and streamflow losses, and recharge from infiltration of areal precipitation. Outflows occur as regional underflow across the southwestern study area boundary (consumptive use of groundwater is minimal within the subdomain). The inflows were estimated from regional modeling studies, stream loss assessments, and tributary basin assessments. The uncertainty in these estimates was also assessed. The June 2004 water table map was prepared on a subregional scale with sufficient detail to incorporate both facility-scale behavior and the broader regional picture of groundwater movement. The June 2004 water table map serves as the basis for steady-state calibration of the two-dimensional model. Hydrographs from selected wells were evaluated to support the contention that the regional water table was in a pseudo-steady-state condition and a steady-state calibration was reasonable. Transient changes in flow directions near INL Site facilities were evaluated using a consistent subset of wells over a 25-year period to create water table maps and stream lines for each time point. The transient changes, inferred to be due to influxes from the Big Lost River system, were seen to impact flow directions locally in the vicinity of the Subsurface Disposal Area at the RWMC, indicating the eventual importance of including transient conditions in transport simulations. In addition to transient influences, however, it currently appears that the extensive dispersion of historically observed contaminants could also be the result of vertically stratified contaminant plumes or other geologic controls. Further study of the transient nature of regional hydrologic conditions and its affect on contaminant transport will be necessary with the three-dimensional flow and transport models.
- Analysis of the historical and 2004 fields of flow was used to locate boundaries of the model domain within the study area. The location of a flow path (no-flow) boundary on the southeastern side of the study area was revised slightly, based on current water-level data. This boundary appears to be unaffected by fluctuations in the water table. Additionally, the northeast part of the study area (Mud Lake) was excluded from the modeling domain. This exclusion was based in the exceptional variability of water table conditions in this area due, in part, to the abundant agricultural use and to poorly understood hydrogeologic conditions. This exclusion will not impact flow conditions and contaminant transport near INL Site facilities.
- Temperature data have been used to infer large-scale movement of water in the SRPA, corroborate the interpretations of flow velocities based on water levels and chemical monitoring, and identify localized heat sources and sinks that can be used to constrain the planned three-dimensional heat flow model. The potential importance of several vertical mixing mechanisms was assessed using vertical two-dimensional models along stream lines. Three-dimensional modeling of heat flow will improve the utility of temperature information and its implications for water movement in the SRPA. A recognized limitation in the thermal modeling is the assumption of a uniform heat flux up through the bottom of the simulation domain.
- Preferential flow paths that are not aligned with the regional gradients have been identified based on isotope sampling. These data have been collected on a relatively sparse network requiring

extrapolation when interpreting the results. As additional groundwater monitoring wells come on line, analyses for isotopes in the new wells will greatly increase the density of data points on which the interpretations are based, thereby improving the confidence in the interpretations and determining to what extent the results can be used as calibration targets for three-dimensional transport simulations.

- An ongoing geochemical study is attempting to identify the flow paths of contaminants from the RTC and INTEC and the potential for commingling of contaminant plumes with contaminants from the RWMC. This study is using four tracers that result from INL Site operations that have unique signatures or fingerprints from each facility.
- Many of the data, such as water levels and water chemistry collected since the early 1950s, are two-dimensional in character—collected either from wells that integrated heads and chemistry over large thicknesses of the SRPA or from wells that sampled only the upper part of the aquifer. Limited vertical water-level, water-chemistry, and temperature data indicate that this system is extremely complex, vertically anisotropic, and three-dimensional in nature. Multi-level sampling wells constructed in fiscal year 2005 will greatly aid in clarifying the three-dimensional aspects of water and contaminant movement in the aquifer in the immediate vicinity of these wells. With the two new wells completed in fiscal year 2005 and as sampling begins, these additional data will result in improved spatial coverage that will greatly benefit the overall understanding and ability to simulate water and contaminant movement.

4.2 Two-dimensional Numerical Modeling Results

The primary conclusions reached for the two-dimensional numerical model are as follows:

- Inverse modeling using the hydraulic conductivity zonation approach, with single property values for each geologic subdomain, results in the least reasonable characterization of the water table. In addition, the estimated hydraulic conductivity values with this approach are highly uncertain, despite the large number of wells that have been used to constrain the model. Normally, geological features determine the distribution of aquifer properties. However, because of the complex fracturing processes of the SRPA, the configuration of known geological features is not necessarily consistent with the hydrogeological properties that govern the flow behavior within the aquifer. Therefore, more effort should be put into analysis of the large-scale hydrogeological features of the system and how they impact the conceptual model and thus the numerical model. Spatial analysis on both the estimated K field from the pilot point approach and pumping test data will help determine the large-scale hydrogeological features.
- Inverse modeling using the pilot-point approach satisfactorily reproduces both the large- and local-scale features of the water table and provides a good match to measured heads. More importantly, the estimated hydraulic conductivity field has the least uncertainty resulting from the calibration process. Some large-scale geological features are also reproduced by this approach. Most pumping tests within the model domain were conducted over a limited vertical interval, and the two-dimensional model represents the lumped effects of the entire aquifer thickness. Therefore, no aquifer test data were incorporated as prior information in the pilot-point approach. However, aquifer test data could be used as prior information in the three-dimensional model after careful examination of the depth interval over which the test was conducted and the aquifer volume that was influenced by the test.
- Inverse modeling using the combined zonation/pilot-point approach provides a slightly better match to measured heads than does the pilot-point approach with the same amount of the calibration effort. Ideally, this coupled approach honors large-scale knowledge of geological

features while allowing variations within each zone. However, the estimated hydraulic conductivity field exhibits large uncertainties. The 95% confidence intervals of most estimated parameters span two to seven orders of magnitude and some are even higher, similar to those that resulted from the zonation approach.

- Comparison of simulated flow paths for the thick and thin scenarios with either the zonation or pilot-point method showed approximately the same flow paths from RTC/INTEC and TAN toward the southern INL Site boundary. For the zonation and the pilot-point approaches, the path line originating from the RTC passes through the immediate RWMC vicinity. However, the pilot-point method, which produced the better head matches and lower property uncertainties, resulted in a different path line originating from the INTEC facility. This path line is more consistent with observed migration direction, based on the tritium plume emanating from INTEC.
- The hydraulic conductivity sensitivity study demonstrates that simulated heads in the southwestern portion of the model domain, close to the southwestern boundary, are most sensitive to hydraulic conductivity, because this area is located closest to the main exit of groundwater flow from the model domain. Unfortunately, this area has very few wells to constrain the calibration process.
- The tributary underflow recharge sensitivity study demonstrates that the heads inside the INL Site boundaries, particularly the heads in the southern portion of the INL Site where most contaminants occur, are relatively insensitive to variations in recharge from tributary underflow. Most importantly, the heads in the southern portion of the INL Site are almost equally sensitive to the underflow rates, indicating that the head gradients in that area are not affected by those underflow rates. Therefore, the uncertainties associated with the estimated underflow fluxes will not propagate to contaminant transport predictions.
- The precipitation infiltration sensitivity study demonstrates that head changes throughout the entire model domain are relatively small in response to the different precipitation infiltration scenarios. Within the INL Site boundaries, the small differences in the water table elevation are relatively uniform, indicating that the variation in the spatial distribution of precipitation recharge has an insignificant impact on the groundwater flow field.

4.3 Two-dimensional Numerical Model Summary

The two-dimensional numerical model is summarized as follows:

- The current two-dimensional flow model adequately achieved the objectives of providing a better understanding of regional- and local-scale features, investigating the validity of various calibration approaches, and determining the feasibility of using all aquifer wells available inside the INL Site and the rest of the model domain as calibration wells.
- The flow model is capable of representing large-scale flow features, including two-dimensional analysis of the direction and gradient of groundwater flow within the model domain.
- The two-dimensional numerical model cannot represent some features critical to estimation of contaminant transport within the complex three-dimensional groundwater system of the SRPA. Based on current analyses, these features—derived from the anisotropic, layered aquifer system—may control preferential groundwater flow and distribution and transport of contaminants.
    - Although the two-dimensional modeling results (primarily the pilot-point approach) are very satisfactory in terms of meeting the above objective, the two-dimensional model has some important limitations, particularly limitations addressing inherently three-dimensional contaminant transport.

- Although we have used variable thickness, the two-dimensional model assumes the hydraulic conductivity and head are the same along the vertical direction. Subsequently, the estimated hydraulic conductivity field and simulated head are the averages across the entire aquifer thickness. However, there is strong evidence that the vertical heterogeneity of the aquifer could lead to potential vertical flow within the system that will have important impacts on contaminant transport predictions.
- Although the two-dimensional flow model has predicted that the travel paths of potential contaminants originated from individual WAGs, no travel time is available along individual travel paths. The travel time prediction requires the input of effective porosity and dispersivity along the travel paths.
- Another limitation of the two-dimensional model is its inability to reproduce the "preferential" flow path identified through geochemical and isotope studies at the INL Site. One hypothesis is that the preferential flow path might be a feature only within the upper portion of the aquifer, while the two-dimensional model can only address the lumped (averaged) effect across the entire thickness of the aquifer. Only a three-dimensional model can incorporate such vertical heterogeneity. If the preferential flow really exists, it will lead to much faster contaminant transport than we expected. A three-dimensional model is necessary to test this hypothesis.
- It is also believed that the contaminants might only be present within the upper portion of the aquifer. However, the two-dimensional model assumes constant concentrations across the entire thickness of the aquifer, which implies that wherever a contaminant flux enters into the aquifer across the water table, the contaminants immediately mix (or dilute) along vertical directions within the whole aquifer. This assumption will lead to significant underestimation of the potential contaminant concentrations within the aquifer when the two-dimensional model is used.

- Because of the limitations of the two-dimensional flow model, we conclude that a fully three-dimensional model that incorporates both horizontal and vertical heterogeneities at various scales is required in order to accurately depict and predict the contaminant transport in the eastern SRPA.

5. REFERENCES

Ackerman, D. J., 1991, *Transmissivity of the Snake River Plain Aquifer at the Idaho National Engineering Laboratory, Idaho*, U.S. Geological Survey Water-Resources Investigations Report 91-4058.

Ackerman, D. J., 1995, *Analysis of Steady-State Flow and Advective Transport in the Eastern Snake River Plain Aquifer System*, *Idaho*, U.S. Geological Survey Water-Resources Investigations Report 94-4257.

Anderson, M. P., and W. W. Woessner, 1992, *Applied Groundwater Modeling, Simulation of Flow and Advective Transport*, San Diego: Academic Press.

Anderson, S. R., M. A. Kuntz, and L. C. Davis, 1999, *Geologic Controls of Hydraulic Conductivity in the Snake River Plain Aquifer at and near the Idaho National Engineering and Environmental Laboratory, Idaho*, U.S. Geological Survey Water-Resources Investigations Report 99-4033.

Arnett, R. C., and R. P. Smith, 2001, *WAG 10 Groundwater Modeling Strategy and Conceptual Model*, INEEL/EXT-01-00768, Rev. B, Idaho National Engineering and Environmental Laboratory, September 2001.

Arnett, R. C., and R. K. Springer, 1993, *Calibration of the Groundwater Flow Model for a Portion of the Snake River Plain Aquifer at the INEL*, ER&EM-EDF-0024-93, Idaho National Engineering Laboratory.

Beasley, T. M., L. D. Cecil, P. Sharma, P. W. Kubik, U. Fehn, L. J. Mann, and H. E. Gove, 1993, "^{36}Cl in the Snake River Plain Aquifer at the Idaho National Engineering Laboratory: Origin and Implications," *Ground Water*, Vol. 31, No. 2, pp. 302–310.

Beasley, T. M., P. R. Dixon, and L. J. Mann, 1998, "^{99}Tc, ^{236}U, and ^{237}Np in the Snake River Aquifer at the Idaho National Engineering and Environmental Laboratory, Idaho Falls, Idaho," *Environmental Science and Technology*, Vol. 32, No. 24, pp. 3875-3881.

Bestland, E. A., P. K. Link, D. Champion, and M. Lanphere, 2002, *Paleoenvironments of Sedimentary Interbeds in the Pliocene-Pleistocene Big Lost Trough (Eastern Snake River Plain, Idaho)*, P. K. Link and L. L. Mink (eds.), Geological Society of America Special Paper 353.

Blackwell, D. D., 1989, "Regional Implications of Heat Flow of the Snake River Plain, Northwestern United States," *Tectnophysics*, Vol. 164, pp. 323-343.

Blackwell, D. D., 1990, *Temperatures and Heat Flow in INEL-GT1 and WO-2 Boreholes, Snake River Plain, Idaho*, EGG-NPR-10690, Idaho National Engineering Laboratory.

Blackwell, D. D., S. Kelley, and J. L. Steele, 1992, *Heat Flow Modeling of the Snake River Plain, Idaho*, EGG-NPR-10792, Idaho National Engineering Laboratory.

Blackwell, D. D., and J. L. Steele, 1992, "Geothermal Map of North America: DNAG Continent-Scale Map-006," *Geological Society of America*, Decade of North American Geology series.

Blair, J. J., and P. K. Link, 2000, "Pliocene and Quaternary Sedimentation and Stratigraphy of the Big Lost Trough from Coreholes at the Idaho National Engineering and Environmental Laboratory, Idaho: Evidence for a Regional Pliocene Lake during the Olduvai Normal Polarity Subchron," L. Robinson (ed.), *Proceedings of the 35th Symposium on Engineering Geology and Geotechnical Engineering, Pocatello, Idaho State University*.

Brott, C. A., D. D. Blackwell, and J. P. Ziagos, 1981, "Thermal and Tectonic Implications of Heat Flow in the Eastern Snake River Plain, Idaho," *Journal of Geophysical Research*, Vol. 86, pp. 11,709-11,734.

Busenberg, E., L. N. Plummer, and R. C. Bartholomay, 2001, *Estimated Age and Source of the Young Fraction of Ground Water at the Idaho National Engineering and Environmental Laboratory*, USGS Water Resources Investigations Report 01-4265.

BYU, 2002, "Groundwater Modeling System Software," Provo, Utah: Environmental Modeling Research Laboratory, Brigham Young University.

Cande, S. C., and D. V. Kent, 1995, "Revised Calibration of the Geomagnetic Polarity Timescale for the Late Cretaceous and Cenozoic," *Journal of Geophysical Research*, Vol. 77, pp. 30573067.

Cecil, L. D., L. F. Hall, and J. R. Green, 2003, *Reevaluation of Background Iodine-129 Concentrations in Water from the Snake River Plain Aquifer, Idaho*, USGS Water Resources Investigations Report 03-4106.

Cecil, L. D., J. R. Pittman, T. M. Beasley, R. L. Michel, R. L. Kubik, P. Sharma, U. Fehn, and H. E. Gove, 1992, "Water Infiltration Rates in the Unsaturated Zone at the Idaho National Engineering Laboratory Estimated from Chlorine-36 and Tritium Profiles, and Neutron Logging," Kharaka Yousifk and Ann S. Maest (eds.), *Proceedings of the 7th International Symposium on Water-Rock Interaction, July 13-18, 1992*, pp. 709-714.

Cecil, L. D., J. A. Welhan, J. R. Green, S. K. Frape, and E. R. Sudicky, 2000, "Use of Chlorine-36 to Determine Regional-Scale Aquifer Dispersivity, Eastern Snake River Plain Aquifer, Idaho/USA," *Nuclear Instruments and Methods in Physics Research*, B 172 (2000), pp. 679-687.

Contor, B. A., 2004, *Recharge on Non-irrigated Lands*, Idaho Water Resource Research Institute Technical Report 04-006, Eastern Snake River Plain Aquifer Model Enhancement Project Scenario Document DDW-003, September 2004.

Crosthwaite, E. G., C. A. Thomas, and K. L. Dyer, 1970, *Water Resources in the Big Lost River Basin, South-Central Idaho*, USGS Open-File Report (unnumbered), 109 pp.

DOE-ID, 2002, *Waste Area Group 10, Operable Unit 10-08, Remedial Investigation/Feasibility Study Work Plan (FINAL)*, DOE/ID-10902, Rev. 0, U.S. Department of Energy Idaho Operations Office, August 2002.

DOE-ID, 2004, *Idaho National Engineering and Environmental Laboratory Operable Unit 10-08 Sitewide Groundwater Model Work Plan*, DOE/NE-ID-11188, Rev. 0, U.S. Department of Energy Idaho Operations Office, December 2004.

Doherty, J., 2005, *PEST Model-Independent Parameter Estimation, User's Guide*, 5th Edition, Watermark Numerical Computing, January 2005.

Doherty, D. J., L. A. McBroome, and M. A. Kuntz, 1979, *Preliminary Geological Interpretation and Lithologic Log of the Exploratory Geothermal Test Well (INEL-1), Idaho National Engineering Laboratory, Eastern Snake River Plain, Idaho*, U.S. Geological Survey Open-File Report 79-1248.

Freeze, R. A., and J. A. Cherry, 1979, *Groundwater*, Englewood Cliffs, New Jersey: Prentice-Hall.

Garabedian, S. P., 1992, *Hydrology and Digital Simulation of the Regional Aquifer System, Eastern Snake River Plain, Idaho*, U.S. Geological Survey Professional Paper 1408-F.

Goode, D. J., and L. F. Konikow, 1990a, "Reevaluation of Large-Scale Dispersivities for a Waste Chloride Plume: Effects of Transient Flow," *International Conference on Calibration and Reliability in Groundwater Modeling, International Association of Hydrological Sciences, The Hague, The Netherlands, September 1990*.

Goode, D. J., and L. F. Konikow, 1990b, "Apparent Dispersion in Groundwater Flow," *Water Resources Research* 26(10):2339-2351.

Greeley, R., 1982, "The Style of Basaltic Volcanism in the Eastern Snake River Plain, Idaho," Bill Bonnichsen and R. M. Breckenridge (eds.), *Cenozoic Geology of Idaho*, Idaho Bureau of Mines and Geology Bulletin 25, pp. 407-421.

Harbaugh, A. W., E. R. Banta, M. C. Hill, and M. G. McDonald, 2000, *MODFLOW-2000, The U.S. Geological Survey Modular Ground-Water Model – User Guide to Modularization Concepts and the Ground-Water Flow Process*, U.S. Geological Survey Open-File Report 00-92.

Helm-Clark, C. M., and D. W. Rodgers, 2004, "New 40Ar/39Ar Data from Pleistocene Basalts on the East Snake River Plain, Idaho, and their Implications for the Subsurface Structure of the Big Lost Trough," *Rocky Mountain/Cordillera Joint Section Meeting of the Geological Society of America (Boise, Idaho), May 3-5, 2004*, Paper No. 46-1.

Helm-Clark, C. M., D. W. Rodgers, and R. P. Smith, 2004, "Borehole Geophysical Techniques to Define Stratigraphy, Alteration and Aquifers in Basalt," *Journal of Applied Geophysics*, Vol. 55, No. 1, p. 3-38.

Hortness, J. E., and J. P. Rousseau, 2003, *Estimating the Magnitude of the 100-Year Peak Flow in the Big Lost River at the Idaho National Engineering and Environmental Laboratory, Idaho,* U.S. Geological Survey Open-File Report 02-4299.

IWRRI, *Research and Education Reports*, http://www.if.uidaho.edu/johnson/ifiwrri/projects.html , Web page visited August 15, 2005.

Johnson, T. M., R. C. Roback, T. L. McLing, T. D. Bullen, D. J. DePaolo, C. Doughty, R. J. Hunt, R. W. Smith, L. D. Cecil, and M. T. Murrell, 2000, "Groundwater Fast Paths'in the Snake River Plain Aquifer—Radiogenic Isotope Ratios as Natural Groundwater Tracers," *Geology*, Vol. 28, No. 10, October 2000, pp. 871-874.

Kjelstrom, L. C., 1986, "Flow Characteristics of the Snake River and Water Budget for the Snake River Plain, Idaho and Eastern Oregon," *U.S. Geological Survey Hydrologic Investigations Atlas*, HA-680, scale 1:1,000,000.

Knutson, C. F., K. A. McCormick, J. C. Crocker, M. A. Glenn, and M. L. Fishel, 1992, *3D RWMC Vadose Zone Modeling (Including FY-89 to FY-90 Basalt Characterization Results)*, EGG-ERD-10246, Idaho National Engineering Laboratory.

Koslow, K. N., 1984, *Hydrological Characterization of Birch Creek Basin*, EGG-PBS-6782, Idaho National Engineering Laboratory, December 1984.

Kuntz, M. A., S. R. Anderson, D. E. Champion, M. A. Lanphere, and D. J. Grunwald, 2002, "Tension Cracks, Eruptive Fissures, Dikes, and Faults Related to Late Pleistocene-Holocene Basaltic Volcanism and Implications for the Distribution of Hydraulic Conductivity in the Eastern Snake River Plain, Idaho," P. K. Link and L. L. Mink (eds.), *Geology, Hydrogeology, and Environmental Remediation: Idaho National Engineering and Environmental Laboratory, Eastern Snake River Plain, Idaho*, Geological Society of America Special Paper 353, pp. 111–33.

Kuntz, M. A., B. Skipp, M. A. Lanphere, W. E. Scott, K. L. Pierce, G. B. Dalrymple, D. E. Champion, G. F. Embree, W. R. Page, L. A. Morgan, R. P. Smith, W. R. Hackett, and D. W. Rodgers, 1994, "Geologic Map of the Idaho National Engineering Laboratory and Adjoining Areas, Eastern Idaho," U.S. Geological Survey Miscellaneous Investigations Map I-2330, scale 1:100,000.

Lapwood, E. R., 1948, "Convection of a Fluid in a Porous Medium," *Proceedings of Cambridge Philosophical Society*, Vol. 44, pp. 508–21.

Leeman, W. P., and W. I. Manton, 1971, "Strontium Isotopic Composition of Basaltic Lavas from the Snake River Plain, Southern Idaho," *Earth and Planetary Science*, Letter 11, 420-434.

Lewis, B. D., and F. J. Goldstein, 1982, *Evaluation of a Predictive Ground-Water Solute-Transport Model at the Idaho National Engineering Laboratory, Idaho*, U.S. Geological Survey Water-Resources Investigations Report 82-25.

Lindholm, G. F., 1996, *Summary of the Snake River Plain Regional Aquifer-System Analysis in Idaho and Eastern Oregon*, U.S. Geological Survey Professional Paper 1408A.

Luo, S., T. Ku, R. Roback, M. Murrell, and T. L. McLing, 2000, "In-situ Radionuclide Transport and Preferential Groundwater Flows at the INEEL (Idaho)," Decay-series Disequilibrium Studies, *Geochimica et Cosmochimica Acta*, Vol. 64, No. 5, pp. 867-881.

Mann, L. J., 1986, *Hydraulic Properties of Rock Units and Chemical Quality of Water for INEL-1—A 10,365-Foot-Deep Test Hole Drilled at the Idaho National Engineering Laboratory, Idaho*, U.S. Geological Survey Water-Resources Investigations Report 86-4020.

Mann, L. J., and T. M. Beasley, 1994, *Iodine-129 in the Snake River Plain Aquifer at and near the Idaho National Engineering Laboratory, Idaho, 1990-91*, U.S. Geological Survey Water-Resources Investigations Report 94-4053.

McCarthy, J. M., R. C. Arnett, R. M. Neupauer, M. J. Rohe, and C. Smith, 1995, *Development of a Regional Groundwater Flow Model for the Area of the Idaho National Engineering Laboratory, Eastern Snake River Plain Aquifer*, INEL-95/0169, Rev. 1, Idaho National Engineering Laboratory, March 1995.

McLing, T. L., R. W. Smith, and T. M. Johnson, 2002, "Chemical Characteristics of Thermal Water beneath the Eastern Snake River Plain," P. K. Link and L. L. Mink (eds.), *Geology, Hydrogeology, and Environmental Remediation: Idaho National Engineering and Environmental Laboratory, Eastern Snake River Plain, Idaho*, Geological Society of America Special Paper 353, pp. 205-211.

Morse, L. H., and M. McCurry, 1997, "Possible Correlations between Basalt Alteration and the Effective Base of the Snake River Plain Aquifer at the INEEL," S. Sharma and J. H. Hardcastle (eds.), *Proceedings of the 32nd Symposium on Engineering Geology and Geotechnical Engineering, College of Engineering, Idaho State University, Pocatello*, pp. 1-13.

Morse, L. H., and M. McCurry, 2002, "Genesis of Alteration of Quaternary Basalts within a Portion of the Eastern Snake River Plain Aquifer," P. K. Link and L. L. Mink (eds.), *Geology, Hydrogeology, and Environmental Remediation, Idaho National Engineering and Environmental Laboratory, Eastern Snake River Plain, Idaho*, Geological Society of America Special Paper, Vol. 353, pp. 213-224.

Mundorff, M. J., E. G. Crosthwaite, and C. Kilburn, 1964, *Ground Water for Irrigation in the Snake River Basin in Idaho*, USGS Water Supply Paper 1654, 224 pp.

Neuman, S. P., 1972, "Theory of Flow in Unconfined Aquifers Considering Delayed Response of the Water Table," *Water Resources Research*, Vol. 8, pp. 1031-1045.

Olmsted, F. H., 1962, *Chemical and Physical Character of Groundwater in the National Reactor Testing Station, Idaho*, IDO-22043-USGS, U.S. Geological Survey.

Olmsted, F. H., 1965, *Radioactive Waste Disposal Data for the National Reactor Testing Station, Idaho*, U.S. Atomic Energy Commission, Idaho Falls, Idaho, 52 pp.

Osmond, J. K., and Cowart, J. B., 1992, *Ground Water in Uranium-series Disequilibrium; Applications to Earth, Marine, and Environmental Sciences*, M. Ivanovich and R. S. Harmon (eds.), Oxford, United Kingdom: Clarendon Press.

Roback, R. C., T. M. Johnson, T. L. McLing, M. T. Murrell, S. Luo, and T. Ku, 2001, *Uranium Isotopic Evidence for Groundwater Chemical Evolution and Flow Patterns in the Eastern Snake River Plain Aquifer, Idaho*, Geological Society of America Bulletin, September 2001.

Robertson, J. B., 1974, *Digital Modeling of Radioactive and Chemical Waste Transport in the Snake River Plain Aquifer at the National Reactor Testing Station, Idaho – 1952-1970*, U.S. Geological Survey Open-File Report IDO-22054.

Rodgers, D. W., W. R. Hackett, and H. T. Ore, 1990, "Extension of the Yellowstone Plateau, Eastern Snake River Plain, Idaho," *Geological Society of America Abstracts with Programs*, 18, pp. 1138-1131.

Smith, R. P., 2002, *Variability of the Aquifer Thickness Beneath the Idaho National Engineering and Environmental Laboratory (INEEL)*, INEEL/EXT-02-01022, Rev. 0, Idaho National Engineering and Environmental Laboratory, August 2002.

Smith, R. P., D. D. Blackwell, and T. L. McLing, 2001, "Temperature Distribution in the Snake River Plain Aquifer beneath the Idaho National Engineering and Environmental Laboratory (INEEL) — Implications for Aquifer Flow and Geothermal Input," *Geological Society of America Abstracts with Programs*, Vol. 33, No. 6, p. A-107.

Southern Methodist University, *Temperature-depth Curve Tutorial*, http://www.smu.edu/geothermal/temperat/frames/mainpagetempex.htm, Web page visited August 18, 2005.

Spatial Climate Analysis Service, Oregon State University, http://www.ocs.oregonstate.edu/prism/, data set created May 2005.

Spinazola, J. M., 1994, *Geohydrology and Simulation of Flow and Water Levels in the Aquifer System in the Mud Lake Area of the Eastern Snake River Plain, Eastern Idaho*, U.S. Geological Survey Water-Resources Investigations Report 93-4227.

Stearns, H. T., L. Crandall, and W. G. Steward, 1939, *Geology and Groundwater Resources of the Mud Lake Region, Idaho, including the Island Park Area*, USGS Water Supply Paper 818, 125 pp.

Swanson, S. A., J. J. Rosentreter, R. C. Bartholomay, and L. L. Knobel, 2002, *Geochemistry of the Little Lost River drainage basin, Idaho*, U.S. Geological Survey Water-Resources Investigations Report 02-4120.

Theis, C. V., 1935, "The Relation between the Lowering of the Piezometric Surface and the Rate and Duration of Discharge of a Well using Groundwater Storage," *Am. Geophys. Union Trans.*, Vol. 16, pp. 519-524.

USGS, *USGS Science for a Changing World*, http://waterdata.usgs.gov/id/nwis, Web page visited August 16, 2005.

Welhan, J. A., and M. Reed, 1997, *Geostatistical Analysis of Regional Hydraulic Conductivity Variations in the Snake River Plain Aquifer, Eastern Idaho*, Bulletin of the Geological Society of America, Vol. 109, pp. 855-868.

Whitehead, R. L., 1992, *Geohydrologic Framework of the Snake River Plain Regional Aquifer System, Idaho and Eastern Oregon*, U.S. Geological Survey Professional Paper 1408-B.

Wood, S. H., and W. Bennecke, 1994, "Vertical Variation in Groundwater Chemistry Inferred from Fluid Specific-Conductance Well Logging of the Snake River Plain Aquifer, Idaho National Engineering Laboratory, Southeastern Idaho," *Proceedings of the 30th Symposium on Engineering Geology and Geotechnical Engineering*, pp. 267-283.

Wylie, A. H., 2003, *Delineating the Bottom of the Aquifer, Eastern Snake Plain Aquifer Model Enhancement*, Model Design and Calibration Document Number DDM-012, Idaho Water Resources Research Institute, University of Idaho, March 2003.

Appendix A

Aquifer Test and Well Completion Summary Information for Wells within the Sitewide Groundwater Model Study Area

Appendix A

Aquifer Test and Well Completion Summary Information for Wells within the Sitewide Groundwater Model Study Area

A-1. INTRODUCTION

A detailed literature search was performed to locate and identify aquifer test information on the Eastern Snake River Plain in the vicinity of the Operable Unit 10-08 study area. Table A-1 summarizes the test information, such as the discharge rate and duration, drawdown, and calculated transmissivity. Table A-2 summarizes the representative hydraulic conductivity and well completion information for the wells listed in Table A-1.

A-2. REFERENCES

Ackerman, D. J., 1991, *Transmissivity of the Snake River Plain Aquifer at the Idaho National Engineering Laboratory, Idaho*, USGS Water Resources Investigations Report 91-4058, 35 p.

Dustin, Jake D., Parsons Environmental Science, Inc., to Timothy S. Green, Lockheed Martin Idaho Technologies Company, September 17, 1996, "Summary of TAN-28 Pumping Test," Letter Number 25:01:086-96.

Golder Federal Services, 1995, "NRF Area Aquifer Tests," Report Number 954-2015.

Hubbell, J. M., and T. R. Wood, 1992, *Hydrogeologic Analysis of Pumping Test Data from the Radioactive Waste Management Complex Production Well and USGS Well 90*, EGG-GEO-10123, Idaho National Engineering Laboratory, 21 p.

Johnson, G. S., and D. B. Frederick, 1997, *Straddle-Packer Aquifer Test Analysis of the Snake River Plain Aquifer at the Idaho National Engineering Laboratory*, INEL Oversight Program, 61 p.

Jolley, W., 2003, "Pumping Test Results from Wells located at the Radioactive Waste Management Complex Fiscal Year 2003," EDF-3777, Rev. 0, Idaho National Engineering Laboratory, June 2003.

Lindholm, G. F., 1996, *Summary of the Snake River Plain Regional Aquifer-System Analysis in Idaho and Eastern Oregon*, USGS Professional Paper 1408-A, 59 p.

Prestwich, S. M., and J. A. Bowman, 1980, *Completion and Testing Report; INEL Geothermal Exploratory Well One (INEL-1)*, IDO-10096, U.S. Department of Energy Idaho Operations Office, February 1980.

Wylie, A., 1993, "TAN RI Aquifer Testing Results," ER-WAG1-25, Rev. 1, Idaho National Engineering Laboratory, August 1993.

Wylie, A., 1996, "Pumping Test of the Pit 9 Production Well," INEL-96/171, Idaho National Engineering Laboratory, June 1996.

Wylie, A., and J. M. Hubbell, 1994, "Aquifer Testing of Wells M1S, M3S, M4D, M6S, M7S, and M10S at the RWMC," ER-WAG7-26, Rev. 1, Idaho National Engineering Laboratory, April 1994.

Wylie, A., EG&G Idaho, to Mike Bennett, U.S. Department of Energy, May 8, 1990, "Aquifer Testing Results," Letter Number AHW-09-90.

Wylie, A. H., J. M. McCarthy, E. Hener, and B. D. Higgs, 1995, "Large-Scale Aquifer Pumping Test Results," ER-WAG7-56, Idaho National Engineering Laboratory, February 1995.

Table A-1. Summary of aquifer tests conducted on or near the Idaho National Laboratory Site from the early 1950s to the present.

Well ID[a]	Well Alias	Aquifer Test Number	Aquifer Test Type	Test Date	Test Duration (min)	Discharge Rate (gpm)	Drawdown (ft)	Specific Capacity (gpm/ft)	Hydraulic Conductivity (ft/day)	Trans-missivity (ft^2/day)	Reference	Comments
69	ANP-01	1	Single well	Apr-57	1658	1066.0	7.8	1.40E+02	NR	NR	Ackerman (1991)	Theis type curve, multiple well test
69	ANP-01	2	Multiple well	Apr-57	360	1325.0	11.9	1.10E+02	NR	NR	Ackerman (1991)	Theis type curve, multiple well test
69	ANP-01	3	Multiple well	Jul-57	1235	1719.0	11.5	1.50E+02	NR	NR	Ackerman (1991)	Regression analysis, multiple well test
69	ANP-01	4	Multiple well	Aug-57	1440	1130.0	10.0	1.10E+02	NR	NR	Ackerman (1991)	Regression analysis, nearby well injecting
69	ANP-01	5	Multiple well	Nov-91	215	1050.0	5.2	1.80E+02	NR	2.90E+04	Ackerman (1991)	Theis type curve, multiple well test
69	ANP-01	6	Multiple well	Jan-97	55	1500.0	0.3	NA	NR	4.00E+05	Wylie (1993)	Theis type curve, multiple well test, pumping well TAN-2 (ANP-02)
70	ANP-02	1	Injection	Aug-57	1440	1130.0	28.7	3.90E+01	NR	NR	Ackerman (1991)	Regression analysis, nearby well pumping
70	ANP-02	2	Multiple well	Nov-57	4320	1220.0	21.3	5.70E+01	NR	1.60E+04	Ackerman (1991)	Theis type curve, multiple well test
70	ANP-02	3	Multiple well	Nov-91	240	1010.0	7.7	1.30E+02	NR	NR	Ackerman (1991)	Theis type curve, multiple well test
70	ANP-02	4	Multiple well	Jan-97	55	1500.0	10.5	1.43E+02	NR	1.00E+04	Wylie (1993)	Neuman type curve, multiple well test, this was the pumping well
71	ANP-03	1	Injection	Sep-70	30	420.0	15.0	2.80E+01	NR	NR	Ackerman (1991)	Regression analysis
71	ANP-03	2	Single well	Jan-90	10	20.0	10.0	2.00E+00	NR	NR	Ackerman (1991)	Regression analysis
71	ANP-03	3	Single well	Jul-91	75	19.7	12.7	1.60E+00	NR	NR	Ackerman (1991)	Neuman type curve
71	ANP-03	4	Single well	Jan-92	340	37.0	27.0	1.40E+00	NR	3.00E+01	Ackerman (1991)	Neuman type curve
71	ANP-03	5	Multiple well	Jul-00	230	70.0	0.1	NR	NR	2.20E+04	Dustin (1996)	Type curve analysis, TAN-28 was pumping well
72	ANP-04	1	Single well	Jan-90	10	30.0	4.0	7.50E+00	NR	NR	Ackerman (1991)	Regression analysis
72	ANP-04	2	Single well	Jul-91	120	20.2	2.4	8.60E+00	NR	1.60E+02	Ackerman (1991)	Neuman type curve
73	ANP-05	1	Single well	Jun-60	1440	418.0	0.4	1.00E+03	NR	1.50E+05	Ackerman (1991)	Regression analysis
73	ANP-05	2	Single well	Sep-60	1020	514.0	0.7	7.90E+02	NR	NR	Ackerman (1991)	Regression analysis

Table A-1. (continued).

Well ID[a]	Well Alias	Aquifer Test Number	Aquifer Test Type	Test Date	Test Duration (min)	Discharge Rate (gpm)	Drawdown (ft)	Specific Capacity (gpm/ft)	Hydraulic Conductivity (ft/day)	Trans-missivity (ft^2/day)	Reference	Comments
74	ANP-06	1	Single well	Sep-60	1380	450.0	0.2	2.80E+03	NR	5.00E+05	Ackerman (1991)	Regression analysis
74	ANP-06	2	Single well	Jan-90	5	45.0	0.1	4.50E+02	NR	NR	Ackerman (1991)	Regression analysis, drawdown less than 0.1 ft
74	ANP-06	3	Single well	Jul-91	180	42.3	0.0	4.20E+03	NR	NR	Ackerman (1991)	Regression analysis, drawdown less than 0.1 ft
77	ANP-09	1	Single well	Jul-63	245	142.0	8.2	1.70E+01	NR	NR	Ackerman (1991)	Regression analysis, developing well
77	ANP-09	2	Single well	Jul-63	180	380.0	15.9	2.40E+01	NR	NR	Ackerman (1991)	Regression analysis, developing well
77	ANP-09	3	Single well	Jul-63	60	470.0	6.4	7.30E+01	NR	6.60E+03	Ackerman (1991)	Regression analysis
80	ARA-1	1	Single well	Sep-61	480	1075.0	1.4	7.80E+02	NR	1.10E+05	Ackerman (1991)	Regression analysis
81	ARA-3	1	Single well	May-63	957	560.0	0.6	8.80E+02	NR	2.10E+04	Ackerman (1991)	Neuman type curve
82	ARBOR TEST	1	Single well	Dec-61	1080	403.0	0.1	3.10E+03	NR	5.60E+05	Ackerman (1991)	Regression analysis
94	CFA-2	1	Single well	Feb-55	193	235.0	15.3	1.50E+01	NR	1.70E+02	Ackerman (1991)	Neuman type curve
98	CPP-01	1	Single well	Dec-54	1080	1260.0	2.9	4.30E+02	NR	NR	Ackerman (1991)	Regression analysis
98	CPP-01	2	Single well	Dec-54	1440	1130.0	1.9	5.90E+02	NR	NR	Ackerman (1991)	Regression analysis
98	CPP-01	3	Multiple well	Mar-55	1409	1140.0	1.9	6.00E+02	NR	NR	Ackerman (1991)	Regression analysis, multiple well test
98	CPP-01	4	Multiple well	Nov-55	1440	1940.0	4.8	4.00E+02	NR	NR	Ackerman (1991)	Regression analysis, multiple well test
98	CPP-01	5	Multiple well	Nov-58	2700	2475.0	5.9	4.20E+02	NR	NR	Ackerman (1991)	Regression analysis, multiple well test
98	CPP-01	6	Single well	Aug-85	760	2500.0	4.5	5.60E+02	NR	7.30E+04	Ackerman (1991)	Regression analysis
99	CPP-02	1	Injection	Apr-55	1440	1030.0	1.0	1.00E+03	NR	NR	Ackerman (1991)	Regression analysis, injection test
99	CPP-02	2	Single well	Jun-55	1440	1850.0	2.7	6.90E+02	NR	NR	Ackerman (1991)	Regression analysis
99	CPP-02	3	Single well	Nov-55	1440	1500.0	2.4	6.30E+02	NR	NR	Ackerman (1991)	Regression analysis, nearby well also pumping

Table A-1. (continued).

Well ID[a]	Well Alias	Aquifer Test Number	Aquifer Test Type	Test Date	Test Duration (min)	Discharge Rate (gpm)	Drawdown (ft)	Specific Capacity (gpm/ft)	Hydraulic Conductivity (ft/day)	Trans-missivity (ft^2/day)	Reference	Comments
99	CPP-02	4	Single well	Nov-58	180	1455.0	1.3	1.10E+03	NR	NR	Ackerman (1991)	Regression analysis, nearby well also pumping
99	CPP-02	5	Single well	Nov-58	1440	2500.0	3.2	7.80E+02	NR	NR	Ackerman (1991)	Regression analysis, nearby well also pumping
99	CPP-02	6	Single well	Aug-85	720	2500.0	2.3	1.10E+03	NR	1.60E+05	Ackerman (1991)	Regression analysis
100	CPP-03	1	Injection	Sep-55	1440	800.0	38.1	2.10E+01	NR	NR	Ackerman (1991)	Regression analysis, injection test
100	CPP-03	2	Injection	Sep-55	930	800.0	0.2	4.00E+03	NR	7.60E+05	Ackerman (1991)	Regression analysis, injection test
100	CPP-03	3	Injection	Oct-90	10	400.0	62.4	6.40E+00	NR	NR	Ackerman (1991)	Regression analysis, injection test
100	CPP-03	4	Injection	Oct-90	32	650.0	104.2	6.20E+00	NR	NR	Ackerman (1991)	Regression analysis, injection test
101	CPP-04	1	Single well	Oct-87	1320	460.0	113.0	4.10E+00	NR	NR	Ackerman (1991)	Regression analysis, ***well later deepened?***
101	CPP-04	2	Single well	Nov-87	210	520.0	129.0	4.00E+00	NR	NR	Ackerman (1991)	Regression analysis, ***well later deepened?***
101	CPP-04	3	Single well	Nov-87	1426	520.0	113.0	4.60E+00	NR	2.50E+02	Ackerman (1991)	Regression analysis, ***well later deepened?***
149	EBR-1	1	Single well	Aug-53	2880	800.0	17.0	4.70E+01	NR	1.30E+03	Ackerman (1991)	Neuman type curve, both tests reported occuring on same day
149	EBR-1	2	Single well	Aug-53	4320	483.0	6.4	7.50E+01	NR	NR	Ackerman (1991)	Regression analysis, ***both tests reported occuring on same day***
150	EBR-II #1	1	Single well	Oct-62	2880	1025.0	0.3	4.10E+03	NR	5.20E+05	Ackerman (1991)	Theis type curve
150	EBR-II #1	2	Single well	May-92	163	1100.0	1.1	1.00E+03	NR	NR	Ackerman (1991)	Regression analysis
151	EBR-II #2	1	Single well	Nov-62	2850	940.0	8.1	1.20E+02	NR	1.10E+04	Ackerman (1991)	Regression analysis
153	EOCR PRODUCTION WELL	1	Single well	Jun-64	2811	920.0	0.8	1.20E+03	NR	1.80E+05	Ackerman (1991)	Regression analysis
154	FET-1	1	Multiple well	Apr-62	960	1830.0	12.1	1.50E+02	NR	3.10E+04	Ackerman (1991)	Theis type curve
155	FET-2	1	Multiple well	May-62	960	1820.0	16.1	1.10E+02	NR	1.10E+04	Ackerman (1991)	Regression analysis
156	FET-3	1	Single well	Nov-61	420	643.0	4.3	1.50E+02	NR	1.50E+04	Ackerman (1991)	Regression analysis

Table A-1. (continued).

Well ID[a]	Well Alias	Aquifer Test Number	Aquifer Test Type	Test Date	Test Duration (min)	Discharge Rate (gpm)	Drawdown (ft)	Specific Capacity (gpm/ft)	Hydraulic Conductivity (ft/day)	Trans-missivity (ft^2/day)	Reference	Comments
156	FET-3	2	Single well	May-72	120	900.0	19.0	4.70E+01	NR	NR	Ackerman (1991)	Regression analysis
158	FIRE STATION WELL	1	Single well	Nov-61	420	663.0	7.2	9.20E+01	NR	NR	Ackerman (1991)	Regression analysis
158	FIRE STATION WELL	2	Single well	Nov-62	2880	435.0	0.6	7.50E+02	NR	1.00E+05	Ackerman (1991)	Regression analysis
184	HIGHWAY 3	1	Single well	Oct-71	15	350.0	>54	<6.5E0	NR	3.30E+02	Ackerman (1991)	Regression analysis
184	HIGHWAY 3	2	Single well	Oct-71	NA	316.0	<54	>5.9E0	NR	NR	Ackerman (1991)	Regression analysis
186	INEL-1	1	Single well	Mar-83	14	125.0	218.0	5.70E-01	NR	2.24E+02	Prestwich and Bowman (1980)	Interval tested 1511-2206
186	INEL-1	2	Single well	Apr-83	43	20.0	459.0	4.00E-02	NR	1.43E+01	Prestwich and Bowman (1980)	Interval tested 3559-3713
186	INEL-1	3	Single well	Apr-83	NR	75.0	359.0	2.00E-01	NR	7.70E+01	Prestwich and Bowman (1980)	Interval tested 3559-4879
229	LPTF DISPOSAL	1	Single well	Jun-61	1440	615.0	55.5	1.10E+01	NR	3.50E+03	Ackerman (1991)	Theis type curve analysis
231	MTR TEST	1	Single well	Jan-90	10	26.0	0.1	2.60E+02	NR	NR	Ackerman (1991)	Regression analysis
231	MTR TEST	2	Single well	Jul-91	1000	26.1	0.0	1.30E+03	NR	2.00E+05	Ackerman (1991)	Regression analysis
239	NPR TEST	1	Single well	Jan-90	15	29.0	0.1	2.90E+02	NR	NR	Ackerman (1991)	Regression analysis
239	NPR TEST	2	Single well	Jun-91	150	25.7	0.3	9.20E+01	NR	8.60E+03	Ackerman (1991)	Regression analysis
240	NRF-1	1	Single well	Jul-54	120	1010.0	57.0	1.80E+01	NR	NR	Ackerman (1991)	Regression analysis, before deepening
240	NRF-1	2	Single well	Aug-54	1452	1010.0	62.3	1.60E+01	NR	NR	Ackerman (1991)	Regression analysis, before deepening
240	NRF-1	3	Single well	Nov-54	76	1410.0	0.5	2.90E+03	NR	5.10E+05	Ackerman (1991)	Regression analysis
240	NRF-1	4	Single well	Mar-61	1793	2300.0	2.0	1.20E+03	NR	NR	Ackerman (1991)	Regression analysis
241	NRF-2	1	Recovery	Jun-55	1440	1245.0	4.8	2.60E+02	NR	NR	Ackerman (1991)	Regression analysis, recovery
241	NRF-2	2	Single well	Aug-55	2880	1430.0	0.5	2.90E+03	NR	NR	Ackerman (1991)	Regression analysis

Table A-1. (continued).

Well ID[a]	Well Alias	Aquifer Test Number	Aquifer Test Type	Test Date	Test Duration (min)	Discharge Rate (gpm)	Drawdown (ft)	Specific Capacity (gpm/ft)	Hydraulic Conductivity (ft/day)	Trans-missivity (ft^2/day)	Reference	Comments
241	NRF-2	3	Single well	Feb-61	2880	2610.0	1.3	2.00E+03	NR	3.40E+05	Ackerman (1991)	Regression analysis
242	NRF-3	1	Single well	Aug-60	2880	1242.0	4.8	2.60E+02	NR	2.90E+04	Ackerman (1991)	Regression analysis
242	NRF-3	2	Single well	Mar-61	2760	2160.0	15.2	1.40E+02	NR	NR	Ackerman (1991)	Regression analysis
244	NRF-S5G TEST WELL	1	Single well	Nov-67	2880	600.0	0.1	6.00E+03	NR	1.20E+06	Ackerman (1991)	Regression analysis
245	NTP-AREA 2	1	Single well	Apr-64	1413	510.0	0.6	8.60E+02	NR	1.20E+05	Ackerman (1991)	Regression analysis, large barometric fluctuations during test
245	NTP-AREA 2	2	Single well	Apr-64	35	840.0	0.8	1.10E+03	NR	NR	Ackerman (1991)	Regression analysis
246	OMRE	1	Single well	Mar-61	900	314.0	116.7	2.70E+00	NR	1.30E+02	Ackerman (1991)	Regression analysis
248	P&W-1	1	Single well	Aug-61	1440	570.0	0.4	1.60E+03	NR	2.50E+05	Ackerman (1991)	Regression analysis
249	P&W-2	1	Single well	Sep-61	1440	550.0	0.6	9.60E+02	NR	1.40E+05	Ackerman (1991)	Regression analysis
249	P&W-2	2	Single well	Jun-91	180	34.4	0.0	1.70E+03	NR	NR	Ackerman (1991)	Regression analysis
250	P&W-3	1	Single well	Nov-61	1440	630.0	4.5	1.40E+02	NR	1.40E+04	Ackerman (1991)	Regression analysis
256	PSTF TEST	1	Single well	Dec-61	1440	714.0	10.7	6.70E+01	NR	5.90E+03	Ackerman (1991)	Regression analysis
266	QUAKING ASPEN BUTTE	1	Single well	Feb-86	57	5.0	47.0	1.10E-01	NR	3.00E+00	Ackerman (1991)	Neuman type curve
268	RWMC PRODUCTION	1	Single well	Nov-78	1440	412.0	5.5	7.50E+01	NR	6.80E+03	Ackerman (1991)	Regression analysis
274	SITE-06	1	Single well	Nov-63	1423	616.0	25.1	2.50E+01	NR	1.80E+03	Ackerman (1991)	Regression analysis
276	SITE-14	1	Single well	Sep-60	1440	419.0	0.8	5.20E+02	NR	6.70E+04	Ackerman (1991)	Regression analysis
276	SITE-14	2	Single well	Jun-91	180	10.5	0.0	1.10E+03	NR	NR	Ackerman (1991)	Regression analysis
279	SITE-19	1	Single well	Jun-64	360	520.0	21.6	2.40E+01	NR	NR	Ackerman (1991)	Regression analysis, before deepening
279	SITE-19	2	Single well	Aug-64	1235	520.0	17.6	3.00E+01	NR	NR	Ackerman (1991)	Regression analysis, before deepening

Table A-1. (continued).

Well ID[a]	Well Alias	Aquifer Test Number	Aquifer Test Type	Test Date	Test Duration (min)	Discharge Rate (gpm)	Drawdown (ft)	Specific Capacity (gpm/ft)	Hydraulic Conductivity (ft/day)	Trans-missivity (ft^2/day)	Reference	Comments
279	SITE-19	3	Single well	Sep-64	1440	600.0	2.2	2.70E+02	NR	3.10E+04	Ackerman (1991)	Regression analysis
279	SITE-19	4	Single well	Jan-90	10	26.0	0.0	2.60E+02	NR	NR	Ackerman (1991)	Regression analysis
279	SITE-19	5	Single well	Jun-91	120	27.4	0.1	3.40E+02	NR	NR	Ackerman (1991)	Regression analysis
280	SPERT-1	1	Single well	Jan-60	240	377.0	21.1	1.80E+01	NR	1.20E+03	Ackerman (1991)	Regression analysis
281	SPERT-2	1	Single well	Apr-64	1441	540.0	0.9	6.00E+02	NR	8.00E+04	Ackerman (1991)	Regression analysis
339	TAN DRAINAGE DISP. 02	1	Multiple well	Jul-00	230	70.0	0.1	NR	NR	3.40E+04	Dustin (1996)	Type curve analysis, TAN-28 was pumping well
342	TAN-03	1	Slug	May-94	NA	NA	NA	NA	1.41E+02	NA	Wylie (1990)	No data, just a cover letter and table, date is date of letter, average value reported
342	TAN-03	2	Multiple well	Jan-97	55	1500.0	0.1	NR	NR	2.00E+05	Wylie (1993)	Pump well TAN-2, Theis curve
343	TAN-04	1	Slug	May-94	NA	NA	NA	NA	4.90E+01	NA	Wylie (1990)	No data, just a cover letter and table, date is date of letter, average value reported
343	TAN-04	2	Multiple well	Jan-97	55	1500.0	0.1	NA	NR	7.00E+04	Wylie (1993)	Pump well TAN-2, Theis curve
344	TAN-05	1	Slug	May-94	NA	NA	NA	NA	2.26E+02	NA	Wylie (1990)	No data, just a cover letter and table, date is date of letter, average value reported
345	TAN-08	1	Slug	May-94	NA	NA	NA	NA	1.00E+01	NA	Wylie (1990)	No data, just a cover letter and table, date is date of letter, average value reported
346	TAN-09	1	Slug	May-94	NA	NA	NA	NA	2.80E+01	NA	Wylie (1990)	No data, just a cover letter and table, date is date of letter, average value reported
346	TAN-09	2	Multiple well	Jul-00	230	70.0	0.1	NA	NR	3.20E+04	Dustin (1996)	Type curve analysis, TAN-28 was pumping well
347	TAN-10	1	Slug	May-94	NA	NA	NA	NA	2.56E+02	NA	Wylie (1990)	No data, just a cover letter and table, date is date of letter, average value reported
347	TAN-10	2	Multiple well	Jul-00	230	70.0	0.1	NA	NR	1.50E+04	Dustin (1996)	Type curve analysis, TAN-28 was pumping well
348	TAN-10A	1	Slug	May-94	NA	NA	NA	NA	3.10E+01	NA	Wylie (1990)	No data, just a cover letter and table, date is date of letter, average value reported
348	TAN-10A	2	Multiple well	Jul-00	230	70.0	0.1	NA	NR	2.20E+04	Dustin (1996)	Type curve analysis, TAN-28 was pumping well
349	TAN-11	1	Slug	May-94	NA	NA	NA	NA	1.60E+01	NA	Wylie (1990)	No data, just a cover letter and table, date is date of letter, average value reported

Table A-1. (continued).

Well ID[a]	Well Alias	Aquifer Test Number	Aquifer Test Type	Test Date	Test Duration (min)	Discharge Rate (gpm)	Drawdown (ft)	Specific Capacity (gpm/ft)	Hydraulic Conductivity (ft/day)	Trans-missivity (ft^2/day)	Reference	Comments
356	TRA-01	1	Multiple well	Mar-54	1230	1160.0	0.5	2.10E+03	NR	NR	Ackerman (1991)	Regression analysis, multiple well test
356	TRA-01	2	Multiple well	May-54	4320	810.0	0.3	2.40E+03	NR	NR	Ackerman (1991)	Regression analysis, multiple well test
356	TRA-01	3	Multiple well	Jul-61	1060	3990.0	3.8	1.00E+03	NR	NR	Ackerman (1991)	Theis type curve, multiple well test
356	TRA-01	4	Multiple well	Jul-61	2880	3940.0	3.3	1.20E+03	NR	7.30E+05	Ackerman (1991)	Theis type curve, multiple well test
356	TRA-01	5	Single well	Mar-72	57	3300.0	2.1	1.60E+03	NR	NR	Ackerman (1991)	Regression analysis
357	TRA-02	1	Single well	Jan-55	1440	750.0	61.0	1.20E+01	NR	7.90E+02	Ackerman (1991)	Regression analysis
357	TRA-02	2	Single well	Mar-55	1200	800.0	61.0	1.30E+01	NR	NR	Ackerman (1991)	Regression analysis
357	TRA-02	3	Single well	Oct-56	4384	590.0	53.5	1.10E+01	NR	NR	Ackerman (1991)	Regression analysis
358	TRA-03	1	Multiple well	Jun-61	2880	4350.0	2.0	2.20E+03	NR	1.00E+05	Ackerman (1991)	Neuman type curve, multiple well test
358	TRA-03	2	Single well	Nov-71	32	3200.0	0.8	4.20E+03	NR	NR	Ackerman (1991)	Regression analysis
358	TRA-03	3	Single well	Feb-72	52	3900.0	1.3	3.10E+03	NR	NR	Ackerman (1991)	Regression analysis
359	TRA-04	1	Single well	May-68	57	1700.0	2.6	6.50E+02	NR	8.70E+04	Ackerman (1991)	Regression analysis
360	TRA DISPOSAL	1	Single well	Feb-90	15	27.0	0.1	2.70E+02	NR	NR	Ackerman (1991)	Regression analysis, drawdown less than 0.1 ft
360	TRA DISPOSAL	2	Single well	Jul-91	60	24.2	0.1	4.80E+02	NR	6.20E+04	Ackerman (1991)	Regression analysis, drawdown less than 0.1 ft
458	USGS-009	1	Single well	Jul-91	350	18.7	0.0	4.70E+02	NR	5.90E+04	Ackerman (1991)	Regression analysis
460	USGS-011	1	Single well	Sep-93	240	16.7	0.0	1.70E+03	NR	7.00E+04	Ackerman (1991)	Regression analysis, drawdown less than 0.01 ft
461	USGS-012	1	Single well	Aug-54	660	535.0	4.9	1.10E+02	NR	1.10E+04	Ackerman (1991)	Regression analysis
463	USGS-014	1	Single well	Sep-93	210	15.9	0.1	2.00E+02	NR	2.20E+04	Ackerman (1991)	Regression analysis
466	USGS-017	1	Single well	Aug-93	260	31.8	8.7	3.70E+00	NR	4.40E+02	Ackerman (1991)	Neuman type curve

Table A-1. (continued).

Well ID[a]	Well Alias	Aquifer Test Number	Aquifer Test Type	Test Date	Test Duration (min)	Discharge Rate (gpm)	Drawdown (ft)	Specific Capacity (gpm/ft)	Hydraulic Conductivity (ft/day)	Trans-missivity (ft^2/day)	Reference	Comments
473	USGS-024	1	Single well	Aug-56	NA	350.0	4.0	8.80E+01	NR	NR	Ackerman (1991)	Regression analysis
473	USGS-024	2	Single well	Apr-57	11	420.0	3.1	1.40E+02	NR	1.40E+04	Ackerman (1991)	Regression analysis
473	USGS-024	3	Single well	Jan-92	60	7.6	0.0	2.50E+02	NR	NR	Ackerman (1991)	Regression analysis
479	USGS-030A, 30B, 30C	1	Single well	Apr-57	960	250.0	0.1	2.50E+03	NR	4.30E+05	Ackerman (1991)	Regression analysis
480	USGS-031	1	Single well	Jul-57	11140	280.0	1.7	1.60E+02	NR	1.70E+04	Ackerman (1991)	Regression analysis
486	USGS-037	1	Single well	Jul-91	120	7.6	0.1	1.50E+02	NR	1.60E+04	Ackerman (1991)	Regression analysis
489	USGS-040	1	Single well	Jul-91	60	6.4	0.0	6.40E+02	NR	8.70E+04	Ackerman (1991)	Regression analysis
492	USGS-043	1	Single well	Jul-91	60	6.0	0.0	6.00E+02	NR	8.00E+04	Ackerman (1991)	Regression analysis
493	USGS-044	1	Packer	1992-1994	NA	NA	NA	NA	4.20E+00	7.56E+01	Johnson and Fredrick (1997)	Interval 496-514
493	USGS-044	1	Packer	1992-1994	NA	NA	NA	NA	3.80E+00	6.84E+01	Johnson and Fredrick (1997)	Interval 536-554
493	USGS-044	1	Packer	1992-1994	NA	NA	NA	NA	7.00E-01	1.26E+01	Johnson and Fredrick (1997)	Interval 557-575
493	USGS-044	1	Packer	1992-1994	NA	NA	NA	NA	5.00E-02	9.00E-01	Johnson and Fredrick (1997)	Interval 467-482
493	USGS-044	1	Packer	1992-1994	NA	NA	NA	NA	5.00E-02	8.50E-01	Johnson and Fredrick (1997)	Interval 519-535
493	USGS-044	1	Packer	1992-1994	NA	NA	NA	NA	7.00E-04	1.40E-02	Johnson and Fredrick (1997)	Interval 580-600
493	USGS-044	1	Packer	1992-1994	NA	NA	NA	NA	7.00E-05	1.40E-03	Johnson and Fredrick (1997)	Interval 600-620
493	USGS-044	1	Packer	1992-1994	NA	NA	NA	NA	7.00E-06	1.05E-04	Johnson and Fredrick (1997)	Interval 480-495
494	USGS-045	1	Packer	1992-1994	65	11.5	NR	6.00E-01	3.30E-01	4.95E+00	Johnson and Fredrick (1997)	Interval 480-495
494	USGS-045	1	Packer	1992-1994	100	17.7	NR	5.00E-03	4.70E-02	7.05E-01	Johnson and Fredrick (1997)	Interval 500-515
495	USGS-046	1	Packer	1992-1994	81	18.0	0.06	6.00E+00	6.70E+00	1.01E+02	Johnson and Fredrick (1997)	Interval 553-571

Table A-1. (continued).

Well ID[a]	Well Alias	Aquifer Test Number	Aquifer Test Type	Test Date	Test Duration (min)	Discharge Rate (gpm)	Drawdown (ft)	Specific Capacity (gpm/ft)	Hydraulic Conductivity (ft/day)	Trans-missivity (ft^2/day)	Reference	Comments
495	USGS-046	1	Packer	1992-1994	78	18.0	0.57	1.70E+00	4.40E-01	7.92E+00	Johnson and Fredrick (1997)	Interval 531-549
500	USGS-051	1	Single well	Jun-91	120	5.4	0.2	3.60E+01	NR	2.90E+03	Ackerman (1991)	Regression analysis
506	USGS-057	1	Single well	Jun-91	120	5.0	0.0	2.50E+02	NR	2.80E+04	Ackerman (1991)	Regression analysis
507	USGS-058	1	Single well	Jan-90	10	26.0	0.1	2.60E+02	NR	NR	Ackerman (1991)	Regression analysis, drawdown less than 0.1 ft
507	USGS-058	2	Single well	Jun-91	120	25.3	0.1	3.20E+02	NR	3.70E+04	Ackerman (1991)	Regression analysis, drawdown less than 0.1 ft
508	USGS-059	1	Packer	1992-1994	68	20.0	NR	5.00E+00	1.80E+01	3.25E+02	Johnson and Fredrick (1997)	Interval 517-535
508	USGS-059	1	Packer	1992-1994	30	20.0	NR	2.00E-01	1.00E+00	1.80E+01	Johnson and Fredrick (1997)	Interval 538-556
508	USGS-059	1	Packer	1992-1994	36	4.7	0.9	1.00E-02	6.10E-02	1.10E+00	Johnson and Fredrick (1997)	Interval 484-502
508	USGS-059	1	Packer	1992-1994	62	4.0	10.8	8.00E-03	1.10E-03	1.98E-02	Johnson and Fredrick (1997)	Interval 462-480
525	USGS-076	1	Single well	Jan-90	5	26.0	0.1	2.60E+02	NR	NR	Ackerman (1991)	Regression analysis, drawdown less than 0.1 ft
525	USGS-076	2	Single well	Jun-91	120	24.9	0.0	1.20E+03	NR	1.90E+05	Ackerman (1991)	Regression analysis, drawdown less than 0.1 ft
531	USGS-082	1	Single well	Jun-91	130	8.8	0.0	4.40E+02	NR	5.60E+04	Ackerman (1991)	Regression analysis, drawdown less than 0.1 ft
531	USGS-082	2	Single well	Jul-91	120	5.6	0.0	5.60E+02	NR	NR	Ackerman (1991)	Regression analysis, drawdown less than 0.1 ft
532	USGS-083	1	Single well	Jun-91	150	6.0	0.4	1.40E+01	NR	9.00E+02	Ackerman (1991)	Neuman type curve analysis
535	USGS-086	1	Single well	Aug-91	150	19.0	3.4	5.60E+00	NR	3.00E+02	Ackerman (1991)	Neuman type curve analysis
536	USGS-087	1	Single well	Jul-91	121	2.3	0.1	1.80E+01	NR	NR	Ackerman (1991)	Regression analysis
536	USGS-087	2	Single well	Oct-92	170	6.0	0.4	1.60E+01	NR	8.50E+02	Ackerman (1991)	Neuman type curve analysis
536	USGS-087	3	multiple well	May-00	1440	150.0	CNM	CNC	NR	CNC	Wylie (1996)	No measurable dd pumping Pit 9 production
537	USGS-088	1	Single well	Sep-88	60	5.0	24.5	2.00E-01	NR	NR	Ackerman (1991)	Neuman type curve analysis

Table A-1. (continued).

Well ID[a]	Well Alias	Aquifer Test Number	Aquifer Test Type	Test Date	Test Duration (min)	Discharge Rate (gpm)	Drawdown (ft)	Specific Capacity (gpm/ft)	Hydraulic Conductivity (ft/day)	Trans-missivity (ft^2/day)	Reference	Comments
537	USGS-088	2	Single well	Jul-91	270	5.0	28.6	1.70E-01	NR	1.30E+01	Ackerman (1991)	Neuman type curve analysis
537	USGS-088	3	Multiple well	Feb-97	83	15.0	0.3	NA	NR	1.00E+03	Wylie and Hubble (1994)	Pump M4D, obs USGS-88, use recovery data
538	USGS-089	1	Single well	Jul-91	210	4.5	6.3	7.10E-01	NR	NR	Ackerman (1991)	Neuman type curve analysis
538	USGS-089	2	Single well	Jul-91	240	4.5	6.7	6.70E-01	NR	4.90E+01	Ackerman (1991)	Neuman type curve analysis
539	USGS-090	1	Single well	Jul-91	105	4.3	0.5	8.10E+00	NR	4.90E+02	Ackerman (1991)	Regression analysis
539	USGS-090	2	Multiple well	Oct-94	cyclic	200.0	CNM	CNC	NR	CNC	Hubble and Wood (1992)	Pumped RWMC production well, drawdown not discernable in this well from baro fluct, recommended 700 gpm/24-hr test
539	USGS-090	3	Multiple well	Nov-94	cyclic	200.0	CNM	CNC	NR	CNC	Hubble and Wood (1992)	Pumped RWMC production well, drawdown not discernable in this well from baro fluct, recommended 700 gpm/24-hr test
546	USGS-097	1	Single well	Jan-90	5	32.0	0.1	3.20E+02	NR	NR	Ackerman (1991)	Regression analysis, drawdown less than 0.1 ft
546	USGS-097	2	Single well	Jun-91	120	27.4	0.1	5.50E+02	NR	7.10E+04	Ackerman (1991)	Regression analysis, drawdown less than 0.1 ft
547	USGS-098	1	Single well	Jan-90	15	31.0	0.1	3.10E+02	NR	NR	Ackerman (1991)	Regression analysis, drawdown less than 0.1 ft
547	USGS-098	2	Single well	Jun-91	120	18.3	0.0	6.10E+02	NR	8.10E+04	Ackerman (1991)	Regression analysis, drawdown less than 0.1 ft
548	USGS-099	1	Single well	Jan-90	15	29.0	0.1	2.90E+02	NR	NR	Ackerman (1991)	Regression analysis, drawdown less than 0.1 ft
548	USGS-099	2	Single well	Jun-91	90	24.5	0.0	8.20E+02	NR	1.10E+05	Ackerman (1991)	Regression analysis, drawdown less than 0.1 ft
549	USGS-100	1	Single well	Jun-91	180	118.0	0.1	1.40E+02	NR	1.40E+04	Ackerman (1991)	Regression analysis
550	USGS-101	1	Single well	Jan-90	60	12.0	0.1	1.20E+02	NR	NR	Ackerman (1991)	Regression analysis, drawdown less than 0.1 ft
550	USGS-101	2	Single well	Jul-91	150	8.5	0.5	1.70E+01	NR	1.20E+03	Ackerman (1991)	Regression analysis
552	USGS-103	1	Single well	Dec-84	2790	96.0	0.1	9.60E+02	NR	NR	Ackerman (1991)	Regression analysis, drawdown less than 0.1 ft
552	USGS-103	2	Single well	Jun-91	120	21.5	0.0	1.10E+03	NR	1.60E+05	Ackerman (1991)	Regression analysis, drawdown less than 0.1 ft
553	USGS-104	1	Single well	Dec-84	1890	21.0	50.7	4.10E-01	NR	NR	Ackerman (1991)	Regression analysis

Table A-1. (continued).

Well ID[a]	Well Alias	Aquifer Test Number	Aquifer Test Type	Test Date	Test Duration (min)	Discharge Rate (gpm)	Drawdown (ft)	Specific Capacity (gpm/ft)	Hydraulic Conductivity (ft/day)	Trans-missivity (ft^2/day)	Reference	Comments
553	USGS-104	2	Single well	Dec-84	1681	20.0	50.2	4.00E-01	NR	NR	Ackerman (1991)	Regression analysis
553	USGS-104	3	Single well	Jan-90	20	24.0	35.0	6.90E-01	NR	NR	Ackerman (1991)	Regression analysis, drawdown greater than 5 ft
553	USGS-104	4	Single well	Jun-91	150	16.2	23.5	6.90E-01	NR	1.40E+01	Ackerman (1991)	Neuman type curve analysis
554	USGS-105	1	Single well	Jan-85	2880	63.0	0.1	6.30E+02	NR	NR	Ackerman (1991)	Regression analysis, drawdown less than 0.1 ft
554	USGS-105	2	Single well	Jun-91	150	19.0	0.0	6.30E+02	NR	8.50E+04	Ackerman (1991)	Regression analysis, drawdown less than 0.1 ft
555	USGS-106	1	Single well	Jan-85	2855	95.0	0.1	9.50E+02	NR	NR	Ackerman (1991)	Regression analysis, drawdown less than 0.1 ft
555	USGS-106	2	Single well	Jan-90	10	24.0	0.1	2.40E+02	NR	NR	Ackerman (1991)	Regression analysis, drawdown less than 0.1 ft
555	USGS-106	3	Single well	Jun-91	180	21.9	0.0	7.30E+02	NR	1.00E+05	Ackerman (1991)	Regression analysis, drawdown less than 0.1 ft
556	USGS-107	1	Single well	Jun-85	1100	120.0	0.1	1.20E+03	NR	NR	Ackerman (1991)	Regression analysis, drawdown less than 0.1 ft
556	USGS-107	2	Single well	Jul-91	110	5.4	0.0	5.40E+02	NR	7.00E+04	Ackerman (1991)	Regression analysis, drawdown less than 0.1 ft
557	USGS-108	1	Single well	Dec-84	2490	90.0	0.1	9.00E+02	NR	NR	Ackerman (1991)	Regression analysis, drawdown less than 0.1 ft
557	USGS-108	2	Single well	Jun-91	120	20.5	0.0	1.00E+03	NR	1.50E+05	Ackerman (1991)	Regression analysis, drawdown less than 0.1 ft
558	USGS-109	1	Single well	Jul-91	329	16.3	0.0	8.20E+02	NR	1.10E+05	Ackerman (1991)	Regression analysis, drawdown less than 0.1 ft
559	USGS-110	1	Single well	Jul-91	135	4.4	0.0	1.10E+02	NR	1.10E+04	Ackerman (1991)	Regression analysis, drawdown less than 0.1 ft
560	USGS-111	1	Single well	Nov-89	100	26.0	18.8	1.40E+00	NR	NR	Ackerman (1991)	Regression analysis
560	USGS-111	2	Single well	May-91	140	14.2	11.0	1.30E+00	NR	2.20E+01	Ackerman (1991)	Neuman type curve analysis
561	USGS-112	1	Single well	Nov-89	30	26.0	0.1	2.60E+02	NR	NR	Ackerman (1991)	Regression analysis, drawdown less than 0.1 ft
561	USGS-112	2	Single well	May-91	120	24.8	0.1	5.00E+02	NR	6.40E+04	Ackerman (1991)	Regression analysis, drawdown less than 0.1 ft
562	USGS-113	1	Single well	Nov-89	30	26.0	0.1	2.60E+02	NR	NR	Ackerman (1991)	Regression analysis, drawdown less than 0.1 ft

Table A-1. (continued).

Well ID[a]	Well Alias	Aquifer Test Number	Aquifer Test Type	Test Date	Test Duration (min)	Discharge Rate (gpm)	Drawdown (ft)	Specific Capacity (gpm/ft)	Hydraulic Conductivity (ft/day)	Trans-missivity (ft^2/day)	Reference	Comments
562	USGS-113	2	Single well	Jun-91	120	24.6	0.0	1.20E+03	NR	1.90E+05	Ackerman (1991)	Regression analysis, drawdown less than 0.1 ft
563	USGS-114	1	Single well	Nov-89	40	6.2	16.3	3.80E-01	NR	1.00E+01	Ackerman (1991)	Neuman type curve analysis
563	USGS-114	2	Single well	May-91	190	8.4	26.2	3.20E-01	NR	NR	Ackerman (1991)	Regression analysis
564	USGS-115	1	Single well	Nov-89	145	18.0	14.4	1.30E+00	NR	NR	Ackerman (1991)	Neuman type curve analysis
564	USGS-115	2	Single well	May-91	130	15.0	14.0	1.10E+00	NR	3.20E+01	Ackerman (1991)	Neuman type curve analysis
564	USGS-115	3	Single well	May-91	180	17.1	14.7	1.20E+00	NR	NR	Ackerman (1991)	Neuman type curve analysis
565	USGS-116	1	Single well	Nov-89	60	24.0	9.1	2.60E+00	NR	NR	Ackerman (1991)	Neuman type curve analysis
565	USGS-116	2	Single well	May-91	209	20.7	8.1	2.60E+00	NR	1.50E+02	Ackerman (1991)	Neuman type curve analysis
566	USGS-117	1	Single well	Dec-91	140	7.2	20.3	3.60E-01	NR	1.40E+01	Ackerman (1991)	Neuman type curve analysis
568	USGS-119	1	Single well	Dec-91	90	3.2	68.8	4.70E-02	NR	1.10E+00	Ackerman (1991)	Regression analysis
568	USGS-119	2	Multiple well	May-00	1440	150.0	CNM	CNC	NR	CNC	Wylie (1996)	No measurable dd pumping Pit 9 production
569	USGS-120	1	Single well	Dec-91	60	21.1	0.0	1.40E+03	NR	2.20E+05	Ackerman (1991)	Regression analysis, drawdown less than 0.1 ft
569	USGS-120	2	Multiple well	Jul-98	51840	3600.0	NA	NA	NR	1.30E+06	Wylie et al. (1995)	Pump LSIT test well (RWMC-PRO-A-064), Kv/Kh = 6E1
595	WATER SUPPLY FOR INEL 1	1	Single well	Jan-83	1412	68.0	20.5	3.30E+00	NR	NR	Ackerman (1991)	Neuman type curve analysis
595	WATER SUPPLY FOR INEL 1	2	Single well	Jan-90	7	30.0	4.2	7.10E+00	NR	NR	Ackerman (1991)	Regression analysis
595	WATER SUPPLY FOR INEL 1	3	Single well	Jun-91	240	26.7	6.4	4.20E+00	NR	3.70E+02	Ackerman (1991)	Neuman type curve analysis
748	TAN-12	1	Multiple well	Jul-00	230	70.0	0.1	NA	NR	3.50E+04	Dustin (1996)	Type curve analysis, TAN-28 was pumping well
765	M1SA	1	Single well	Nov-96	68	3.4	8.4	4.10E-01	NR	2.00E+01	Wylie and Hubble (1994)	Cooper-Jacob

Table A-1. (continued).

Well ID[a]	Well Alias	Aquifer Test Number	Aquifer Test Type	Test Date	Test Duration (min)	Discharge Rate (gpm)	Drawdown (ft)	Specific Capacity (gpm/ft)	Hydraulic Conductivity (ft/day)	Trans-missivity (ft^2/day)	Reference	Comments
766	M3S	1	Single well	Nov-96	39	4.3	0.2	1.90E+01	NR	1.00E+03	Wylie and Hubble (1994)	Regression analysis
766	M3S	2	Multiple well	Feb-96	398	200.0	CNM	CNC	NR	CNC	Wylie and Hubble (1994)	Pump RWMC production well. Obs in this well, drawdown detectable but not discernable from baro fluctuations
766	M3S	3	Multiple well	May-00	1440	150.0	CNM	CNC	NR	CNC	Wylie (1996)	No measurable dd pumping Pit 9 production
767	M4D	1	Multiple well	Feb-97	83	15.0	>80	CNC	NR	4.00E+00	Wylie and Hubble (1994)	Cooper-Jacob, this was pumping well. USGS-88 was observation well
768	M6S	1	Single well	Feb-97	62	2.6	3.0	8.80E-01	NR	3.00E+01	Wylie and Hubble (1994)	Regression analysis
769	M7S	1	Single well	Feb-97	75	3.6	0.3	1.40E+01	NR	1.00E+03	Wylie and Hubble (1994)	Cooper-Jacob
770	M10S	1	Single well	Nov-01	82	3.1	21.5	1.40E-01	NR	4.00E+00	Wylie and Hubble (1994)	Regression analysis, Cooper-Jacob
790	TAN-18	1	Packer	Sep-96	288.0	7.8	NR	NR	NR	7.30E+03	Wylie (1993)	Test interval 448-490
790	TAN-18	2	Slug	Jan-97	NA	NA	NA	NA	NR	6.00E+03	Wylie (1993)	Test interval 448-516
791	TAN-19	1	Packer	Jul-92	NR	6.3	CNM	CNC	NR	CNC	Wylie (1993)	Test interval 335-359, no measuable dd
791	TAN-19	2	Packer	Aug-92	NR	5.9	5.0	1.2	NR	2.00E+02	Wylie (1993)	Test interval 448-490,
791	TAN-19	3	Slug	Jan-93	NA	NA	NA	NA	NR	6.00E+00	Wylie (1993)	Test interval 390-418,
791	TAN-19	4	Multiple well	Jan-93	55	1500.0	0.1	NA	NR	4.00E+05	Wylie (1993)	Pump well TAN-2, Theis curve
792	TAN-20	1	Packer	Jun-92	4.3	3.2	68.0	0.0	NR	4.00E+00	Wylie (1993)	Test interval 258-271
792	TAN-20	2	Packer	Jun-92	144.0	7.4	13.0	0.6	NR	4.00E+01	Wylie (1993)	Test interval 346-366
792	TAN-20	3	Packer	Jun-92	NR	CNM	CNM	CNC	NR	CNC	Wylie (1993)	Test interval 391-400, pumped dry before water reached land surface
793	TAN-21	1	Packer	Jun-92	288.8	6.5	0.9	7.2	NR	2.00E+02	Wylie (1993)	Test interval 208-261
793	TAN-21	2	Packer	Jun-92	14.4	5.9	38.0	0.2	NR	2.00E+01	Wylie (1993)	Test interval 250-298
793	TAN-21	3	Packer	Jun-92	2.9	6.5	1.8	3.6	NR	3.00E+02	Wylie (1993)	Test interval 305-345

Table A-1. (continued).

Well ID[a]	Well Alias	Aquifer Test Number	Aquifer Test Type	Test Date	Test Duration (min)	Discharge Rate (gpm)	Drawdown (ft)	Specific Capacity (gpm/ft)	Hydraulic Conductivity (ft/day)	Trans-missivity (ft^2/day)	Reference	Comments
793	TAN-21	4	Packer	Jun-92	14.4	6.5	0.1	65.0	NR	5.00E+02	Wylie (1993)	Test interval 385-403
795	TAN-22A	1	Packer	Jun-92	144.0	7.7	CNM	CNC	NR	7.00E+03	Wylie (1993)	Test interval 495-525, no measuable dd, min T reported
795	TAN-22A	2	Slug	Jan-93	NA	NA	NA	NA	NR	4.00E+03	Wylie (1993)	Test interval 505-534
796	TAN-23	1	Packer	Jun-92	288.0	7.7	CNM	CNC	NR	7.00E+03	Wylie (1993)	Test interval 366-381.5, no measuable dd, min T reported
796	TAN-23	2	Packer	Jun-92	288.0	7.9	CNM	CNC	NR	7.00E+03	Wylie (1993)	Test interval 429-439, no measuable dd, min T reported
796	TAN-23	3	Packer	Jun-92	360.0	7.5	CNM	CNC	NR	7.00E+03	Wylie (1993)	Test interval 447-472, no measuable dd, min T reported
797	TAN-23A	1	Slug	Jan-93	NA	NA	NA	NA	NR	2.00E+03	Wylie (1993)	Test interval 429-462
798	TAN-24	1	Packer	Aug-92	2.9	7.2	0.4	18.9	NR	3.00E+03	Wylie (1993)	Test interval 288-324, leakage around packer, max T reported
798	TAN-24	2	Packer	Aug-92	4.3	7.6	2.5	3.0	NR	2.00E+02	Wylie (1993)	Test interval 335-398
799	TAN-24A	1	Packer	Aug-92	72.0	7.6	CNM	CNC	NR	7.00E+03	Wylie (1993)	Test interval 445-456, no measuable dd, min T reported
799	TAN-24A	2	Slug	Jan-93	NA	NA	NA	NA	NR	4.00E+03	Wylie (1993)	Test interval 213-243
1008	TANT-MON-A-028	1	Multiple well	Jul-00	230	70.0	5.3	1.33E+01	NR	1.70E+04	Dustin (1996)	Dist-drawdown, this was the pumping well
1009	TANT-MON-A-027	1	Multiple well	Jul-00	230	70.0	0.1	NA	NR	1.80E+04	Dustin (1996)	Type curve analysis, TAN-28 was pumping well
1010	TANT-MON-A-029	1	Multiple well	Jul-00	230	70.0	0.1	NA	NR	2.20E+04	Dustin (1996)	Type curve analysis, TAN-28 was pumping well
1012	TANT-MON-A-030A	1	Multiple well	Jul-00	230	70.0	0.2	NA	NR	1.70E+04	Dustin (1996)	Type curve analysis, TAN-28 was pumping well
1079	NRF-MON-A-008	1	Single well	Aug-95	30	22.0	CNM	3.00E+03	NR	7.70E+04	Golder (1995)	Very little measurable drawdown
1080	NRF-MON-A-009	1	Single well	Aug-95	70	30.0	CNM	3.30E+03	NR	1.00E+05	Golder (1995)	T is minimum value as minimal drawdown was measured
1081	NRF-MON-A-010	1	Single well	Aug-95	32	30.0	CNM	NR	NR	1.00E+05	Golder (1995)	T is minimum value as minimal drawdown was measured
1082	NRF-MON-A-011	1	Single well	Aug-95	42	28.0	CNM	2.80E+03	NR	9.80E+04	Golder (1995)	T is minimum value as minimal drawdown was measured

Table A-1. (continued).

Well ID[a]	Well Alias	Aquifer Test Number	Aquifer Test Type	Test Date	Test Duration (min)	Discharge Rate (gpm)	Drawdown (ft)	Specific Capacity (gpm/ft)	Hydraulic Conductivity (ft/day)	Trans-missivity (ft^2/day)	Reference	Comments
1083	NRF-MON-A-012	1	Single well	Aug-95	30	30.0	CNM	8.57E+02	NR	3.00E+04	Golder (1995)	T is minimum value as minimal drawdown was measured
1084	NRF-MON-A-013	1	Single well	Aug-95	100	1.1	10.2	1.10E-01	NR	3.77E+00	Golder (1995)	Cooper-Jacob
1117	TANT-MON-A-024	1	Multiple well	Jul-00	230	70.0	0.1	NA	NR	2.10E+04	Dustin (1996)	Type curve analysis, TAN-28 was pumping well
1118	TANT-MON-A-025	1	Multiple well	Jul-00	230	70.0	0.1	NA	NR	2.70E+04	Dustin (1996)	Type curve analysis, TAN-28 was pumping well
1131	RWMC-MON-A-065	1	Multiple well	Jul-98	51840	3600.0	NR	NA	NR	3.00E+06	Wylie et al. (1995)	Upper section, 614-735 ft bgs, pump LSIT test well (RWMC-PRO-A-064), Kv/Kh = 1e2
1131	RWMC-MON-A-065	2	Multiple well	Jul-98	51840	3600.0	NR	NA	NR	4.50E+06	Wylie et al. (1995)	Lower section, 740-1000 ft bgs, pump LSIT test well (RWMC-PRO-A-064)
1132	RWMC-MON-A-066	1	Multiple well	Jul-98	51840	3600.0	CNM	NA	NR	3.00E+06	Wylie et al. (1995)	Upper section, 621-777 ft bgs, pump LSIT test well (RWMC-PRO-A-064), Kv/Kh = 3e1
1132	RWMC-MON-A-066	2	Multiple well	Jul-98	51840	3600.0	NR	NA	NR	CNC	Wylie et al. (1995)	Lower section, 782-1000 ft bgs, pump LSIT test well (RWMC-PRO-A-064), no drawdown measured
1162	RWMC-OBS-A-084	1	Single well	Apr-98	195	2300.0	4.8	8.77E+02	NR	5.00E+05	NA	Step test, maxQ 2300 gpm, T and spec cap from cooper-jacob analysis of 1000 gpm step
1212	SOUTH-MON-A-001	1	Single well	Dec-02	42	9.0	0.7	1.30E+01	4.61E+01	2.44E+03	Jolley (2003)	Theis type curve analysis, M11S
1214	SOUTH-MON-A-003	1	Single well	Dec-02	22	9.0	1.6	6.00E+00	8.50E+00	3.40E+02	Jolley (2003)	Regression analysis, M13S
1215	SOUTH-MON-A-004	1	Single well	Dec-02	101	6.0	2.1	3.00E+00	8.70E+00	2.09E+02	Jolley (2003)	Theis type curve analysis, M14S
1219	TANT-INJ-A-003	1	Multiple well	Jul-00	230	70.0	0.1	NA	NR	2.10E+04	Dustin (1996)	Type curve analysis, TAN-28 was pumping well
1327	RWMC-MON-A-162	1	Single well	Dec-02	57	22.0	5.6	4.00E+00	1.20E+01	5.04E+02	Jolley (2003)	Theis type curve analysis, M17S
1337	SOUTH-MON-A-010	1	Single well	Dec-02	56	6.0	1.0	6.00E+00	3.00E+01	3.12E+02	Jolley (2003)	Theis type curve analysis, M14S
1338	SOUTH-MON-A-009	1	Single well	Dec-02	64	7.0	0.5	1.40E+01	4.60E+01	9.27E+02	Jolley (2003)	Regression analysis, M15S
SWGM1	Lindholm Well 20	1	Single well	NA	4440	5450.0	2.9	1.88E+03	NR	3.09E+05	Lindholm (1996)	Well logs downloaded from IDWR database
SWGM2	Lindholm Well 21	1	Single well	NA	4440	7160.0	2.9	2.47E+03	NR	4.26E+05	Lindholm (1996)	Well logs downloaded from IDWR database
SWGM3	Lindholm Well 23	1	Single well	NA	4800	2560.0	NA	NA	NR	7.10E+05	Lindholm (1996)	Well logs downloaded from IDWR database

Table A-1. (continued).

Well ID[a]	Well Alias	Aquifer Test Number	Aquifer Test Type	Test Date	Test Duration (min)	Discharge Rate (gpm)	Drawdown (ft)	Specific Capacity (gpm/ft)	Hydraulic Conductivity (ft/day)	Trans-missivity (ft^2/day)	Reference	Comments
SWG M4	Butte City	1	Single well	Jun-60	NR	125.0	15.0	8.33E+00	NR	5.01E+02	IDWR	Well logs downloaded from IDWR database, regression analysis
SWG M5	Howe Water District	1	Single well	Sep-75	12	50.0	30.0	1.67E+00	NR	7.44E+01	IDWR	Well logs downloaded from IDWR database, regression analysis
SWG M6	Russell Mays	1	Single well	May-78	3	3100.0	100.0	3.10E+01	NR	2.38E+03	IDWR	Well logs downloaded from IDWR database, regression analysis
SWG M7	Bob Mays	1	Single well	Nov-79	11	1600.0	277.0	5.78E+00	NR	3.25E+02	IDWR	Well logs downloaded from IDWR database, regression analysis
SWG M8	Roe Ownes	1	Single well	May-73	2	30.0	0.1	3.00E+02	NR	3.51E+04	IDWR	Well logs downloaded from IDWR database, regression analysis
SWG M9	ID HWY Dept	1	Single well	Oct-70	24	115.0	0.1	1.15E+03	NR	1.72E+05	IDWR	Well logs downloaded from IDWR database, regression analysis
SWG M10	Western Potato #2	1	Single well	Mar-65	NR	4000.0	0.1	4.00E+04	NR	1.16E+07	IDWR	Well logs downloaded from IDWR database, regression analysis
SWG M11	James Rire	1	Single well	Aug-74	NR	20.0	0.1	2.00E+02	NR	2.17E+04	IDWR	Well logs downloaded from IDWR database, regression analysis
SWG M12	Leon Dance	1	Single well	Apr-79	540	2400.0	35.0	6.86E+01	NR	6.10E+03	IDWR	Well logs downloaded from IDWR database, regression analysis
SWG M13	BAS	1	Single well	Dec-87	60	40.0	10.0	4.00E+00	NR	2.10E+02	IDWR	Well logs downloaded from IDWR database, regression analysis
SWG M14	Elmer Lamprecht	1	Single well	Apr-79	NR	80.0	0.1	8.00E+02	NR	1.12E+05	IDWR	Well logs downloaded from IDWR database, regression analysis
SWG M15	TS Vanderford1	1	Single well	May-53	120	2880.0	20.0	1.44E+02	NR	1.47E+04	IDWR	Well logs downloaded from IDWR database, regression analysis
SWG M16	TS Vanderford2	1	Single well	Feb-53	120	2160.0	20.0	1.08E+02	NR	1.04E+04	IDWR	Well logs downloaded from IDWR database, regression analysis
SWG M17	IF BLM	1	Single well	Jul-70	60	15.0	0.1	1.50E+02	NR	1.54E+04	IDWR	Well logs downloaded from IDWR database, regression analysis
SWG M18	Charles Behrend	1	Single well	Jul-71	60	1500.0	2.0	7.50E+02	NR	1.04E+05	IDWR	Well logs downloaded from IDWR database, regression analysis
SWG M19	Don Everingham	1	Single well	Apr-76	60	35.0	8.0	4.38E+00	NR	2.34E+02	IDWR	Well logs downloaded from IDWR database, regression analysis
SWG M20	Bill Dishman	1	Single well	Jun-74	60	40.0	9.0	4.44E+00	NR	2.38E+02	IDWR	Well logs downloaded from IDWR database, regression analysis
SWG M21	Ralph Furniss	1	Single well	Apr-68	150	1800.0	0.1	1.80E+04	NR	4.49E+06	IDWR	Well logs downloaded from IDWR database, regression analysis
SWG M22	Dan Polatis	1	Single well	May-72	NR	2500.0	0.1	2.50E+04	NR	6.63E+06	IDWR	Well logs downloaded from IDWR database, regression analysis

Table A-1. (continued).

Well ID[a]	Well Alias	Aquifer Test Number	Aquifer Test Type	Test Date	Test Duration (min)	Discharge Rate (gpm)	Drawdown (ft)	Specific Capacity (gpm/ft)	Hydraulic Conductivity (ft/day)	Trans-missivity (ft^2/day)	Reference	Comments
SWG M23	BLM	1	Single well	Oct-72	900	35.0	0.1	3.50E+02	NR	4.21E+04	IDWR	Well logs downloaded from IDWR database, regression analysis
	Pit 9 Production	1	Single well	Apr-00	90	175.0	56.9	3.08E+00	NR	1.54E+02	Wylie (1996)	Step test, well could not supprt further steps
	Pit 9 Production	2	Multiple well	May-00	1440	150.0	40.0	3.75E+00	NR	1.00E+03	Wylie (1996)	This was the pumping well, observation wells were USGS-87, USGS-119, and M3S

a. From the Hydrogeologic Data Repository at the Idaho National Laboratory Site.

CNC = could not calculate
CNM = could not measure
IDWR = Idaho Department of Water Resources
NA = not applicable or not available
NR = not reported

Table A-2. Well completion information and representative hydraulic conductivity for wells within the sitewide groundwater model study area.

Well ID[a]	Well Alias	Ground Surface Elev (ft AMSL)	Reported Trans-missivity (ft/day)	Screen Top 1 (ft bgs)	Screen Bottom 1 (ft bgs)	Open Thick-ness 1 (ft)	Screen Top 2 (ft bgs)	Screen Bottom 2 (ft bgs)	Open Thick-ness 2 (ft)	Screen Top 3 (ft bgs)	Screen Bottom 3 (ft bgs)	Open Thick-ness 3 (ft)	Screen Top 4 (ft bgs)	Screen Bottom 4 (ft bgs)	Open Thick-ness 4 (ft)	Screen Top 5 (ft bgs)	Screen Bottom 5 (ft bgs)	Open Thick-ness 5 (ft)	Total Exposed Thick-ness (ft)	Hydraulic Conductivity (ft/day)
69	ANP-01	4789.6	4.00E+05	200.0	355.0	155.0	—	—	0.0	—	—	0.0	—	—	0.0	—	—	0.0	155.0	2.58E+03
70	ANP-02	4793.4	1.60E+04	235.0	335.0	100.0	—	—	0.0	—	—	0.0	—	—	0.0	—	—	0.0	100.0	1.60E+02
71	ANP-03	4782.2	2.20E+04	180.0	244.0	64.0	269.0	305.0	36.0	—	—	0.0	—	—	0.0	—	—	0.0	100.0	2.20E+02
72	ANP-04	4791.5	1.60E+02	219.0	319.0	100.0	—	—	0.0	—	—	0.0	—	—	0.0	—	—	0.0	100.0	1.60E+00
73	ANP-05	4874.0	1.50E+05	296.2	316.4	20.2	332.1	389.9	57.8	—	—	0.0	—	—	0.0	—	—	0.0	78.0	1.92E+03
74	ANP-06	4797.5	5.00E+05	210.6	255.6	45.0	265.7	295.8	30.2	—	—	0.0	—	—	0.0	—	—	0.0	75.2	6.65E+03
77	ANP-09	4786.4	6.60E+03	236.6	313.8	77.2	—	—	0.0	—	—	0.0	—	—	0.0	—	—	0.0	77.2	8.55E+01
80	ARA-1	5058.3	1.10E+05	618.3	640.8	22.5	662.0	704.2	42.2	723.1	766.4	43.3	—	—	0.0	—	—	0.0	108.0	1.02E+03
81	ARA-3	5051.9	2.10E+04	978.0	1340.0	362.0	—	—	0.0	—	—	0.0	—	—	0.0	—	—	0.0	362.0	5.80E+01
82	ARBOR TEST	5164.0	5.60E+05	679.9	730.5	50.6	737.5	787.0	49.5	—	—	0.0	—	—	0.0	—	—	0.0	100.1	5.60E+03
94	CFA-2	4931.2	1.70E+02	521.0	651.0	130.0	661.0	681.0	20.0	—	—	0.0	—	—	0.0	—	—	0.0	150.0	1.13E+00
98	CPP-01	4912.1	7.30E+04	459.9	485.9	26.0	527.4	576.8	49.4	—	—	0.0	—	—	0.0	—	—	0.0	75.4	9.68E+02
99	CPP-02	4913.4	1.60E+05	551.1	600.3	49.2	—	—	0.0	—	—	0.0	—	—	0.0	—	—	0.0	49.2	3.26E+03
100	CPP-03	4916.0	7.60E+05	412.0	452.0	40.0	490.0	593.0	103.0	—	—	0.0	—	—	0.0	—	—	0.0	143.0	5.31E+03
101	CPP-04	4909.3	2.50E+02	450.0	700.0	250.0	—	—	0.0	—	—	0.0	—	—	0.0	—	—	0.0	250.0	1.00E+00
149	EBR-1	5024.1	1.30E+03	600.0	750.0	150.0	750.0	1075.0	325.0	—	—	0.0	—	—	0.0	—	—	0.0	475.0	2.74E+00
150	EBR-II #1	5121.2	5.20E+05	645.0	745.0	100.0	—	—	0.0	—	—	0.0	—	—	0.0	—	—	0.0	100.0	5.20E+03
151	EBR-II #2	5121.7	1.10E+04	650.0	750.0	100.0	—	—	0.0	—	—	0.0	—	—	0.0	—	—	0.0	100.0	1.10E+02
153	EOCR PROD. WELL	4939.9	1.80E+05	1051.6	1237.0	185.4	—	—	0.0	—	—	0.0	—	—	0.0	—	—	0.0	185.4	9.71E+02
154	FET-1	4780.7	3.10E+04	230.0	330.0	100.0	—	—	0.0	—	—	0.0	—	—	0.0	—	—	0.0	100.0	3.10E+02
155	FET-2	4780.7	1.10E+04	209.3	448.4	239.1	—	—	0.0	—	—	0.0	—	—	0.0	—	—	0.0	239.1	4.60E+01
156	FET-3	4782.7	1.50E+04	174.6	294.5	119.9	—	—	0.0	—	—	0.0	—	—	0.0	—	—	0.0	119.9	1.25E+02
158	FIRE STATION WELL	4901.1	1.00E+05	427.0	466.8	39.9	501.3	511.3	10.0	—	—	0.0	—	—	0.0	—	—	0.0	49.9	2.01E+03
184	HIGHWAY 3	4981.6	3.30E+02	680.0	750.0	70.0	—	—	0.0	—	—	0.0	—	—	0.0	—	—	0.0	70.0	4.71E+00
229	LPTF DISPOSAL	4787.1	3.50E+03	189.5	313.9	124.4	—	—	0.0	—	—	0.0	—	—	0.0	—	—	0.0	124.4	2.81E+01
231	MTR TEST	4917.1	2.00E+05	447.0	588.0	141.0	—	—	0.0	—	—	0.0	—	—	0.0	—	—	0.0	141.0	1.42E+03
239	NPR TEST	4933.1	8.60E+03	504.0	532.0	28.0	—	—	0.0	—	—	0.0	—	—	0.0	—	—	0.0	28.0	3.07E+02

Table A-2. (continued).

Well ID[a]	Well Alias	Ground Surface Elev (ft AMSL)	Reported Trans-missivity (ft/day)	Screen Top 1 (ft bgs)	Screen Bottom 1 (ft bgs)	Open Thick-ness 1 (ft)	Screen Top 2 (ft bgs)	Screen Bottom 2 (ft bgs)	Open Thick-ness 2 (ft)	Screen Top 3 (ft bgs)	Screen Bottom 3 (ft bgs)	Open Thick-ness 3 (ft)	Screen Top 4 (ft bgs)	Screen Bottom 4 (ft bgs)	Open Thick-ness 4 (ft)	Screen Top 5 (ft bgs)	Screen Bottom 5 (ft bgs)	Open Thick-ness 5 (ft)	Total Exposed Thick-ness (ft)	Hydraulic Conductivity (ft/day)
240	NRF-1	4848.7	5.10E+05	394.0	478.0	84.0	483.0	530.0	47.0	—	—	0.0	—	—	0.0	—	—	0.0	131.0	3.89E+03
241	NRF-2	4849.7	3.40E+05	372.6	397.3	24.7	421.9	448.1	26.2	497.1	523.2	26.1	—	—	0.0	—	—	0.0	77.0	4.42E+03
242	NRF-3	4850.2	2.90E+04	484.1	543.2	59.1	—	—	0.0	—	—	0.0	—	—	0.0	—	—	0.0	59.1	4.91E+02
244	NRF-S5G TEST WELL	4848.0	1.20E+06	1298.0	1340.0	42.0	—	—	0.0	—	—	0.0	—	—	0.0	—	—	0.0	42.0	2.86E+04
245	NTP-AREA 2	5128.4	1.20E+05	675.9	721.9	46.0	741.9	813.8	71.9	843.8	875.8	31.9	—	—	0.0	—	—	0.0	149.8	8.01E+02
246	OMRE	4936.4	1.30E+02	535.0	626.0	91.0	920.0	938.0	18.0	—	—	0.0	—	—	0.0	—	—	0.0	109.0	1.19E+00
248	P&W-1	4895.6	2.50E+05	321.9	371.9	50.0	—	—	0.0	—	—	0.0	—	—	0.0	—	—	0.0	50.0	5.00E+03
249	P&W-2	4890.9	1.40E+05	312.6	382.7	70.1	—	—	0.0	—	—	0.0	—	—	0.0	—	—	0.0	70.1	2.00E+03
250	P&W-3	4885.3	1.40E+04	322.3	401.3	78.9	—	—	0.0	—	—	0.0	—	—	0.0	—	—	0.0	78.9	1.77E+02
256	PSTF TEST	4786.4	5.90E+03	189.8	315.9	126.1	—	—	0.0	—	—	0.0	—	—	0.0	—	—	0.0	126.1	4.68E+01
266	QUAKING ASPEN BUTTE	5190.0	3.00E+00	1036.0	1074.0	38.0	—	—	0.0	—	—	0.0	—	—	0.0	—	—	0.0	38.0	7.89E-02
268	RWMC PRODUCTION	5007.2	6.80E+03	590.0	610.0	20.0	625.0	635.0	10.0	—	—	0.0	—	—	0.0	—	—	0.0	30.0	2.27E+02
274	SITE-06	4836.6	1.80E+03	366.0	464.3	98.3	—	—	0.0	—	—	0.0	—	—	0.0	—	—	0.0	98.3	1.83E+01
276	SITE-14	4793.9	6.70E+04	535.0	716.7	181.7	—	—	0.0	—	—	0.0	—	—	0.0	—	—	0.0	181.7	3.69E+02
279	SITE-19	4926.3	3.10E+04	472.4	512.4	39.9	532.6	572.5	39.9	596.7	616.7	20.0	780.7	862.6	81.9	—	—	0.0	181.7	1.71E+02
280	SPERT-1	4923.2	1.20E+03	481.5	491.5	10.0	521.7	541.7	20.0	551.7	581.7	30.0	596.7	616.7	20.0	631.7	651.7	20.0	100.0	1.20E+01
281	SPERT-2	4923.7	8.00E+04	951.0	1217.0	266.0	—	—	0.0	—	—	0.0	—	—	0.0	—	—	0.0	266.0	3.01E+02
339	TAN DRAINAGE DISP. 02	4779.9	3.40E+04	116.0	125.6	9.6	201.4	221.5	20.1	231.5	251.2	19.7	—	—	0.0	—	—	0.0	49.4	6.88E+02
342	TAN-03	4790.9	2.00E+05	231.4	263.7	32.3	—	—	0.0	—	—	0.0	—	—	0.0	—	—	0.0	32.3	6.19E+03
343	TAN-04	4801.3	7.00E+04	213.5	245.0	31.5	—	—	0.0	—	—	0.0	—	—	0.0	—	—	0.0	31.5	2.22E+03
346	TAN-09	4780.7	3.20E+04	300.4	322.4	22.0	—	—	0.0	—	—	0.0	—	—	0.0	—	—	0.0	22.0	1.45E+03
347	TAN-10	4780.3	1.50E+04	213.6	245.3	31.7	—	—	0.0	—	—	0.0	—	—	0.0	—	—	0.0	31.7	4.74E+02
348	TAN-10A	4780.7	2.20E+04	216.4	249.5	33.1	—	—	0.0	—	—	0.0	—	—	0.0	—	—	0.0	33.1	6.65E+02
356	TRA-01	4913.0	7.30E+05	480.5	580.5	100.0	—	—	0.0	—	—	0.0	—	—	0.0	—	—	0.0	100.0	7.30E+03
357	TRA-02	4914.8	7.90E+02	490.0	566.0	76.0	558.0	567.0	9.0	640.0	740.0	100.0	—	—	0.0	—	—	0.0	185.0	4.27E+00
358	TRA-03	4918.0	1.00E+05	470.0	497.0	27.0	518.0	592.0	74.0	—	—	0.0	—	—	0.0	—	—	0.0	101.0	9.90E+02
359	TRA-04	4913.5	8.70E+04	900.0	965.0	65.0	—	—	0.0	—	—	0.0	—	—	0.0	—	—	0.0	65.0	1.34E+03

Table A-2. (continued).

Well ID[a]	Well Alias	Ground Surface Elev (ft AMSL)	Reported Trans-missivity (ft/day)	Screen Top 1 (ft bgs)	Screen Bottom 1 (ft bgs)	Open Thick-ness 1 (ft)	Screen Top 2 (ft bgs)	Screen Bottom 2 (ft bgs)	Open Thick-ness 2 (ft)	Screen Top 3 (ft bgs)	Screen Bottom 3 (ft bgs)	Open Thick-ness 3 (ft)	Screen Top 4 (ft bgs)	Screen Bottom 4 (ft bgs)	Open Thick-ness 4 (ft)	Screen Top 5 (ft bgs)	Screen Bottom 5 (ft bgs)	Open Thick-ness 5 (ft)	Total Exposed Thick-ness (ft)	Hydraulic Conductivity (ft/day)
360	TRA DISPOSAL	4923.1	6.20E+04	512.0	697.0	185.0	935.0	1070.0	135.0	1183.0	1267.0	84.0	—	—	0.0	—	—	0.0	404.0	1.53E+02
458	USGS-009	5031.9	5.90E+04	620.1	650.1	30.0	—	—	0.0	—	—	0.0	—	—	0.0	—	—	0.0	30.0	1.97E+03
460	USGS-011	5066.9	7.00E+04	672.5	703.8	31.3	—	—	0.0	—	—	0.0	—	—	0.0	—	—	0.0	31.3	2.23E+03
461	USGS-012	4819.6	1.10E+04	587.0	692.0	105.0	—	—	0.0	—	—	0.0	—	—	0.0	—	—	0.0	105.0	1.05E+02
463	USGS-014	5133.1	2.20E+04	720.0	746.0	26.0	—	—	0.0	—	—	0.0	—	—	0.0	—	—	0.0	26.0	8.46E+02
466	USGS-017	4834.0	4.40E+02	437.8	444.8	7.0	495.8	498.0	2.2	—	—	0.0	—	—	0.0	—	—	0.0	9.2	4.78E+01
473	USGS-024	4795.8	1.40E+04	255.0	265.0	10.0	270.0	275.0	5.0	285.0	325.0	40.0	—	—	0.0	—	—	0.0	55.0	2.55E+02
479	USGS-030A, 30B, 30C	4794.8	4.30E+05	290.0	300.0	10.0	392.5	397.5	5.0	717.5	722.5	5.0	725.0	750.0	25.0	—	—	0.0	45.0	9.56E+03
480	USGS-031	4786.3	1.70E+04	270.0	304.0	34.0	306.0	428.0	122.0	—	—	0.0	—	—	0.0	—	—	0.0	156.0	1.09E+02
486	USGS-037	4929.4	1.60E+04	507.0	571.5	64.5	—	—	0.0	—	—	0.0	—	—	0.0	—	—	0.0	64.5	2.48E+02
489	USGS-040	4916.2	8.70E+04	452.0	678.8	226.8	—	—	0.0	—	—	0.0	—	—	0.0	—	—	0.0	226.8	3.84E+02
492	USGS-043	4916.1	8.00E+04	450.5	675.8	225.3	—	—	0.0	—	—	0.0	—	—	0.0	—	—	0.0	225.3	3.55E+02
500	USGS-051	4918.7	2.90E+03	475.2	659.0	183.8	—	—	0.0	—	—	0.0	—	—	0.0	—	—	0.0	183.8	1.58E+01
506	USGS-057	4922.5	2.80E+04	474.0	732.0	258.0	—	—	0.0	—	—	0.0	—	—	0.0	—	—	0.0	258.0	1.09E+02
507	USGS-058	4918.4	3.70E+04	218.0	473.0	255.0	473.0	503.0	30.0	—	—	0.0	—	—	0.0	—	—	0.0	285.0	1.30E+02
525	USGS-076	4929.7	1.90E+05	457.0	718.0	261.0	—	—	0.0	—	—	0.0	—	—	0.0	—	—	0.0	261.0	7.28E+02
531	USGS-082	4907.0	5.60E+04	470.0	570.0	100.0	593.0	693.0	100.0	—	—	0.0	—	—	0.0	—	—	0.0	200.0	2.80E+02
532	USGS-083	4941.6	9.00E+02	516.0	752.0	236.0	—	—	0.0	—	—	0.0	—	—	0.0	—	—	0.0	236.0	3.81E+00
535	USGS-086	5077.0	3.00E+02	48.0	691.0	643.0	—	—	0.0	—	—	0.0	—	—	0.0	—	—	0.0	643.0	4.67E-01
536	USGS-087	5017.4	8.50E+02	585.0	673.0	88.0	—	—	0.0	—	—	0.0	—	—	0.0	—	—	0.0	88.0	9.66E+00
537	USGS-088	5021.3	1.00E+03	584.0	635.0	51.0	—	—	0.0	—	—	0.0	—	—	0.0	—	—	0.0	51.0	1.96E+01
538	USGS-089	5029.9	4.90E+01	576.0	646.0	70.0	—	—	0.0	—	—	0.0	—	—	0.0	—	—	0.0	70.0	7.00E-01
539	USGS-090	5011.8	4.90E+02	577.0	626.0	49.0	—	—	0.0	—	—	0.0	—	—	0.0	—	—	0.0	49.0	1.00E+01
546	USGS-097	4858.9	7.10E+04	388.0	510.0	122.0	—	—	0.0	—	—	0.0	—	—	0.0	—	—	0.0	122.0	5.82E+02
547	USGS-098	4883.3	8.10E+04	401.0	421.0	20.0	463.0	505.0	42.0	—	—	0.0	—	—	0.0	—	—	0.0	62.0	1.31E+03
548	USGS-099	4872.4	1.10E+05	449.0	450.0	1.0	340.0	449.0	109.0	—	—	0.0	—	—	0.0	—	—	0.0	110.0	1.00E+03
549	USGS-100	5158.5	1.40E+04	662.0	750.0	88.0	—	—	0.0	—	—	0.0	—	—	0.0	—	—	0.0	88.0	1.59E+02
550	USGS-101	5251.6	1.20E+03	750.0	865.0	115.0	—	—	0.0	—	—	0.0	—	—	0.0	—	—	0.0	115.0	1.04E+01

Table A-2. (continued).

Well ID[a]	Well Alias	Ground Surface Elev (ft AMSL)	Reported Trans-missivity (ft/day)	Screen Top 1 (ft bgs)	Screen Bottom 1 (ft bgs)	Open Thick-ness 1 (ft)	Screen Top 2 (ft bgs)	Screen Bottom 2 (ft bgs)	Open Thick-ness 2 (ft)	Screen Top 3 (ft bgs)	Screen Bottom 3 (ft bgs)	Open Thick-ness 3 (ft)	Screen Top 4 (ft bgs)	Screen Bottom 4 (ft bgs)	Open Thick-ness 4 (ft)	Screen Top 5 (ft bgs)	Screen Bottom 5 (ft bgs)	Open Thick-ness 5 (ft)	Total Exposed Thick-ness (ft)	Hydraulic Conductivity (ft/day)
552	USGS-103	5007.4	1.60E+05	575.0	760.0	185.0	—	—	0.0	—	—	0.0	—	—	0.0	—	—	0.0	185.0	8.65E+02
553	USGS-104	4988.7	1.40E+01	550.0	700.0	150.0	—	—	0.0	—	—	0.0	—	—	0.0	—	—	0.0	150.0	9.33E-02
554	USGS-105	5095.1	8.50E+04	400.0	800.0	400.0	—	—	0.0	—	—	0.0	—	—	0.0	—	—	0.0	400.0	2.13E+02
555	USGS-106	5015.4	1.00E+05	400.0	605.0	205.0	605.0	760.0	155.0	—	—	0.0	—	—	0.0	—	—	0.0	360.0	2.78E+02
556	USGS-107	4917.5	7.00E+04	270.0	690.0	420.0	—	—	0.0	—	—	0.0	—	—	0.0	—	—	0.0	420.0	1.67E+02
557	USGS-108	5031.4	1.50E+05	400.0	760.0	360.0	—	—	0.0	—	—	0.0	—	—	0.0	—	—	0.0	360.0	4.17E+02
558	USGS-109	5043.6	1.10E+05	600.0	800.0	200.0	—	—	0.0	—	—	0.0	—	—	0.0	—	—	0.0	200.0	5.50E+02
559	USGS-110	5000.0	1.10E+04	580.0	780.0	200.0	—	—	0.0	—	—	0.0	—	—	0.0	—	—	0.0	200.0	5.50E+01
560	USGS-111	4920.5	2.20E+01	430.0	442.0	12.0	442.0	600.0	158.0	—	—	0.0	—	—	0.0	—	—	0.0	170.0	1.29E-01
561	USGS-112	4927.8	6.40E+04	430.0	444.0	14.0	444.0	563.0	119.0	—	—	0.0	—	—	0.0	—	—	0.0	133.0	4.81E+02
562	USGS-113	4925.3	1.90E+05	443.0	561.0	118.0	—	—	0.0	—	—	0.0	—	—	0.0	—	—	0.0	118.0	1.61E+03
563	USGS-114	4920.1	1.00E+01	440.0	560.0	120.0	—	—	0.0	—	—	0.0	—	—	0.0	—	—	0.0	120.0	8.33E-02
564	USGS-115	4918.8	3.20E+01	437.0	580.0	143.0	—	—	0.0	—	—	0.0	—	—	0.0	—	—	0.0	143.0	2.24E-01
565	USGS-116	4916.0	1.50E+02	401.0	438.0	37.0	438.0	572.0	134.0	—	—	0.0	—	—	0.0	—	—	0.0	171.0	8.77E-01
566	USGS-117	5012.7	1.40E+01	550.0	653.0	103.0	—	—	0.0	—	—	0.0	—	—	0.0	—	—	0.0	103.0	1.36E-01
568	USGS-119	5031.9	1.10E+00	639.0	705.0	66.0	—	—	0.0	—	—	0.0	—	—	0.0	—	—	0.0	66.0	1.67E-02
569	USGS-120	5040.6	1.30E+06	638.1	705.0	66.9	—	—	0.0	—	—	0.0	—	—	0.0	—	—	0.0	66.9	1.94E+04
595	WATER SUPPLY FOR INEL 1	4872.8	3.70E+02	340.0	497.0	157.0	507.0	594.5	87.5	—	—	0.0	—	—	0.0	—	—	0.0	244.5	1.51E+00
748	TAN-12	4780.7	3.50E+04	362.8	382.0	19.2	—	—	0.0	—	—	0.0	—	—	0.0	—	—	0.0	19.2	1.82E+03
765	M1SA	5011.1	2.00E+01	608.0	638.0	30.0	—	—	0.0	—	—	0.0	—	—	0.0	—	—	0.0	30.0	6.67E-01
766	M3S	5016.2	1.00E+03	602.8	632.8	30.0	—	—	0.0	—	—	0.0	—	—	0.0	—	—	0.0	30.0	3.33E+01
767	M4D	5022.5	4.00E+00	798.0	828.0	30.0	—	—	0.0	—	—	0.0	—	—	0.0	—	—	0.0	30.0	1.33E-01
768	M6S	5065.8	3.00E+01	638.0	668.0	30.0	—	—	0.0	—	—	0.0	—	—	0.0	—	—	0.0	30.0	1.00E+00
769	M7S	5004.9	1.00E+03	598.0	628.0	30.0	—	—	0.0	—	—	0.0	—	—	0.0	—	—	0.0	30.0	3.33E+01
770	M10S	5021.6	4.00E+00	618.0	648.0	30.0	—	—	0.0	—	—	0.0	—	—	0.0	—	—	0.0	30.0	1.33E-01
791	TAN-19	4803.4	4.00E+05	396.0	416.0	20.0	—	—	0.0	—	—	0.0	—	—	0.0	—	—	0.0	20.0	2.00E+04
1008	TANT-MON-A-028	4781.4	1.70E+04	220.0	260.0	40.0	—	—	0.0	—	—	0.0	—	—	0.0	—	—	0.0	40.0	4.25E+02
1009	TANT-MON-A-	4780.4	1.80E+04	220.4	250.4	30.0	—	—	0.0	—	—	0.0	—	—	0.0	—	—	0.0	30.0	6.00E+02

Table A-2. (continued).

Well ID[a]	Well Alias	Ground Surface Elev (ft AMSL)	Reported Trans-missivity (ft/day)	Screen Top 1 (ft bgs)	Screen Bottom 1 (ft bgs)	Open Thick-ness 1 (ft)	Screen Top 2 (ft bgs)	Screen Bottom 2 (ft bgs)	Open Thick-ness 2 (ft)	Screen Top 3 (ft bgs)	Screen Bottom 3 (ft bgs)	Open Thick-ness 3 (ft)	Screen Top 4 (ft bgs)	Screen Bottom 4 (ft bgs)	Open Thick-ness 4 (ft)	Screen Top 5 (ft bgs)	Screen Bottom 5 (ft bgs)	Open Thick-ness 5 (ft)	Total Exposed Thick-ness (ft)	Hydraulic Conductivity (ft/day)
	027																			
1010	TANT-MON-A-029	4781.2	2.20E+04	222.3	262.3	40.0	—	—	0.0	—	—	0.0	—	—	0.0	—	—	0.0	40.0	5.50E+02
1012	TANT-MON-A-030A	4781.4	1.70E+04	299.9	319.9	20.0	—	—	0.0	—	—	0.0	—	—	0.0	—	—	0.0	20.0	8.50E+02
1117	TANT-MON-A-024	4781.4	2.10E+04	217.0	297.0	80.0	—	—	0.0	—	—	0.0	—	—	0.0	—	—	0.0	80.0	2.63E+02
1131	OW-1	5041.6	3.00E+06	623.0	1000.0	377.0	—	—	0.0	—	—	0.0	—	—	0.0	—	—	0.0	377.0	7.96E+03
1132	OW-2	5043.7	3.00E+06	600.0	1000.0	400.0	—	—	0.0	—	—	0.0	—	—	0.0	—	—	0.0	400.0	7.50E+03
1162	LSIT Test Well	5042.0	5.00E+05	603.0	857.0	254.0	—	—	0.0	—	—	0.0	—	—	0.0	—	—	0.0	254.0	1.97E+03
1212	SOUTH-MON-A-001	4995.6	2.44E+03	559.0	569.0	10.0	604.0	624.0	20.0	—	—	0.0	—	—	0.0	—	—	0.0	30.0	8.13E+01
1214	SOUTH-MON-A-003	5026.9	3.40E+02	623.1	643.1	20.0	—	—	0.0	—	—	0.0	—	—	0.0	—	—	0.0	20.0	1.70E+01
1215	SOUTH-MON-A-004	5032.5	2.09E+02	583.6	604.6	21.0	624.6	634.6	10.0	—	—	0.0	—	—	0.0	—	—	0.0	31.0	6.74E+00
1219	TAN-31	4780.8	2.10E+04	205.0	310.0	105.0	—	—	0.0	—	—	0.0	—	—	0.0	—	—	0.0	105.0	2.00E+02
1327	RWMC-MON-A-162	5026.9	5.04E+02	598.5	628.5	30.0	—	—	0.0	—	—	0.0	—	—	0.0	—	—	0.0	30.0	1.68E+01
1337	SOUTH-MON-A-010	5032.5	3.12E+02	578.0	598.0	20.0	598.0	613.0	15.0	—	—	0.0	—	—	0.0	—	—	0.0	35.0	8.91E+00
1338	SOUTH-MON-A-009	5019.2	9.27E+02	600.0	620.0	20.0	—	—	0.0	—	—	0.0	—	—	0.0	—	—	0.0	20.0	4.64E+01
SWGM1	Lindholm Well 20	4868.8	1.10E+06	10.0	110.0	38.0	—	—	0.0	—	—	0.0	—	—	0.0	—	—	0.0	38.0	2.89E+04
SWGM2	Lindholm Well 21	4793.3	6.60E+05	80.0	120.0	75.0	—	—	0.0	—	—	0.0	—	—	0.0	—	—	0.0	75.0	8.80E+03
SWGM3	Lindholm Well 23	4793.3	7.10E+05	9.0	300.0	60.0	—	—	0.0	—	—	0.0	—	—	0.0	—	—	0.0	60.0	1.18E+04
SWGM4	Butte City	5321.5	5.01E+02	461.0	475.0	14.0	—	—	0.0	—	—	0.0	—	—	0.0	—	—	0.0	14.0	3.58E+01
SWGM5	Howe Water District	4793.3	7.40E+01	130.0	177.0	47.0	—	—	0.0	—	—	0.0	—	—	0.0	—	—	0.0	47.0	1.57E+00
SWGM6	Russell Mays	4793.3	2.38E+03	417.0	645.0	228.0	—	—	0.0	—	—	0.0	—	—	0.0	—	—	0.0	228.0	1.04E+01
SWGM7	Bob Mays	4813.0	3.25E+02	535.0	540.0	5.0	563.0	572.0	9.0	—	—	0.0	—	—	0.0	—	—	0.0	14.0	2.32E+01

Table A-2. (continued).

Well ID[a]	Well Alias	Ground Surface Elev (ft AMSL)	Reported Trans-missivity (ft/day)	Screen Top 1 (ft bgs)	Screen Bottom 1 (ft bgs)	Open Thick-ness 1 (ft)	Screen Top 2 (ft bgs)	Screen Bottom 2 (ft bgs)	Open Thick-ness 2 (ft)	Screen Top 3 (ft bgs)	Screen Bottom 3 (ft bgs)	Open Thick-ness 3 (ft)	Screen Top 4 (ft bgs)	Screen Bottom 4 (ft bgs)	Open Thick-ness 4 (ft)	Screen Top 5 (ft bgs)	Screen Bottom 5 (ft bgs)	Open Thick-ness 5 (ft)	Total Exposed Thick-ness (ft)	Hydraulic Conductivity (ft/day)
SWG M8	Roe Ownes	4796.6	2.29E+03	400.0	602.0	202.0	—	—	0.0	—	—	0.0	—	—	0.0	—	—	0.0	202.0	1.13E+01
SWG M9	ID HWY Dept	4901.6	1.72E+05	115.0	194.0	79.0	—	—	0.0	—	—	0.0	—	—	0.0	—	—	0.0	79.0	2.18E+03
SWG M10	Western Potato #2	5009.8	1.16E+07	470.0	570.0	100.0	—	—	0.0	—	—	0.0	—	—	0.0	—	—	0.0	100.0	1.16E+05
SWG M11	James Rire	4973.7	1.42E+03	530.0	695.0	165.0	—	—	0.0	—	—	0.0	—	—	0.0	—	—	0.0	165.0	8.58E+00
SWG M12	Leon Dance	4881.9	6.10E+03	503.0	640.0	137.0	—	—	0.0	—	—	0.0	—	—	0.0	—	—	0.0	137.0	4.45E+01
SWG M13	BAS	5167.3	2.10E+02	60.0	65.0	5.0	—	—	0.0	—	—	0.0	—	—	0.0	—	—	0.0	5.0	4.20E+01
SWG M14	Elmer Lamprecht	5180.4	1.12E+05	69.0	75.0	6.0	—	—	0.0	—	—	0.0	—	—	0.0	—	—	0.0	6.0	1.87E+04
SWG M15	TS Vanderford1	4616.1	1.47E+04	240.0	265.0	25.0	—	—	0.0	—	—	0.0	—	—	0.0	—	—	0.0	25.0	5.88E+02
SWG M16	TS Vanderford2	4606.3	1.04E+04	208.0	240.0	32.0	—	—	0.0	—	—	0.0	—	—	0.0	—	—	0.0	32.0	3.26E+02
SWG M17	IF BLM	4763.8	1.54E+04	690.0	720.0	30.0	—	—	0.0	—	—	0.0	—	—	0.0	—	—	0.0	30.0	5.14E+02
SWG M18	Charles Behrend	4580.0	1.04E+05	177.0	305.0	128.0	—	—	0.0	—	—	0.0	—	—	0.0	—	—	0.0	128.0	8.12E+02
SWG M19	Don Everingham	4507.9	2.33E+02	98.0	140.0	42.0	—	—	0.0	—	—	0.0	—	—	0.0	—	—	0.0	42.0	5.55E+00
SWG M20	Bill Dishman	4648.9	2.38E+02	109.0	145.0	36.0	—	—	0.0	—	—	0.0	—	—	0.0	—	—	0.0	36.0	6.61E+00
SWG M21	Ralph Furniss	4671.9	4.99E+06	105.0	268.0	163.0	—	—	0.0	—	—	0.0	—	—	0.0	—	—	0.0	163.0	3.06E+04
SWG M22	Dan Polatis	4619.4	6.63E+06	140.0	300.0	160.0	—	—	0.0	—	—	0.0	—	—	0.0	—	—	0.0	160.0	4.14E+04
SWG M23	BLM	5318.2	4.21E+04	994.0	1046.0	52.0	—	—	0.0	—	—	0.0	—	—	0.0	—	—	0.0	52.0	8.10E+02

a. From the Hydrogeologic Data Repository at the Idaho National Laboratory Site.

AMSL = above mean sea level
bgs = below ground surface

Appendix B

Notation and Parameter Values Used in Equation 3-2

Appendix B

Notation and Parameter Values Used in Equation 3-2

As arranged, the PDE Toolbox described in Subsection 3.2 solves the following elliptical partial differential equation:

$$\mathrm{div}(c \cdot \mathrm{grad}(u)) + a \cdot u = f \tag{B-1}$$

where

u = temperature

c, a, and f = coefficients.

Advective transport is included by specifying that the coefficient "f" depends on temperature gradient and a specified velocity, effectively altering the equation to a parabolic form. The value of "a" is zero. The "c" term is a tensor, thus allowing a means of scaling transport in the x and y directions independently. Under the base case scenario, the "c" term is as follows, except that the c_{11} value is divided by 200 to scale the length in the x-direction to 200 km (124 mi):

$$\begin{pmatrix} \kappa_{eff} + \alpha_x \cdot q_x \cdot C_{eff} & 0 \\ 0 & \kappa_{eff} + \alpha_y \cdot q_x \cdot C_{eff} \end{pmatrix} = \begin{pmatrix} 5.9 & 0 \\ 0 & 2.321 \end{pmatrix} \frac{kg \cdot m}{s^3 \cdot K} \tag{B-2}$$

Here α_x and α_y are the longitudinal and transverse dispersivities, respectively; q_x is the horizontal groundwater flux density; and other coefficients are as summarized as follows:

Porosity

$n := 0.05$

Specific heats

$c_w := 2060 \frac{joule}{kg \cdot K}$ $\quad c_w = 2.06 \times 10^3 \frac{1}{kg \cdot K} J$

$c_s := 0.2 \cdot kcal \cdot (kg \cdot K)^{-1}$ $\quad c_s = 837.36 \frac{1}{kg \cdot K} J$

Heat capacities

$C_w := \rho_w \cdot c_w$ $\quad C_w = 2.06 \times 10^6 \frac{1}{m^3 \cdot K} J$

$C_s := \rho_s \cdot c_s$ $\quad C_s = 2.303 \times 10^6 \frac{1}{m^3 \cdot K} J$

Effective heat capacity

$C_{eff} := n \cdot \rho_w \cdot c_w + (1 - n) \cdot \rho_s \cdot c_s$ $\quad C_{eff} = 2.291 \times 10^6 \frac{1}{m^3 \cdot K} J$

Thermal conductivity

$\kappa_w := 0.11 \cdot cal \cdot m^{-1} \cdot s^{-1} \cdot K^{-1}$ $\quad \kappa_w = 0.461 \frac{1}{m \cdot K} watt$

$\kappa_s := 2 \cdot watt \cdot m^{-1} \cdot K^{-1}$ $\quad \kappa_s = 2 \frac{1}{m \cdot K} watt$

Reduction in thermal conductivity due to totuosity

$Ktort := 0$

Effective thermal conductivity

$\kappa_{eff} := n \cdot \kappa_w + (1 - n) \kappa_s - \kappa_s \cdot Ktort$ $\quad \kappa_{eff} = 1.923 \frac{1}{m \cdot s \cdot K} joule$